The Feasibility of a Novel Sensing System for Robotic Cochlear Electrode Array Feed for Hearing Preservation

LEI HOU

Brunel Institute for Bioengineering
Brunel University London

A thesis submitted for the degree of
Doctor of Philosophy

May 2019

To my wife, Qunfang Jiang

my father and mother

Changjiang Hou & Minge Feng

For their unconditional love and support

Declaration of Authenticity

I hereby declare that I am the sole author of this thesis.

LEI HOU

Abstract

A cochlear implant (CI) was a small electronic device that could provide direct electrical stimulation to the auditory nerve. Unlike a hearing aid, a cochlear implant turned sounds into electrical pulses which were sent directly to the auditory nerve. During a cochlear implant surgery, intracochlear electrode array insertion was considered to be a crucial process. However, the behaviour of the intracochlear electrode array during the insertion remained unclear to surgeons and the behaviour was hardly diagnosed by normal methods. In order to minimize or eliminate the trauma induced by electrode array insertion, we proposed an electrode capacitive sensing method to discriminate among certain signal patterns and notify the surgeons whether the array was placed correctly during the insertion process.

In this thesis, we firstly investigated the mechanical behaviour of a CI electrode array during the insertion process. A force model simulating the first contact between the array tip and cochlear inner wall was proposed. Experimental results demonstrated that insertion force was not an effective method for detecting the array behaviours inside of the cochlea. Secondly, we investigated the theory and influencing factors of the capacitive sensing measurements. The relationship between capacitance measured and environmental effect, structural effect and applied force were examined and assessed. Our exploration demonstrated that the measured bipolar capacitive signals were recognised to be sensitive, consistent and reliable. Experiment results revealed that electrode capacitance values were systematically affected by intracochlear forces between the scala tympani wall and the contact electrode. Thirdly, by analysing the bipolar capacitance experimental results, three CI electrode array insertion patterns between the array and the cochlear lateral wall were classified. The possibility of the three patterns which an unknown insertion would fall into could be discriminated by the Principal Component Analysis (PCA) and The Pearson Correlation Coefficient (PCC) analysis. Experiment results showed the overall identification success rate was over 80%. Finally, a multi-channel switch board was proposed to measure multiple electrode pairs at the same time during the array insertion. Measurements and verification based on the board were carried out and shown to be efficient for capacitive signals measuring and recording.

Acknowledgements

I would like to express my special appreciation and thanks to my supervisors Dr. Xinli Du, Dr. Nikolaos V. Boulgouris and Professor Peter Brett.

Grateful acknowledgement was made to Chris Coulson, Richard Irving and Philip Begg for their help and support on clinical matters.

Special thanks to Professor Colin Clark, Dr. Yu Zhang, Jenny Kume, Roger Patton and all participants and support members of this project.

I would like to thank my family, friends and colleagues for all their encouragement and support during this project.

Publication List

1. HOU, L., Du, X. and Boulgouris, N.V. (2018). *A Novel Sensing System for Robotic Cochlear Implants Electrode Array Placement*. In: 2018 7th IEEE International Conference on Biomedical Robotics and Biomechatronics (Biorob). IEEE, pp.1133 -1137. DOI: 10.1109/BIOROB.2018.8487984

2. HOU, L., Du, X. and Boulgouris, N.V. (2018). *Capacitance Measures duringCochlear Implants Electrode Array Positioning*. In: 10th International Conference on Bioinformatics and Biomedical Technology (ICBBT '18). New York, NY, USA: ACM, pp.78-82.DOI: 10.1145/3232059.3232069

3. L.Hou, X.Du, N.V. Boulgouris, *A Novel Sensing System for Cochlear Implant Electrode Array Placement to Discriminate Failure Insertion Patterns*. (Submitted to Hearing Research)

Contents

List of Figures

List of Tables

Abbreviations

3D	Three Dimensional
AC	Alternative Current
AOS	Advance Off-Stylet
BP	Bipolar
CG	Common Ground
CIM	Continuous Impedance Measurement
DAQ	Data Acquisition Module
DoF	Degree-of-Freedom
EAS	Electric Acoustic Stimulation
EFI	Electrical Field Imaging
ESR	Equivalent Series Resistance
FDM	Finite Difference Methods
GUI	Graphical User Interface
MONO	Monopolar
MRA	Modiolar Research Array
OP	Open Circuit
PCA	Principal Component Analysis
PCC	Pearson Correlation Coefficient
PDMS	Poly Dimethyl Siloxane
QUAD	Quadrupolar Mode
RW	Round Window
SC	Short Circuit
SIT	Standard Insertion Technique
SM	Scala Media
SNHL	Sensorineural Hearing Loss
SSCOM	Serial Port Debug Tool
ST	Scala Tympani
SV	Scala Vestibuli

Chapter 1

Introduction

1.1 Research Motivation

During the cochlear implant surgery, surgeons inserted long, thin and flexible electrode arrays into the scala tympani canal. To date, the insertion of electrode array was conducted by hand, and the tools used by surgeons did not provide any signal feedback. Surgeons might not notice the trauma until post-operation. To preserve the cochlea and minimize the intracochlear trauma, a sensing system could be developed to discriminate the electrode array three insertion patterns.

There were two reasons why the sensing system was necessary. Firstly, by 2016, approximately 12,000 registered devices had been implanted in the UK [1]. However, more than 900,000 people in the UK were severely or profoundly deaf [2]. One of the significant reasons for the difference was that the current cochlear implant surgery would destroy all the remaining hearing in the implanted ear.

Thus, the cochlear implant was only considered when the sound field of individual was below 25dB at 4000 Hz frequency and for those who could not benefit more from an acoustic hearing aid [3]. By preserving the residual hearing, more adults and children with profound hearing loss could be benefited from the cochlear implant.

Secondly, during a cochlear implant surgery, atraumatic electrode array insertion was a crucial step. A cochlear implant surgery might result in intra-cochlear trauma and misplacement of the electrode array. Due to the variations of the cochlear shape and size, the electrode array tip might buckling inside of the scala tympani or even fold-over during the array insertion. These scenarios would cause of trauma to the cochlear structures or result in the malfunctions of the cochlear implant array. The displacement of the electrode array would not be noticed until the operation was finished. Revision required re-opening the incisions and reinsertion of the electrode array. The operation would cause more trauma to the patients.

Based on the reasons discussed above, a sensing system should be developed to help surgeons guide the electrode array in. With the assisting of the system, the extensive incision between the array and the cochlear structures would be detected and minimised to preserve the patients' residual hearing. Certain behaviours of the electrode array inside of the cochlea could be discriminated by the system.

1.2 Background

In this section, the background knowledge of anatomy of the human auditory system, three types of hearing loss and their treatments as well as the cochlear implant were introduced.

1.2.1 Anatomy of Auditory System

This section described the anatomy of the human auditory system, in particular, the inner ear structure. There were three main components of the human auditory system: the outer ear, middle ear and inner ear [4]. The structure of the human auditory system are shown in Figure 1-1

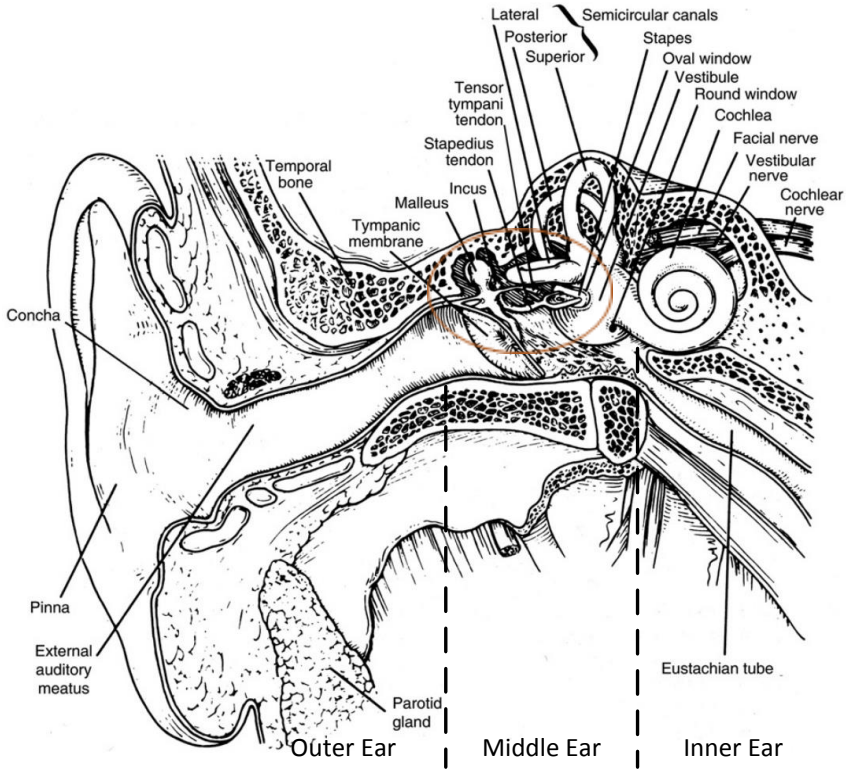

Figure 1-1: The human auditory system structure. (Image from [4])

1.2.1.1 Outer Ear

The outer ear consisted of the pinna and external auditory meatus. Pinna was the visible part of the ear which collected sound waves in human adult. The external auditory meatus was a 2.5 cm tube ending at the tympanic membrane [5]. The function of the outer ear was to guide sound waves to the middle ear. Pinna could increase the sensitivity of the ear to the front side of the head [6].

1.2.1.2 Middle Ear

The middle ear consisted of the tympanic membrane (ear drum), attached to the inner ear through three bones (known as the ossicular chain: the malleus, incus, and stapes). The primary function of the middle ear was to transmit sound waves from the air to the fluids in the inner ear [6].

1.2.1.3 Inner Ear and the Cochlea

Within the inner ear, the cochlea was a significant portion of the system. The human cochlea was a spiral-shaped cavity with $2\frac{1}{2}$ to $2\frac{3}{4}$ turns that could be divided into three different chambers (Figure 1-2): the scala vestibuli (SV), the scala tympani (ST) and scala media (SM). Each of the chambers was receptive to different frequencies of vibration [7]. A cross section of the cochlea showing the three chambers is shown in Figure 1-2.

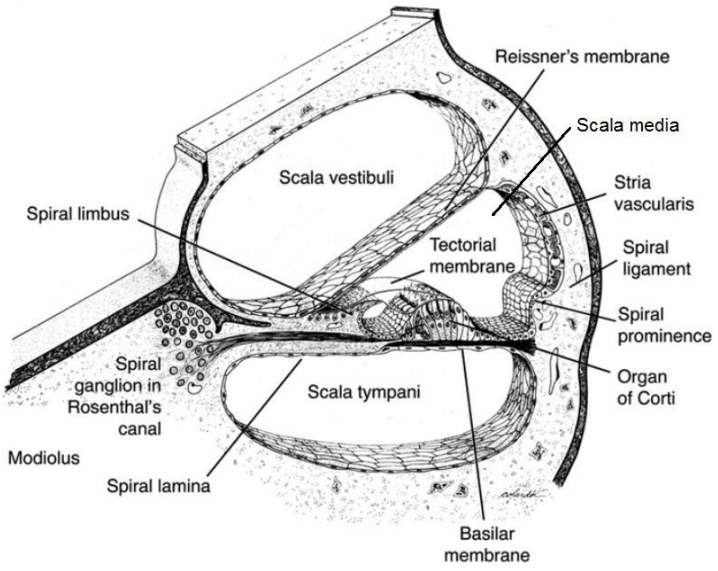

Figure 1-2: The Cochlear cross section diagram. The diagram showed the location of the three chambers: the scala vestibuli, the scala tympani and scala media. (Image from [6])

The cochlea transfers mechanical signals from the middle ear into a complex series of electrical signals to the auditory nerve, where it was interpreted as sound. Sound waves travelled through the ear canal and cause the tympanic membrane and ossicular chain to vibrate. Movement of the stapes located at the end of the ossicular chain vibrates the oval window of the cochlea. The primary fluid in the cochlea was the perilymph. When the cochlea receives sound in the form of vibration, the hair cells at the basilar membrane were disturbed transforming the vibrational energy into nerve impulses interpreted by the brain as sound [8].

1.2.2 Hearing Loss and Treatment

Hearing loss was classified by which part of the auditory system was damaged. There were three categories of hearing loss: Conductive hearing loss, Sensorineural hearing loss, and Mixed hearing loss [9].

Conductive hearing loss was due to problems of mechanical transmission of sound. It happened at the ear canal, ear drum, middle ear and ossicular chain. It could be treated surgically or medically [10].

Sensorineural hearing loss (SNHL) resulted from inner ear or auditory nerve dysfunction. The causes of damage to the cochlear were various: include loud sound exposure, powerful antibiotics, diseases, auditory tumour and hearing decline with age [11]. Different hearing solutions were available for various hearing levels and types of hearing loss. A cochlear implant was the first line therapy for the treatment of bilateral, severe to profound hearing loss patients [12]. The device stimulated the hearing receptors directly. Children could also be the patients for the cochlear implant surgery as young as 12 months [13].

Mixed hearing loss was the combination of conductive hearing loss and sensorineural hearing loss. The treatment focused on the conductive component first.

In conclusion, the auditory system was responsible for the sense of hearing. It consisted of three main divisions: the outer ear, middle ear and inner ear. Hearing loss was classified by which part of the auditory system was damaged, and it had three categories. A cochlear implant was the first line of therapy for the treatment of bilateral, severe to profound deafness patients.

1.2.2.1 History of the Cochlear Implants

Stimulating hearing by electrical methods began in the late 18th century when Alessandro Volta discovered the electrolytic cell [14]. He was the first to stimulate the auditory system electrically. In the 1940's and 1950's, researchers in electrophonic hearing discovered hearing was produced by transducing sound vibrations into electrical signals [15]. In 1950, one of the first documented operations to stimulate the auditory nerve was performed by Lunderg. Unfortunately, his patient could only hear noise after the surgery [15]. In 1957, Djourno and Eyries provided the first detailed explanation of directly stimulating the auditory nerve [16]. In 1964, Doyle et al. inserted an electrode array bundle into the cochlea of a total perceptive deafness patient. This operation was significant as the patient was able to hear spoken phrases [14]. In 1972, a speech processor was designed to interface with an electrode implant, and it was the first to be commercially marketed [17]. After that, between 1972 to the mid-1980s, more than 1,000 of the devices were implanted.

Through the 1990s, with the development of clinical and basic science studies, electrode and speech processor design had been improved significantly with a higher performance level. The cochlear implants had been increasingly accepted and recommended for implant patients.

1.2.3 Cochlear Implant

A Cochlear electrode implant referred to as a CI, was a small electronic device that could provide direct electrical stimulation to the auditory nerve which was located in the inner ear [18]. Unlike a hearing aid, a cochlear implant turned sounds into electrical pulses which were sent directly to the auditory nerve [19]. Adults and children with severe or profound hearing loss could be helped with a cochlear implant [20]. In this section, the structure and function of the normal cochlea would be introduced. The cochlear implant consisted of two parts: external (outside) part and internal part. They combined to assist patients to perceive sound. The configuration of the cochlear implant system is shown in Figure 1-3.

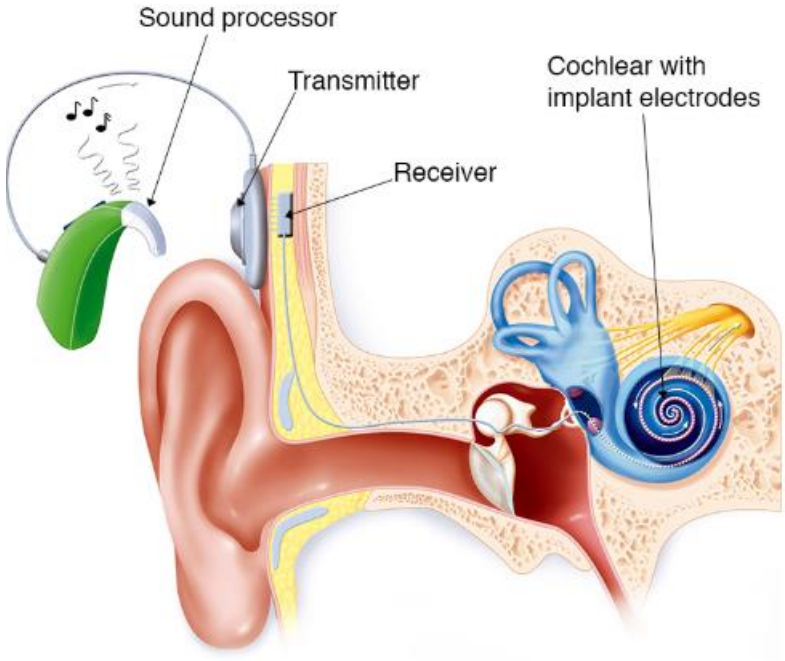

Figure 1-3: Structure of a cochlear implant device. Configuration the External Device and Internal part of a Cochlear Implant in Human ear. (Image from [21])

1.2.3.1 External part

The external part consisted of a signal-processing chip, a connecting cable, a microphone and a transmitter. The external parts were worn behind the ear. The microphone was designed to detect incident sound from the environment and transmitted the signal to the processing chip. The signal-processing chip analysed and digitised the sound signals and output to the transmitter. The transmitter was placed behind the ear and transmits the coded signals to the radio receiver under the skin.

1.2.3.2 Internal Part

The internal part of the cochlear implant consisted of a radio receiver and a cochlear implant electrode array [22]. They were surgically placed under the skin. The receiver could detect the coded electric impulses and outputs to the electrode array that was surgically implanted into the cochlea. The electric impulses stimulated the auditory nerve, and they were interpreted by the brain as sound.

1.2.3.3 The Cochlear Implant Electrode Array

Electrode arrays had the capacity of electrical stimulation of the auditory nerve in the cochlea that was differentially sensitive to sound frequencies to initiate sound sensations. Picture of an electrode array is shown in Figure 1-4.

Figure 1-4: Example of an electrode array. (Image from [23])

An electrode array was composed of conductive, corrosion-resistant, noble metal platinum-iridium alloy that was separated by insulating material, for example, poly dimethyl siloxane (PDMS) [24]. Ideally, each electrode should be placed directly to contact with a single nerve ending that allowed receiving sound waves of appropriate frequencies. The number of electrodes in the array depend on the manufacturer but typically was between 4 to 22 that was less than 1% of the number of hair cells present in the cochlea [24].

1.2.3.4 The Cochlear Implant Electrode Insertion

Insertion of the cochlear implant electrode array was the most crucial step in the cochlear implant surgery. The electrode array should be optimally inserted into the scala tympani. A cross section diagram of the electrode array insertion from round window and cochleostomy is shown in Figure 1-5.

The electrode array insertion progress was a pierce event: the round window (RW) membrane was incised, or a cochleostomy drilled, as shown in Figure 1-5. Round window insertion caused greatest initial intra-cochlear damage, circled in the Figure. It was due to the inserting electrode being bent significantly to follow the cochlear canal [15]. The insertion also resulted in more abnormal tissue formation in the basal cochlea. The cochleostomy technique exposed the scala in preparation for insertion of a cochlear electrode array as shown in Figure 1-5 [15]. The technique allowed surgeons to adjust the electrode insertion trajectory to minimise the contact force between a cochlear array and the scala tympani (ST) wall.

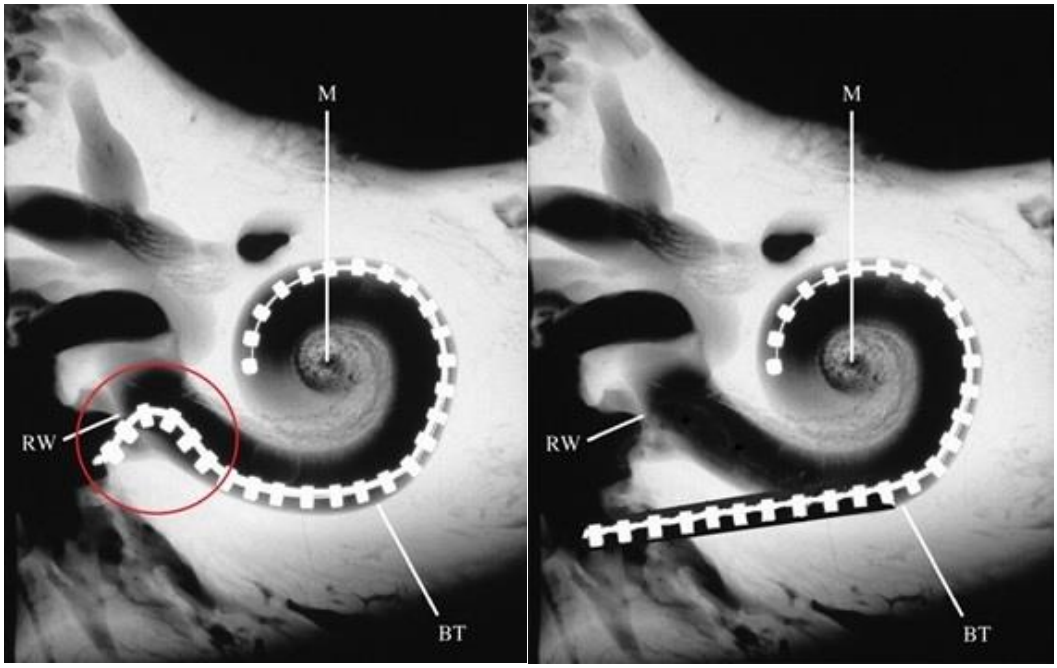

Figure 1-5: (Left) a cross section diagram of the electrode array round window insertion. (Right) a cross section diagram of the electrode array Cochleostomy insertion, where RW was round window, BT was basal turn, M was modiolus of the cochlea. (Image from [15])

To date, the insertion of an electrode to the scala tympani was done by hand. The electrode array was small, flexible and has a particular orientation to align with the tissue structure [25]. The method reflected as electrode feed and placement was a particularly skilled surgical task. It would be expected that a more experienced surgeon will enhance the ideal result. Although the insertion of the array had many procedures and variations, the process was still a crucial step. The suboptimal or even improper insertion of the electrode array would result in poor cochlear implant function.

Different kinds of complications might be caused by the insertion of the array. These complicates could be classified into minor and major issues. The minor complications included postoperative dizziness, taste disturbance, infection and facial numbness [26]. These minor complications commonly emerged after the surgery but would relief and disappear over time. The major complications would cause more serious symptom and would suffer longer period. These complications often needed revision surgery that should be avoided. Among them, two types of the electrode array misplacement: fold-over and buckling are highlighted in Figure 1-6.

Figure 1-6: Two types of the major complications: fold-over (left) and buckling (right). (Image from [27])

According to a research [27], 33 (10.5%) patients were found to have major compilations out of 315 and 20 of them (6.3%) did the revision surgeries. Misplacement of the electrode array could happen in an anomalous cochlea or by incorrect insertion [28].

In some cases, the complications happened in several months or a few years after wearing the cochlear implant. Thus, it was essential to detect these scenarios during the array insertion process.

1.3 Aim and Objectives

The overall aim was to investigate a new conceptual sensing system for the electrode array feed into the cochlea. Instead of applying sensors to the array, the transient force, displacement and capacitance information from the feed point of the array could be gathered and analysed to determine the state and behaviour of the electrode array. In order to achieve this aim, the following objectives of this project had to be fulfilled.

1. To investigate the efforts of speed, position and trajectory angle of the electrode array insertion into a plastic cochlear model. By controlling of the insertion speed and insertion angle, the extensive incision between the electrode array and the cochlear wall could be minimised.

2. A sensing system should be developed to discriminate whether the electrode array was doing the correct insertion. If not, particular failure behaviours of an inserting electrode array could be detected and classified.

3. A demonstration system would be developed using a relevant phantom.

1.4 Contributions

In previous investigations, electrode array insertion force was assessed as a key element of intra-cochlear trauma and residual hearing loss [29]. The electrode array design and mechanical behaviour were on the basis of insertion force profiles. However, the method could not detect behaviours of the electrode array inside the cochlea. Continuous Impedance Measurement (CIM) was recognized to fulfil the research gap [109]. This method confirmed that real-time impedance was easily obtainable and changing apparently with electrode intrascalar position changes [30]. Further to that, the main contributions of this research could be summarised as the follows:

1. The capacitive signals from electrodes only were gathered and evaluated. Capacitance signal was consistent, reliable, and sensitive to the press force between the array and the cochlear wall.
2. Principal Component Analysis and Eigenface-based recognition were applied to the capacitive sensing results to discriminate electrodes array certain insertion patterns (smooth, buckling, fold over).
3. The electrode capacitance measurement was improved from one coupled electrodes continuous measurement to three coupled electrodes discrete measurement. During the continuous capacitive measurement, the two measured electrodes were activated and the behaviour and movement of the remaining electrodes remained unknown. These electrodes might damage the intra-cochlear structures. The capacitive sensing method was improved by activating three pairs of electrodes to extend the sensing area.

1.5 Structure of Thesis

There were eight chapters in the thesis. A summary of each chapter was shown as follows:

Chapter 1 - Introduction - This chapter provided the background information of the research topic, included the anatomy of the human auditory system, hearing loss types and cochlear implant. Based on the background information, the research motivation and contributions were shown at the end of this chapter.

Chapter 2 - Literature Review - This chapter provided the review of recent literature in three sectors: Robotic-assisted Cochlear Implant Surgery, CI Electrode Array Insertion Force and CI Electrode Array Bipolar Capacitance Measurement.

Chapter 3 - Methodology and Experimental Tools - The materials and experimental methods for the electrode array insertion were introduced in this section. The overall expectation of the automated feed system was that once it was placed in position, it would feed an electrode into the cochlea automatically by controlling the velocity, the state of tissue interactions and also the final position of the electrode array.

Chapter 4 - Force Measurement of the Cochlear Implant Electrode Array Insertion in Vitro - Force profiles of the CI electrode array were developed and analysed. An algorithm was developed to discriminate the patterns of insertion force. A plastic bending mathematical model was developed to help to investigate and understand the performance of the electrode array insertion process.

Chapter 5 - Capacitance Measurement of the Cochlear Implant Electrode Array - Capacitive sensing results of the electrode array insertion were developed and analysed. The capacitive information included the smooth, buckling and fold-over insertion patterns.

Chapter 6 - Single Pair of Electrodes Capacitance Measurement Discrimination Process - This chapter provided the discrimination process of the three insertion patterns based on the measurement results in Chapter 5. Among the three patterns, The Principal Component Analysis was employed to discriminate the buckling insertion pattern with a success rate over 80%. The fold-over pattern was discriminated by the Pearson Correlation Coefficient analysis with a success rate over 95%.

Chapter 7 - Multi-Channel Capacitive Sensing Method - The feasibility of applying multiple pairs of electrodes for the sensing task was analysed. Further improvements were suggested in the chapter.

Chapter 8 - Conclusion

Chapter 2

Literature Review

During cochlear implant surgery, surgeons inserted long, thin and lithe electrodes into the scala tympani canal. To date, the insertion of electrode array was performed by hand, and the tools used by surgeons did not provide any force feedback or other means of sensing. This electrode array insertion would damage the cochlear structures, such as the basilar membrane and cochlear wall. A robotic system could be applied to provide control of the electrode array to minimise the interaction trauma between electrode array and cochlear lateral wall. One of the traditional haptic feedbacks of the insertion was the applied force. Due to the fact that insertion force of the cochlear implant electrode array applied to the intracochlear structures was a key element to damage the residual hearing and intracochlear trauma. It was necessary to assess the electrode array insertion force and friction force. However, the insertion force varied significantly from individual insertions, and the method cannot detect the CI electrode array behaviours inside the cochlea. To replace the insertion force detection method, electrodes impedance measurement was proposed and approved as a possible source of information to help discriminate the relation of the electrode array to the lateral wall during surgery.

The structure of this chapter was as follows. Section 2.1 reviewed five kinds of traditional robotic assistant system applied in the cochlear implant surgery. Section 2.2 reviewed the past and current attempts to evaluate the insertion and friction forces. Section 2.3 reviewed the past application of electrodes impedance measurement.

2.1 Robotic-assisted Cochlear Implant Surgery

To date, the insertion of electrode array was finished by hand, and the tools used by surgeons do not provide any signal feedback. The electrode array insertions would damage the intracochlear structures, such as the basilar membrane and cochlear lateral wall. A robotic system provided some control of the electrode array to minimise the interaction trauma between the array and the cochlea. In this section, robotic assistant systems applied in the past cochlear implant surgery were reviewed.

In 2005, Roland [31] first evaluated the manual insertion characteristics of Contour electrode arrays with the Advance Off-Stylet (AOS) versus the Standard Insertion Technique (SIT). Five Contour Advance electrode arrays with the AOS technique were evaluated in a plastic cochlear model and in a right and left temporal bone. The automated insertion system is introduced in Figure 2-1.

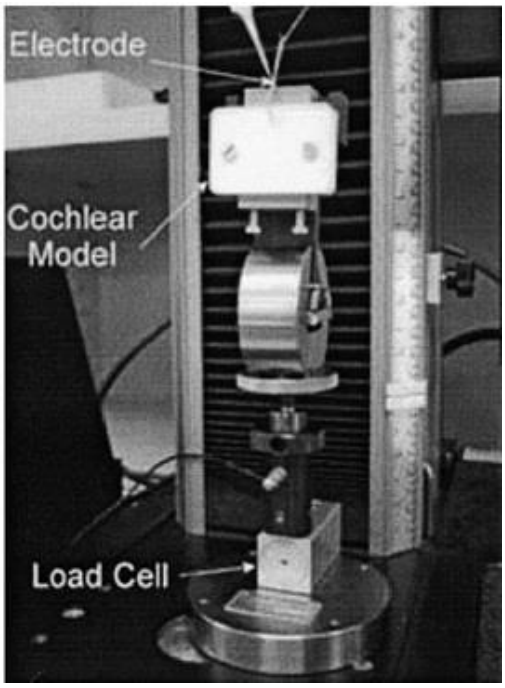

Figure 2-1: Automated insertion system with the cochlear model and load cell underneath. (Image from [31])

Five Contour electrode arrays with the Standard Insertion Technique (SIT) were evaluated in the same cochlear models and temporal bones. The applied forces during electrode arrays insertion in the cochlear model and in whole human temporal bones were measured by a load cell. According to the experimental force results, the average

insertion forces in human temporal bones could be twice as high as those recorded in a plastic cochlear model.

A preliminary study of robotic assistance using novel steerable electrode array for cochlear implant surgery was proposed in 2006 by Zhang *et al.* at Columbia University [17]. They developed the mathematic model, path planning and calibration for the cochlear steerable electrode array in an effort to minimise the interaction forces between the electrode array and the cochlea. An experimental robotic system was designed to compare the insertion forces of steerable electrode arrays with those non-steerable electrode arrays. The experimental system is shown in Figure 2-2.

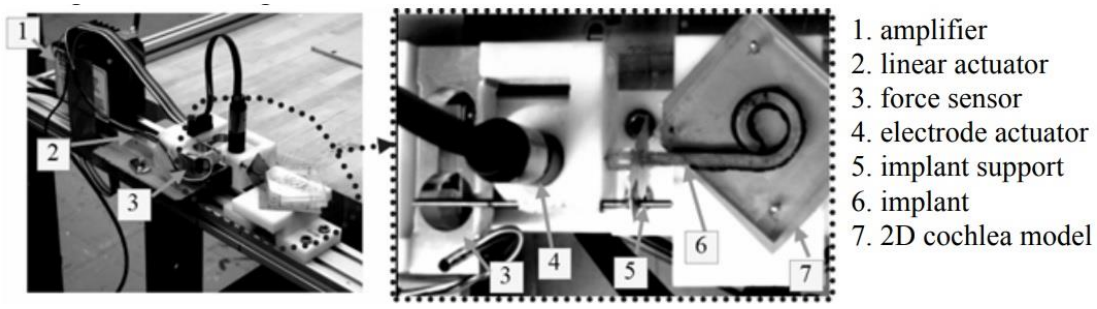

Figure 2-2: Experimental system for the robot-assisted cochlear steerable electrode array insertion. (Image from [17])

A hypothesis that the trauma in cochlear implant surgery could be significantly minimised by the reduction of electrode array insertion forces. Based on the hypothesis, the potential benefited of applying the steerable electrodes for reducing trauma in surgery were quantified. An experimental system was presented to compare the insertion forces when using steerable versus non-steerable electrodes. The results demonstrated that about 70% of insertion forces were reduced by using the steerable electrode arrays with the proposed path planning [17]. In 2008, Zhang *et al.* [32] improved the steerable electrode array to adjust its angle of approach according to the opening of scala tympani. The angle of approach from the steerable electrode arrays using a two degree-of-freedom (DoF) robot versus a four DoF robot were reviewed and stimulated. Stimulation and experimental results showed that four DoF insertions decrease the electrode deformation against the ST wall better than two DoF insertions. It also demonstrated that changing the angle of approach by a four DoF robot could further reduce the electrode array insertion forces [32].

Hussong *et al.* [33] developed a prototype automated insertion system for the cochlear implant surgery in 2008. The mechatronic device was capable of achieving the Advance Off-Stylet (AOS) technique and proofed the tool's ability in cochlear implant surgery. The first experimental result demonstrated that the device has the capability to perform general automatically cochlear implant electrodes insertions [33]. Model of the automated insertion tool is shown in Figure 2-3.

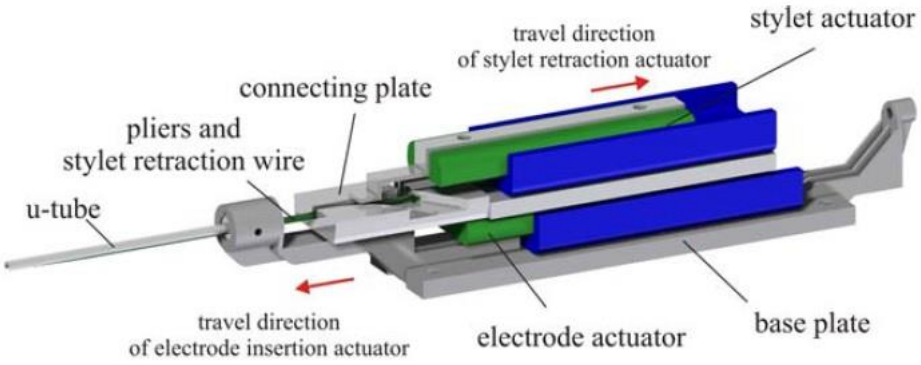

Figure 2-3: Model of the automated insertion tool with detailing its components. (Image from [33])

After that, they improved the automated insertion tool and developed a mathematical model to stimulate the entry angel and path-planning. 30 insertions were performed by the device to insert into an artificial model. Under the condition of lubrication, the electrode array was inserted into the model in 29 out of 30 insertions, with one electrode tip fold-over. It was claimed that the automated insertion tool was the only possibility for cochlear implant electrodes insertion at that time [33]. Force application of the automated insertion tool was evaluated later this year [34]. A transparent artificial scala tympani model was utilised to achieve standard experimental conditions. The experimental setup is shown in Figure 2-4.

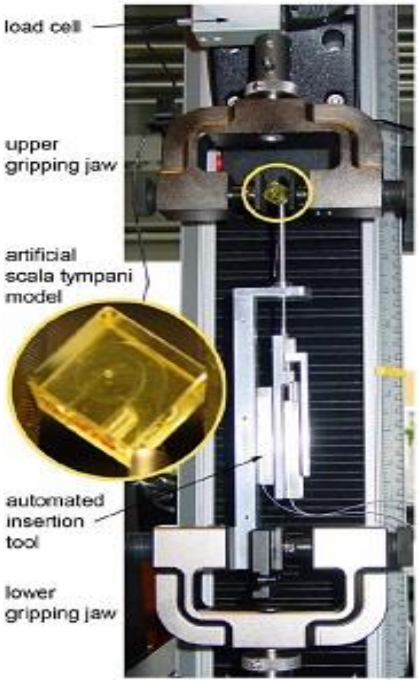

Figure 2-4: Experimental setup of the automated insertion system. (Image from [34])

The geometry and shape of the model were based on the average size of an adult human cochlea. Lubrication was applied to stimulate the similar frictional conditions within the scala tympani. During the AOS electrode array insertion process, the force exerted onto the model was recorded by a force measurement system. Overall, five contour advanced electrodes completed 20 2-Diementional insertions. The insertion forces recorded to be in a range of 5mN to 50mN [34]. One reason for the Intracochlear forces was the curled electrode array exerted onto the surface in the beginning configuration.

However, the major drawback of the system was lacking of an integrated haptic feedback. Haptic feedback was necessary for minimally invasive surgery as it represented the only available source of information about possible damage to tissue structures. The force measurement and feedback had to be integrated into the automated insertion tool. Secondly, the measurement system only applied in a plane but not in 3D of the cochlea. Lastly, the recorded force data by the automated insertion system had to be compared and evaluated with the manual insertion under the same conditions in three dimensions. This research gap was fulfilled by Majdani *et al.* in 2010.

The force data of the Advance Off-Stylet (AOS) technique during the cochlear implant electrodes insertion operated by human and by an automated insertion tool was collected by Majdani *et al.* [35]. The force data was recorded and compared by three experienced surgeons who inserted the CI electrode array 26 times and by the robotic insertion tool 8 times. Experimental results demonstrated that although the average insertion force of the insertion tool was larger than that of the surgeons, the automated device was more reliable during the insertions [35].

In the same period, Schurzig et al, [36] improved the automated insertion tool which could not only sense insertion forces but also setup the insertion velocity profiles and settings repeatable. The electrode array automated insertion system is shown in Figure 2-5.

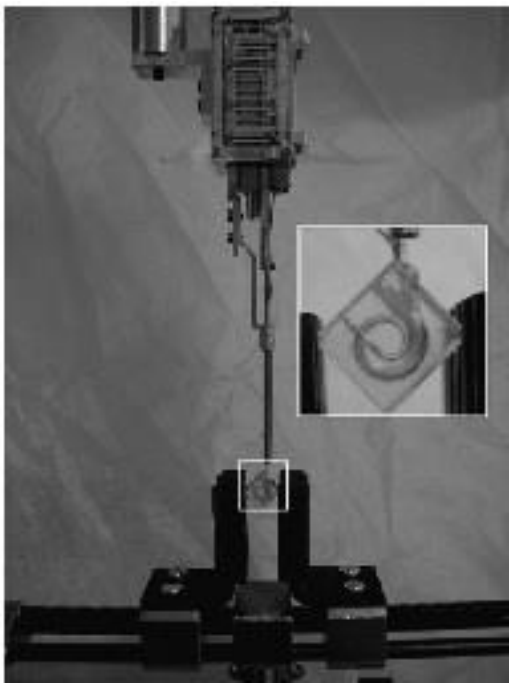

Figure 2-5: The electrode array automated insertion system by Schuzig. (Image [36])

These insertion profiles helped to quantify the insertion characteristics such as electrode forces, velocities and displacements. The insertion system was able to insert an electrode with a resolution of 1µm, inserting velocities up to 5mm/sec and forces as small as 5mN. After assembling and testing in a two dimensions cochlea model, the tool demonstrates a significant reduction in insertion forces as it could eliminate the first contact between the electrode array and the scala tympani wall [36]. The automatic system could be improved by testing in a three dimensions model. The force

data recorded by the robotic insertion tool could be compared with the insertion by experienced surgeons

However, among the robotic tools mentioned above, the electrode insertion paths had to be planned prior experiments. This indicated that a high-resolution CT scanner would be required to obtain a high-resolution image of the cochlea before operations. The process would increase the cost to a great extent and extend the operation time significantly [37]. Also, additional actuators and sensors would need to be integrated into the electrode to control the shape of the electrode. The study provided a significant indication to the potential improvement of robotic-assisted cochlear implant surgery.

In 2012, Clark *et al.* [38] proposed a new prototype device to reduce electrode insertion forces. They utilised a manipulator magnet to guide a magnetically tipped cochlear implant electrode during the insertion. The prototype system setup is shown in Figure 2-6.

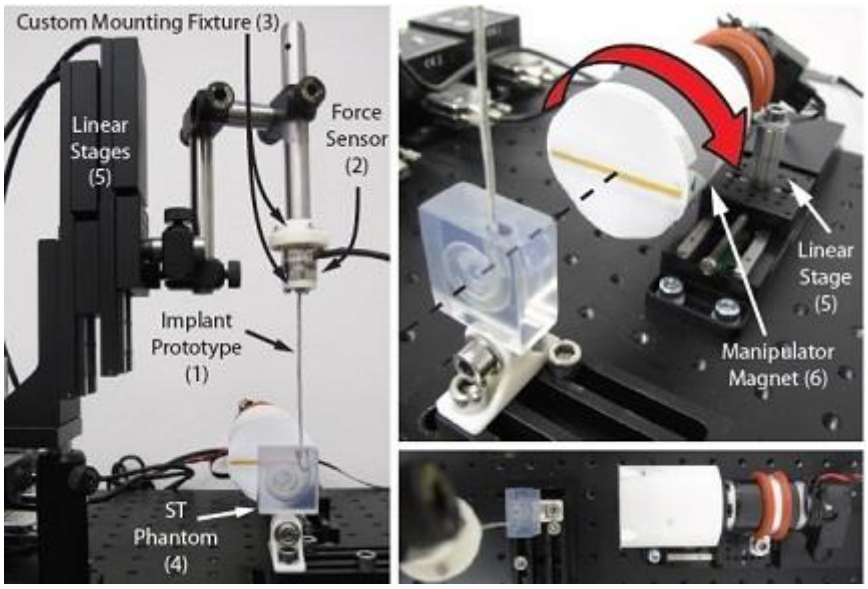

Figure 2-6: Experimental setup of the magnetic insertion system. Cochlear implant electrode array (1) was attached to the 6-axis force sensor (2) with a custom mounting fixation (3). Electrode array was inserted into a scala tympani phantom (4) using one linear stage (5). (Image [38])

In the scaled experimental study, the forces of non-guided insertion and magnetically guided insertion were compared. The results demonstrated that in the scaled experimental study, the insertion forces had been reduced by approximately 50% using the magnetic guidance method. However, crucial concerns were raised on the machine

regarding alignment of the manipulator axis with the cochlear central axis, the magnetic resonance scanners safety and the magnet implant off-axis effect.

The first reported master-slave–assisted cochlear implant cochleostomy using the da Vinci Si system was performed in 2014 [39]. In the operation, some processes—including refinement of cochleostomy and insertion of an electrode into the cochlea—had to be performed manually. It was because surgeons feel hindered by the loss of the haptic and sensation. The system also took a long learning process and extremely high cost.

2.2 Literature Review on CI Electrode Array Insertion Force

2.2.1 Introduction

When Lehnhardt [40] first described the intracochlear electrode array insertion technique in 1993, protection of the intracochlear structures had not been a topic of concern. In 1997, Hodges *et al.* [41] described how about 50% of patients who had cochlear implant surgery experienced residual hearing, postoperatively. However, at that time, patients' postoperative residual hearing was limited. The overall cochlear implant performance had not been improved by the hearing remnants [42]. In 1999, von Ilberg *et al.* first described the electric acoustic stimulation (EAS) of the human auditory system [43]. This technique combined remaining cochlear functions with electric stimulation of a cochlear implant. The EAS technique has demonstrated greatly improved speech and music perception results compared to the use of cochlear implant stimulating mode alone [43] [44]. These promising results of EAS patients created strong interest in intracochlear preservation in cochlear implant surgery. It was commonly believed that intracochlear trauma caused by electrode array insertions determines whether intraoperative hearing preservation was successful or not [45]. Several mechanical properties, such as electrode array insertion speed, stiffness, use of lubricants, electrode array types, and different insertion tools, were reviewed [46]. Among them, insertion force directly applied to the intracochlear structures was a key element of intracochlear trauma and residual hearing loss [29]. Electrode array insertion force as low as 26mN to 35mN may result in a rupture of the basilar membrane [47]. Consequently, the assessment of array insertion force was necessary to evaluate the electrode array's design and its mechanical behaviour. A summary of previously published insertion force investigations was listed in Table 2.1

Table 2.1: Published largest and average insertion forces for various electrode arrays and insertion methods. TB: temporal bone, AOS: advance off stylet, AIT: automated insertion tool, SIT: standard insertion technique.

First Author	Year	Electrode Array Type	TargetMaterial	Number of Insertions	Insertion Method	Largest Force (mN)	Mean Force (mN)	Insertion Length/Angle
Roland	2005	Contour and Contour Advance, Cochlear	Human TB/ Phantom model	40	Manual, SIT	240	170 ± 50	8mm
				10	Manual, AOS	75	30 ± 9	8mm
Adunka	2006	C40+,MED-EL	Phantom model	14	Manual	105	75.9	27mm
		FLEX^{soft}		8		68	53.5	27mm
Todd	2007	Contour, Cochlear	Phantom model	11	AIT,SIT	194	95	16mm
		Practice		5		178	98	16mm
		Contour, Cochlear	Phantom model	26	Partial stylet withdrawal	115	57	16mm
		Practice		8		120	50	16mm
		Contour Advance, Cochlear	Phantom model	34	AIT,AOS	50		16mm
Radeloff	2009	C40+,MED-EL	Phantom model	16	Manual, insertion tool	40	32.92 ± 7.72	352° - 459°
Rau	2010	Contour Advance, Cochlear	Phantom model	20	AIT,AOS	40	20	12mm
Schurzig	2010	Freedom Advance, Cochlear	Phantom model	4	AIT,AOS	34	8 ± 6	17mm
				4	AIT, Straight	93	46±27	17mm
Majdani	2010	Contour Advance, Cochlear	Phantom model	8	AIT,AOS	40	5 ± 14	<255°
				26	Manual, SIT	100	4 ± 1	<255°
Briggs	2011	MRA, Cochlear	Phantom model	3	Manual, insertion tool	13 ± 2	NA	390° - 450°
		Nucleus® Straight, Cochlear		3		6 ±.5		
		Hybrid™ L24, Cochlear		3		3 ± 3		
		Freedom Advance, Cochlear		3		29 ± 5		
Kontorinis	2011	Contour Advance, Cochlear	Phantom model	116	Manual, SIT	367	139	17mm
		HiFocus Helix, Advanced Bionics						
		Standard C40+ MED-EL						
		Hybrid-L Nucleus						
Helbig	2011	FLEXEAS 20, MED-EL	Human TB	10	Manual, SIT	35	<25	320°-370°
Miroir	2012	HiFocus 1J, Advanced Bionics	Human TB	4	AIT	350	190 ± 13	<20mm
Nguyen	2012	Digisonic SP, Oticon		8	AIT	120	30 ± 64	270° ± 140°
		Prototype, Oticon		15	AIT	60	10 ± 12	202°± 96°
Nguyen	2014	HiFocus 1J, Advanced Bionics	Human TB	10	Manual, SIT	317	256 ± 61	NA

Nguyen	2014	HiFocus 1J, Advanced Bionics	Human TB	8	Manual, insertion tool	382	327 ± 55	NA
				8	AIT	320	255 ± 75	~350°
Kobler	2014	Contour Advance, Cochlear	Phantom model	20	AIT,AOS	150	~100	10mm
Pile	2014	Contour Advance, Cochlear	Phantom model	95	AIT,AOS	190	37 - 62	NA
			Human TB	8		284	46 - 71	NA
Rohani	2014	Nucleus CI422, MED-EL	Human TB	2	Manual, SIT	56 - 469		360° - 600°
		Standard MED-EL		2				
		Custom MED-EL		2				
Wade	2014	Cochlear array	Porcine cochlea	6	Manual, SIT	254	~75	3.5mm
Seta	2017	Flex 28 array, MED-EL	Human TB	12	Manual, insertion tool	59.4 ± 19.9	59.4 ± 19.9	>240°
Avci	2017	HiFocus 1J, Advanced Bionics	Human TB	27	AIT	218 ± 44	16.4 - 19.2	327° ± 22°
Mirsalehi	2017	Hybrid™ L24, Cochlear	Human TB	10	Manual, SIT	300 ± 28	3 ± 5	196°–276°

2.2.2 Force Profiles of Previously Published Electrode Array Insertions

In 2005, Roland [29] first evaluated the manual insertion characteristics of Contour electrode arrays with the Advance Off-Stylet (AOS) versus the Standard Insertion Technique (SIT). The force measurement system was introduced in Figure 2.7. Five Contour electrode arrays with the Standard Insertion Technique (SIT) were evaluated in the same cochlear models and temporal bones. Insertion mean force profiles of the SIT and AOS techniques are shown in Figure 2-7.

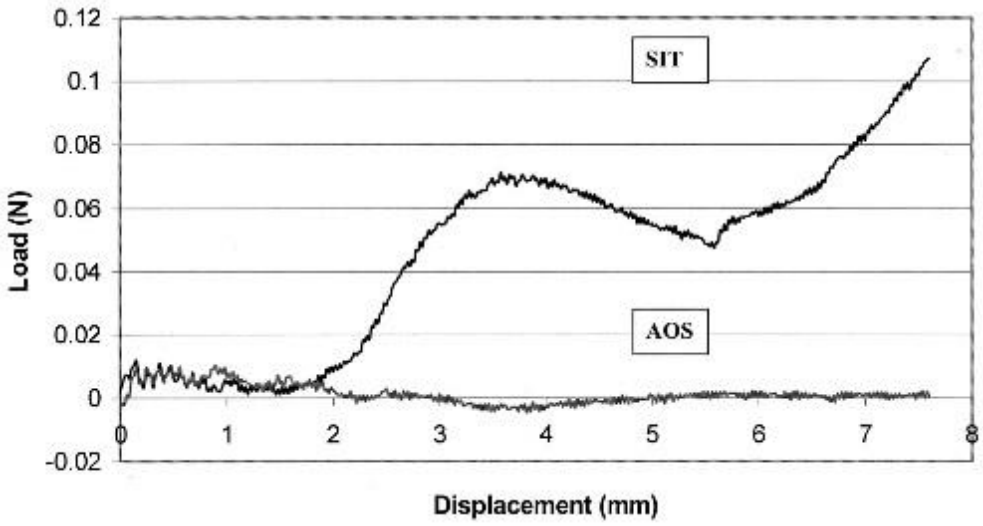

Figure 2-7: Mean force profiles of the Standard Insertion Technique (SIT) and the Advance Off-Stylet (AOS) with the insertion depth up to 8mm. (Image from [29])

Average insertion forces of the Contour SIT in the cochlear model were 75±10 mN, with the insertion length of 7.5 mm. The average insertion forces of the Contour Advance AOS technique in the cochlear model was 13±9 mN, with the insertion length of 7.5 mm. The peak force recorded was 91mN for the SIT and 26 mN for the AOS technique. Regarding the temporal bones, average insertion forces of the Contour Standard Insertion Technique were 170±50 mN, with the insertion length of 8mm. The peak force of the technique was measured to be 240 mN. Average insertion forces of the Contour Advance AOS technique in the cochlear model was 30±9 mN, with the insertion length of 8mm. During the standard array insertions in the cochlear model and temporal bones, the insertion forces rose to a peak, and then fell. After that, insertion forces continually rose to a second peak, nearing complete insertion. According to the force results, the average insertion forces in human temporal bones could be twice as high as those recorded in a plastic cochlear model.

In 2006, Adunka and Kiefer [48] investigated the impact of cochlear implant electrode arrays' deep insertion depth 27mm on intracochlear trauma. Fourteen C40+ standard and eight FLEX$_{soft}$ electrodes were manually inserted into an acrylic model to the depth of 27 mm. The force measurement of each insertion step was recorded by a load cell. The force profiles of the FLEX$_{soft}$ and Standard array are shown in Figure 2-8.

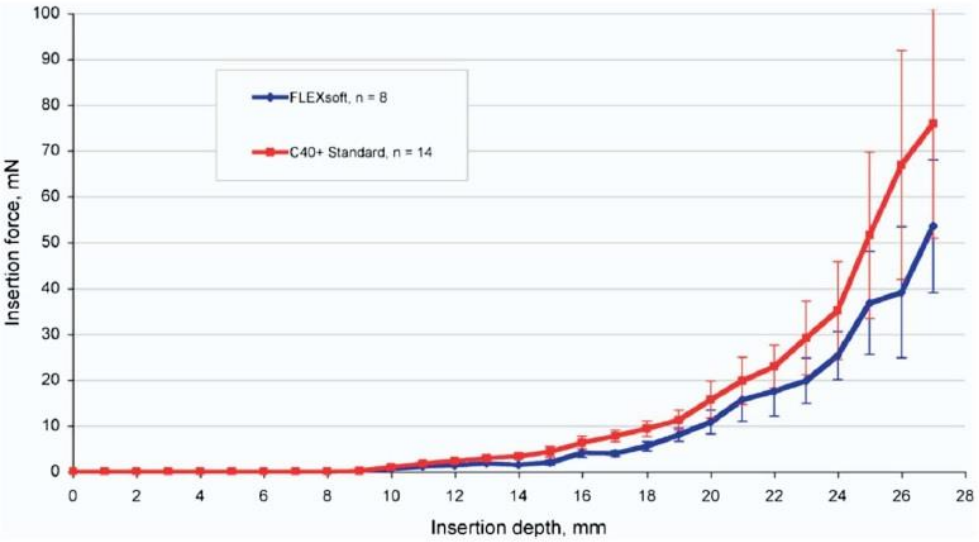

Figure 2-8: The mean force profiles of the C40+ standard array and the FLEXsoft array up to insertion depth 28mm. Force results demonstrated average insertion force would rise significantly beyond the depth of 18-20mm. (Image from [48])

At the complete insertion point, the average force of the C40+ standard array was 75.9 mN and the mean force of the $FLEX_{soft}$ array was 53.5 mN. Measurement results demonstrated that the insertion forces for both electrodes increased along with the depth. Insertion forces increased significantly beyond the depth of 18-20mm.

Electrode array force properties and insertion trajectories during CI surgery were studied by Todd [49]. The Standard Insertion Technique (SIT) for Practice electrode arrays and Contour electrode arrays was implemented 5 times and 11 times, respectively. The Partial Stylet withdrawal insertion technique for Practice electrode arrays and Contour electrode arrays was implemented eight times and 26 times, respectively. Insertion of the Advance Off-Stylet (AOS) was repeated 34 times. All of the insertions were performed by an automated insertion machine to the depth of 16 mm. The net force, which was a force along the longitudinal axis of insertion, and the friction force were measured by a load cell. The force profiles for a SIT, Partial Stylet withdrawal and an AOS insertion are shown in Figure 2-9.

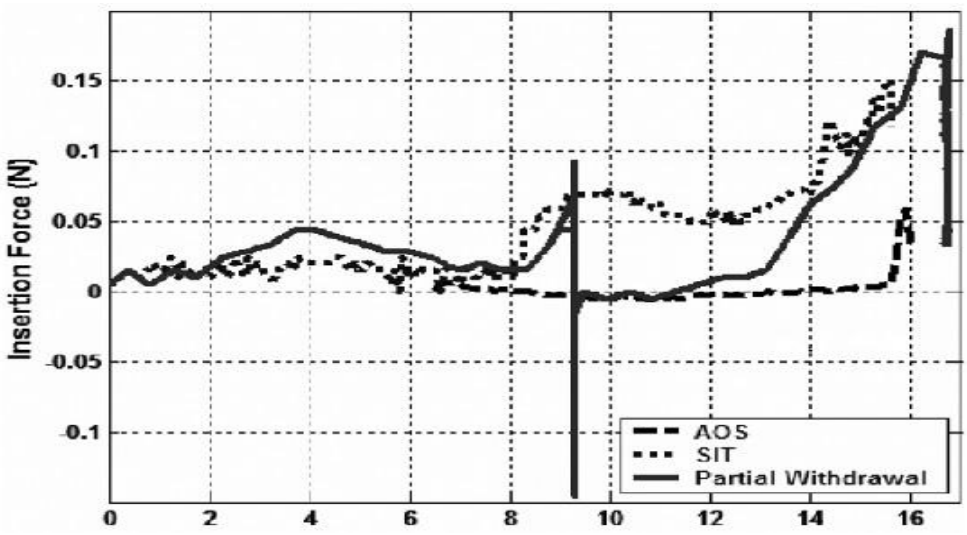

Figure 2-9: The mean force profiles of the Standard Insertion Technique (SIT), Partial Stylet withdrawal and an Advance Off-Stylet (AOS) insertion up to 17mm. First spike in the output force was 9.5 mm (vertical line). (Image from [49])

In regards to the standard insertion technique, the average forces were 95 mN and 98mN for the Contour and Practice electrode arrays, respectively. The peak forces were 194 mN (Contour) and 178 mN (Practice) at the completion point. For the partial withdrawal technique, the average forces at the lateral wall were 57 mN and 50 mN for the Contour and Practice electrode arrays, respectively. The peak forces were 115

mN and 120 mN. The average peak forces for the AOS technique were 50 mN. Experimental force results demonstrated that array forces impacted on the scala tympani wall depend on array strength, insertion trajectory, and frictional forces.

Eight uncoated and eight coated electrode array carriers were manually inserted into a transparent scala tympani model with an insertion tool [50]. The electrode array carrier used was the MED-EL C40+. The measured insertion forces increased along with the increasing insertion depth of up to 29 mm. The mean forces for the uncoated electrode carrier at 29mm (362^o) were 32.92±7.72 mN. Whereas, the mean forces for the coated electrode carrier were 17.17±4.66 mN at the completely inserted position (459.4^o).

In 2008, Rau *et al.* developed an automated insertion tool [34]. In order to evaluate the tool, five Contour Advanced electrode carriers were inserted into a transparent, artificial cochlear model. In total, twenty insertions were performed by the means of the AOS technique. According to the force results, the average measured forces varied between 5 mN and 23 mN, and the peak force could be up to 40 mN. However, in four insertions, the temporary array tips folded over in the beginning section of the insertion. The average forces in these insertions were 60±35 mN, and the peak force rose up to 117mN.

In 2010, another comparison between the standard electrode array insertion and AOS technique was performed by Schurzig et al [36]. In his research, an automated CI array insertion tool integrated with a force sensor was applied. The electrode array insertion robot had been introduced in Figure 2.10. Four straight insertions and four AOS insertions were performed into a transparent cochlear model. In all eight insertions, the electrode array was inserted to the depth of 17mm. The force profiles for SIT and AOS insertion are shown in Figure 2-10.

During the 7 mm of insertion, the average forces for straight insertions were 8±4 mN and 4±6 mN for the AOS technique. Inside the spiral of the model, average forces were 46±27 mN for the straight insertion and 8±6 mN for the AOS. The peak forces were 93 mN for the straight insertion and 34mN for the AOS. The force difference between straight and AOS insertions became significant from the insertion depth of 9.74 mm.

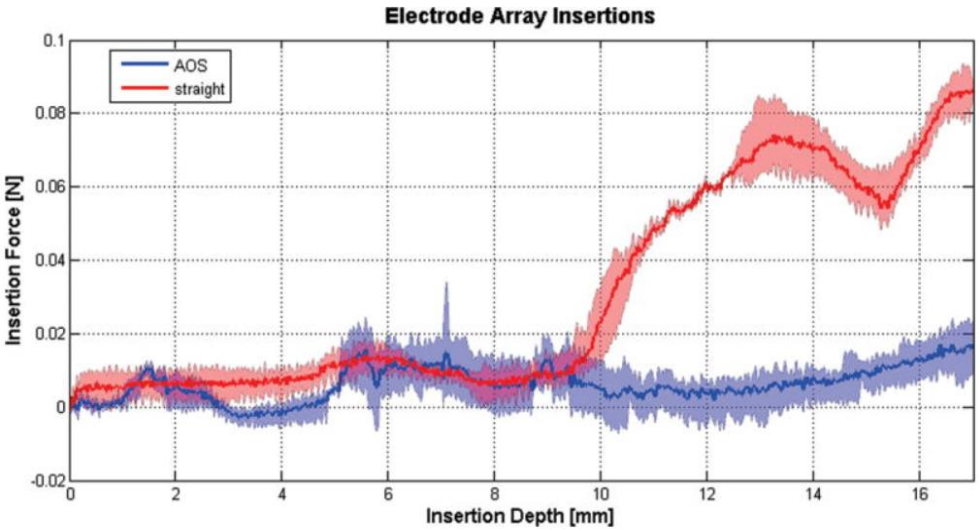

Figure 2-10: The force profiles of the Standard Insertion Technique (SIT) and Advance Off-Stylet (AOS) insertions up to 17 mm. The peak forces were 93 mN for SIT and 34 mN for the AOS. (Image from [36])

The automated insertion tool was also applied to compare with manual insertion by experienced surgeons [35]. Twenty-six manual insertions were performed by three surgeons using the AOS technique. Robotic AOS insertions were implemented eight times. All of the insertions were performed into a transparent model up to 255°. The average insertion force for the surgeon was 4±1 mN and 5±14 mN for the robotic tool. The average insertion force of the surgeons was smaller than that of the robotic tool. However, the transient peak force of the surgeons was larger than that of the robotic tool.

In 2011, a modiolar research array (MRA) had been evaluated by Briggs et al [51]. In the experiments, the peak insertion forces of the MRA and other electrode arrays were compared. Each of the electrode arrays was inserted into a cochlear model three times. The average peak contact force was 13±2 mN for the MRA sheath, 6±5 mN for the Nucleus straight electrode array, 3±3 mN for the Hybrid™ L24 electrode array, and 29±5 mN for the Contour Advance electrode array.

The impact of an electrode array insertion speed on the insertion forces was investigated by Kontorinis *et al.* [52]. Four different types of electrode array carriers were examined, which were the Nucleus 24 Contour Advance electrodes, the HiFocus Helix Advanced Bionics electrodes, the Standard C40+ MED-EL electrodes, and the Hybrid-L Nucleus electrodes. In total, 116 insertions were manually implanted into an

artificial, human cochlear model. For the Contour Advance electrodes, insertion forces were recorded with the increasing insertion speeds. Measured results demonstrated that the progressive increase of the insertion speed would lead to an increasing force. For insertion speed increased from 10 mm/min to 200 mm /min, mean forces rose from 90 mN to 185 mN, and the peak force rose from 180 mN to 420 mN. In conclusion, a higher array insertion speed will lead to a larger insertion force.

The insertion properties of an atraumatic prototype electrode carrier FLEXEAS 20, Med-El were evaluated by Helbig *et al.* [53]. Four electrode array carriers were manually inserted into ten human temporal bones through the round window membrane. The insertion angle of the cochlear implants ranged from 320 degrees to 370 degrees. The measured mean insertion forces were 25 mN, with the peak force of 35 mN.

Insertion force profiles, including friction forces, speed, and tube materials of the Hifocus 1J electrode arrays, were evaluated by Miroir *et al.* [54]. Eighteen identical electrode array carriers were inserted into four types of the cochlear models: metal only, metal with lubricant, plastic only, and plastic with lubricant. Three different insertions speeds - 0.15, 0.5, and 1.5 mm/s were performed by a motorized insertion tool. From the force results, the speed did not influence the insertion forces in either the metal tube or in the plastic tube. The friction forces in the metal models were larger than in the plastic models at all speeds. In the plastic model, friction forces decreased with the array carrier insertion depth. The average insertion forces were 190±13 mN in the insertion angle of 180 degrees. As expected, friction forces in the model with lubricant were lower than the model without. The friction forces remained stable and decreased in the first 17 mm of insertion. As the model slope changed, the forces increased rapidly in the last 8 mm of insertion. In the force results curve, the first contact between the carrier's tip and the lateral wall could not be detected.

Three array carriers were inserted into three human temporal bones at a constant speed of 1.5mm/s. The insertion force was recorded by a one-axis force sensor, and the friction forces were recorded by a six-axis force sensor. From the insertion force result curve, there were three phases that could be distinguished. Below the insertion depth of 10mm, the average insertion force remained stable and under 100 mN. Between the depths of 10mm and 15mm, the insertion forces increased slowly and under 200mN.

In the last 5mm, a dramatic increase to 350 mN was observed. The average friction force measured by the six-axis sensor was 40±3 mN (n=3). The significant differences between the force profiles were due to the gradual decrease of scala tympani diameter in temporal bones.

Insertion force profiles of a standard CI electrode array [55] were compared with a prototype array [56] in 2012 [57]. Twenty-nine human temporal bones were prepared and each of them was inserted for only one array. These temporal bones were divided into two types: micro-dissected cochlea (n=23) and intact cochlea (n=6). All the insertions were performed by an automated insertion tool. For the micro-dissected cochlea, insertions of the two electrode array designs, standard array and prototype array, were performed 15 times and eight times, respectively. The average force of the standard array was 30±64 mN, with the insertion degree of 270±140°. The average force of the prototype array was 10±12 mN, with the insertion degree of 202±96°. During the first 200-degree insertion, the insertion forces were lower than 20 mN. For the rest of the insertion, the standard array insertion force increased to 100 mN, while the prototype array insertion force remained below 50 mN. For the intact cochlea, three standard electrode arrays and three prototype arrays were inserted into six human temporal bones. However, only two standard arrays and two prototype arrays were fully inserted to 260°, 360° and 360°, 450°, respectively. The peak insertion forces for all the fully-inserted arrays were below 150 mN. The mean insertion forces for the partially-inserted standard array and fold-over prototype array were higher than the fully-inserted arrays. The mean force profiles of the standard insertions and mistaken insertions are compared in Figure 2-11.

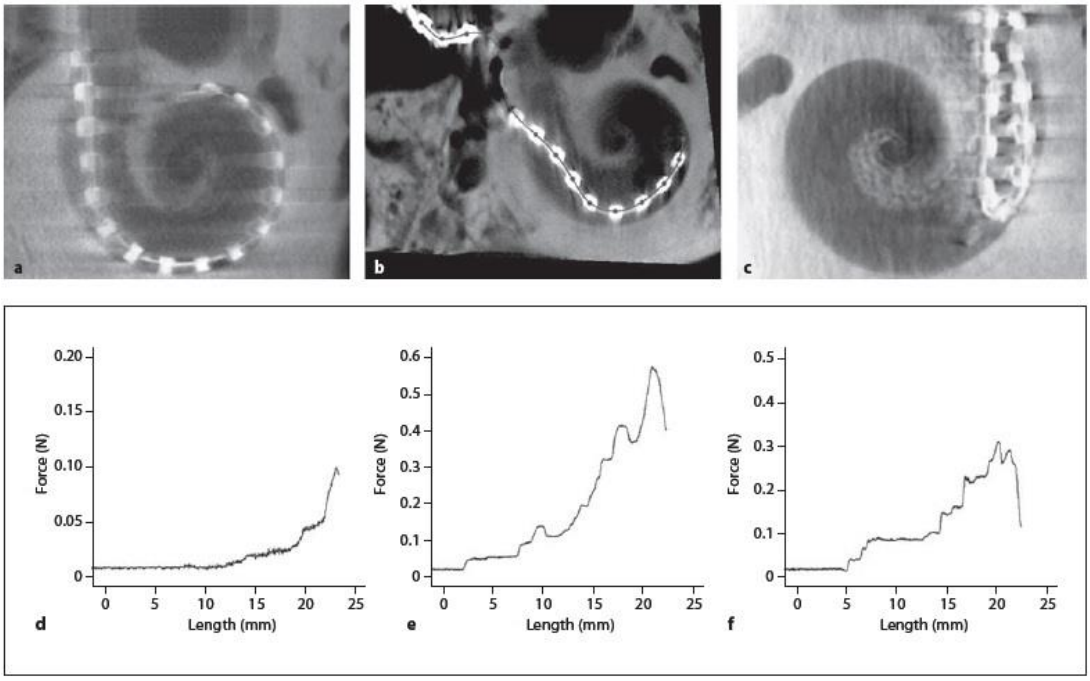

Figure 2-11: CT scan images and the mean force profiles of the standard array insertions (a and d), partially insertions (b and e) and prototype array fold-over (c and f). The behaviour of force profiles were distinctly under different insertion conditions. (Image from [57])

Also in 2014, Nguyen *et al.* compared the insertion forces of three different insertion techniques: manually insertion with forceps, with a commercial tool, and with a motorized tool [58]. Twenty human temporal bones were prepared for the implantation. Each temporal bone was inserted by an electrode array (Hifocus 1J arrays, Advanced Bionics) with the three insertion techniques. A six-axis force sensor was integrated on the bottom of the specimen. The average force for the manual insertion with forceps was 1160 ± 505 mN, 1337 ± 408 mN for the commercial tool, and 1573 ± 764 mN for the motorized tools. The three insertion techniques had no differences based on these force momentum results.

In 2014, Kobler [59] introduced a novel prototype of an automated insertion tool. Unlike previous insertion tools, a force sensor was integrated into the insertion mechanisms. Twenty insertions were performed into an artificial cochlear model based on the insertion tool. In total, 17 insertions were successful and the average forces were 100 mN. The measured insertion forces increased along with the increasing insertion depth of up to 10 mm.

Insertion forces of another robotic electrode array insertion technique - path planning - was evaluated by Pile, Wanna, and Simaan [60]. Perimodiolar CI electrode arrays were inserted into both plastic models and human temporal bones. The peak force of 95 plastic model insertions was 190 mN. The peak force of eight cadaveric specimen insertions was 284 mN.

Forces and trauma associated with an image-guided cochlear implant electrode array insertion were evaluated by Rohani *et al.* [61]. Two each of CI422 Nucleus, Standard MED-EL, and Custom MED-EL were implanted into six human temporal bones. Thus, each of the temporal bones was inserted for only one array carrier. All of the insertions were performed manually. Insertion forces were collected by a six-axis sensor placed under the temporal bone. The measured peak force ranged from 56 mN to 469 mN. Average insertion forces ranged from 9 mN to 78 mN, with a minimum insertion angle of 360^{o}.

In 2014, Wade *et al.* measured the tip forces during the insertion of a CI electrode array [62]. An optical fibre-based sensor was inserted into six porcine cochlear bones. The average force remained stable and low before the insertion depth of 2.6mm. After that distance, the average force rose dramatically to 230 mN at the completed insertion distance of 3.5mm. Measured force results showed the maximum tip force was up to 254 mN.

Electrode array insertion force applied to the cochlea should be controlled to limit the intracochlear damage. Correction between insertion force and cochlear trauma was investigated by Seta *et al.* [46]. The long, straight Flex 28 array, MED-EL, was implanted into twelve human temporal bones at a constant speed by an automated insertion tool. The measured temporal bone was attached to a six-axis force sensor. Histologic images demonstrated that six atraumatic insertions, five scalar translocations, and one basilar membrane rupture occurred. All of the five scalar translocations occurred in the region of 150 degrees to 180 degrees. The peak forces for the atraumatic insertions were 59.4 ± 19.9 mN. Force profiles for all the atraumatic insertions were similar. The frictional forces remained low before 150 degrees, and then increased continuously to the peak force at the complete insertion. Force profiles of the traumatic insertions were irregular. The peak force (29.56 ± 18.2 mN) occurred when the tip of the array made contact with the inner wall of the temporal bone.

The impact of the cochlear array geometry on insertion forces and intracochlear trauma was investigated by Avci et al [63]. The electrode array carrier used in this project was a research electrode array of the same design as the HiFocus 1J, Advanced Bionics. Ten human temporal bones were prepared to be implanted. In total, 27 insertions were done by an automated insertion tool. The mean force profiles of the three insertions are shown in Figure 2-12.

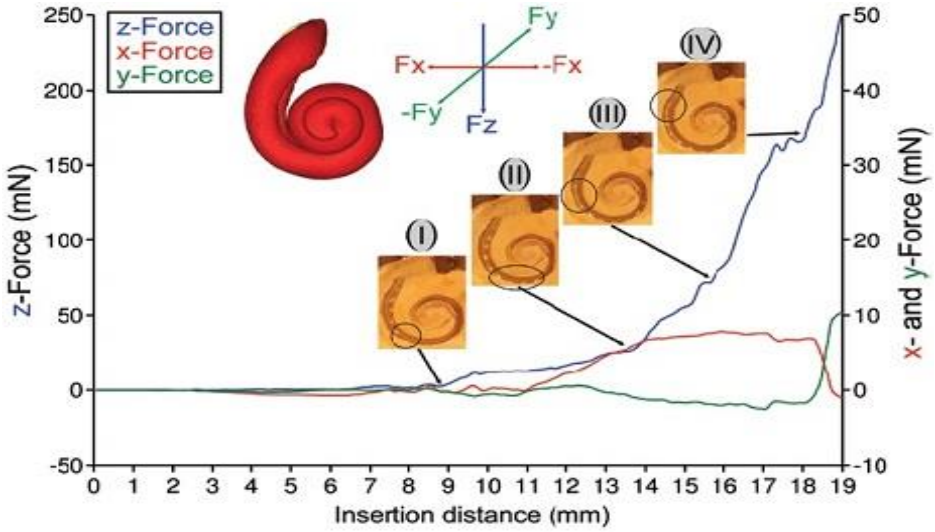

Figure 2-12: The mean force profiles of three insertions up to 19mm. Blue line indicates the mean force of z axis, red line shows the x force (horizontally) and green line shows the y force (vertically). The circle in each image (I-IV) demonstrated the contraction between the electrode array and cochlear wall. (Image from [63])

In the repeatability experiments, insertion forces demonstrated no significant changes with the increasing of the array insertion speed. The mean depth of the ten temporal bone insertions was 18.8 ± 0.6 mm (327° ± 22°). From the overall force results, the mean x-axis peak force was 19.5 ± 8.6 mN, the mean y-axis peak force was 25.0 ± 12.2 mN, and the z-axis peak force was 218 ± 44 mN. Overall, force profiles showed that before the first contact between the array tip and the lateral wall, x-, y-, and z-axis forces remained low and stable. After the contact point, the z-axis force continuously rose. At 18.5mm, a bulking of the electrode array occurred which changed the insertion force to maxima.

The insertion force profiles of a straight electrode array, Nucleus Hybrid^{TM} L24, were evaluated [64]. The electrode array was inserted manually into ten human temporal bones. A 1-D load cell force sensor was mounted on the bottom of the bone specimens

for the force data collection. Seven out of ten electrode arrays were inserted completely. Their mean insertion angle was 239° ± 26° (range of 196°–276°). The scalar translocation (from the scala tympani to the scala vestibuli) occurred in four specimens. From the force results, the mean force of the complete insertions was 3 ± 5 mN. The mean force of the partial insertions was similar to the complete insertions (3 ± 6 mN).

2.3 Literature Review on Cochlear Implant Electrode Array Bipolar Impedance Measurement

2.3.1 Introduction

During the cochlear implantation, it was essential to preserve residual hearing and improve clinical outcomes by reducing electrode insertion trauma [65]. Insertion of an electrode array into a cochlea caused immediate damage to the inner ear and was considered responsible for a loss of residual hearing.

One possible source of information to help determine the relation of the cochlea to the cochlear walls during surgery was the use of electrodes impedance measurements. Previously, this method was only applied postoperatively in cochlear implant functions and electrodes integrity verification. Nowadays, the impedance information from the electrodes and intracochlear tissue was found to change apparently with electrode array movement. By analysing the impedance information, certain behaviours of the electrode array intracochlearly could be discriminated.

The section begins with reviewing the previous electrodes electric stimulation model. Mechanisms of electrodes charge transferring had been described by several stimulation models. Secondly, four widely accepted electrodes stimulation modes were reviewed. The bipolar impedance measurement was the most appropriate sensing method that was adopted in this project. Lastly, current electrode capacitance sensing applications were reviewed to determine the similarities and limitations.

2.3.2 Electric Stimulation Modelling

There were a lot of models on modelling the impedance for inner ear electric stimulation. Varley [66] was the first to measure the capacitance of an electrode-electrolyte interface. The first aluminium oxide electrolytic capacitor was created by Pollak [67]to convert alternating current to direct current.

The first electrode-electrolyte interface was introduced by Helmholtz [68] proposed that a double-layer charge existed at the electrolyte interface. The concept is shown in Figure 2-13.

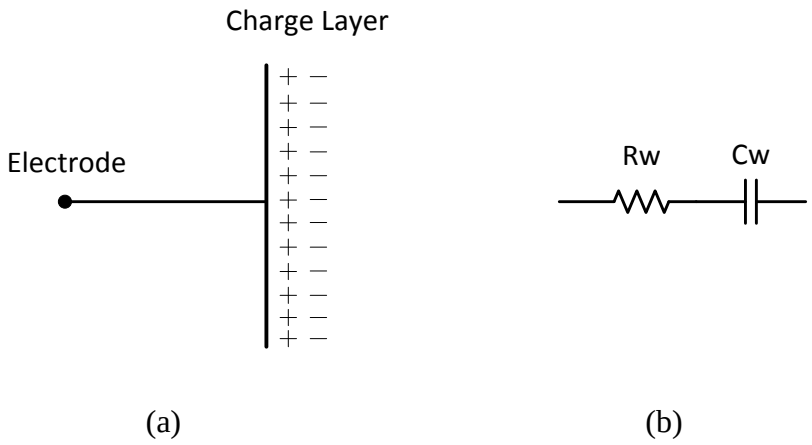

Figure 2-13: (a) A double-layer charge existed at the electrolyte interface (b) Warburg model was a capacitor (Cw) connected with a resistor (Rw) in series.

The concept of the double-layer charge was significant as it firstly indicated the interface was similar to a capacitor. Hence, any stimulating model for the interface must contain capacitance and resistance. Warburg [69] simplified the interface model as a capacitor (C_w) connected with a resistor (R_w) in series, which was shown in Figure 2.13 (b). The model stated that for an infinitely low current, the capacitance C_w varied inversely with the square root of the input frequency. However, Warburg did not interpret the electrical behaviour of the interface when passing the direct current [70]. Based on Warburg's model, Fricke [71] further interpreted the electrode capacitance, phase and reactance with the input frequency range from 100 to 3500 Hz. Again, Fricke did not address the direct current interface behaviour.

The relationship between the electrolyte temperature and concentration and electrodes impedance had been investigated in 1930 [72]. Zimmerman used small area gold and platinum to measure electrodes impedance in a varied range of electrolyte

concentration, temperature and input frequencies. After that, many physical chemists had built models to interpret the electrode-electrolyte interface [73][74][75][76][77][78][79][80][81]. Among them, models developed by Sluyters-Rehbach and Sluyters in 1970 [75] and Geddes and Baker in 1975 [77] were the most influential work to interpret the electrode-electrolyte interface. The two models are shown in Figure 2-14.

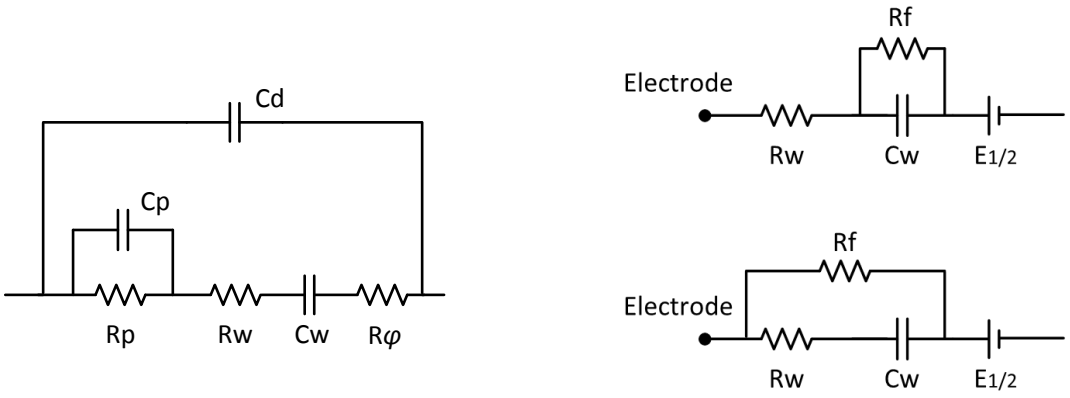

(a) (b)

Figure 2-14: (a) Sluyters-Rehbach and Sluyters model. (b) Geddes and Baker model that applied half-cell potential to account for the direct current behaviours.

In 1947, Randles [74] proposed a model that a double layer capacitor C_p was connected in parallel with the Warburg model. However, the passage of direct current through the interface was not considered either. A more complex model was created by Sluyters-Rehbach and Sluyters. A resistance $R\varphi$ and a parallel resistance R_p were connected in series with the Warburg impedance (R_w and C_w). These components were shunted by a capacitance C_d . Although this model was popular and widely accepted, it did not account for the direct current properties.

Based on the impedance-frequency properties for electrodes in saline, Geddes and Baker [77] proposed two circuit models for the electrode-electrolyte interface. The voltage potential was $\frac{E}{2}$ for both circuit models. The half-cell voltage potential was connected in series with the Warburg impedance (R_w and C_w). In the first circuit model (Figure 2.14 (b) top), the Warburg capacitance C_w was shunted by the Faradic resistance R_f to account for direct current. In the second circuit model (Figure 2.14 (b) bottom), the Faradic resistance R_f was placed in parallel with the Warburg impedance

(R_w and C_w). It was used to simulate the passage of direct current in the interface. The Faradic resistance (R_f) was the highest impedance that an electrode-electrolyte interface could reach [82].

Since 1989, Suesserman and Spelman [83][84][85] did a series of measurements to evaluate the electrical impedance of inner ear tissues. Suesserman and Spelman [85] introduced a lumped-parameter model. This model simulated the electrical properties of an electrode array which had been implanted into a porcine cochlea in *vivo*. Two paired implanted electrodes and one paired reference electrodes were employed in the measurement. The two reference electrodes located outside of the cochlea. The lumped-parameter model of the implanted electrode array is shown in Figure 2-15.

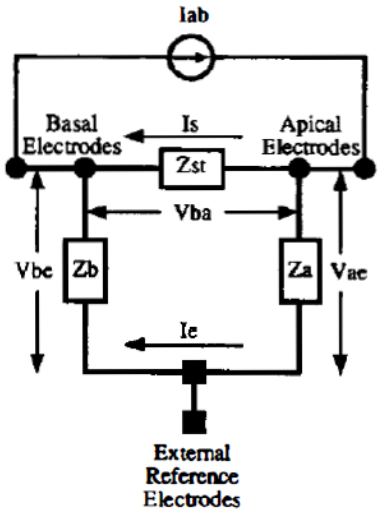

Figure 2-15: The lumped-parameter model of the implanted electrode array. (Image from [83])

Electrical current was driven from one electrode (the right-most) while the other electrodes were responsible for paired voltage measurements. Z_{st} indicated the intra-scalar impedance while Z_a and Z_b indicated the two trans-scalar impedances. V_{ba} was the voltage drop between the apical electrode and basal electrode. V_{be} was the voltage drop between the basal electrode and the external reference electrodes and V_{ae} was the voltage drop between the apical electrode and the external references electrodes.

The lumped-parameter model reproduced the impedance and phase of the three paired electrodes. The simulation results from the model were within 50% of the experimentally measured results. The differences between them were within 30%

when the frequency was below 5 kHz. It was the first time to explain the monopolar electrical properties of the multi-electrode array inside of the cochlea. However, the model only simulated the impedance of 3 electrodes at a static state. The monopolar measurements would have limited contributions to the bipolar measuring of a dynamic electrode array insertion.

2.3.3 Four Stimulation Modes

The three stimulation modes: Bipolar (BP), Common Ground (CG) and Monopolar (MONO) had been compared and reviewed by Busby *et al.* [86]. Nine patients who had been implanted the cochlear array with 22 electrodes [87] [88] were selected in this experiment. For the bipolar stimulation, two electrodes separated by one and two electrodes were stimulated by a current flow in eight patients and one patient respectively. For the common ground stimulation, one electrode was stimulated while the remaining electrodes were connected together to be the return path. For the monopolar stimulation, only the most basal electrode and an electrode were activated. Experimental results revealed that different stimulation modes would lead to differences in threshold (T), comfortable listening (C) levels and the range of usable hearing (DR). The bipolar stimulation results confirmed the current distribution was limited, which was consistent with the previous studies [89][62][63][92][93][94]. The results also indicated that there were significant differences between BP and CG stimulation in the T and C levels. However, it had not been clarified by the authors which mode was the best among the three.

In 1996 Jolly [95] investigated the cochlear electrode array for the stimulation in quadrupolar (QUAD) mode. A simulation model was created and examined with the experimental results. He claimed that quadrupolar stimulation mode had benefits in focusing the voltage potential and minimizing the current spreading. The mode would reduce unpleasant sensations of the patients than other techniques such as MONO, BI and CG modes.

In 1998, the electrodes impedance in the common ground mode was measured intra-operatively and post-operatively [96]. Impedance measurements were useful in discriminating whether the implanted electrodes were integral, short circuit, open

circuit or exposed in air. From the experimental results, low (< 1 kOhm) intra-operative impedance values occurred between the electrodes 1 to 13. However, these low impedances were caused by abnormal surrounding fluids instead of short circuits occurring along the array. The intra-operative impedance measurements had to be monitored in real-time to avoid fault pattern recognition.

A novel method to measure the Faradic (direct-current) resistance had been proposed by Geddes and Roeder [82]. The circuit model for two identical electrodes filled with a conducting liquid is shown in Figure 2-16.

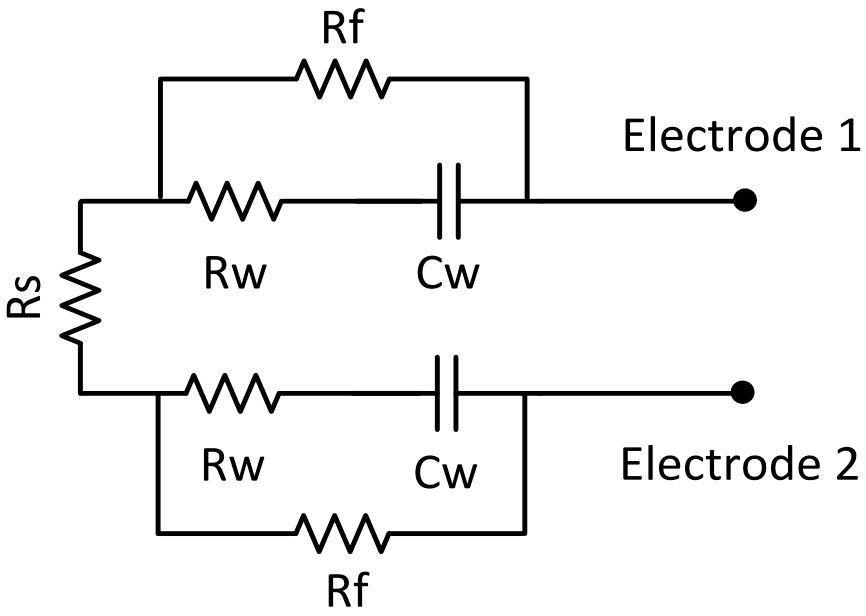

Figure 2-16: Equivalent circuit model of two identical electrodes (Electrode 1 and 2) filled with a conducting liquid. (Image adapted from[82]).

In the model, R_w and C_w were the Warburg impedance and its reactance $X_w = \frac{1}{2}\pi f C_w$. R_f represents the Faradic resistance and R_s was the resistance of the liquid between the electrodes. The model demonstrated that the Warburg resistance (R_w) and reactance (X_w) would decrease with the increase frequency. Therefore, at a sufficiently high frequency (100 kHz), the impedance between electrode 1 and electrode 2 was R_s. Hence, the liquid intervening resistance could be calculated.

In order to calculate the Faradic resistance R_f, a constant current rectangular pulse was applied. The input current pulse and response voltage are shown in Figure 2-17.

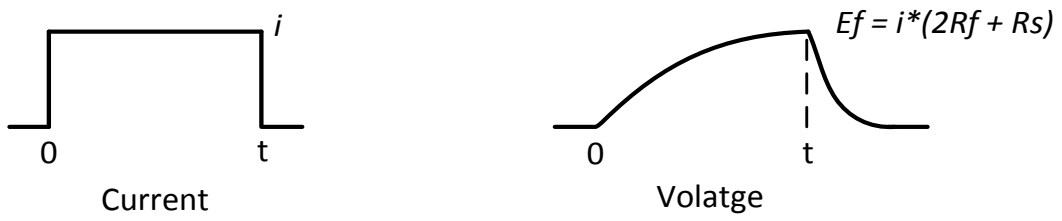

(a) (b)

Figure 2-17: (a) Rectangular direct current pulse (*i*) of duration t. (b) The response voltage across two electrodes. Ef was the maximum voltage when charging the Warburg capacitor (Cw). Therefore, no current flows through Rw and Cw.

When C_w was fully charged, the voltage across the two electrodes was $E_f = i(2R_f + R_s)$. By applying the measured resistance R_s, small direct current (i = ±1.5 mA) and long enough charging time (t = 2s), the Faradic resistance could be calculated. The Faradic resistance properties of eight electrode materials had been investigated. The results demonstrated that all the Faradic resistance decreased exponentially with the increase of current density. The relationship follows the expression.

$$R_f = R_{f0}e^{-\partial i}$$

Where R_{f0} was the Faradic resistance at no input current, i was the input rectangular direct current pulse and ∂ was the damping constant. In the paper, chloride silver was found to have the lowest Faradic impedance, whereas carbon was the highest. The highest resistance of an electrode-electrolyte interface could reach was the no input current Faradic resistance (R_{f0}). Therefore, it was a significant factor in selecting the electrode materials.

In order to precisely control the intra-cochlear current flow, an electrical equivalent model was proposed by Vanpouck *et al* [97]. The model simulated both of the electrode-electrode impedance and electrode-tissue impedance. An objective measurement: electrical field imaging (EFI) technique was applied. The technique could measure voltage potential and current flow between active electrodes. After analysing the measurement data, the method could be used to detect the electrode array physical movement that affects conductivity. Based on the conception, Choi *et al.* [98] proposed a finite element model. By analysing the results from the model, impedance

values between electrodes could be calculated. Based on these impedance values, an impedance matrix of all electrodes in the array had been created.

2.3.4 Impedance Sensing Application

Electrodes impedance measurements were usually applied for diagnostic purposes. Carlson *et al.* [99] showed that 66% of electrode failures happened intra-operatively and 8% of which occurred at the first activation. The remaining electrode failures happened within one year after the array implantation. Impedance measurements at the initial activation were useful for evaluating the integrity of the electrodes. Several papers have evaluated electrode failure properties at the early stage of activating CI array [99][100][101][102][103][104][105][106]. By applying the monopolar impedance measurements, abnormal electrodes (open circuit (OP) and short circuit (SC)) could be diagnosed intra-operatively and post-operatively [104]. However, monopolar sensing was considered to have poor sensitivity in detecting the electrodes short circuit. The incidence of SCs might be underestimated. For the post-operatively impedance measurements, several papers [104][107][108] assessed long-term electrode impedance changes and CI array failures.

Tan *et al.* [30] developed a prototype software system to extend the functionalities to measure continuous electrodes impedance values during the electrode array insertion. Impedance feedback values were useful to guide robotic electrode insertion, to guide surgeons to achieve atraumatic electrode insertion and to provide electrode position in the cochlea. In their latest version [30], the recorded impedance values could be processed and plotted in real time to allow users to see how the impedance was changing throughout the process of insertion. One of the impedance measurement results is shown in Figure 2-18.

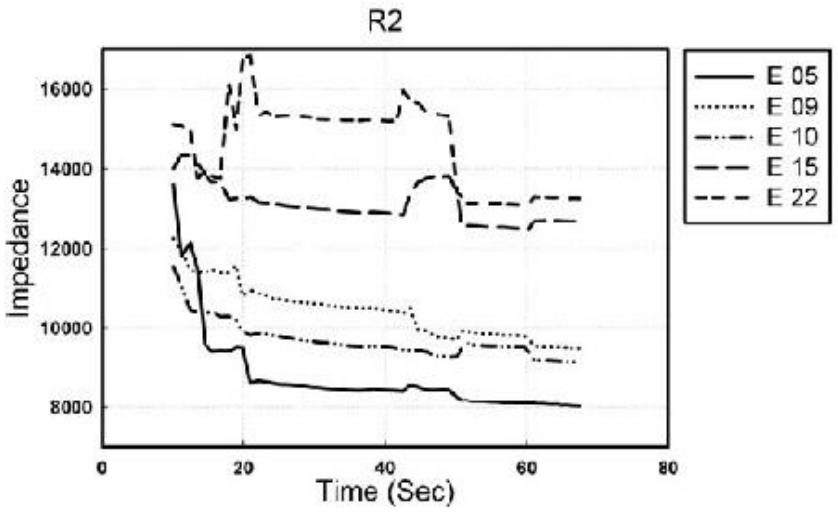

Figure 2-18: Real-time electrodes impedance changes against with time. E indicated which electrode was applied in sensing. (Image from [30])

The working principle of continues impedance measurement (CIM) system was that when a known voltage between two or more electrodes were applied, the current passing between them could be measured. The measured impedance was determined by dividing the voltage and the current passed by. A continuous series of impedance values could be recorded and entered into a text log. Therefore, insertion trauma could be detected and prevented before it occurred.

By analysing the impedance values, the electrode array status and any physical events that might affect the impedance were capable of being recognized. Ideally, an electrode array should not touch the cochlear walls during insertion to prevent any intracochlear trauma. The impedance of the measured electrodes was higher when the electrodes touched the cochlear wall compared to those measured electrodes stay in the middle of the scala. It was due to that perilymph had a ten times higher conductivity than cochlear walls, especially when the stimulating electrodes were on a single side that facing to the cochlear modiolus [30].

Bipolar impedance measurement was applied by Pile *et al.* [109] to differentiate between the standard insertion techniques (SIT) and the Advance off Stylet technique (AOS). Perimodiolar electrode arrays were inserted into temporal bone specimens. Buffered saline was used as the conductive liquid due to the similar electrical properties as the perilymph. Bipolar impedance measurement results demonstrated that there were significant differences between the SIT and AOS techniques [109].

Therefore, bipolar impedance could be applied to detect electrode arrays motion and optimize the electrode arrays intracochlear placement.

2.4 Conclusion

Tn the literature review, force profiles of various types of CI electrode array insertions into distinct types of tympani models was fully investigated. Insertion force measurement had the advantage in providing feedback information to the insertion system. However, the method could not detect behaviours of the electrode array inside the cochlea. The states and movements of the electrode array might not be reflected in the force profiles. In order to fully understand the movements and behaviours of the electrode array intracochlearly, bipolar impedance sensing method could be employed.

Continuous impedance measurement (CIM) has confirmed that real-time impedance was easily obtainable and changing apparently with electrode intrascalar position changes. However, several limitations of the CIM existed.

1. The CIM system could not discriminate electrode states and notify surgeons in real-time. Hence, the automated discrimination of the electrode array insertion could not be achieved.

2. The precision of the electrodes impedance measurement remained unknown. It was due to the lacking of reference information (like insertion force) and comparison with other sensing information.

3. During the continuous capacitance measurement, only the two measured electrodes were activated. The behaviour and movement of the remaining electrodes remained unknown. The remaining electrodes might damage the intracochlear structures. The capacitance sensing method could be improved by activating more electrodes or all electrodes of the array.

Chapter 3

Methodology and Experimental Tools

The overall expectation of the automated feed system was that once it was placed in position, it would feed an electrode into the cochlea automatically by controlling the velocity, the state of tissue interactions and also the final position of the electrode array. The designed feed system would have the ability to avoid excessive disturbance by accounting for pressure, force and toque transient as well as the interactions between the electrode array tip and internal tissue structure of the cochlea.

The goal of this chapter was to describe the signal-sensing methodology including the force and capacitance signals during the electrode array insertion. In this chapter, the hardware and software design of the experimental tool and the cochlear model would be introduced.

The rest of this chapter was organised as follows: Section 3.1 highlighted the basic principle of the automated feed system. Section 3.2 described the electrode array utilised in the project. Section 3.3 covered the movement stages and their drivers, including both the hardware and software applications. Section 3.4 described the force measurement methodology of the electrode array. Section 3.5 introduced the capacitance-sensing methodology of the electrode array, including a cochlear model, LCR meter and channel switching board. Finally, Section 3.6 concluded the chapter.

3.1 Overview of the Automated Feed System

The proposed automated feed system was intended for research clinical applications. Algorithms would be developed to fulfil the offline data processing tasks. Key requirements of the system were listed before detailed discussion.

- The system should have the ability to detect the feeding force and discriminate three patterns during an electrode array insertion.
- A controller operating system was developed to control the electrode array insertion angle, velocity and position. The insertion progress could be repeated to achieve consistent electrode array insertions.
- A vision system was created to serve as an interface between the user and device in order to demonstrate the insertion progress of the electrode array.

The overview block diagram of the proposed experimental feed system is shown in Figure 3-1.

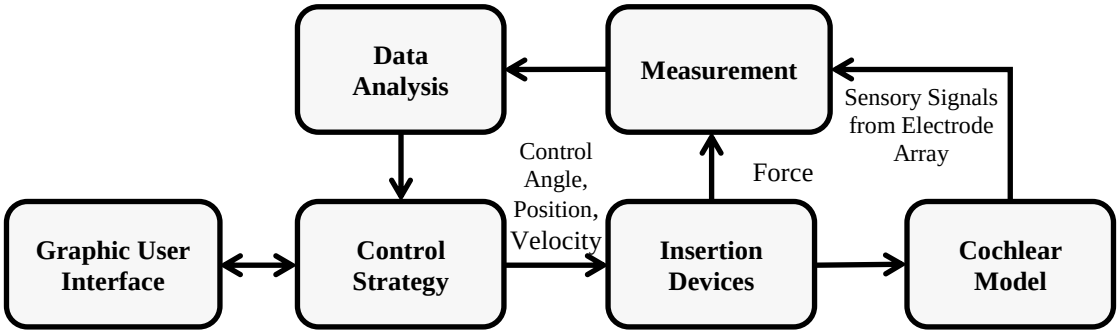

Figure 3-1: The overview block diagram of the proposed experimental feed system.

The goal of the proposed feed system was to achieve safe and consistent implantation by controlling the electrode array feeding into the cochlea model. Electrode capacitive signals and insertion force data would be used to interpret the state of the electrode array during the insertion. Based on these sensory signals, the control strategy would be applied to control the electrode array feed rate, position and velocity of insertion devices. This would augment the process of determining sensing and control strategies. In our research, all data interpretation algorithms, control strategies, and the user interface would be produced with software on a computer. Similarly, results from the insertion process and states of the electrode array insertion progress would be demonstrated in *silico*.

Experimental tools of the system are shown in Figure 3-2.

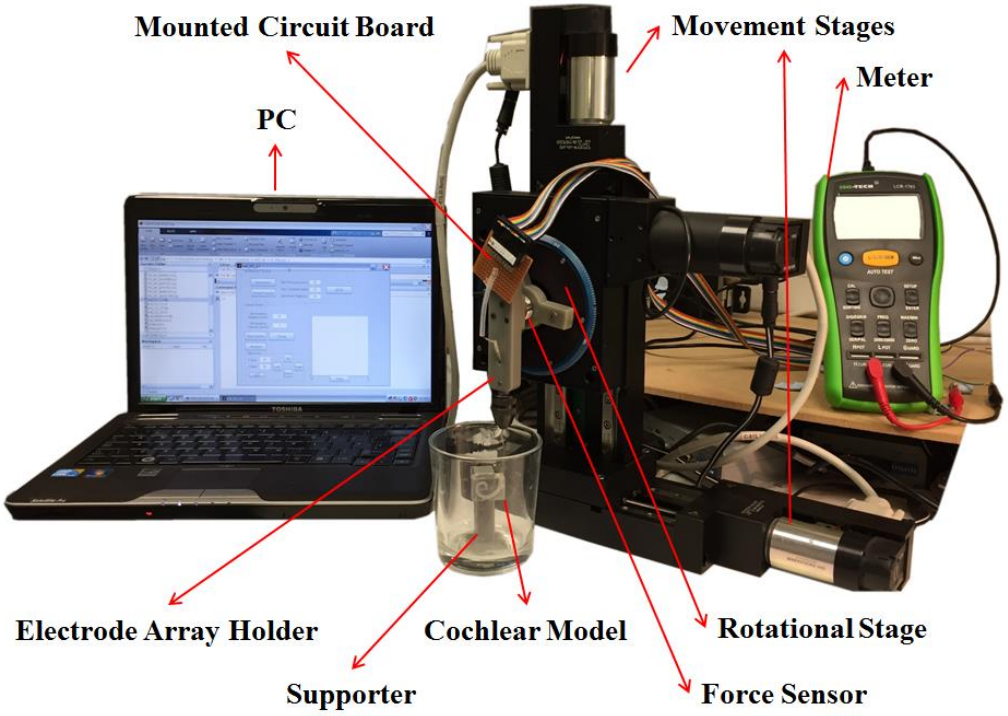

Figure 3-2: Experimental tools of the automated feed system.

There were several aspects of designing the phantom unit, including hardware development, model creation, software integration development, testing and refinement. The hardware included two translation stages, one rotation stage, three LCR meters (ISO-TECH, LCR1703), cochlear models, an electrode array and its holder. The mechanism of LCR meters were detailed in Section 3.5.2. The movement stages were professional assembled and calibrated by Physik Instrumente (PI) staff. The remaining parts were designed and assembled by the author. Software integrated with the feeding device were developed to generate a user interface to realise and control the real-time visualization system of the whole drilling procedure of the electrode array. MATLAB software was utilised to program and control the continuous feed machine system. A three-dimensional (3D) model of the human cochlea was formulated, as the cochlear model creation based on real human cochlea was difficult and expensive to obtain. The model had a similar stiffness and proportional size to real cochlea. Further, the model helped in understanding and examining the whole process of the electrode array feeding. A switch channel board was developed to measure the capacitance from multiple pairs of electrodes.

3.2 Cochlear Implant Electrode Array

The electrode array utilised in this project was a Digisonic® SP electrode-array which was manufactured and supplied by a cochlear implant manufacturing company Oticon. The electrode array had basal diameter of 0.5mm and apex diameter of 0.4mm [56]. Picture of the apex part of the electrode array is shown in Figure 3-3.

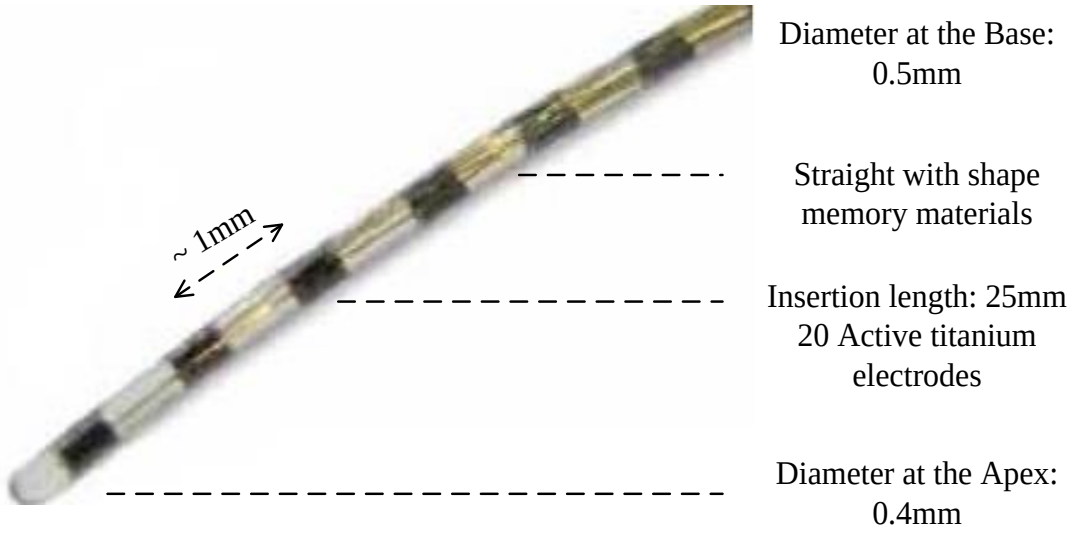

Figure 3-3: The apex part of the electrode array utilised in the project. (Image from [52])

Comparing to standard specifications, the electrode-array had the advantages in the smooth surface, reduced diameter, and flexibility [52]. Its smooth surface, small diameter and memory shape ensured that the inner cochlear structures were preserved as much as possible.

The electrode array was formed by three parts: electrode contacts, electrodes carrier and wires. The electrode array had 20 micro-machined titanium-iridium electrodes with the stimulating area 0.46 to 0.60 mm^2 [56]. All electrodes were surrounded by a silicon carrier and each electrode was connected with a wire.

3.2.1 Electrodes

The electrode array held 20 active titanium-iridium contact electrodes and had deep insertion length of 25 mm [56]. These contact electrodes had the capacity to simulate the complete sound spectrum of the human cochlea. Distance between the adjacent electrodes was around 1 mm. The shape of the electrode is shown in Figure 3-4.

(a) (b)

Figure 3-4: (a) Structure of a cochlear implant electrode (b) An electrode on finger. Average active area of an electrode ranges from 0.46mm^2 to 0.6mm^2. (Image from [52])

Each electrode was made of platinum iridium with the average activing area 0.46mm^2 to 0.6mm^2 [56]. Surface of the electrode was a smooth semi-cylinder that attached to the electrodes carrier. Each electrode was controlled and stimulated through a wire. All the 20 wires were squeezed inside of the electrode cylinder chamber and the electrodes carrier. The electrodes probe was manufactured and supplied by a cochlear implant manufacturing company Oticon. Each electrode was so tiny and dedicate that any extra sensor would destroy the usability and functionality.

3.2.2 Electrodes Carrier

Material of the electrodes carrier was silicon. The shape of the electrodes carrier was straight with shape memory. This design would minimise the array insertion force and preserve the residual hearing. There were two push rings located at the base that would assist the electrode array insertion.

3.2.3 Electrodes Wires

In order to implement a precise measurement, each wire output from an electrode was soldered to a pin of a 20-pin male dual row header connector. The electrode array and the mounted circuit board are shown in Figure 3-5.

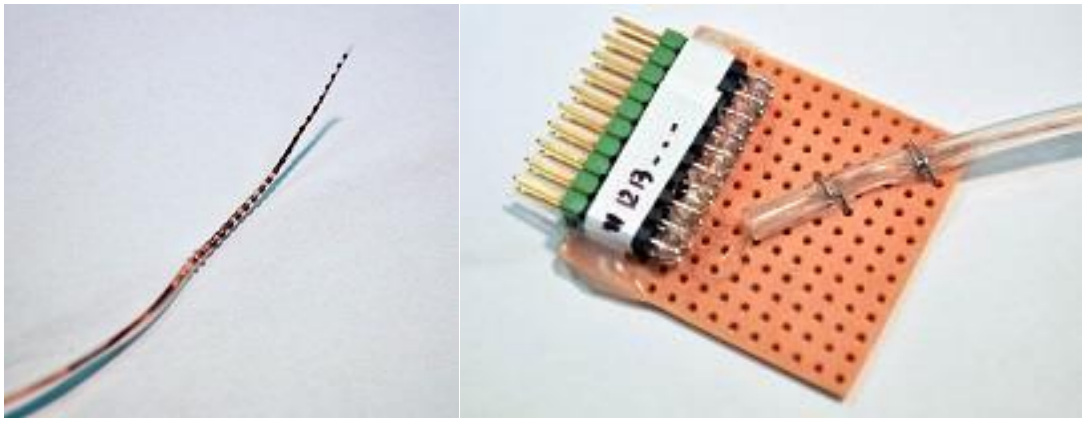

(a) (b)

Figure 3-5: Electrode array and mounted circuit board. (a) The electrode array utilised in the project that held 20 active platinum contact electrodes. (b) The electrode array was fixed onto a circuit board with wires connected to a 20-pin male dual row header connector.

The connector, as well as the electrode array, was mounted onto a circuit board to avoid damaging the wires. This mounted circuit board forced the distance fixation between each wire. It minimised the environment capacitance disturbance and was consistent for implementing the measurement. The board would be firmly glued onto the vertical movement stage.

3.3 Insertion Devices

The electrode array insertion system consisted of two main components- hardware and software. With the hardware, two translation stages, one rotation stage and an electrode array holder would be described in detail in section 3.3.1. For the software, a MATLAB program was developed to control the insertions would be discussed in section 3.3.2. A Graphical User Interface (GUI) was crafted to demonstrate control progress and record the array position in real-time.

3.3.1 Hardware Development

Two translation stages, one rotation stage and an electrode array holder would be described. A picture of the electrode array feed system is shown in Figure 3-6.

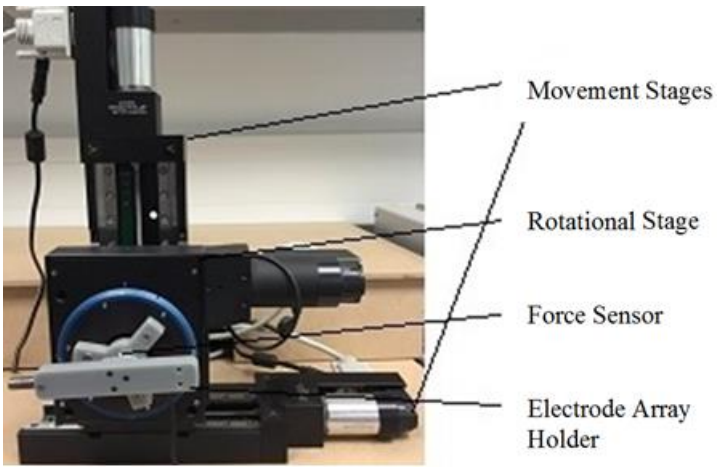

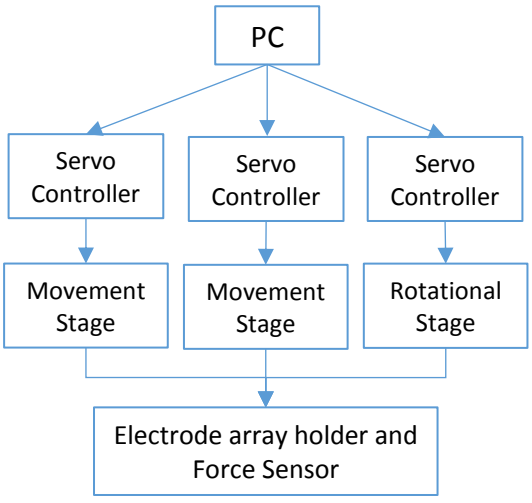

Figure 3-6: (top) The electrode array feed system was composed of two axis movement stages, one rotation stage, a force sensor and a CI electrode array holder. (bottom) Schematic diagram of the electrode array feed system.

3.3.1.1 Physik Instrumente Translation Stages

The translation stages utilised in the project were the Physik Instrumente (PI) product, M-404 precision translation stages, with the objective of generating movement of the horizontal and vertical axis. The translation stages had the advantages of cost-effective design, wide travel range (100 mm) and minimum incremental motion (0.25 µm) [110]. The high-resolution movement satisfied the high-precision requirement of the cochlear implant electrode array surgery.

Drivers of the stages were the Physik Instrumente (PI) product C-863 mercury servo controller [111]. Each stage was controlled by a single controller. RS-232 serial communication cables were employed to facilitate communication between stage controllers. The address of each stage controller was separated by the 8-bit DIP switch. An image of the controller is seen in Figure 3-7.

Figure 3-7: C-863 mercury servo controller.

The C-863 mercury servo controller could be controlled through USB/ RS-232 serial cable [111]. The RS-232 out port was utilised to communicate with another controller. The 8-bit DIP switch dominated the device address (switches 1-4), communication baud rate (switches 5-6), limit switch mode (switch 7), and firmware update mode (switch 8). From Figure 3-7 settings of the controller were: device address was 1, baud rate was 9600, limit switch mode was off and firmware update mode was off. Apart from the device address, settings of the other controllers were identical.

3.3.1.2 Physik Instrumente Rotation Stage

Another part of the hardware was the Physik Instrumente (PI) product M-061 precision rotation stage [112]. It provided continues rotation range with the high incremental resolution 17.5 μrad. The rotational stage was applied to investigate the optimal insertion path by adjusting the angle.

One rotation stage was integrated onto the force sensor and the vertical translation stage that was shown in Figure 3-6. Identical to the translation stage, the controller to the rotation stage was the C-863 Mercury servo controller.

3.3.1.3 An Electrode Array Holder

The electrode array holder was created by a three-dimensional laser printer that could be fully mounted onto the force sensor. The holder is shown in Figure 3-8.

Figure 3-8. An electrode array holder.

In this method, a clamp held the electrode array by various forces to simulate the holding by surgeons. Electrode wires passed through the central lumen of the holder to connect to the circuit board. Fixation of the electrode array enabled consistent measurements as the insertions noises were minimised.

3.3.2 Software Development

3.3.2.1 Automated Control system

The software used to drive the PI system was based on the MATLAB and a specific tool library was used that was PI_Mercury. In order to achieve the best performance of the PI system, a Graphical User Interface (GUI) was created in MATLAB to help the user to control the three stages. The initial interface of the GUI is shown in Figure 3-9.

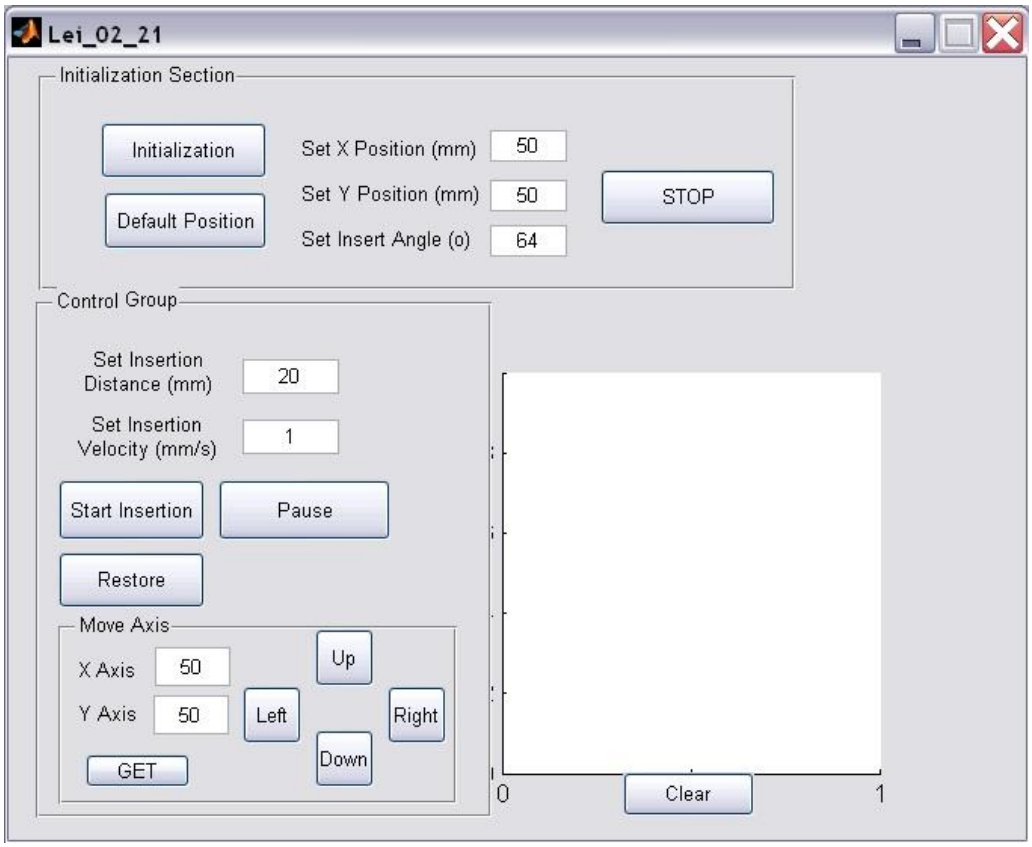

Figure 3-9: initial interface of the GUI based in MATLAB.

From the GUI interface, there were two main functions: moving by controlling of the speed and directions and the other one was moving to a certain position. From Figure 3-9, the initial communication between the feed system and PC was the 'Initialization'. The communication was achieved by initializing the settings and sending commands to give each device a separated address to fully control of the devices. The codes of the initialization wrote in MATLAB are shown Figure 3-10.

```
% --- Executes on button press in Start.
function Start_Callback(hObject, eventdata, handles)
% hObject    handle to Start (see GCBO)
% eventdata  reserved - to be defined in a future version of MATLAB
% handles    structure with handles and user data (see GUIDATA)

    clc; clear;
    hold off


    % Create Instance of controller class
    if(~exist('Controller'))
        Controller = Mercury_GCS_Controller();
    end;
    if(~isa(Controller,'Mercury_GCS_Controller'))
        Controller = Mercury_GCS_Controller();
    end;
    stagename = 'M-404.4PD';
    stagename1 = 'M-404.4PD';
    stagename2 = 'M-061.PD';

    % connect using the serial port
    if(~Controller.IsConnected)
        Controller = Controller.ConnectRS232(3,9600);
        Controller = Controller.InitializeController();
    end
```

Figure 3-10. Initialization Code.

From the code above, the device controller was defined and the model of each stage was specified. Under the initialization, each stage was initialized and split by separated address to allow the parallel real-time communication and controlling by the users.

The other initialization part of the program was the 'Reference Position' that was shown in the move to position section. Similar to the 'Initialization', the 'Reference Position' would build the communication between the devices and the PC. But more than 'Initialization', the device would move to the reference position with a specific speed as soon as the communication was built.

Apart from the initialization program, there were many functions programed to manually control the device such as the 'STOP', 'PAUSE', 'MOVE FORWARD/UP/DOWN/BACK' and 'CLOCKWISE/ANTICLOCKWISE/STOP ROTATION'. Among them, the 'STOP' key would break the whole communication between the device and PC; the 'PAUSE' key would pause the device movement and keep the communication. The codes are shown in Figure 3-11.

```
% --- Executes on button press in Stop.
function Stop_Callback(hObject, eventdata, handles)
% hObject    handle to Stop (see GCBO)
% eventdata  reserved - to be defined in a future version of MATLAB
% handles    structure with handles and user data (see GUIDATA)

a=1;
save 'file_a.mat',a;
```

```
% --- Executes on button press in Pause.
function Pause_Callback(hObject, eventdata, handles)
% hObject    handle to Pause (see GCBO)
% eventdata  reserved - to be defined in a future version of MATLAB
% handles    structure with handles and user data (see GUIDATA)

m=0;
n=0;
a=0;
save 'file_a.mat',a;
```

Figure 3-11. 'STOP' function code and 'PAUSE' function code.

From the code above, 'STOP' function sent '1' to break the communication however the 'PAUSE' function would keep the communication but set the movement speed to 0 to pause the device movements.

The other functions in the axis control panel were move Up/Down/Forward/Backward and clockwise/anticlockwise rotation. The speed of the movement was typed in manually or sliding from the speed slider box. Due to similarity in structure, the codes of the forward movement are shown as an example in Figure 3-12.

```
% --- Executes on button press in Move_forward.
function Move_forward_Callback(hObject, eventdata, handles)
% hObject    handle to Move_forward (see GCBO)
% eventdata  reserved - to be defined in a future version of MATLAB
% handles    structure with handles and user data (see GUIDATA)

l=get(handles.Speed_Text,'String');
m= (0.05*(str2num(l))^2);
a=0;
save 'file_a.mat',a;
```

Figure 3-12. Moving forward function.

The principle of the axis movement and rotation was by returning of the speed string to algorithm so that the speed value could be stored into a string and passed to the main function. In this method, the axis movement and rotation speed could follow the speed in real-time. The speed of this system was limited between 0 and 10 mm/s to avoid the any fast movement damage to affect the precise movement. Fast stage movements caused huge momentum that affected the stages stabilization. Also, the speed was too fast and unnecessary in this precise project.

Apart from the ‘Reference Position’, the other functions in the ‘Move to Position’ section included the ‘STOP REF’, ‘X POSITION’ and ‘Y POSITION’. Similar to the ‘STOP’ function in axis control section, the ‘STOP REF’ would break the whole communication between the devices and PC. ‘X POSITION’ and ‘Y POSITION’ would allow users to enter the specific X and Y position that the device moved to with the default speed. The function allowed the stages automatically move to the desired position repeatedly.

3.4 Three-Axis Force Sensor

One three-axis force sensor (Nano17 Titanium Transducer, ATI Industrial Automation, USA) was integrated between the electrode array holder and the rotational device to collect force data from all three Cartesian Coordinates [113]. Picture of the force sensor is shown in Figure 3-13. Force data was collected by a data acquisition card (DAQ) device [114]. Before each experiment, the system was calibrated by a supplied load file to convert the input voltage signal to a force reading.

Figure 3-13: The three-axis force sensor.

The force measurement system included a force sensor (Nano17 Titanium) and an electrode array claw. The setup was by using force sensor to detect the force insertion of the electrode array. The Data Acquisition Module (DAQ) was formed by an ATI data acquisition device and NI USB6211 multi-functional input/output device. The handling software was able to collect the three axis forces at 10Hz, which indicated there were 10 signals per axis per second was recorded. The software was possible to operate in any operating system like Windows XP.

With respect to the software, the Calibration file was FT15407.cal. It was used to convert input signals into the three forces and torque. The force X, force Y and force Z indicated the three axes that was horizontal, vertical and perpendicular to the surface force. The X, Y and Z were marked on the sensor, thus before the measurement, these forces were necessary to be calibrated to have the same direction with the electrode array holder. In this experiment, the vertical angle in the software was adjusted 40^{o} clockwise to match the vertical axis.

3.5 The Capacitance Sensing Methodology

3.5.1 Three-Dimensional Cochlear Phantom Model

A translucent 3D cochlear model of proportional size of the human cochlea and its supporter were printed by 3D printers. The printing materials were Veroclear and Accura 60 respectively. Both of them were non-conductive materials. The models were built by the 3D CAD design software SOLIDWORKS (SOLIDWORKS, Dassault Systèmes SolidWorks Corporation, the U.S.).

In the study, a cochlear implant electrode array was robotically inserted into an artificial model. The model was 3D printed with an identical opening size to the real cochea. However, the 2D inner path was twice the average size of a real cochlea with a proportional central curvature. Unlike a manual CI array insertion, only at this design the robotic could fully insert the array into the model. However, the longer and 2D insertion path might significantly affect the measured signals values. The methodology was based on an assumption that capacitive signals trending was similar between an actual cochlear size and the enlarged model.

The translucent 3D cochlear model was firmly glued onto a supporter and the supporter was glued onto the bottom of a glass before insertions. The glass was filled with conducting liquid to simulate the environment of the inner human cochlea. The inner path was carefully washed by a needle to avoid any air bubbles attaching to the inner track. The electrode array holder was screwed onto the rotational device. It has a central lumen to clip the electrode array straight. The tip of the clinically used electrode array was placed at the entry of the cochlear model. The preparation and alignment is shown in Figure 3-14.

Figure 3-14. Before the insertion, the electrode array was clipped straight at the entry of the translucent cochlear model. It was placed in close proximity to the inner side wall.

The whole insertion progress was recorded by a HD video camera (FS200, Canon, Japan) to analyse the behaviour of the electrode array inside of the model. The start position of the first spiral was defined as 0^o following the horizontal axis, as shown in Figure 3-15.

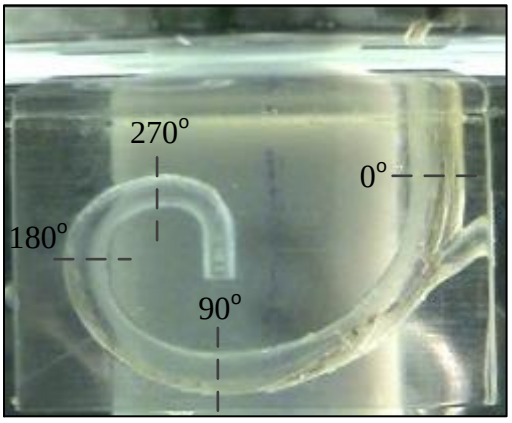

Figure 3-15. Definition of the angle of insertion. The start position of the first spiral was defined to be 0^o.

The path above the start position of spiral was straight, which simulated the round window insertion. The finish position of the first spiral was defined to be 90^o which followed the vertical axis. The finish position of the second spiral was defined to be

180^{o} and the finish of the third spiral was defined to be 270^{o}. This logarithmic spiral shape followed the biological structure of the cochlea. However, during the insertion, the electrode array would only follow the spiral curve until full contact occurs between the first two electrodes with the outer side wall.

Using this model, an insertion angle against capacitance/ force plotting was produced based on the synchronized insertion length data. Data were presented in the result section as capacitance and average force versus angle of insertion.

An insertion example was portrayed in Figure 3-16. By comparing the recorded video with the capacitance fluctuation, the movement of the electrode array was shown in the screen cut. There were four sections of the electrode array insertion up until 180^{o}: before 7 mm, between 7 mm and the first contact at the bottom of the outer wall, between when the tip first makes contact and the slide along the wall, and, lastly, the continually sliding section following along the cochlear wall. The corresponding four insertion lengths of changing were: 9 mm, 13 mm 16 mm, and 19mm. The video screenshot of these insertion lengths are shown in Figure 3-16.

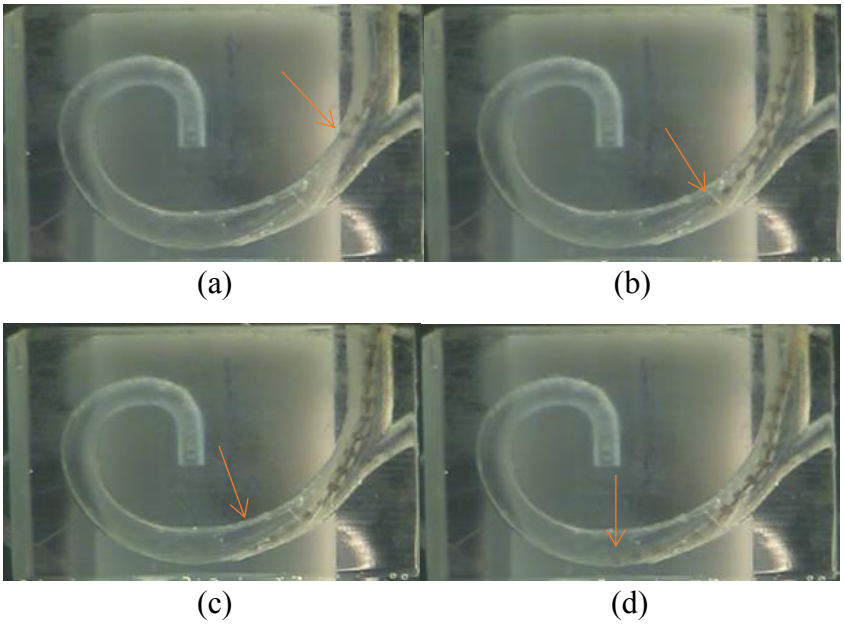

Figure 3-16: Different insertion progress states. (a) 9mm insertions, the tip of the electrode started to touch the inner wall. (b) The electrode array had already separated from the inner cochlear wall. (c) The electrode array touched the outer cochlear wall. (d) 19mm; the electrode array laid down at the bottom of the model.

In the beginning, before the angle was 0 degree, the electrode array was inserting along a straight, inner wall, where there was limited force applied to the electrode array. During the second stage, there were many activities. First, both of the electrodes made contact with the inner wall. After 11mm, the tip of the electrode started to move away from the inner wall, leading to an increase of the capacitance due to the conductivity effect. At 13mm, the first electrode started to make contact with the bottom wall. The buckling and releasing event caused fluctuations of the electrode array. From the insertion length, both of the electrodes contacted the bottom wall. After 20mm, the electrode array had been inserted smoothly was shown as stable.

3.5.2 LCR Meter and Channel Switchboard

3.5.2.1 LCR Meters

There were 20 contact electrodes in the electrode array and each of them had a wire connect to a pin header. The capacitance between coupled electrodes was measured by a LCR meter [115] at a frequency 100 KHz. The AC test voltage was 600mVrms with a high accuracy ± 0.05% [115].

The three LCR meters (ISO-TECH, LCR1703) used in the project were based on the ES51919/ES51920 Cyrystek chipset [136]. The chipset could measure inductance, capacitance, resistance with secondary parameters, such as dissipation factor (D), quality factor (Q), phase angle (θ), equivalent series and parallel resistance (ESR and Rp) [136]. In the project, the operation frequency was set to be 100 KHz at the parallel mode. The equivalent circuit of the parallel capacitor mode is shown in Figure 3.17.

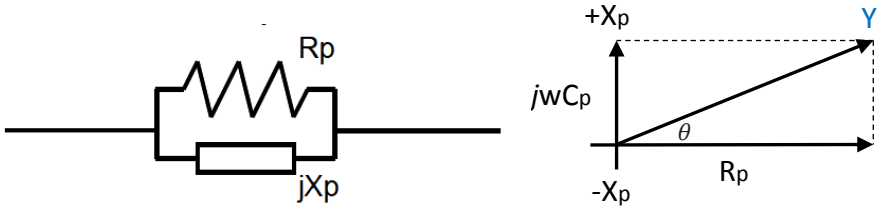

Figure 3.17. Impedance in parallel mode. (Left) The impedance consisted of resistance (Rp) and reactance (Xp). (Right) Phase relationship between resistance and reactance. (Figure from [136])

To minimise the parasitic impedance, the maximum measuring frequency of 100 KHz was selected. It was due to the fact that with higher measuring frequencies, capacitors became lower impedances. In the equivalent circuit of capacitors, series resistance (Rs) and parallel resistance (Rp) were both existed, but Rp was dominant in small capacitors (<2nF) (± 0.1pF) and Rs was dominant in large capacitors [136]. As the capacitance measured was relatively small in the project, parallel mode was used to perform the measuring.

Unlike a general multi-meter, the LCR meter could measure DC resistance and AC impedance. In the equivalent circuit, the admittance, *Y*, was the reciprocal of impedance *Z*. They had a relationship:

$$Y = \frac{1}{Z} = \frac{1}{R_p} + \frac{1}{jX_p}$$

Where R_p was the real part resistance and jX_p was the imaginary part reactance in parallel mode. In the capacitive circuit, capacitance could be determined by finding the ratio of the resistance to the reactance. Hence, *D*, the dissipation factor, was employed to symbolize the ratio of the real part of impedance to the imaginary part, $D = \cot \theta$. The reciprocal of the ratio *Q* was known as the quality factor, $Q = 1/D$.

Before each experiment, the self-open/short calibration procedure of the meter was conducted by shorting the SMD test probe. The procedure was necessary to reduce the parasitic effect of the test fixture to get a better accuracy for impedance measurement. The LCR meter connected to the PC through a standard USB cable. The measured data was recorded in the PC and stored in the software WINDMM700 at a frequency 2 Hz.

Therefore, the capacitive values measured would only be useful for others under the same experimental conditions, such as same saline concentration, temperature, model geometry, materials, CI array manufacturer, type and etc. However, the signals trending information during the CI array insertion could be useful for other relevant research. The trending information indicated the changes of capacitance during a CI electrode array insertion. In addition, the experimental methodology, pattern discrimination method and switching board would be helpful for other researcher to continue on this work.

3.5.2.2 The Channel Switch board

In conducting liquid, the measuring voltage across electrodes disturbed each other when measuring two or more couples of electrodes at the same time. The reasons and outcome would be described in detail in Chapter 5. In order to measure three pairs of electrodes during the electrode array insertion, a switching board was developed to measure one pair of electrodes at a time. Setup of the LCR meters and channel switchboard is shown in Figure 3-178. Mechanisms of the channel switch aboard would be detailed in Section 7.1.

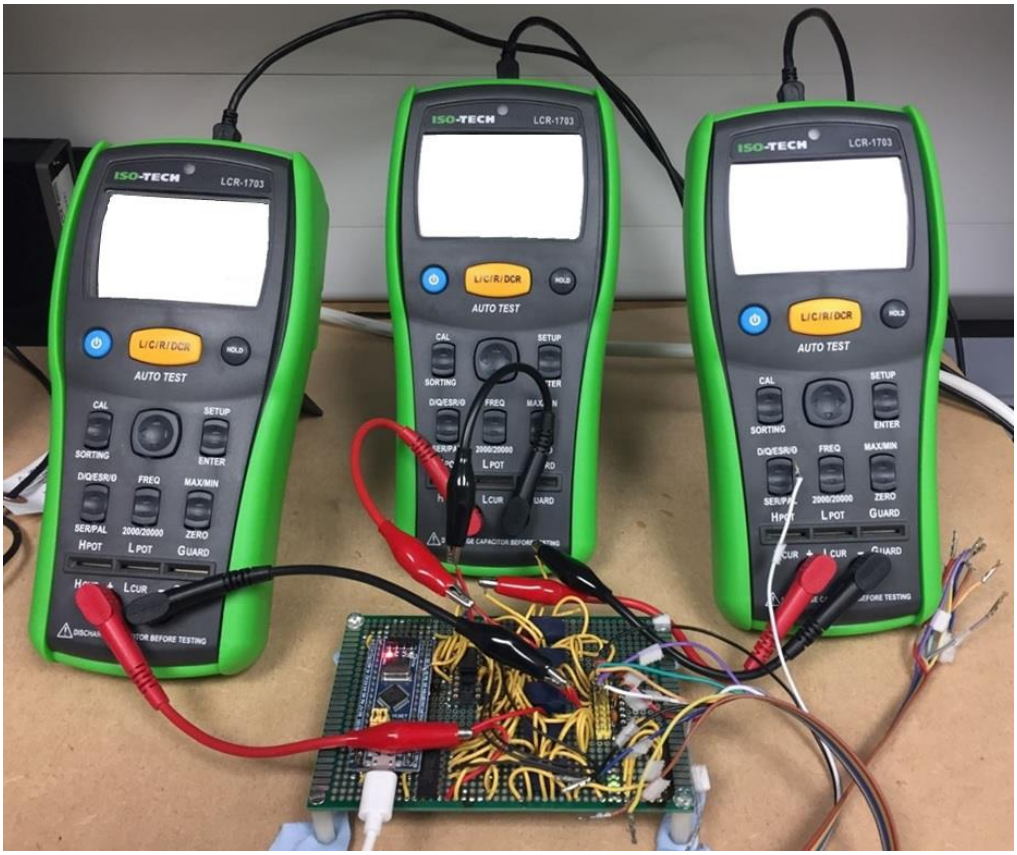

Figure 3-17: Three LCR Meters and a Channel Switchboard.

The channel switchboard was built based on a microcontroller (STM32F103C8T6.2015) and a transistor array (ULN2003). The microcontroller incorporated ARM® Cortex®-M3 32-bit RISC core and it operates at 72 MHz frequency [116]. The device worked from 2.0 V to 3.6 V, supplied by the PC connected to it. The microcontroller was programmed to control the on and off states of five transistor arrays. It sent 6 different output signals to operate with the transistor arrays to realise the 3 channels switching activities. Each transistor array had two output wires. By sending commands to the microcontroller, each channel was switched to be 'ON' and 'OFF'. A mini USB cable was used to communicate with the PC to control the channels ON, OFF and the whole activating time. The operation and results would be explained and discussed in detail in Chapter 7. The embedded programming environment was ARMKeil - MDK 5.17 [117] and a serial port debug tool SSCOM was used to send commands to the microcontroller.

In the software section, the embedded programming environment was ARMKeil - MDK 5.17 [117]. A serial port debug tool (SSCOM) was used to communicate between the microcontroller and the PC.

There were three channels of the board and the measuring time (ON) was set to be 500ms and the switching time (OFF) was 50ms. To compare the continuous capacitance measurement and the switching board capacitance measurement, each of the three channels were continually measured three times. The switching board capacitance measurements were performed three times.

3.6 Conclusion

In this section, the feed system sensing methodology and experimental tools were detailed described. Hardware and software of the system work corporately to implement force and capacitance sensing activities. These sensing data during the electrode array insertion were gathered and analysed to discriminate different insertion features.

The hardware of the system included:

- A cochlear implant electrode array for clinical use.
- Two movement stages and one rotational stage.
- An integrated force sensor.
- An array holder, a translucent Cochlear model and its supporter. They were built by 3D printers.
- Three LCR meters and a channel switchboard.

The software of the system included:

- A graphic user interface (GUI) based on MATLAB. MATLAB would also implement the data analysis task.
- An ATI data acquisition (DAQ) system with a voltage-force calibration file.
- 3D CAD Design Software – SOLIDWORK.
- Capacitance data acquisition software WINDMM700.
- Embedded programming software ARMKeil - MDK 5.17 (Keil).
- A serial port debug tool (SSCOM).

Chapter 4

Force Measurement of the Cochlear Implant Electrode Array Insertion in Vitro

Within this Chapter, the theoretical analysis and experimental results of the insertion force were presented. According to the literature review, the electrode array insertion force was currently the principal means to evaluate insertion behaviours. A force model simulating the first contact between the array tip and cochlear inner wall was proposed. Force profiles of a phantom array and electrode array insertions would be evaluated and discussed.

The structure of this chapter was organised as follows[1]. Section 4.1 covered the theoretical analysis of the mechanical behaviour of an electrode array. Section 4.2 investigated the force profiles of a phantom array and evaluation process. In Section 4.3, the electrode array insertion force profiles were illustrated and analysed. Lastly, Section 4.4 concluded the chapter.

[1] The contents of this chapter have partly appeared in "Capacitance Measures during Cochlear Implants Electrode Array Positioning" by HOU, L., Du, X. and Boulgouris, N.V. (2018). *Capacitance Measures during Cochlear Implants Electrode Array Positioning*. In: 10th International Conference on Bioinformatics and Biomedical Technology (ICBBT '18). New York, NY, USA: ACM, pp.78-82. DOI: 10.1145/3232059.3232069

4.1 Mathematical Model for Cochlear Electrode Array Deflection during Insertion

4.1.1 Introduction

The purpose of the theoretical analysis was to analyse the mechanical behaviour of an electrode array. When inserting a cochlear implant electrode array into a cochlea straight, the array would bend during the insertion along the outer wall of scala tympani (ST). Exerted force between a cochlear array and the scala tympani (ST) wall during the first turn was the primary cause of trauma in cochlea [29]. Therefore, it was essential to minimise the extorted force that was also known as the resultant force felt by surgeon during the electrode insertion. The model created was able to interpret the deformation when electrode tip slides along the ST wall. In order to analyse the behaviour of electrode array, a numerical analysis method: finite difference methods (FDM) was applied to divide the electrode into finite segments. Each of the segments was treated as a small deflection cantilever beam with the linearly elastic material [30].

4.1.2 Mathematical Model for the Array First Contact

For this study, a long, slender cantilever beam made of the linear elastic material was modelled. It was assumed that the beam was inextensible because any change in length was assumed negligible compared with the original beam length. The cross section of the beam was assumed to be constant which indicated the effect of Poisson's ratio was neglected [31]. It was also assumed that the Bernoulli-Euler bending theory was valid. Lastly, the deflection due to the weight of the beam was assumed negligible.

Although the overall interaction between the electrode and the scala tympani was three dimensional, the following analysis and model developed could be extended to electrode behaviour and tip contact. At any of the contact point, the directional insertion force would be represented by F. It was composed of an insertion force from surgeons and the array's own weight. When contacting to the inner wall, the force F could be decomposed into an advancing force F_1 and the force exerted on the ST wall F_s in basal turn. The insertion force breakdown diagram is shown in Figure 4-1.

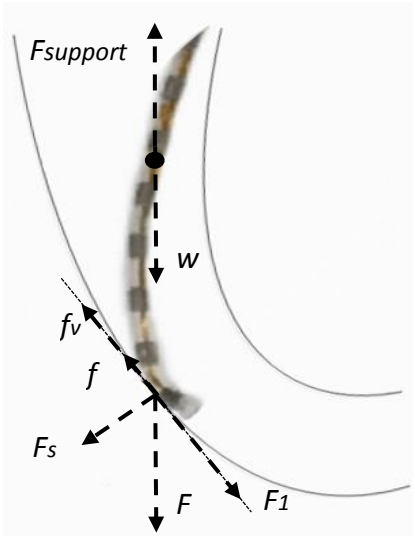

Figure 4-1: Insertion force diagram when electrode first contacts the ST outer wall in the plane of the basal turn.

From the figure, insertion force *F* composed of an insertion force from surgeons and the array's own weight. It determined an advancing force F_1 and a force perpendicular to ST wall F_s. The angle of the electrode impacted onto the ST was represented by β. The relationship between them was shown in Equations (4.1) and (4.2).

$$F_s = F\sin\beta \tag{4.1}$$

$$F_1 = F\cos\beta \tag{4.2}$$

It was assumed the insertion speed was slow and constant, thus the electrode insertion could be treated as quasi-steady. Hence, the advancing force F_1 was equal to the sum of resisting friction force *f* and viscous force f_v. By definition, friction was equal to $f = \mu F_s$, where μ was the coefficient of friction between the electrode and the ST outer wall. Thus

$$F_1 = F\cos\beta = \mu F_s + f_v \tag{4.3}$$

In a fully lubricated pipe, the viscous force f_v was assumed to be 0. Hence, with respect to the electrode array, the only the support force F_s acts at the tip. Orthogonal components of F_s was composed of vertical axis force F_y and horizontal axis force F_x. The breakdown of support force F_s in the x and y directions is redrawn in Figure 4-2.

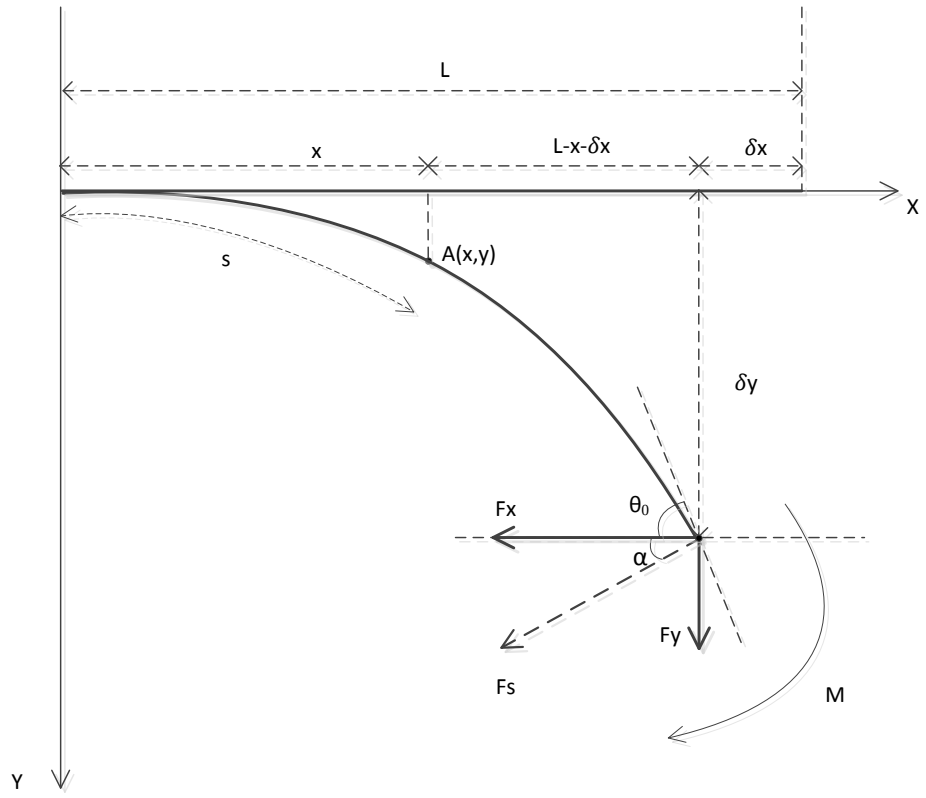

Figure 4-2: Breakdown of support force in the x and y axis.

Figure 4-2 showed a cantilever beam of length L with a concentrated force Fs applied at the free end. In the figure, θ_0 represented the maximum slope of the beam. δx and δy were the horizontal and vertical displacements at the free end. The origin of the coordinate system was the fixed end of the beam and point A represents any point along the beam with coordinates (x,y). s was the arc length between point A and the fixed end of the beam. M was the bending moment as a function of the distances x and y. Fx and Fy were the reaction forces in the x and y directions. α was the constant angle where force F was applied, yielded the following

$$Fy = F\sin\alpha \quad \text{and} \quad Fx = F\cos\alpha \tag{4.4}$$

The Euler–Bernoulli bending moment-curvature equation was

$$M_{(x,y)} = EI\frac{d\theta}{ds} \tag{4.5}$$

Where $M_{(x,y)}$ was the bending moment as a function of the distances x and y; E was the modulus of elastic of the material, and I was the 2nd moment of inertia of the beam

cross section. Where s was the arc length between point A and the fixed end of the beam, θ represented the angle at any point along the beam. M was the bending moment as a function of the distances x and y. *Fx* and *Fy* were the reaction forces in the x and y directions. α was the constant angle where force F was applied,

Moment equilibrium at any points along the beam was

$$M_{(x,y)} = Fy(L - \delta x - x) + Fx(\delta y - y) \tag{4.6}$$

Substituting equations (4.4) and (4.5) into equation (4.6) to yield

$$EI\frac{d\theta}{ds} = F\sin\alpha\,(L - \delta x - x) + F\cos\alpha\,(\delta y - y) \tag{4.7}$$

The first deviation with respect to s of equation (4.7) could be taken.

$$\frac{d}{ds}[EI\frac{d\theta}{ds}] = \frac{d}{ds}[F\sin\alpha\,(L - \delta x - x)] + \frac{d}{ds}[F\cos\alpha\,(\delta y - y)] \tag{4.8}$$

Under a constant force *F*, *L E*, *I* and the deflections δx, δy were constants, which leads to

$$EI\frac{d^2\theta}{ds^2} = -(F\sin\alpha)\frac{dx}{ds} - (F\cos\alpha)\frac{dy}{ds} \tag{4.9}$$

In order to solve the equation, the relationship between x,y and θ had to be found. For an infinitesimally small section of the cantilever beam, an arc length could be approximated as a straight line.

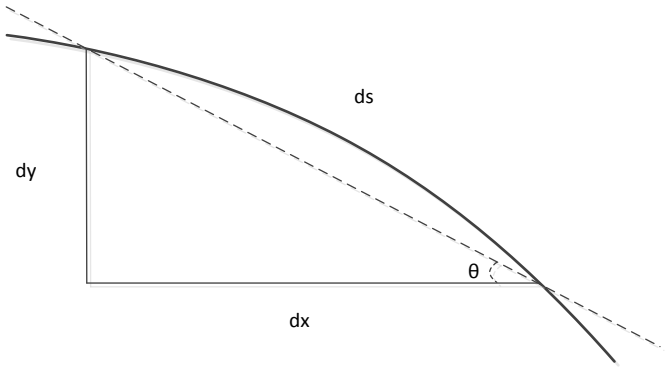

Figure 4-3: An infinitesimally small section of the cantilever beam.

Figure 4-3 showed an infinitesimally small section of the cantilever beam. Where s indicated of the an infinitesimally small arc length and θ was its tangent angle

Its trigonometry relationship was described in equation (4.10)

$$\sin\theta = \frac{dy}{ds} \text{ and } \cos\theta = \frac{dx}{ds} \tag{4.10}$$

Substituting equation (4.10) into equation (4.9), equation (4.9) could be expressed as

$$EI\frac{d^2\theta}{ds^2} = -(F\sin\alpha)\cos\theta - (F\cos\alpha)\sin\theta \tag{4.11}$$

Equation (4.11) described the deflection curve of a cantilever beam under a concentrated load at the free end. As the equation was a non-linear differential equation, an analytical solution would be developed.

Multiplying $\frac{d\theta}{ds}$ to both sides of the equation (4.11) with the limit θ_0 to obtain

$$EI\frac{d^2\theta}{ds^2}\frac{d\theta}{ds} = -(F\sin\alpha)\cos\theta\frac{d\theta}{ds} - (F\cos\alpha)\sin\theta\frac{d\theta}{ds}$$

$$EI\frac{d^2\theta}{ds^2}\frac{d\theta}{ds} + (F\sin\alpha)\cos\theta\frac{d\theta}{ds} + (F\cos\alpha)\sin\theta\frac{d\theta}{ds} = 0 \tag{4.12}$$

The equation could be integrated under the limit 0 to s to yield

$$\frac{d}{ds}[\frac{1}{2}EI(\frac{d\theta}{ds})^2 + (F\sin\alpha)\sin\theta - (F\cos\alpha)\cos\theta] = 0 \tag{4.13}$$

At the free end of the beam, $\theta(L) = \theta_0$ where θ_0 was unknown, equation (4.13) could be integrated as

$$\frac{1}{2}EI(\frac{d\theta}{ds})^2 + (F\sin\alpha)\sin\theta - (F\cos\alpha)\cos\theta + C = 0 \tag{4.14}$$

Where C was a constant. Rearranging the equation to yield

$$C = -\frac{1}{2}EI(\frac{d\theta}{ds})^2 - (F\sin\alpha)\sin\theta + (F\cos\alpha)\cos\theta \tag{4.15}$$

Applying boundary conditions $\frac{d\theta}{ds}$=0 at S=L and θ= θ_0 at S=L to equation (4.15) to yield

$$C = -(F\sin\alpha)\sin\theta_0 + (F\cos\alpha)\cos\theta_0 \tag{4.16}$$

Substituting equation (4.16) into equation (4.13), yielding

$$\frac{1}{2}EI(\frac{d\theta}{ds})^2 + (F\sin\alpha)(\sin\theta - \sin\theta_0) - (F\cos\alpha)(\cos\theta - \cos\theta_0) = 0 \tag{4.17}$$

Rearranging the equation

$$(\frac{d\theta}{ds})^2 = \frac{2F}{EI}[(\sin\alpha)(\sin\theta_0 - \sin\theta) - (\cos\alpha)(\cos\theta_0 - \cos\theta)] \tag{4.18}$$

Taking the square root of both sides of the equation (4.18)

$$\frac{d\theta}{ds} = \sqrt{\frac{2F}{EI}[(\sin\alpha)(\sin\theta_0 - \sin\theta) - (\cos\alpha)(\cos\theta_0 - \cos\theta)]} \tag{4.19}$$

Solving *ds* from the equation (4.19), yielding

$$dx = \sqrt{\frac{EI}{2F}}\frac{d\theta}{\sqrt{(\sin\alpha)(\sin\theta_0 - \sin\theta) - (\cos\alpha)(\cos\theta_0 - \cos\theta)}} \tag{4.20}$$

Substituting *ds* to the equation (4.20) for solving *dx* and *dy*, yields

$$dx = \sqrt{\frac{EI}{2F}}\frac{(\cos\theta)d\theta}{\sqrt{(\sin\alpha)(\sin\theta_0 - \sin\theta) - (\cos\alpha)(\cos\theta_0 - \cos\theta)}} \tag{4.21}$$

$$dy = \sqrt{\frac{EI}{2F}}\frac{(\sin\theta)d\theta}{\sqrt{(\sin\alpha)(\sin\theta_0 - \sin\theta) - (\cos\alpha)(\cos\theta_0 - \cos\theta)}} \tag{4.22}$$

Equations (4.21) and (4.22) should be integrated to describe the vertical and horizontal deflections at any points along the cantilever beam. However, there was no exact analytical solution to these equations. In order to find the deflected shape of the beam, a numerical integration was applied to find to the solution.

4.1.3 MATLAB Solution and Verification

4.1.3.1 MATLAB Solution

In order to solve equations (4.21) and (4.22) the value of the maximum angle θ_0 under constant force *F* had to be calculated. An integrating function *quadl* in MATLAB was employed to integrate θ from 0 to θ_0. The function separated the beam into 100 sections. Each section was assumed to be small enough that its arc length was approximated as a straight line. Thus, the maximum angle θ_0 in each section was calculated by the equation (4.19). The goal of calculating the correct maximum angle θ_0 in each section was accomplished by using the bisection method. The bisection method was a root finding algorithm. It repeatedly bisected an interval and then selected a subinterval where the root must located [32]. The error between the exact maximum angle and the approached root was controlled within 1x10^-4, which was 0.1‰ larger than the exact maximum angle. Next, the maximum angle θ_0 in each section was substituted into equations (4.21) and (4.22) to calculate the *x* and *y* coordinates. After storing the first section coordinates in MATLAB, the process repeated itself to find *x* and *y* coordinates in the next section. Lastly, coordinates in every section were gathered and plotted as the deflected beam curvature.

There were a few limitations of the MATLAB numerical solution. First, the maximum angle at the free end was limited between zero and ninety degrees. Also, the program could only compute deflections of beams with a constant force applied at the free end. Lastly, during the electrode insertion, electrode length (*L*) inside of the cochlea would continually increase. The program could be expanded to incorporate a beam with increasing length. This could be achieved by adding a variable *L(s)* to the deflection curve equation in place of the *L*. Moreover, the program could be adjusted to handle the maximum angle greater than ninety degrees.

4.1.3.2 Verification

The above numerical integration gave a solution to the large beam deflection. The solution to the equation was approximated by MATLAB to further investigate the behaviour of the electrode array. In order to prove the approximation was correct, a commercial finite element analysis software ANAYS was employed. ANSYS was a Finite Element Analysis commercial software for engineering modelling and

simulation [33]. Results executed from the MATLAB program were compared with ANSYS stimulation results.

In this example, parameters were input both into the MATLAB program and ANAYS. Concentrated force of 100 N were applied vertically downward and horizontally leftward at the free end of an aluminium beam. The beam exhibited a length of 1.5m, a width of 30mm and a height of 3cm. The beam was made of aluminium with Young's modulus 6.9 $x10^{11}$ pa and an area moment of inertia of 6.75 $x10^{-8}$ m^4 [34]. After calculating these parameters, result curves from MATLAB and ANSYS were plotted and compared. In order to perform the comparison, ANSYS result curve was input into MATLAB. Curves of the deflected cantilever aluminium beam under a constant force at the free end simulated by MATLAB and ANAYS were shown in the Appendix 4. These two curves were compared, exhibiting a maximum y direction error of 2%. It demonstrated that the beam deflection theory and MATLAB programming was accurate to derive the large deflections of a cantilever beam.

However, the model could only simulate the array deflection less than 90 degree in two dimensional. Large array deflection would involve highly non-linear analysis and could not use the model. In a real CI electrode array surgery, the insertion depth could up to 290 degree in three dimensional. Hence, the model was useful in simulating the first contact between the array tip and cochlear inner wall. In addition, the stiffness of the electrode array was soft. The force conduction mechanism might be different and the force model should be improved based on the array with low stiffness and large deflection.

4.2 Evaluation of a Phantom Array Insertion Force

In the previous sensing experiments in Chapter 3, a force applied to the electrodes supplied the major effects of the variations of the capacitance. A force sensor was integrated to examine the insertion force during the electrode array insertion progress.

The force meter applied was the ATI six-axis Force/Torque Sensor System. It was used to determine whether the insertion force had a relationship with the capacitance reading from the system. However, based on the CI electrode array was being so delicate, a similar stiffness soft plastic was applied to establish the insertion behaviour of the electrode array.

4.2.1 Experiment Setup

The force measurement system included a force sensor (Nano17 Titanium) and an electrode array claw. The setup of this experiment was by using force sensor to detect the force insertion of the electrode array. The experiment arrangement included a soft plastic to simulate the electrode array, a force Transducer and data acquisition module (DAQ). The DAQ module was formed by an ATI data acquisition device and NI USB6211 multi-functional input/output device. The handling software was able to collect the three axis forces at 10Hz which indicated there were 10 signals per axis per second was recorded. The software was possible to operate in any operating system such as Windows XP.

In the software, the Calibration file was FT15407.cal. It was applied to convert input signals into the three forces and torque. The force X, force Y and force Z indicated the three axes that was horizontal, vertical and press force. The X, Y and Z were marked on the sensor, thus before the measurement, these forces were necessary to be calibrated to have the same direction with the electrode array holder. In this experiment, the vertical angle in the software was adjusted 40^{o} clockwise to match the vertical axis.

4.2.2 Insertion Strategy

During the phantom array insertion, buckling occurred. Hence, it was important to find an insertion strategy to assist in inserting the electrode array. The method was to adjust the position of the electrode array holder by moving the actuator left; and right, while also rotating it to examine whether the electrode could be fully inserted.

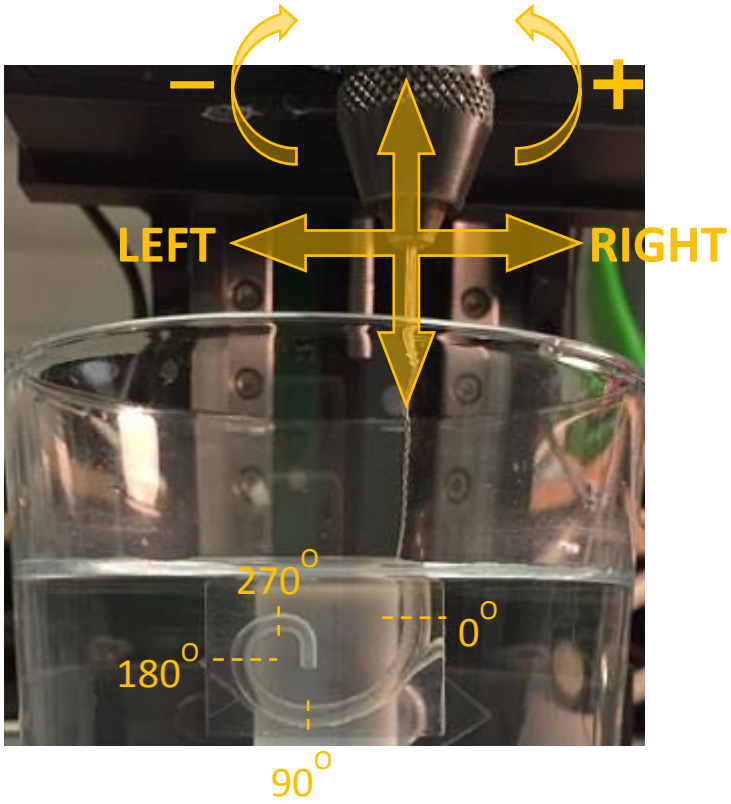

Figure 4-4: Diagram of the testing insertion strategies.

A series of experiments were carried out to determine insertion progress. Insertion attempts were listed in Table 4.1

Table 4.1 Electrode Array Insertion Strategies. The first column showed the array insertion speed. The second, third and fourth column demonstrated the position of the electrode array holder by moving the actuator left, right and angle turned. Each insertion speed combined with different position and insertion angle were tested.

Speed (mm/s)	Left(mm)	Right(mm)	Angle (Degree)
0.1	0	0	0
0.2	1	1	-2
0.3	2	2	-4
0.5	3	3	-6
0.6	4	4	-8
0.8	5	5	
1			

The electrode array was inserted from 0^o to 270^o (as shown in Figure 4-4) and the insertion strategy and path was recorded. Different insertion positions and speeds were attempted in order to eliminate buckling phenomena. During the insertion, the force data from the actuator was gathered to establish the best insertion strategy. The length of the electrode array was another critical issue for full insertion. The shorter the length was, the easier the insertion would be. In the experiments, it was found that the longest complete electrode array insertion was 29 mm.

4.2.3 Observational Result

During the insertion tests, buckling was caused by the friction between the electrode array and the cochlear wall. Various speeds did not aid in eliminating the buckling phenomena. During these attempts, it was observed that only an insertion of -1mm left of the centre of the entry hole could be applied to fully insert the electrode array. That meant that the electrode array had to be inserted close to the inner track, which would slide along the inner path. It was also observed that higher insertion speeds did not aid in eliminating the buckling phenomena. When the insertion speed was higher than 0.4mm/s, buckling was more likely to happen than lower insertion speeds. Also, lower insertion speed provided more measured samples during the insertion, so that 0.1 mm/s

was set for future tests. Based on the strategy, each the insertion was repeated five times. One of the successful insertions' force data was presented in Figure 4-5. With low-speed (0.1mm/s) insertions, the information gathered was several times larger than the high-speed insertions. This was because these low-speed insertions' time consumed was greater than with the high-speed insertions. It also had more of a chance to compensate or cease the insertion, rather than permitting buckling to continue.

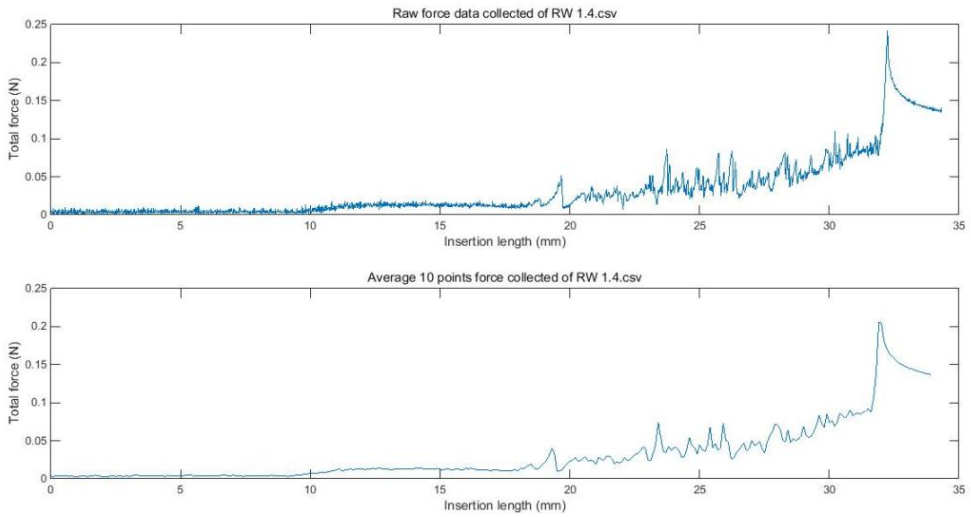

Figure 4-5: Raw force data collected from one of the successful insertions (top panel) and the average force of 10 points along the raw data (bottom panel). An array was inserted into cochlear model with a constant low speed of 0.1mm/s to the insertion length of 29mm.

From the Figure 4.6, x-axis indicated the insertion length and y-axis representd the detected insertion force. Up to the insertion length around 19 mm, the insertion force was stable and low. It called the stage 1: smooth insertion. At 19mm, a small force peak occurred that indicated a contact between the electrode array and the wall happened. It was separated as the stage 2: contact. Between 19mm to the last peak around 33mm, the insertion force fluctuated, and the average force was higher than before. It was due to the electrode array had to conquer the friction force against to the wall. This type of force was represented as stage 3: buckling/rushing. Up to the insertion length of 33mm, the insertion force was stable, and the maximum force was below 0.1N that was acceptable during the surgery. The maximum peak force was significant as it reached 0.24 N that could cause damages to the inner wall. Hence, the stage was treated as danger and should be discriminated.

4.2.4 Discrimination Algorithm

A discrimination of the electrode array insertion state was created. The algorithm was based on MATLAB programming. When detecting the insertion force, the algorithm would detect different states of insertion progress. In general, there were four stages that had to be discriminated

Stage 1 smooth insertion
Stage 2 making contact with the cochlear wall
Stage 3 buckling/rushing
Stage 4 danger, where the force exceeds the threshold

The flow chart of the discrimination algorithm is shown in Figure 4-6.

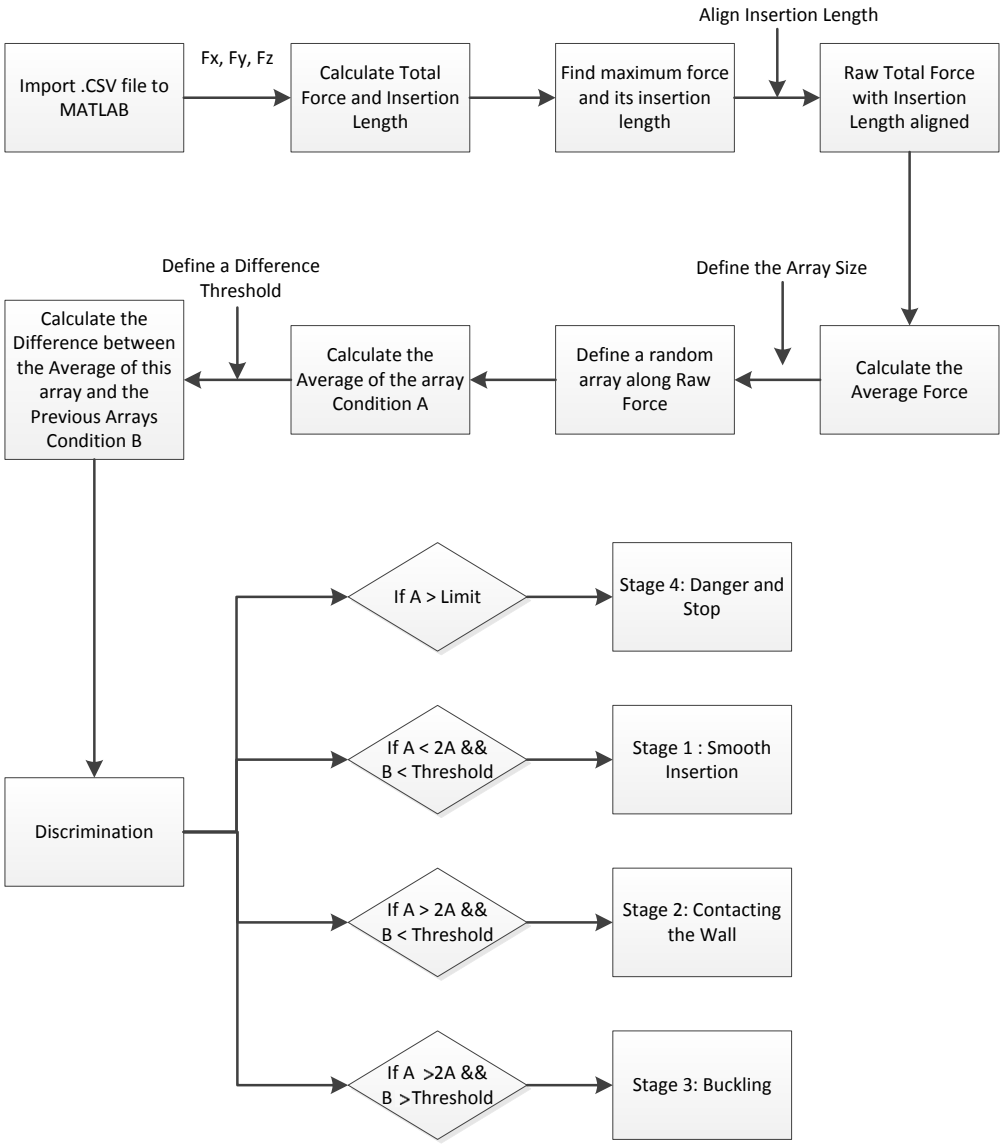

Figure 4-6: Flow chart of the discrimination algorithm. Four stages could be discriminated by the algorithm. The code was shown in the Appendix 1.

In order to detect these stages offline, three parameters were applied: the average value between 10 points, differential threshold, and force threshold. At stage one, the average force of 10 past points was below twice the value, and the maximum differential value was below the threshold. For stage two, the 10 points' average value was larger than twice that of the beginning value, and the differential value was below the differential threshold. Stage three was the rushing stage, where the electrode array would bend the release and progress was repeated. Thus, the 10 values would be higher than the differential threshold. So, if the average value was larger than twice of its first 20 values, and the maximum differential within 10 points was larger than the differential threshold, the electrode array was at stage three. During stage four, a force threshold was decided upon depending on the force penetrating the membrane. Based on these conditions, an algorithm was developed in MATLAB. The results of the simulation with the algorithm were found in the Results section.

4.2.5 Simulation Results Discrimination

The algorithm was applied in MATLAB and simulated for every point along the curve. The simulation results directly reflected each point at every stage. The simulation results of the algorithm are shown in Figure 4-7

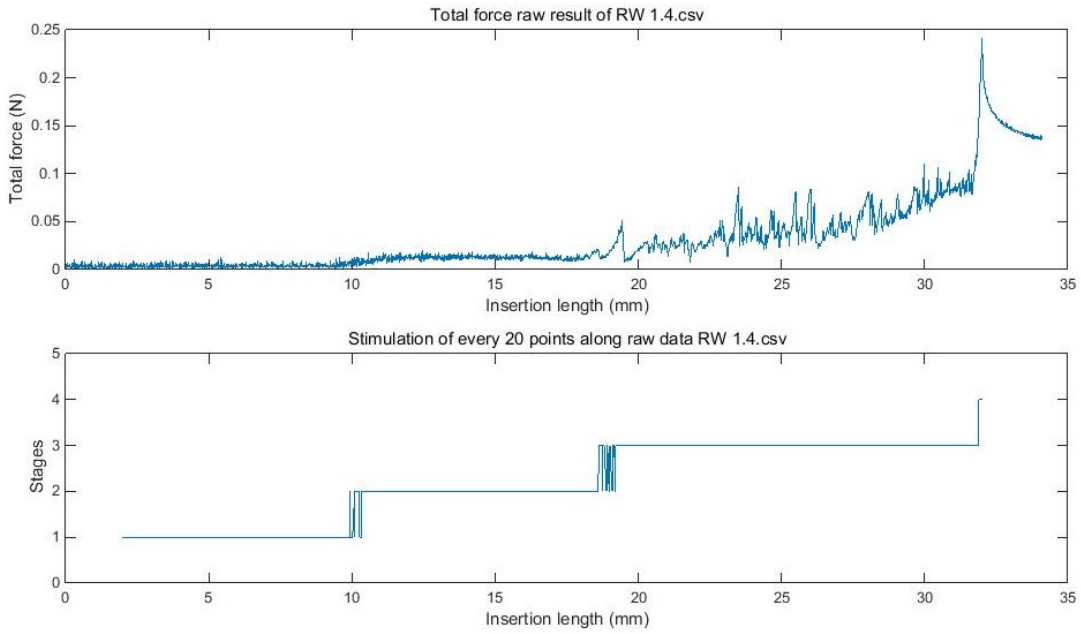

Figure 4-7: Simulation results of every point along the force curve.

From the findings, it appeared stages discrimination was clean throughout. However, there were fluctuations with the rises of the stages, though this was acceptable for such an application. These stages would give a clear indication to the surgeon, during the different stages, and the fluctuations would demonstrate the changing of the stages.

4.3 The Electrode Array Insertion Force Profiles

In the last section (4.2), the insertion force profiles of a phantom array were evaluated. This same methodology would be applied to a pre-clinically used electrode array. The goal of this section was to investigate the cochlear implant electrode array insertion force profiles. The array was inserted into a translucent cochlear model at different speed and patterns.

The insertion force profiles were collected by the same methodology introduced in Section 4.1. The record frequency was 10 Hz, which indicated 10 points were recorded per second. Before insertions, the electrode array tip was placed at the opening of the cochlear model as in Figure 3-14. In Section 4.1, three insertion patterns were introduced: smooth insertion, buckling insertion and fold-over insertion. Two different insertion speeds of 0.1 mm/s and 0.05 mm/s were applied to the smooth insertion pattern to determine the insertion profiles. The force profiles of 40 electrode array smooth insertions were depicted in Figure 4-8.

Within Figure 4-8, average force for insertion speed of 0.1mm/s was stable and low (<0.1N) before 270 sample length. After that, insertion force started to fluctuate but within the acceptable limit of 0.15N. Likewise, the average force for insertion speed of 0.5mm/s was stable and low (<0.1N) before 600 sample length. However, it increased to large insertion force (>0.15N) after 650 sample length that should be avoided.

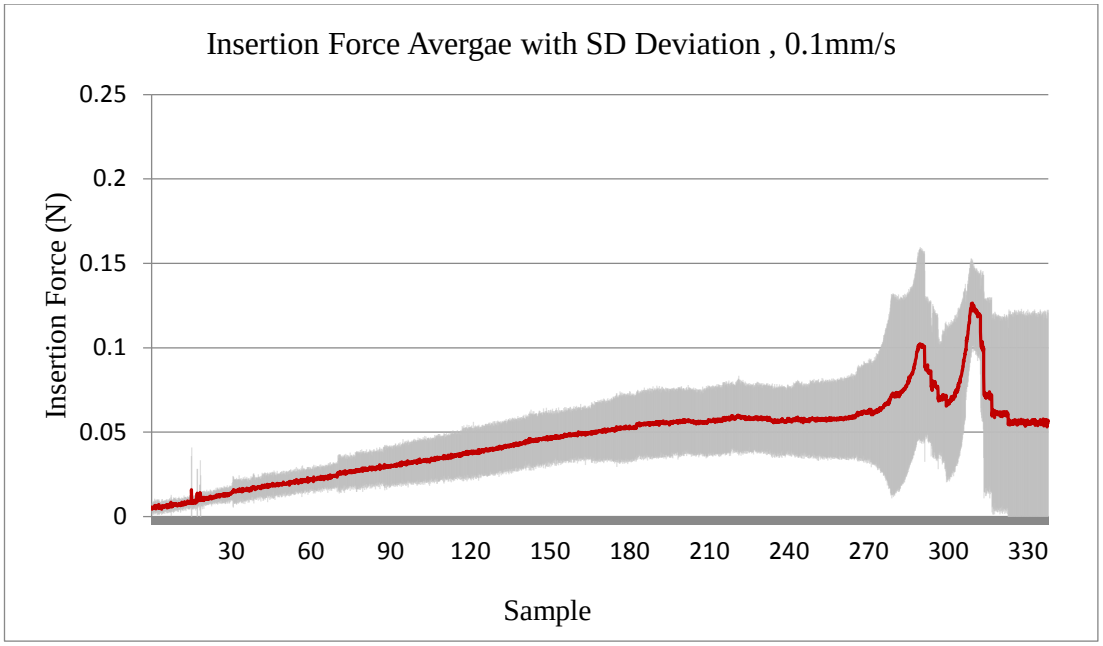

(a)

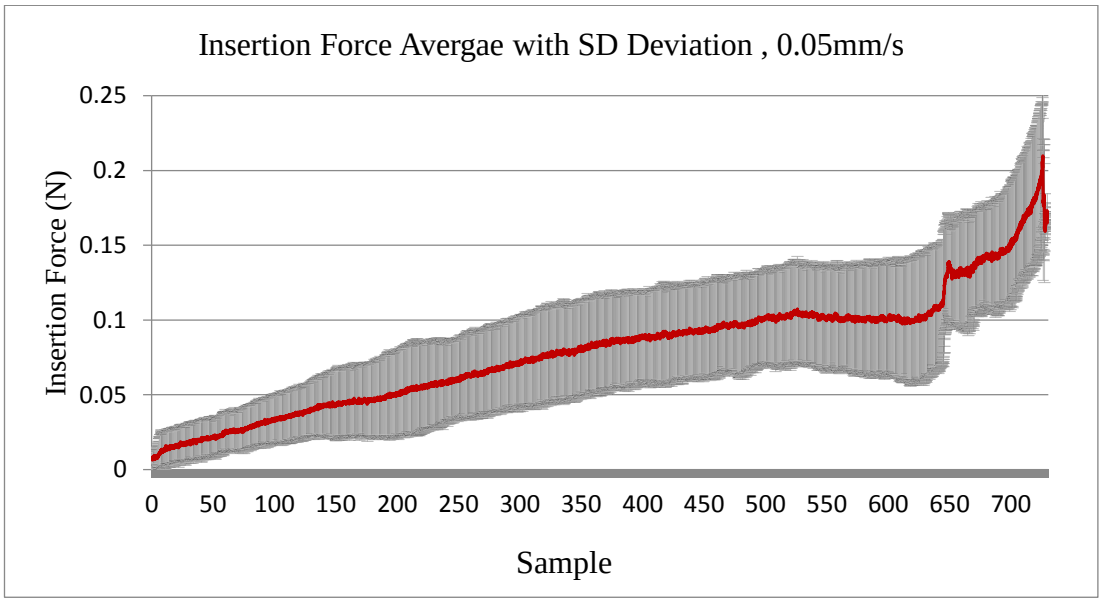

(b)

Figure 4-8: Average insertion force profiles of the electrode array for 40 smooth insertions with the speed (a) 0.1mm/s (b) 0.05mm/s. The red curve represented the average insertion force of 40 insertions and the grey area was the standard deviation of them. The y-axis indicated the insertion force in N, and the x-axis showed the recording sample length. Two insertion speed was tested and depicted in a and b respectively.

The sample length could be easily converted to an insertion length in mm as well as insertion degree. The electrode array insertion length could be achieved through sample length * insertion speed (mm/s). For example, 100 sample was equal to 100 x 0.1 = 10 mm, at a insertion speed of 0.1 mm/s, and was equal to 100 x 0.05 = 5 mm at a insertion speed of 0.05 mm/s.

Therefore, in Figure 4-8 (a), the electrode array insertion length was 33 mm and in Figure 4-8 (b) the insertion length was 36mm. In Figure 4-8 (a), the average insertion force increased gradually until the sample length of 270. The maximum force in the section was 0.626N (±0.03N). Afterwards, the average force value fluctuated frequently with the maximum force of 0.127 N (±0.025 N) occurring at 30.9 mm. In Figure 4-8 (b), before the sample length reached 600, the average insertion force value kept rising constantly until the maximum force of 0.107 N (±0.03 N) was reached. Subsequent to sample 625, the average insertion force raised rapidly to the maximum of 0.21 N (±0.05 N) at 36.3mm. The maximum average force of the 0.05 mm/s (0.23N) that was nearly twice the maximum average force of 0.1mm/s (0.127N). Therefore, the speed of the electrode array insertions was selected to be 0.1mm/s.

The average force profiles for 35 electrode array buckling insertions are portrayed in Figure 4-9.

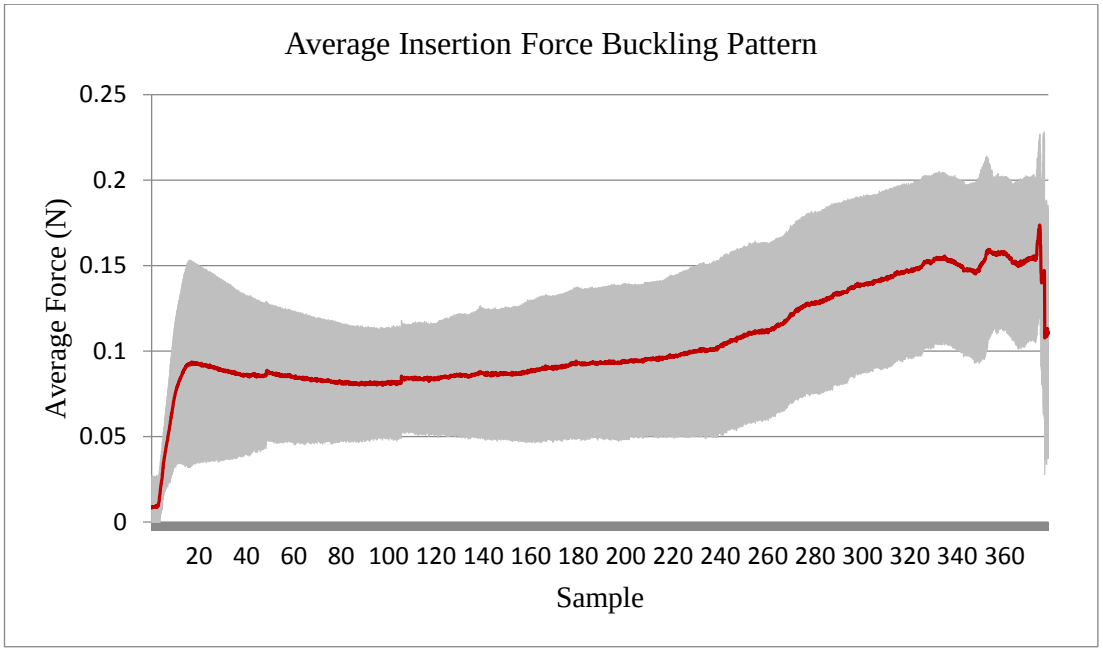

Figure 4-9: Force profiles of the electrode array buckling insertions with the speed of 0.1mm/s.

In Figure 4-9, the red curve indicated the average insertion force of 35 insertions and the grey area was the standard deviation of them. The y-axis indicated the insertion force in N, while the x-axis showed the recording sample length. The full insertion length was 37.5 mm.

Different from the smooth insertions, the average insertion force increased dramatically at the beginning of the buckling insertions. This was because in order to create the buckling pattern, the array tip start position was slightly posterior to that of the smooth insertions. The alignment resulted in contact between the model wall and the tip at the start of the insertions. Thereafter, the average insertion force increased slowly to the maximum of 0.174 N (±0.054 N). Small fluctuations were evident at the end of the insertions.

The force profiles of 30 electrode array fold-over insertions are shown in Figure 4-10.

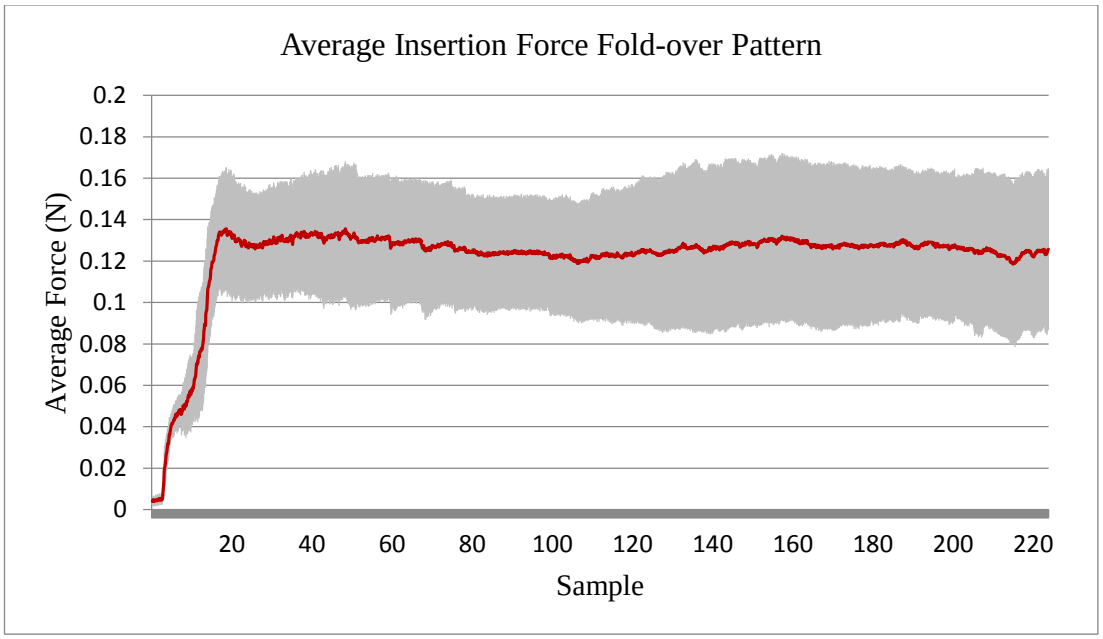

Figure 4-10: Force profiles of the electrode array fold-over insertions with the speed of 0.1 mm/s. The red curve indicated the average insertion force of 30 insertions and the grey area was the standard deviation of them. The y-axis indicated the insertion force in unit Newton, and the x-axis showed the recording sample length. The full insertion length was 22 mm.

Different from insertions in Figure 4-8 and Figure 4-9, the fold-over insertion length was only 22 mm. This was because the fold-over pattern existed at approximately 8mm and the insertion should be stopped immediately. The maximum average insertion force was 0.136 N (±0.028 N) at the insertion length of 1.9 mm, where the array tip first contacted the model wall.

The discrimination of the buckling pattern and the fold-over pattern from smooth insertions was difficult by comparing the average force profiles. For the buckling pattern, the phenomenon occurred at the end of the electrode array. The body of the electrode array deformed in the model track. However, from the force profiles, the faulty behaviour only resulted in small fluctuations at the sample length of 340 in Figure 4-9.

For force profiles of the fold-over pattern in Figure 4-10, the largest force value was apparent when the array tip firstly contacted the model wall. It reflected from the figure that a quick force increased from 0 to 0.14 N occurred within 20 sample length. The

largest force value was only 6.6% higher than the average force of 0.127 N. Subsequently, the average force remained stable with minor fluctuations. The fold-over pattern could not be discriminated in the force profiles.

Most importantly, the insertion force could not identify the position where the buckling or fold-over pattern occurred. The force measured was the overall insertion force applied at the entry point of the cochlear model. The insertion force was a complex force including advancing force, support force, friction force, viscous force, etc. Even whether the insertion was smooth or which faulty pattern occurred could be recognized, it was impossible to identify where the error took place. The process was like inserting an array into a black box that surgeons would know when errors happened, but could not identify the exact location of the errors. During the electrode array insertion process, behaviours of the array inside of the cochlea remained unknown for surgeons.

Besides, in all of the force profiles, the force deviation was much larger than the standard value. The deviation value changed from a range between 20% and 30%. This suggested that there were significant differences between each individual insertion. Some of the insertion force profiles were shown in the Appendix 2 to demonstrate the differences. The differences and deviations made pattern discrimination impossible from the insertion force.

Therefore, the force sensing method was not sufficient in discrimination of the faulty patterns. In order to solve the problem, an electrodes bipolar capacitive sensing system was proposed. The method was found highly sensitive at conducting solutions. By activating different pairs of electrodes, the CI electrode array behaviour inside of the cochlear model could be detected.

4.4 Conclusion

A mathematical model for the cochlear electrode array first contacting the cochlear wall was created. It helped analysing the mechanical behaviour of an inserting electrode array. Deflection equations at any points along a cantilever beam were developed. Proposed solutions by the finite element analysis were verified by commercial software, specifically ANSYS.

Results revealed that the insertion force was useful in designing CI arrays and insertion strategies. It was able to record the contact force between the array and cochlear inner wall at the first around. The average force profile was similar to the results in some literature review. Based on the insertion force, the efforts of speed, position and trajectory angle of the electrode array insertion into a plastic cochlear model had been investigated. The results demonstrated that the array had to be inserted closely to the inner track of the model with a low insertion speed 0.1mm/s to avoid the buckling and damage.

Force profiles for the three insertion patterns were evaluated. Most importantly, the insertion force could not identify the position where the buckling or fold-over pattern occurred. The force measured was the overall insertion force applied at the entry point of the cochlear model. Even whether the insertion was smooth or which faulty pattern occurred could be recognized, it was impossible to identify where the error took place. During the electrode array insertion process, behaviours of the array inside of the cochlea remained unknown for surgeons. Besides, in all of the force profiles, the force deviation was much larger than a standard value. The deviation value changed from a range between 20% and 30%. This suggested that there were significant differences between each individual insertion. The differences and deviations made CI array insertion pattern discrimination lack of accuracy from the insertion force.

In account for the unknown behaviour and location information, small force variations and large deviations, the force sensing method was not sufficient in discrimination of the faulty patterns. In order to solve the problem, an electrodes bipolar capacitive sensing system was proposed.

Chapter 5

Capacitance Measurement of the Cochlear Implant Electrode Array

As per what we concluded in Chapter 4, insertion force was not an effective method for detecting the array behaviours inside of the cochlea. The bipolar electrode capacitance-sensing method should be investigated, which was applied to control processes in many industrial applications and machine diagnostic tasks. It could assist us discriminating two insertion failure patterns. The theory and influencing factors of the sensing measurements would be investigated in this chapter. The relationship between capacitance measured and environmental effect, structural effect and applied force would be examined and assessed.

The structure of this chapter was as follows[2]. Section 5.1 covered the modelling and simulation of an electrode-electrolyte interface. Section 5.2 investigated how the environmental parameters and force affect capacitance measurement. In Section 5.3, the results of three electrode array insertion patterns would be presented. Finally, Section 5.4 concluded this chapter.

[2] HOU, L., DU, X. and Boulgouris, N.V. (2018). *A Novel Sensing System for Robotic Cochlear Implants Electrode Array Placement*. In: 2018 7th IEEE International Conference on Biomedical Robotics and Biomechatronics (Biorob). IEEE, pp.1133 - 1137. DOI: 10.1109/BIOROB.2018.8487984

5.1 Modelling and Simulation of an Electrode-Electrolyte Interface

5.1.1 Introduction

Continuous capacitance values were measured by an LCR meter during an electrode array insertion. During the insertion, reasons for the possible capacitance noises would be analysed and the best insertion method would be recommended to minimise experimental disturbances.

A capacitor was used for storing charge and energy that was formed by two parallel plates [124]. The area of the two parallel plates and their separation distance dominated their capacitance [124]. According to Gauss's law [125], the electric field between the two plates was:

$$E = \frac{Q}{\varepsilon A} \text{ and } Ed = V = \frac{Qd}{\varepsilon A} \tag{5.1}$$

Where E was the electric field, Q was the total charge stored in the plates, ε was permittivity of the material and A was the area overlap between the two plates in square meters, d was the separation between the plates in meters.

Due to the capacitance was defined by $V = \frac{Q}{C}$. Capacitance was expressed as [126]

$$C = \varepsilon_r \varepsilon_o \frac{A}{d} \tag{5.2}$$

where ε_r was the relative static permittivity of the material between the plates and ε_o was the electric constant $\varepsilon_o \approx 8.854\times10^{-12}$ Fm^{-1}. From Equation (5.2) capacitance was evidently positive proportional to the metal area overlap and inversely proportional to the plate separation distance.

5.1.2 Helmholtz Model Analysis

Helmholtz [68] created the first double layer model in 1879. He proposed that a double layer charge existed at the electrode-electrolyte interface [68]. An inhomogeneous region was generated by the electric field between a metallic electrode and an electrolyte solution. The schematic diagram of the cochlear implant electrodes and Helmholtz model are shown in Figure 5-1.

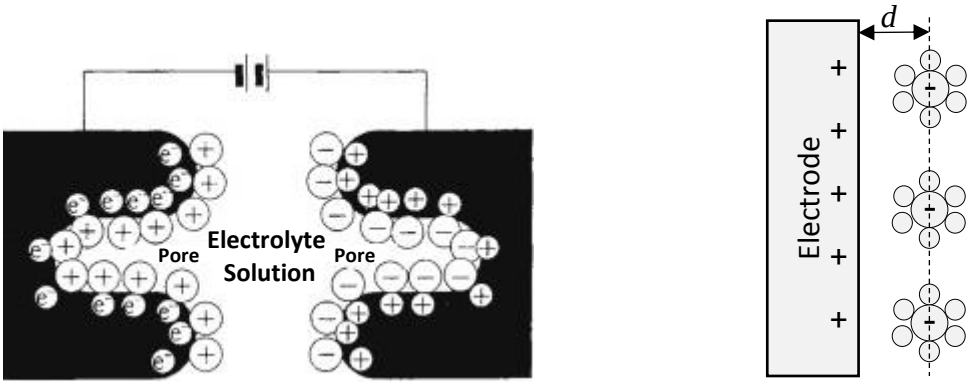

Figure 5-1: (left) Schematic illustrations of the cochlear implant electrodes. The two charged CI electrodes filled with the electrolyte solvent repelled common ions while attracting counter ions of charge to the surfaces. (right) Schematic diagram of Helmholtz model. The separation of the charged layers was represented by *d*. (Figure from [126])

When immersing with electrolyte solvent, charged CI electrodes repelled common ions while attracting counter ions of charge to the surfaces. According to Helmholtz model, a separation was generated by the electric field. The behaviour of electric double layer was comparable to the classical parallel-plate capacitor. From the introduction of the CI electrodes in Section 3.2.1, the electrodes structure was semi-circular cylinder with the activing area 0.46 mm^2 to 0.6 mm^2. Therefore an assumption on the layer distance (*d*) could be made.

The apical two electrodes measured capacitance was selected to be C = 1700pF. It was due to that they had a constant activing area. The area was assumed one fifth of the smallest area in the datasheet (A = 0.46/5= 0.092 mm^2), as only one outer surface contacted to the solution. The relative permittivity of saline solution was 80 in 20°C [126]. Therefore, by using the equation (5.2), distance d between the layers could be calculated as:

$$d = 80 * 8.854\times10^{-12} * 9.2\times10^{-8} / 1.7\times10^{-9} = 3.833\times10^{-8}\,(\text{m}) = 38.3\,(\text{nm})$$

The distance approximation was at a same magnitude of the thickness of the concentrated electrical double layer (several to dozens nanometre) [135]. The assumption indicated the capacitance value measured was reasonable. The theoretical model also explained that when electrodes touched the wall, the relative permittivity would rise and increase the capacitance measured.

However, the Helmholtz model was the simplest approximation for electric double layer. The model did not account for important factors such as ions size, ions diffusion and mixing in solution, electrodes surface adsorption and interaction between electrodes and solution dipole moments. The model could not be applied in quantifying the thickness between electrodes and layers. However, the model was a foundation for more complex models, such as Gouy-Chapman model, Stern model and Randles model that was introduced in Literature Review Section 2.3.

The capacitance measurements were performed by applying two electrodes in an electrolyte solution. The simplified circuit diagram for the two electrodes is shown in Figure 5-2.

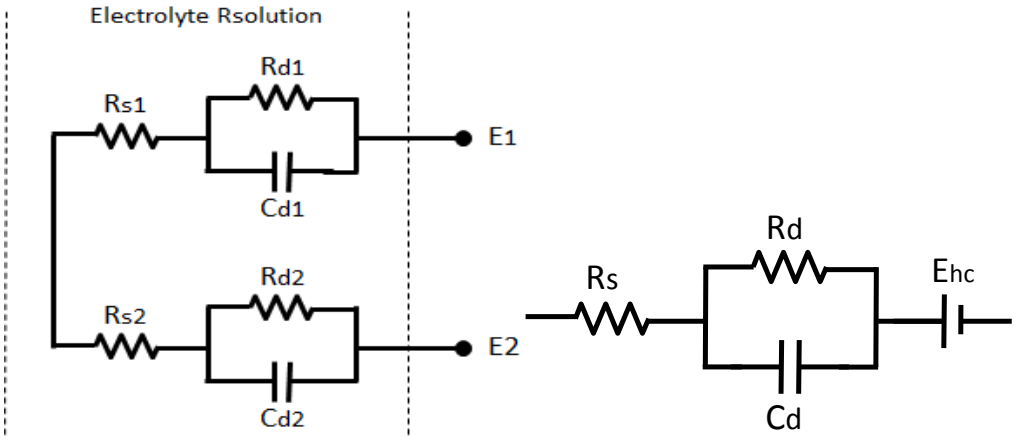

Figure 5-2. (a) The equivalent circuit model for electrode-electrolyte interfaces. (b) The half-cell equivalent circuit model for an electrode-electrolyte interface.

In order to simulate the capacitance variations for a single electrode, the total impedance value was divided by two. This approach was reasonable if the two electrodes were identical in size, material and manufacturing [139]. Therefore, circuit components value for the two electrodes were identical ($C_d = C_{dl} = C_{d2}$; $R_s = R_{s1} = R_{s2}$;

$R_d = R_{d1} = R_{d2}$). An equivalent circuit model for an electrode-electrolyte interface was shown in Figure 5-4 (b). The half-cell potential (E_{hc}) demonstrated the potential difference between the electrode and the electrolyte. The equivalent circuit model consisted of the double-layer capacitance (C_d), the electrode resistance (R_d) and the solution resistance (R_s). C_{dl} simulated the charging process in the electrolyte at the electrode surface. R_s represented the tissue and solution resistance. It was important to note that C_{dl} was not a simple and constant capacitor and it should be adjusted with changing frequency. The impedance for the electrode-electrolyte interface was expressed as

$$Ze = Rs + \frac{R_d}{1 + j2\pi f C_d R_d}$$

where Z_e was the impedance for the interface and f was the frequency in Hertz (Hz).

To analysis the model, Electrochemical Impedance Spectroscopy (EIS) by using a simulation software LTspice [140] was applied. The EIS method was an experimental technique that modelling electrochemical cell's physical and chemical parameters [141]. EIS focused on the impedance modelling in the form of spectrum, usually with Nyquist or Bode plots. In the Nyquist diagram, the imaginary part against the real part of measured impedance for every frequency were plotted. A Bode diagram was a graph of the impedance magnitude and phase against frequency, impedance magnetite. The EIS was particularly useful in extracting different physical characteristics from a single analysis [142.].

In the study, reasonable assumptions were made in the electrode circuit model components (C_d, R_d and R_s). The estimated average values for the double layer capacitance C_d was 1.7 nF, the electrode charge transfer resistance was 250Ω and a solution resistance of 100 Ω were assumed. A current source 1A was applied to the equivalent circuit model and the frequency sweep ranged from 1 Hz to 100 MHz were analysed. The Nyquist and Bode plots for the circuit simulation are described in Figure 5-3.

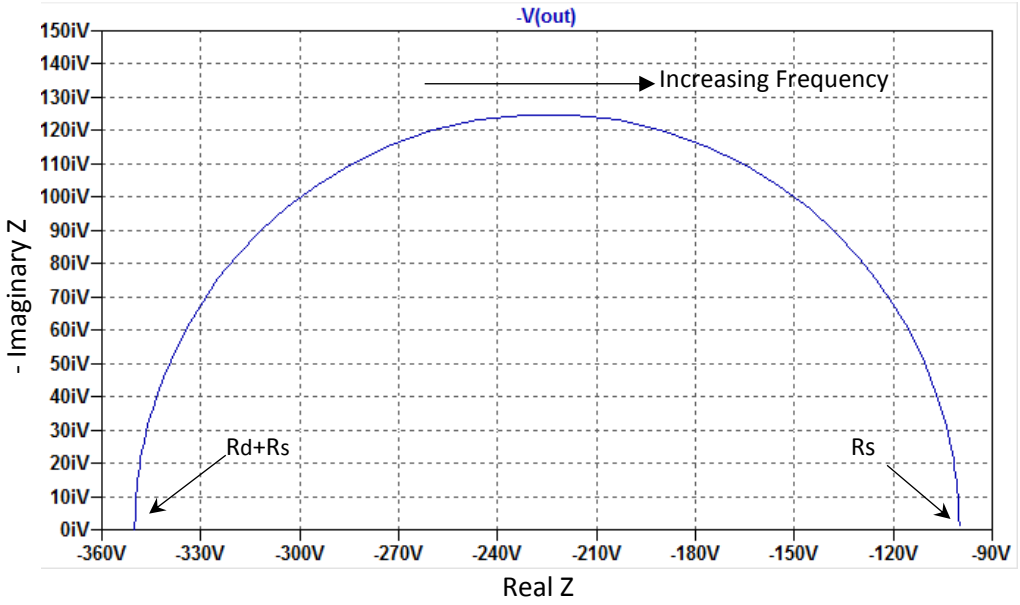

(a)

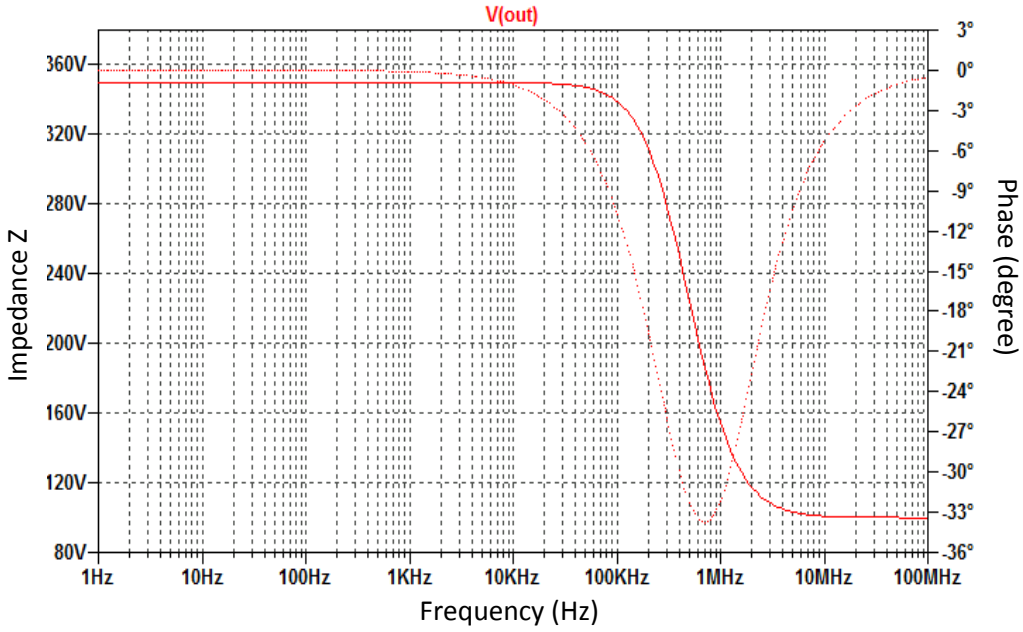

(b)

Figure 5-3. Simulation results from a half-cell equivalent circuit model for an electrode-electrolyte interface. (a) Simulated Nyquist diagram described the real and imaginary parts for the overall impedance Ze. (b) Simulated Bode diagram with logarithmic plot described the variation of impedance (Ze) and phase angle respect to change in frequency.

In Figure 5-3 (a), the Nyquist plot for the equivalent circuit model was a semicircle. By sweeping the input frequency， the real part (x axis) and the imaginary part (y axis) for the overall impedance Z_e were displayed in the same diagram. The real part of impedance indicated circuit resistance and the imaginary part was the double layer

capacitance. From the plot, the solution resistance (R_s) could be recognised at the highest frequency intercept, where located near the right end. The real part of impedance at the lowest frequency was the sum of the electrode charge transfer resistance and solution resistance. The negative sign indicated the voltage direction was opposite to the current source. From the Nyquist plot, double layer capacitance could be calculated if knowing the frequency.

In Figure 5-3 (b), a bode plot was generated from the same set of data. Model impedance and phase angle were depicted against log of input frequency. The diagram described the variation of impedance with respect to the frequency. From the plot, the cut off frequency for this model was around 200KHz.

Based on the model, the relationship between the solution concentrations and the measured impedance could be simulated. When voltage passed through an electrolytic solution, ions acted as resistors between a working electrode and an electrolyte interface [142]. The electrolyte resistance would directly influence the electrode-electrolyte interface impedance. Many solution parameters would affect the impedance of an electrolytic solution, such as solution concertation, ions type, temperature and carrier area geometry. In the thesis, as the solution properties were fixed, how different solution concentrations and distance to the wall affect the impedance would be simulated. The resistance of an electrolytic solution followed the equation: [143]:

$$R = \frac{1}{\sigma}\frac{l}{A}$$

Where σ was solution conductivity that had SI units of siemens per metre (S/m), l was the length of the carrier specimen and A was the cross-sectional area. Therefore, solution conductivity had an inversely proportional with its resistance.

To investigate how different solution resistance affect the capacitance of the model, a solution step resistance sweep was performed. The solution resistance was simulated from 1Ω to 1KΩ with a step increase of 100Ω. Same to previous assumptions, the double layer capacitance C_d was 1.7 nF and the electrode charge transfer resistance (R_d) was 250Ω. The Nyquist and Bode plots for the solution step resistance simulation are depicted in Figure 5-4.

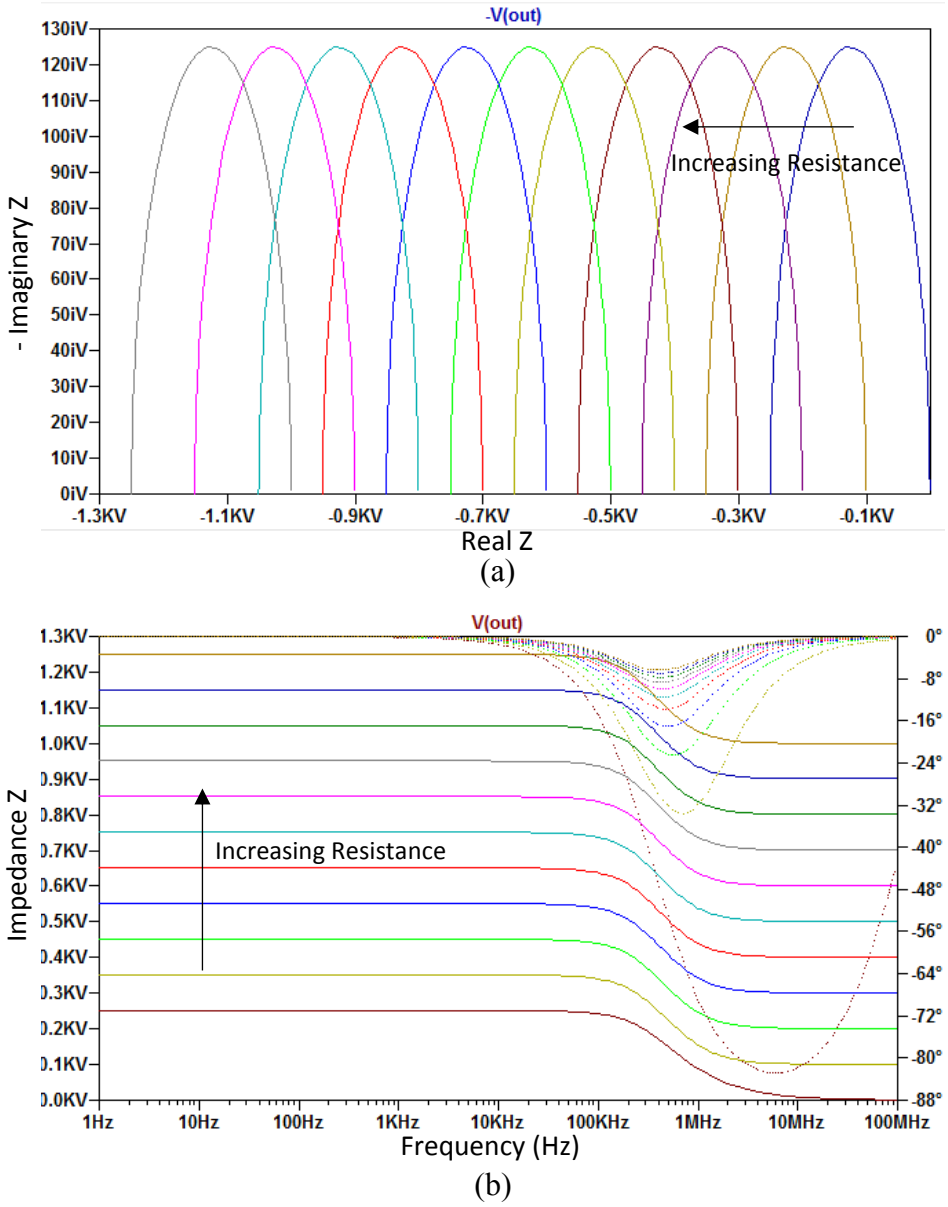

Figure 5-4 Impedance simulation results for an electrode-electrolyte interface with a step solution resistance sweep from 1Ω to 1KΩ with an increment of 100Ω. (a) Simulated Nyquist diagram described the real and imaginary parts for the overall impedance Z_e. (b) Simulated Bode diagram with logarithmic plot described the variation of impedance (Z_e) and phase angle respect to change in frequency.

By sweeping the input frequency and solution resistances, the real part (x axis) and the imaginary part (y axis) for the overall impedance Z_e were displayed in the same diagram in Figure 5-4 (a). With the increasing of the solution resistance, the Nyquist diagrams of them were similar and their simulated semicircle shifted to the left. It had a larger solution resistance and the overall impedance. In Figure 5-4. (b), bode plots were generated from the same set of data. With the increasing of solution resistance,

the curve simulated were similar and moved up linearly. The cut-off frequency for them was around 200KHz.

From the two diagrams, the impedance of the electrode-electrolyte interface circuit model was assumed to have a linear relationship with the solution resistivity. It linearly increased with the increasing of the solution resistance but inversely proportional to the solution concentration.

To investigate how electrode distance to the wall affect the capacitance of the model, a capacitor step sweep was performed. The capacitance was simulated from 100pF to 2nF with a step increase of 100pF. The solution resistance (Rs) was 100 Ω and the electrode charge transfer resistance (R_d) was 250Ω. The Bode plot for capacitance sweeps simulation are shown in Figure 5-5

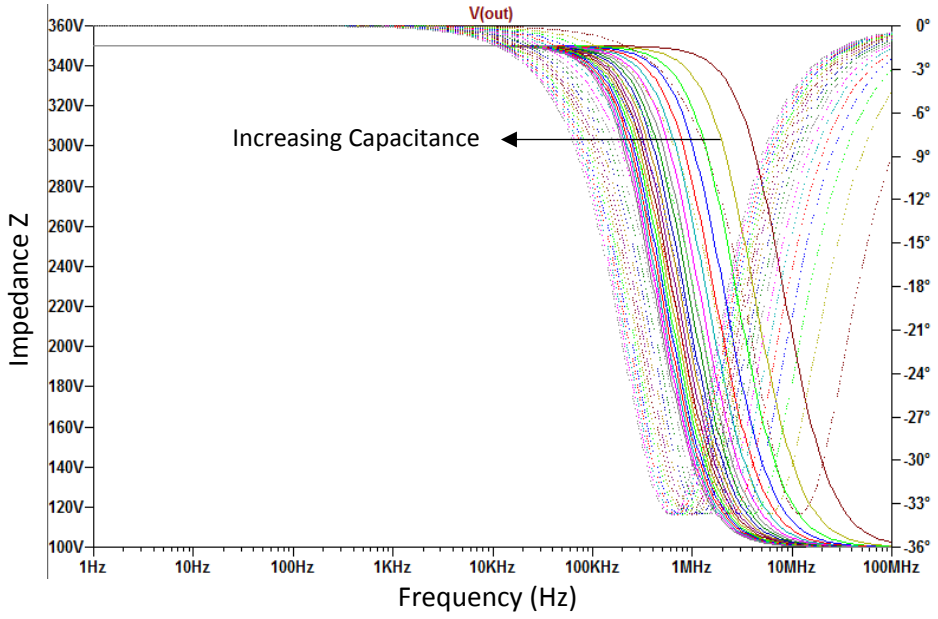

Figure 5-5 Impedance simulation results for an electrode-electrolyte interface with a step capacitance sweep from 100pF to 2nF with a step increase of 100pF. Simulated Bode diagram with logarithmic plot described the variation of impedance (Z_e) and phase angle respect to change in frequency.

By sweeping the input frequency and capacitance, the real part (x axis) and the imaginary part (y axis) for the overall impedance Z_e were displayed in the same diagram. With the increasing of the capacitance, the Bode plots were shifted to the left with a lower cut-off frequency. The Nyquist diagrams were not demonstrated here, as they overlapped each other. At 2nF that was the maximum capacitance measured in

experiments, the cut-off frequency was still around 150KHz. As such, the LCR meters measurement frequency 100KHz was capable to measure the capacitance during the CI insertion. Therefore, according to the equation (5.2), the interface distance *d* had an inversely relationships with the capacitance. The distance described the distance between the measuring electrode and the electrolyte/wall.

However, the above assumptions were based on ideal conditions. In practical, most electrochemical interface did not have uniform current distribution through solution area. Values of double layer capacitance depended on many variables and conditions that beyond the purpose of assumptions in the thesis. Therefore, simulations of the model only estimated the trending of double layer capacitance under certain conditions.

5.2 Environmental Factors and Applied Force Affecting Capacitance Measurements

5.2.1 Effects of Solution Conductivity on Capacitance Measurement

As in the previous section, conductivity of the solution was determined to affect the measured electrode capacitance to a great extent. The aim of this section was to investigate how the electrode capacitance values would vary with the electrode array shape deformation in the same solution.

The measurement system included an electrode array, LCR meters, and a PC to record capacitance result. Electrodes 1 and 2 of the capacitive-sensing probe contributed to the measurement. The distance between the measured electrodes was estimated to be roughly 1mm. A temperature probe was used for the temperature measurement prior to the insertion of the electrode array. The temperature of all the liquid was 24±1 ^{o}C at room temperature.

Seven solutions with different conductivities were used in this thesis's conductivity experiments: virgin oil, distilled water, tap water and distilled water with 1 g salt, 3 g salt, and 5 g salt. The capacity of distilled water was 300 mL. In the experiments, electrodes were fully filled with liquid without making contact with the wall for three minutes. An LCR meter was utilised to measure the capacitance between electrodes under a frequency of 100 KHz. When filled with the liquid, electrode capacitance increased owing to the transferring electron effect with the liquid [118]. The increase was also demonstrated in the 1g, 3g and 5g salt water measurements. The capacitance results are portrayed in Figure 5-6.

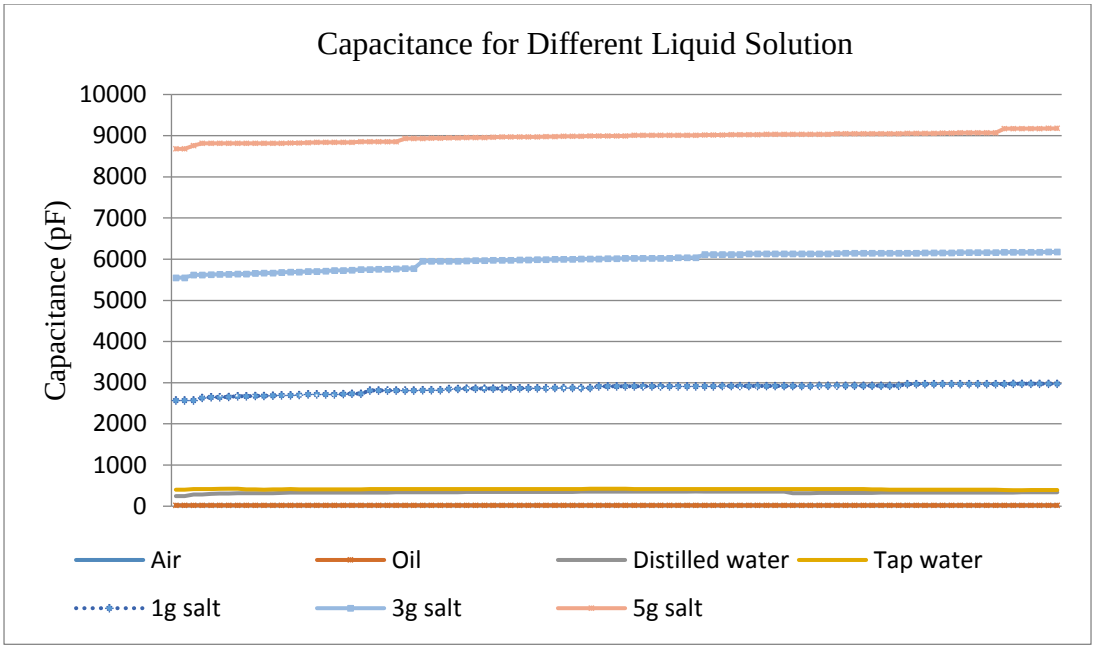

Figure 5-6: Capacitance variations of electrodes 1 and 2 filling with six different solutions at a steady state (Oil, Distilled water, Tap water, 1g salt in distilled water, 3g salt in distilled water, 5g salt in distilled water).

The average capacitances measured at different concentrations of liquid are depicted in Figure 5-7

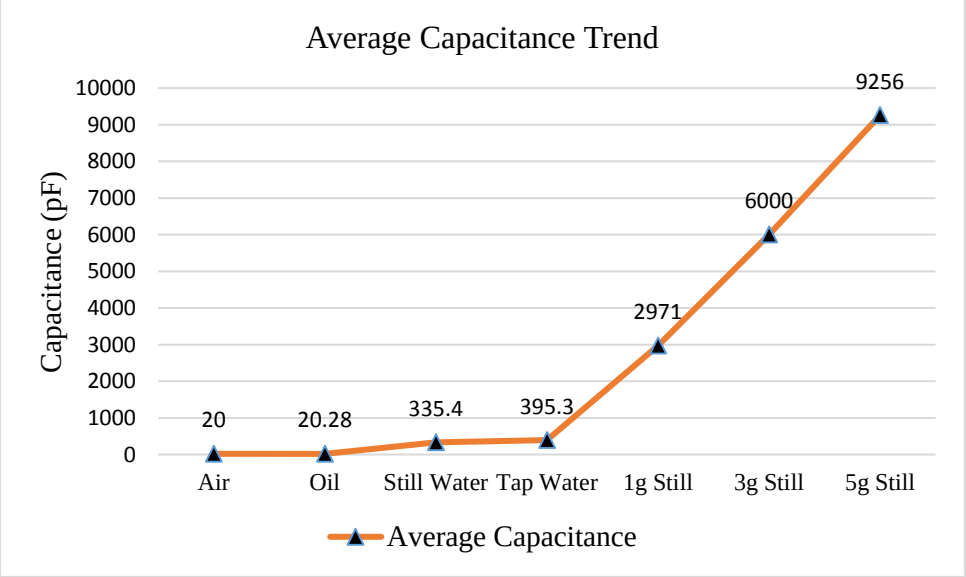

Figure 5-7: Average electrode capacitance and their polynomial trend. Average capacitance was shown as the solid line and its polynomial trend was shown as the dashed line.

Within Figure 5-7, the average capacitance with seven solutions and their polynomial trends were plotted. In the air, oil, tap water, and distilled water states, there was less transfer of charge between electrodes and electrons. The results indicated that the average capacitance under these conditions was close to 0 pF. However, under the condition of high concentration liquid, in 1 g, 3 g, and 5 g salt water, the capacitance measured gradually increased following the rise in conductivity. Among them, 5 g salt water featured the highest average capacitance value of 9000 pF, whereas for the distilled water state, the capacitance measured was 395 pF. The notable 22.7 fold capacitance increased for different water liquids was indicative of the high sensitivity of the electrodes. Also, the average capacitance increased relatively linearly with the concentration of solution. It proved the assumption we made in the modelling section.

The concentration of salt water used in the rest of this thesis was 0.8%. Table salt (NaCl) was an electrolyte and becomes ions when dissolved in distilled water. The sodium ions (Na^+) and chloride ions (Cl^-) in salt water conducted electricity [119]. A NaCl liquid density of 0.8% (weight/volumn) was recognised to have a conductivity of 1.43 (S/m) [120] [121], where W/V represented the percent of NaCl weight in the total volume of liquid. S/m was the SI unit of liquid conductivity, which was Siemens per meter [122].

Accordingly, the conductivities of the cochlear tissues, which were derived from [123][84] the conductivity of the liquid in scala tympani and scala vestibule, were 1.43 S/m. Therefore, salt water with a concentration of 0.8% could be used to simulate the inner cochlear liquid conductivity.

In conclusion, the capacitance value recorded by the meter was produced not only by the electrodes capacitance, but also by the capacitance owing to liquid conductivity. In order to achieve a precise electrode capacitance measurement, the fluid capacitance should be deduced from the measured values. The LCR meter reading was greatly affected by solution conductivity variations.

When electrodes were filled with conductivity solutions only, the capacitance rose with an increasing of solution conductivity. The measurements also demonstrated that electrodes in the array provided a sensitive method for investigating the conductivity of the liquid.

5.2.2 Slides of the Electrode Array along the Surface of Different Materials

The goal of this section was to establish how the permittivity was affect electrode capacitance. The electrode array was held by the automated insertion arm to slide along two surfaces: glass and resin. Resin was the material used in the production of the cochlear 3D model. The capacitance between electrodes 1 and 2 was measured during the electrode array sliding. The insertion speed, which was 0.1 mm/s, was controlled to be identical during each insertion. The solution temperature was kept at room temperature at 25±0.5^{o}C. The liquid utilised in the experiments was saline solution with a concentration of 0.8%.

First, the electrode array was held by the machine arm and gradually filled with the solution exclusively. The results from the experiments, which are shown in Figure 5-9, could be treated as the reference for the rest of the insertions. Then, the electrode array was controlled to slide along the surface of the two masteries. During the insertion, the electrode array tip was kept in contact with the materials. The capacitance results during sliding are depicted in Figure 5-10 and Figure 5-11.

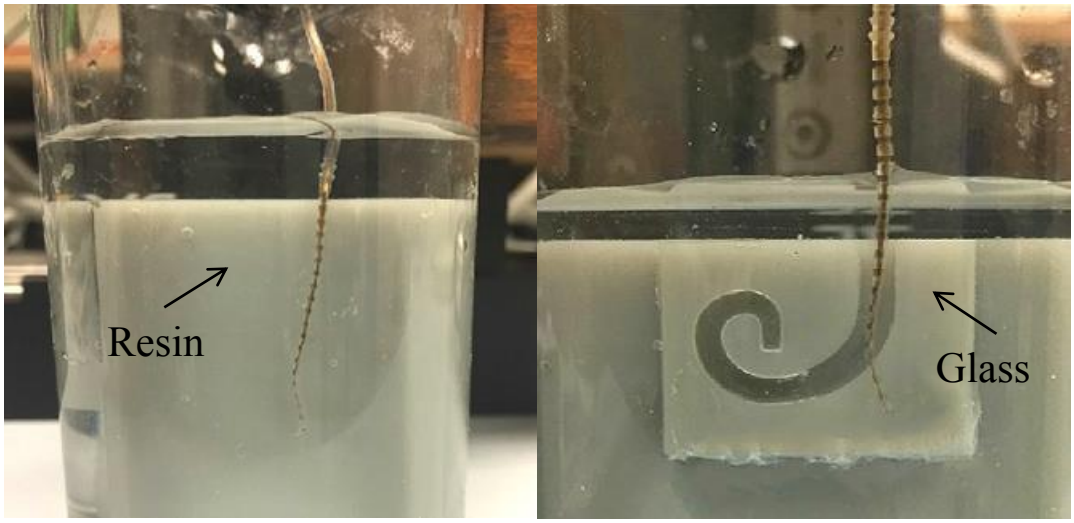

(a) (b)

Figure 5-8: Slide the electrode array along different masteries. (a) The electrode array was sliding along the material Resin. (b) The electrode array was sliding along a piece of glass, which covered the surface of the model.

In the first experiment, the electrode array was filled with liquid by the robot, and the procedure repeated 10 times. Capacitance data of them is presented in Figure 5-9.

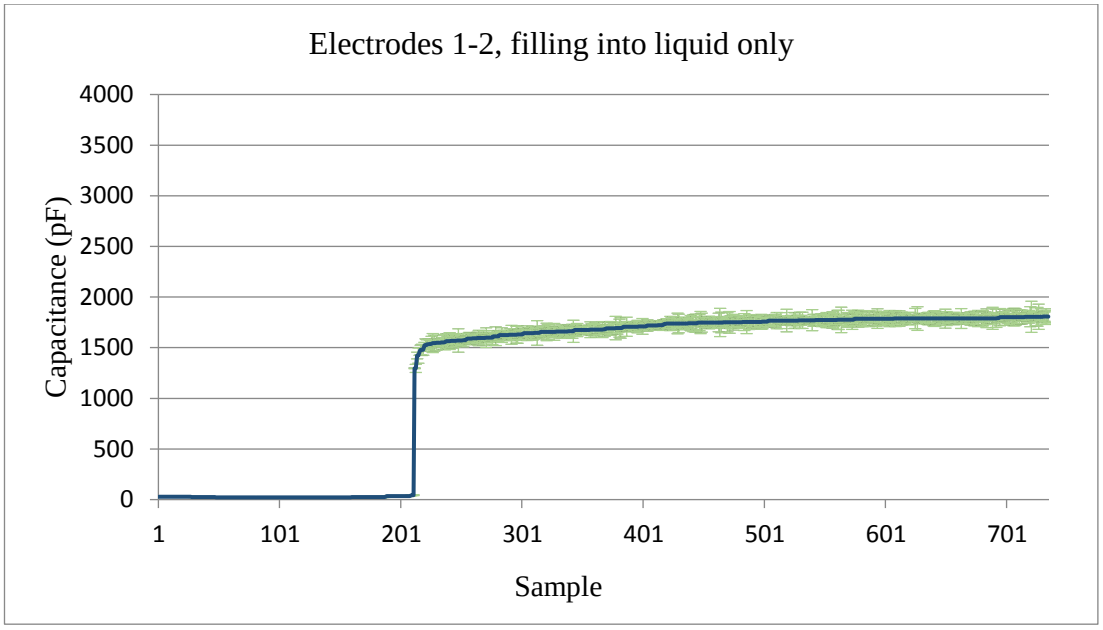

Figure 5-9: Capacitance variations when filling the electrode array with the liquid only (mean results ± standard deviation). The y-axis represented the capacitance measured between electrodes 1 and 2 in pF. The x-axis represented the sample length. Samples were generated with a frequency of 2 Hz, which meant two samples were generated in a second by the LCR meter. Green noises were the standard deviation of 10 measurements of insertions.

In the beginning, the capacitance measured was approximately 30 pF. This was because the two electrodes were exposed to air. At around the sample length of 200, the capacitance rose dramatically to 1.5 ± 0.1nF. This was also because both of the two measured electrodes were completely filled with the liquid. Liquid conductivity was the domination of the capacitance. Owing to the continuous charge transferred between the electrodes and liquid, the capacitance gradually rose after the sample length of 200. The average capacitance for the 10 insertions after the sample length of 450 was 1.793 nF.

In the second and third experiments, the electrode array slide along the surface of two materials 10 times respectively. The capacitance measured results are shown in Figure 5-10 and Figure 5-11.

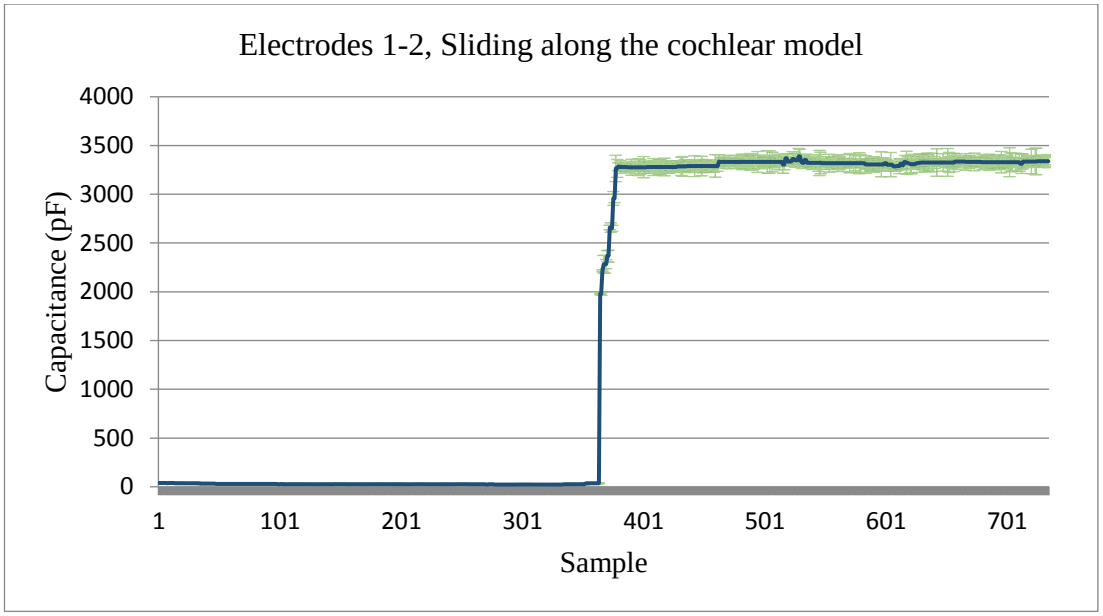

Figure 5-10: Capacitance variations when sliding the electrode array along the cochlear model (mean result± standard deviation). The y-axis represented the capacitance measured between electrodes 1 and 2 in pF. The x-axis represented the sample length. Samples were generated with a frequency of 2 Hz, green noises were the standard deviation of 10 measurements.

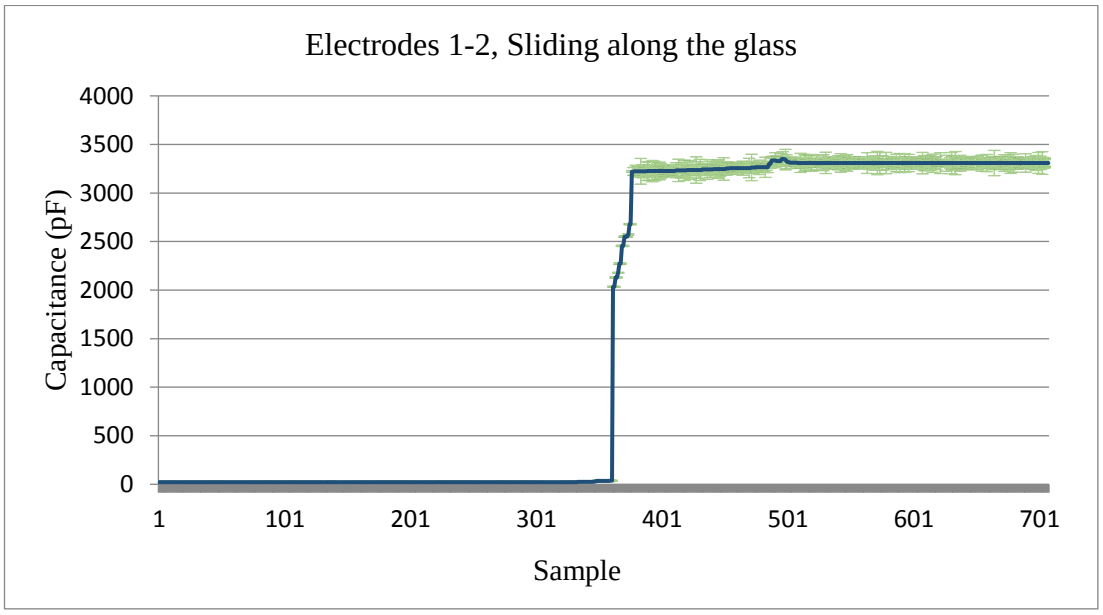

Figure 5-11: Capacitance variations when sliding the electrode array along a piece of glass (mean result ± standard deviation). The y-axis represented the capacitance measured between electrodes 1 and 2 in pF. The x-axis represented the sample length. Samples were generated with a frequency of 2 Hz, green noises were the standard deviation of 10 measurements.

Within Figure 5-10 and Figure 5-11, the overall capacitance behaviours were similar. In the beginning, the capacitance signals remained approximately 30 pF. After filling electrodes 1 and 2 with the solution, the capacitance rose to 3.5±0.13 nF and becomes stable thereafter. The average capacitances for sliding along the glass and resin were 3.23 nF and 3.25 nF, respectively. They were 80% higher than when filling with the solution only. This was because the permittivity of the glass and resin contributed significantly to the capacitance measured. According to the equation (5.2), capacitance increased with the relative material permittivity between the electrodes.

In conclusion, the measured electrode capacitance was approximately 30 pF when exposed to air. The capacitance would increase as much as 50 fold when filling the electrodes with just electrolyte solution. This value would gradually rise based on the electron transfer event between the electrode and solution. When sliding along insulation materials, such as glass and resin, the measured electrode capacitance would be 80% higher than when filling with the solution only.

5.2.3 Effects of Vertical Tensile Force on Capacitance Measurement

This section investigated the relationship between the electrode distance and capacitance measured in the vertical direction. From Equation (5.2), distance (*d*) between the measured electrodes was inversely proportional to the capacitance. It was essential to investigate how the tension force in the vertical direction affects capacitance.

Three pieces of blue-tack were attached to the tip of the electrode array one by one, when filling the measured electrodes with liquid completely. Blue-tack was used in the experiments due to the fact that its weight could be easily adjusted and it could be attached to the end of the array without damaging it. The experimented setup is illustrated in Figure 5-12.

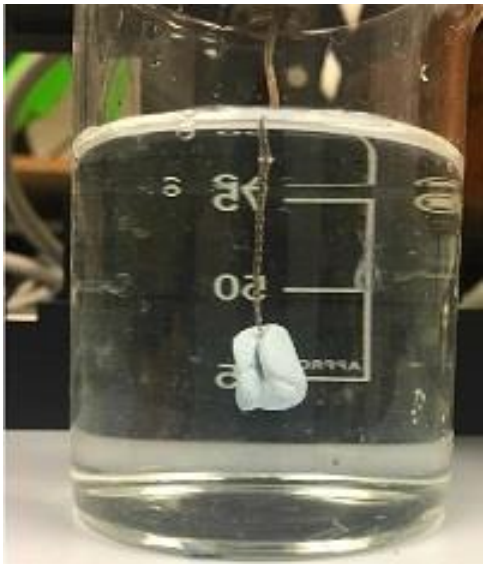

Figure 5-12: An example piece of blue-tack was attached to the tip of the electrode array. In total, three pieces of blue-tack were attached to the electrode array tip one by one to adjust the vertical tension force.

The electrode array was filled with the conducting solution at a concentration of 0.8% prior to the experiment. The temperature of the liquid was measured to be 25.3^{o}C. The end of the electrode array was held by the automated insertion arm. The electrode array was placed in the centre of the solution to prevent contacting the glass wall.

A plastic tweezer was used in the experiments in order to prevent any conductivity effects. Three pieces of blue- tacks were stuck at the tip of the electrode array one by one to simulate three vertical tension force applied to the end. Weights of the three

pieces of blue- tack were 3.4 g, 5.5 g and 7.1 g. Three pairs of electrodes were selected to receive the measurements, which were electrodes 15-16, 15-17 and 16-17. The three electrode pairs were chosen based on the fact that they were at the middle of the electrode array and could not contact the blue- tacks. When measuring the capacitance of electrodes pair 15-16, the lightest blue-tack was attached. Then, the second piece of blue-tack (5.5g-3.4g=2.1g) was attached to the first one. Lastly, the third piece of blue-tack (7.1g-5.5g=1.6g) was attached to the second one. In the experiment, the capacitance variations were recorded and depicted in the Figure 5.9(a). The experimental procedure repeated for measuring the capacitance of electrode pairs 15-17 and 16-17. The capacitance variations of them are shown in the Figure 5.9(b) and Figure 5.9(c) respectively. The whole operations were carefully conducted to prevent any touching of the measuring electrodes.

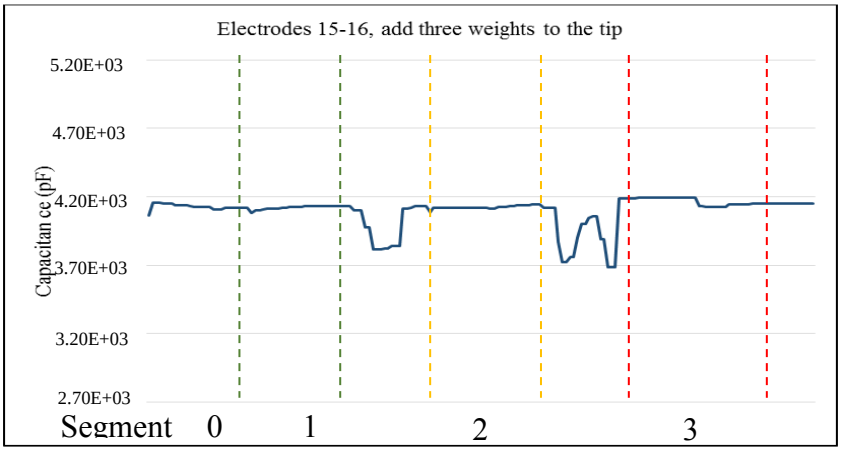

(a)

Figure 5-13 (a): Capacitance measurement between electrodes 15 and 17 by adding three weights to the tip of the electrode array one by one. The average capacitance for electrode 15-16 was 4.15 nF in segment 0, 4.17 nF in segment 1, 4.18 nF in segment 2 and 4.20 nF in segment 3. The capacitance incremented from weight segments 1, 2 and 3 compared to segment 0 were 0.5%, 0.7% and 1.2%, respectively.

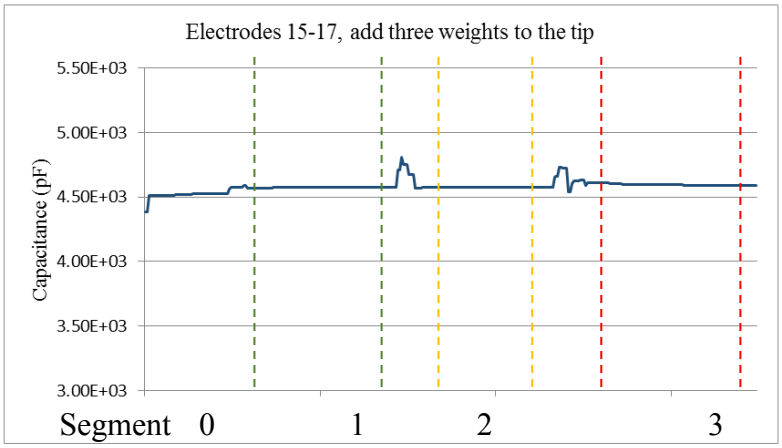

(b)

Figure 5-14 (b): Capacitance measurement between electrodes 15 and 16 by adding weights to the tip of the electrode array one by one. The average capacitance for electrodes 15-17 was 4.5 nF in segment 0, 4.56 nF in segment 1, 4.57 nF in segment 2 and 4.56 nF in segment 3. The capacitance incremented from weight segments 1, 2 and 3 compared to segment 0 were 1.3%, 1.5% and 1.3% respectively.

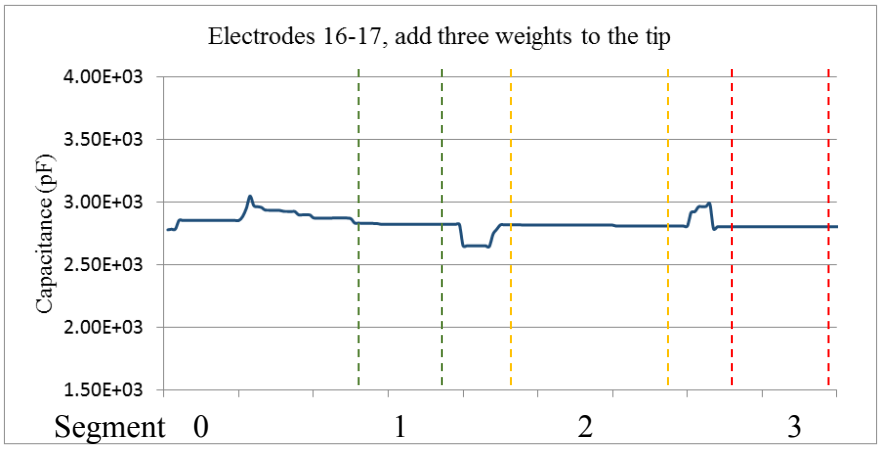

(c)

Figure 5-15 (c): Capacitance measurement between electrodes 16 and 17 by adding weights to the tip of the electrode array one by one. The average capacitance for electrode 16-17 was 2.86 nF in segment 0, 2.83 nF in segment 1, 2.82 nF in segment 2 and 2.82 nF in segment 3. The capacitances incremented from weight segments 1, 2 and 3 compared to segment 0 were -1.1%, -1.4% and -1.4% respectively.

From Figure 5-15, in all of the three figures, the y-axis represented the capacitance in pF with the increments of 500 pF and the x-axis represented the segment of adding weights. Segment 0 showed there to be no weight added. Segments 1, 2 and 3

represented the three weights of 3.4 g, 5.5 g and 7.1 g were attached to the tip of the electrode array, respectively.

A maximum capacitance increase of 1.5% was detected by placing the 5.5 g weight on the tip of the electrode array. Capacitance fluctuations occurred in the process of placing the weights. These fluctuations were caused by randomly reducing the distances between the two electrodes during weight-placing progress. Apart from that, changes in capacitance owing to the vertical tensile force were limited (±1.5%). The results demonstrated that electrodes were fixed at the silicon carrier and cannot be stretched. However, it was difficult to quantify the relationship because of the weight gravity and the buoyancy from the conducting liquid. The relationship between electrode space distance and capacitance would be investigated in Section 5.2.4.

In conclusion, the vertical tensile force at the tip of the electrode array led to limited changes in the capacitance measured. A maximum capacitance increase of 1.5% was detected during the measurement between electrodes 15-17, 15-16 and 16-17. During the experiments, capacitance fluctuations took place in the process of placing the weights.

5.2.4 Effects of Changing Distance on Capacitance Measurement

The goal of this section was to investigate how the electrode space distance would affect the capacitance measured. Distance between electrode 20 and electrode 7 was shortened from 15 mm to 10 mm and 5 mm in liquid. Graph paper with a regular grid (5 mm) was used to measure the distance. The setup of the experiment is found in Figure 5-16.

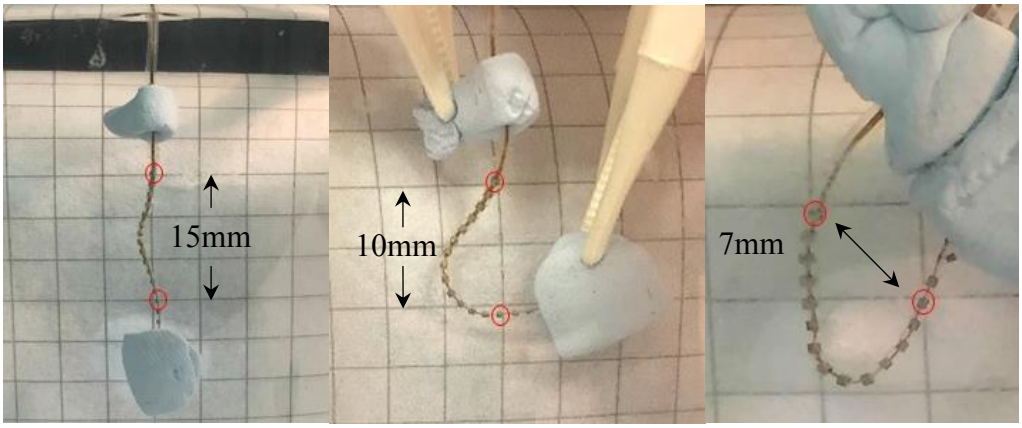

(a) (b) (c)

Figure 5-16: Shortening electrode distance would affect the capacitance measured, from 15 mm to 7 mm.

Within Figure 5-16, electrodes 20 and 7 were highlighted in red circuits. The distance between them was reduced and released. Graph paper with a regular grid (5 mm) was employed to measure the distance. Distances between electrodes 20 and 7 in Figure 5-16 were (a) 15mm, (b) 10mm and (c) 7mm.

The original and released distance between electrode 20 and 7 was 15mm. Distance between them was reduced from 15mm to 10mm and recovered. Afterwards, the distance between the two electrodes was reduced from 15 mm to 7 mm and recovered. The capacitance results are shown in Figure 5-17.

The hypothesis was that according to the capacitance theory equation, capacitance increased linearly with the distance (d) decreasing. The theory of the hypothesis was introduced in equation (5.2)

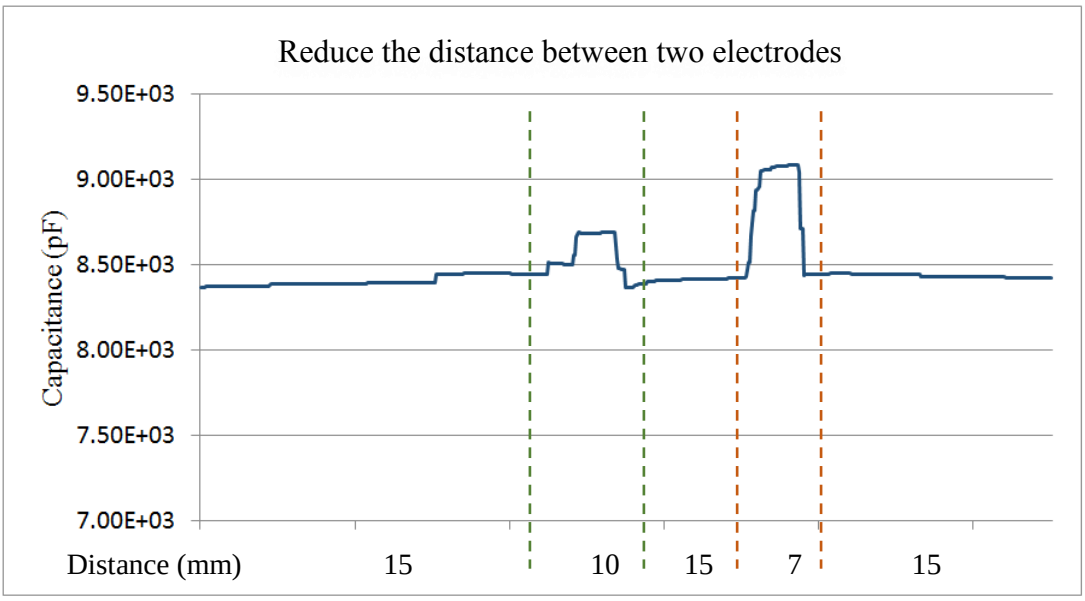

Figure 5-17: Reducing electrode distance would lead to the increment of the capacitance measured.

Within Figure 5-17, the y-axis represented the capacitance in pF and the x-axis was the sample length, which had been converted to the distance between two electrodes. A plastic tweezer and blue- tacks were utilised in the experiments. Firstly, the distance between electrode 20 and 7 was reduced from 15mm to 10 mm. The capacitance measured during the process rose from 8.46 nF to 8.7 nF, which was a 2.8% increment. After a pause of a few seconds, the distance was recovered back to 15 mm, which led to a capacitance decrease from 8.7 nF to 8.4 nF (-3.4%). Then, the distance between electrode 20 and 7 was diminished from 15 mm to 7 mm and recovered. Correspondingly, the capacitance measured rose from 8.4 nF to 9.1 nF with an 8.1% increment and recovered back to the original value (-8.1%).

The distance between two electrodes affected the capacitance measured. Shortening the distance resulted in incremental changes in capacitance, which fellow the capacitance equation (5.2). However, because the shape of the electrodes was polygonal, it was difficult to calculate the overlaid electrodes area during the electrode array insertion process. When accounting for the fact that permittivity between two electrodes measured changes frequently, it became more difficult to quantify the relationship between the capacitance measured and the distance between them.

5.2.5 Effects of Force on Electrode on Capacitance Measurement

In various experiments, when two electrodes were squeezed inside of an artificial cochlear model, the capacitance measured decreased instead of increasing. The results violated the basic capacitance equation (5.2) and electrode distance measurement resulted in Section 5.2.4. The observations demonstrated that there was a domination parameter affecting the capacitance during electrode array insertion. After sets of examinations, the domination parameter was considered to be the force applied on top of the electrodes.

The objective of this section was to investigate the relationship between the force applied on electrodes and capacitance measured. During experiments, the direct force applied to the surface of two measured electrodes was considered to be one of the domination factors that affect capacitance. In order to select suitable electrodes for insertion measurements, electrode pairs 1-2, 1-3, 1-4, 2-3, 2-4, 14-15, 14-16 and 15-16 were evaluated. Electrodes 1, 2, 3 and 4 constituted the tip section of the electrode array. Meanwhile, electrodes 14, 15 and 16 comprised the middle section, where the buckling pattern was observed. The experimental setup is depicted in Figure 5-18.

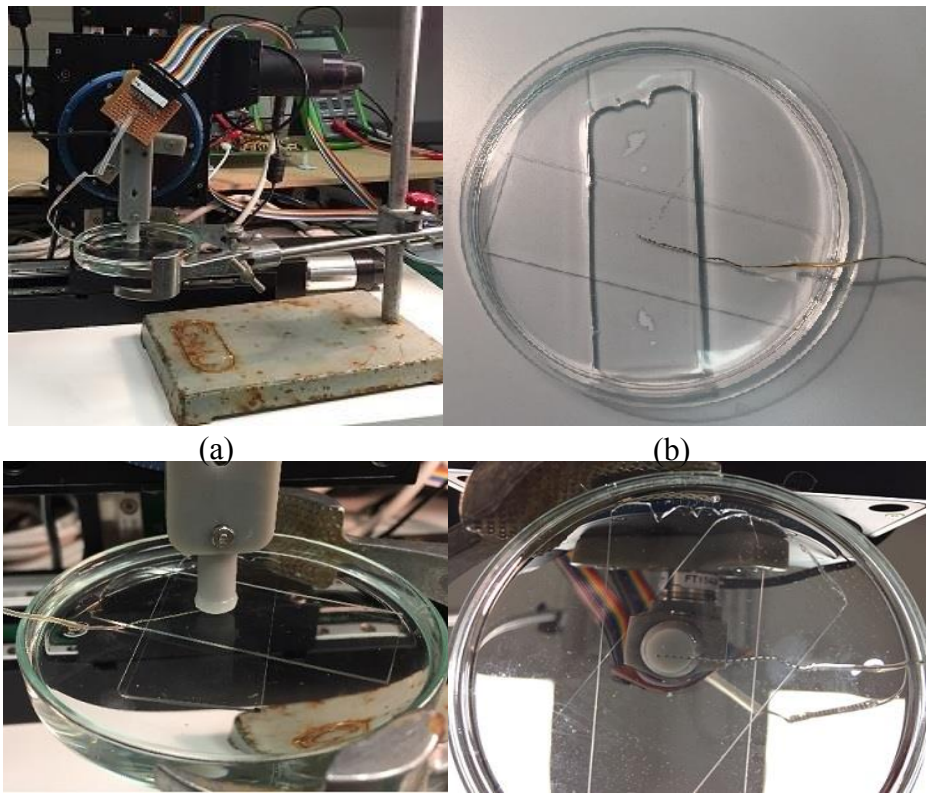

(a) (b)

(c) (d)

Figure 5-18: Force on the top experiment, four different photographic positions

In Figure 5-18 (a), a 3D printed cylinder was attached to the electrode holder. The vertical movement of the cylinder generated force on the glass top. A force sensor, which was introduced in Section 3.1, was utilised to measure and record the applied force. The two electrodes measured were placed in the middle two microscope glasses to maintain their distance and conductivity, which was shown in Figure 5-18 (b). Front and back views of a cylinder during pressing were shown in Figure 5-18 (c) and (d).

In the experiments, five levels of force were applied on the top and the procedure repeated five times for each electrode pair. The diameter of the cylinder bottom was designed to cover four electrodes to avoid moving the array during measurements. The solution temperature was kept at room temperature of 25±0.5^{o}C. The liquid used in the experiments was saline solution with a concentration of 0.8%. For example, one of the force experiments between electrodes 1 and 2 as well as the capacitance responses are shown in Figure 5-20.

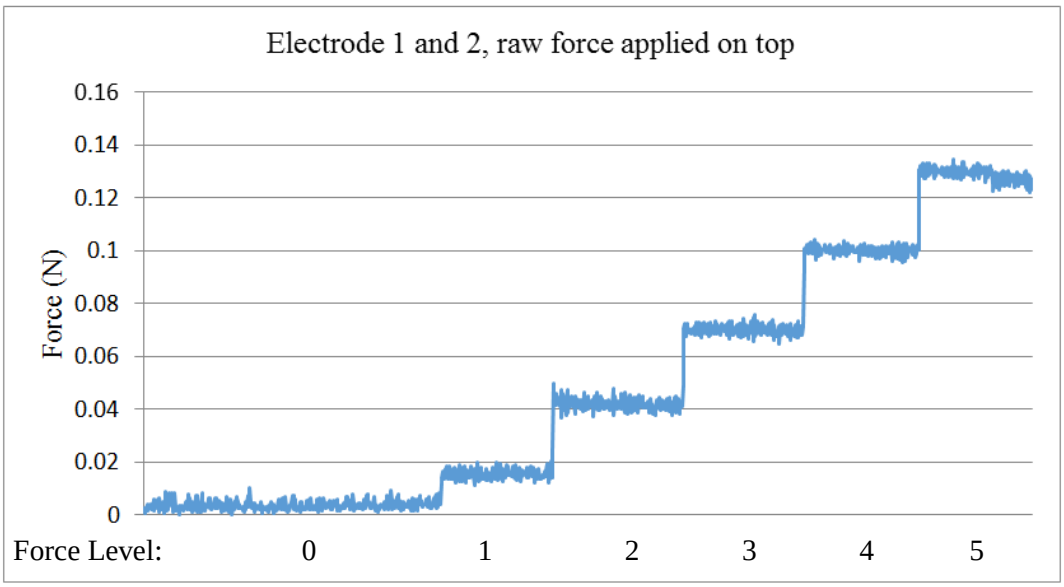

(a)

Figure 5-19 (a): five levels of raw force applied on the top of electrodes 1-2 in one of the force on top experiments. The x-axis showed the force level and the y-axis represented the value of force in N.

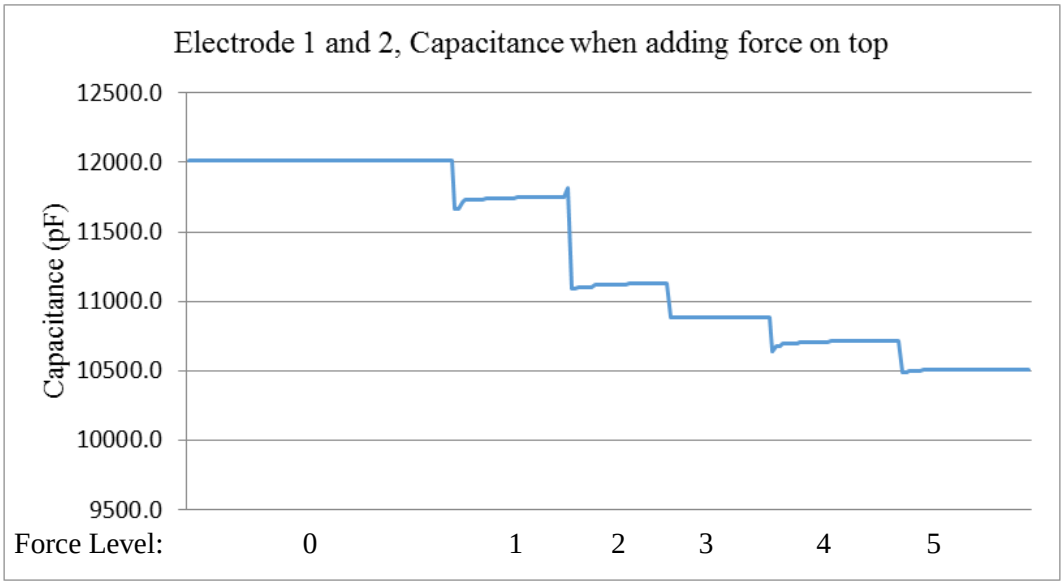

(b)

Figure 5-20 (b): the capacitance measurement results responding to the five levels of force. The x-axis showed the force level and the y-axis represented the responding five levels of capacitance in pF

The evaluation procedure was repeated five times for each electrode pair: 1-2, 1-3, 1-4, 2-3, 2-4, 3-4, 15-16, 15-17 and 16-17. The average applied force at each level against the corresponding capacitance is portrayed in Figure 5-21.

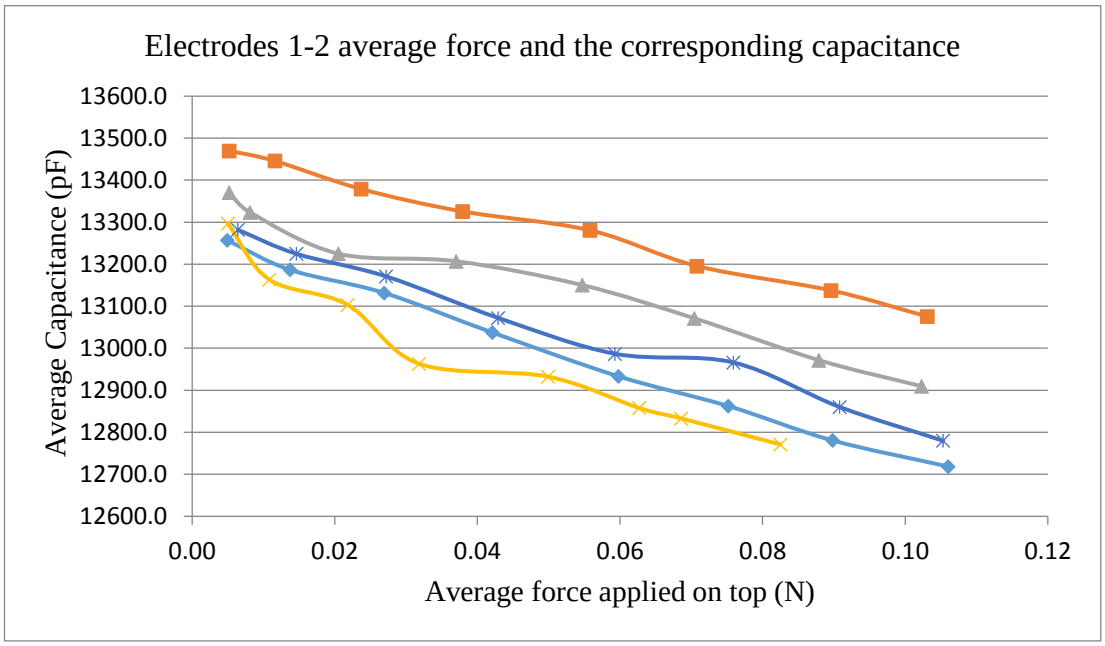

(a)

Figure 5-21 (a): Average force applied on top against to the corresponding capacitance for electrode pair 1-2.

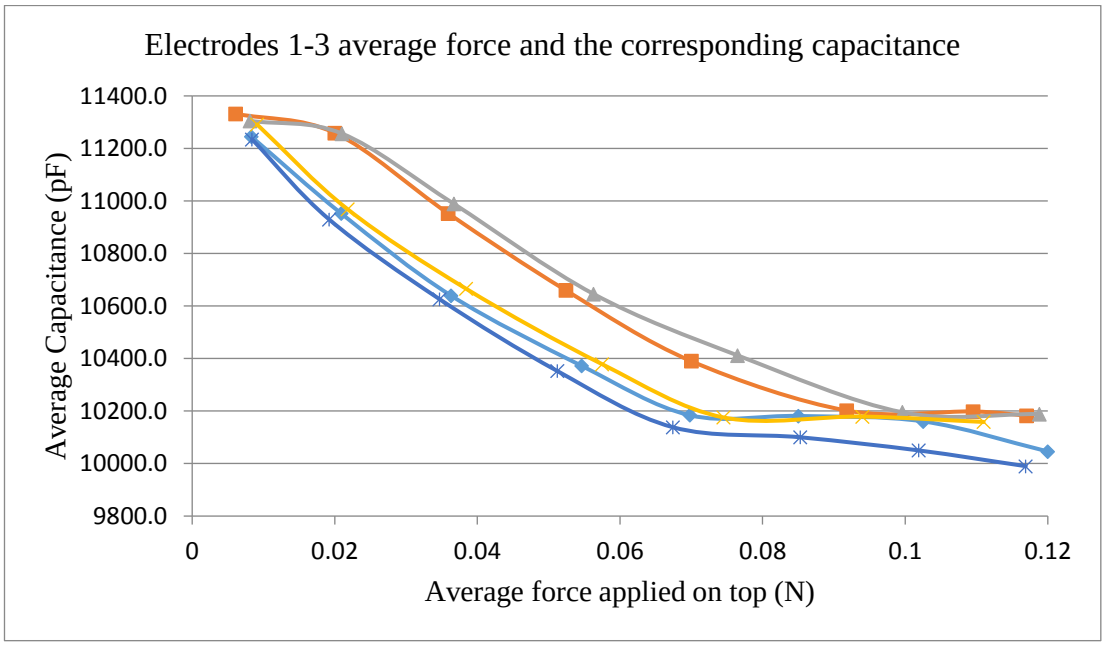

(b)

Figure 5-22 (b): Average force applied on top against to the corresponding capacitance for electrode pair 1-3.

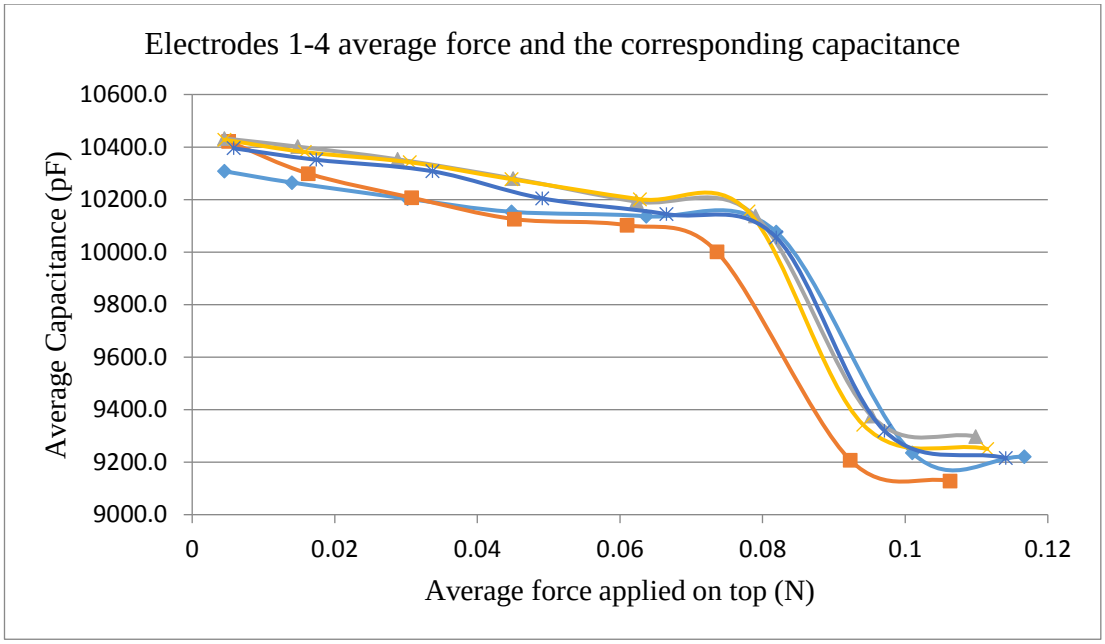

(c)

Figure 5-23 (c): Average force applied on top against to the corresponding capacitance for electrode pair 1-4.

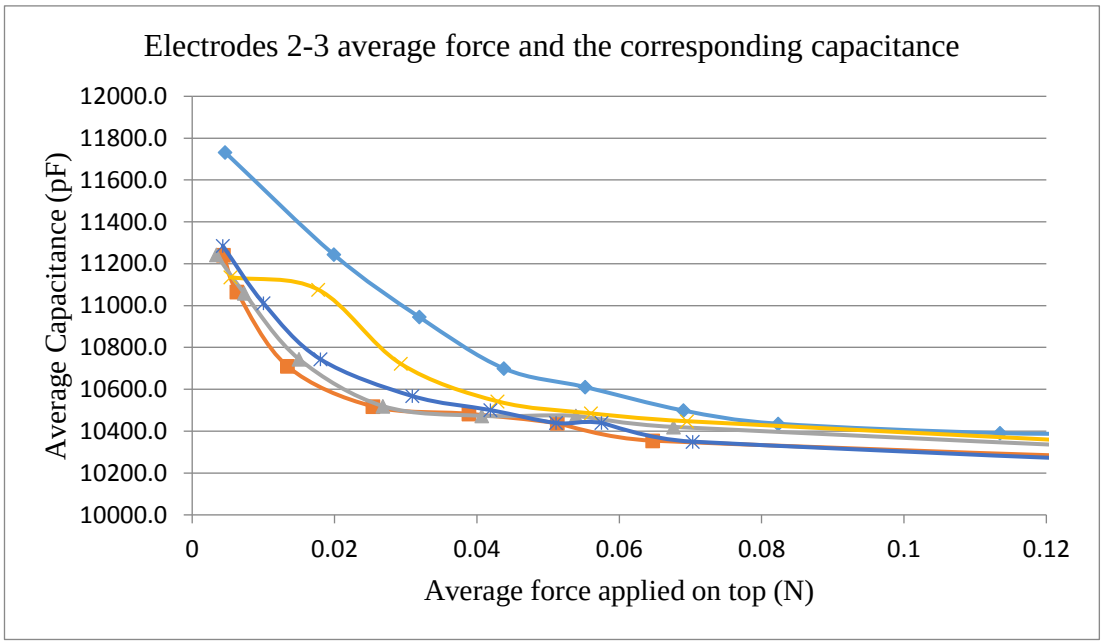

(d)

Figure 5-24 (d): Average force applied on top against to the corresponding capacitance for electrode pair 2-3.

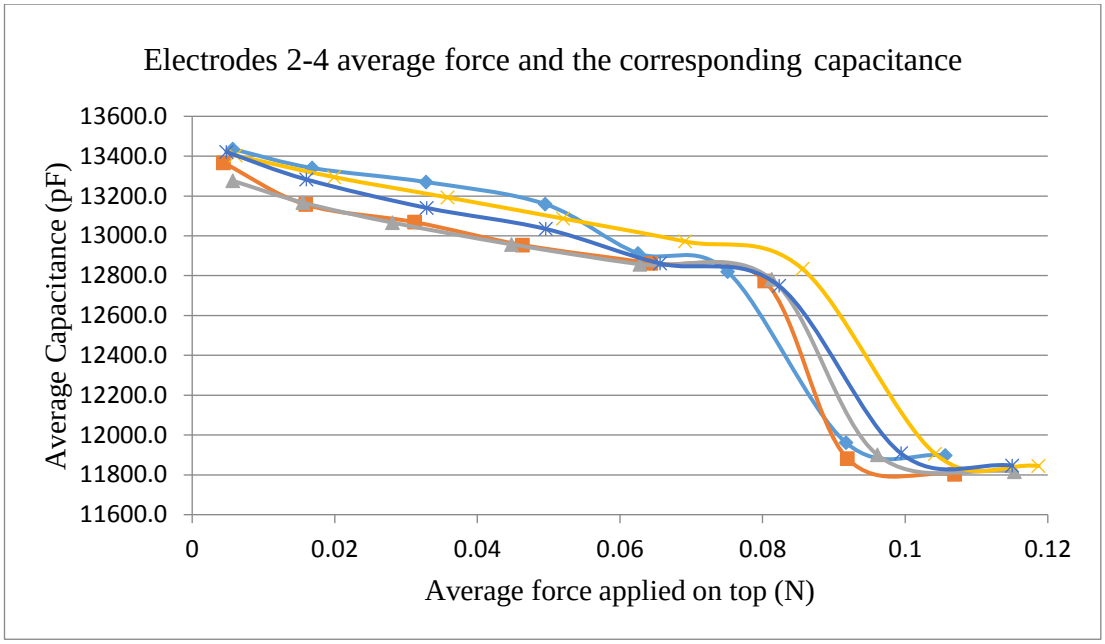

(e)

Figure 5-25 (e): Average force applied on top against to the corresponding capacitance for electrode pair 2-4.

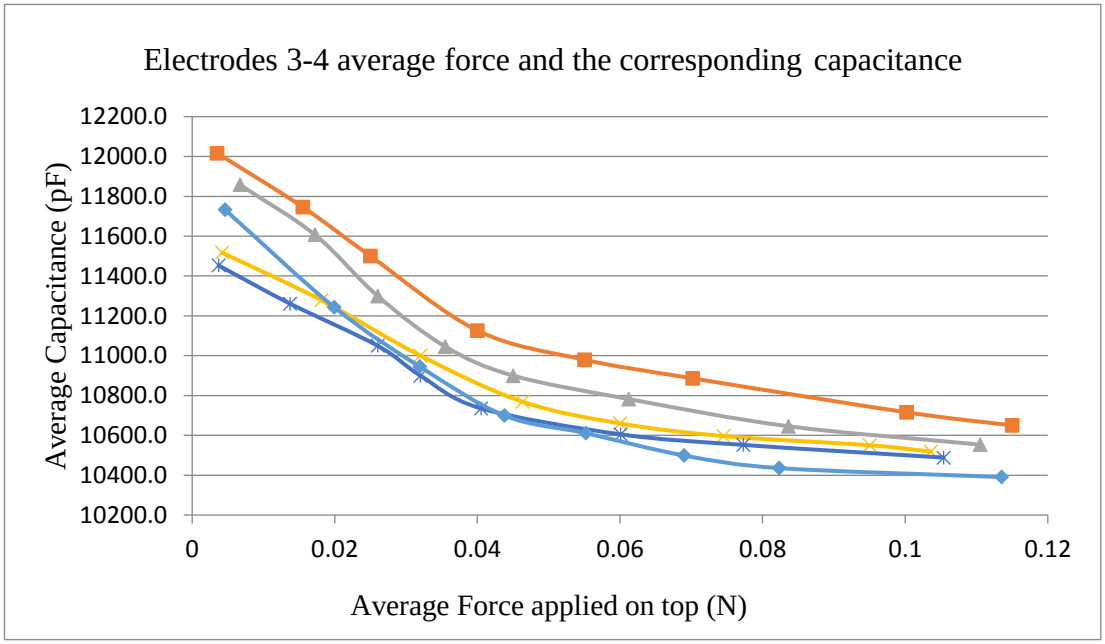

(f)

Figure 5-26 (f): Average force applied on top against to the corresponding capacitance for electrode pair 3-4.

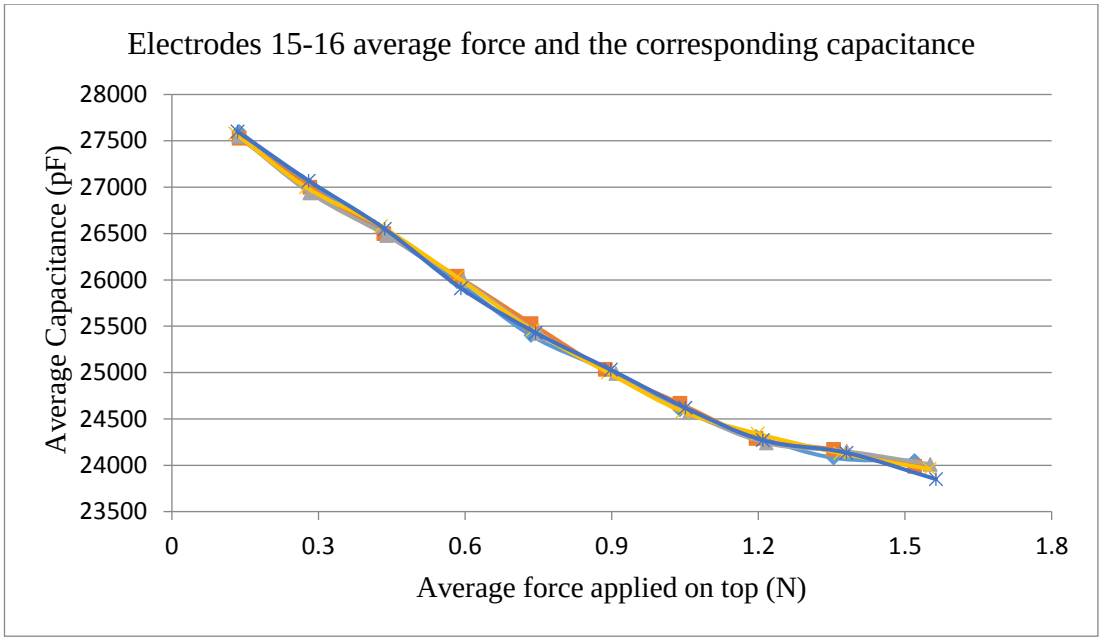

(g)

Figure 5-27 (g): Average force applied on top against to the corresponding capacitance for electrode pair 15-16

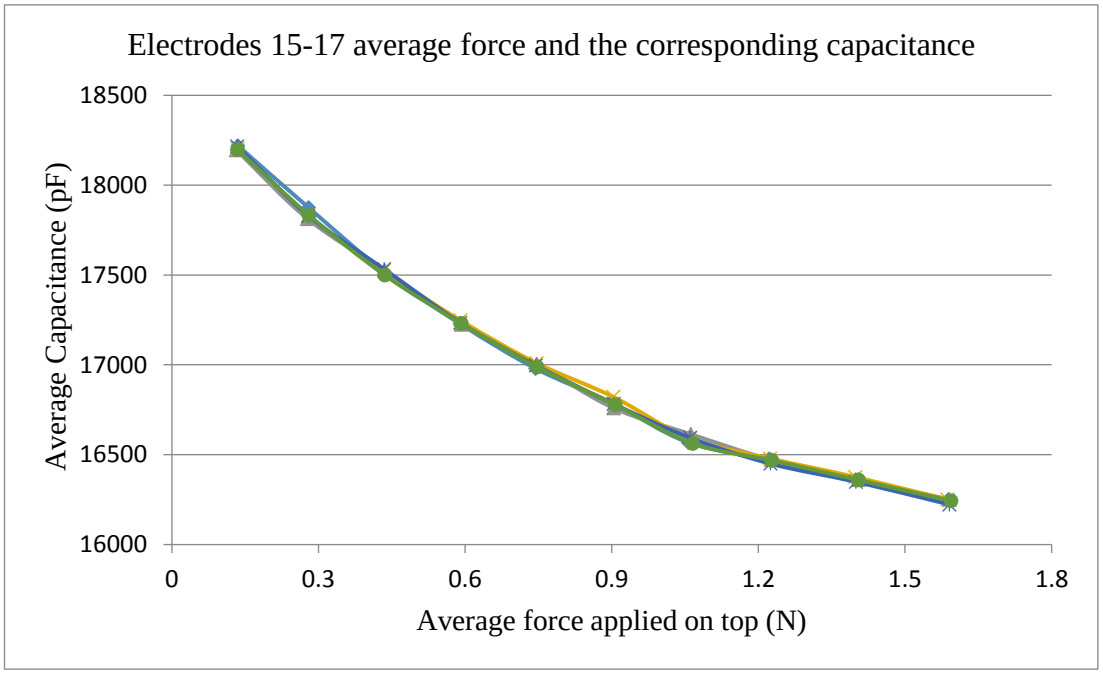

(h)

Figure 5-28 (h): Average force applied on top against to the corresponding capacitance for electrode pair 15-17.

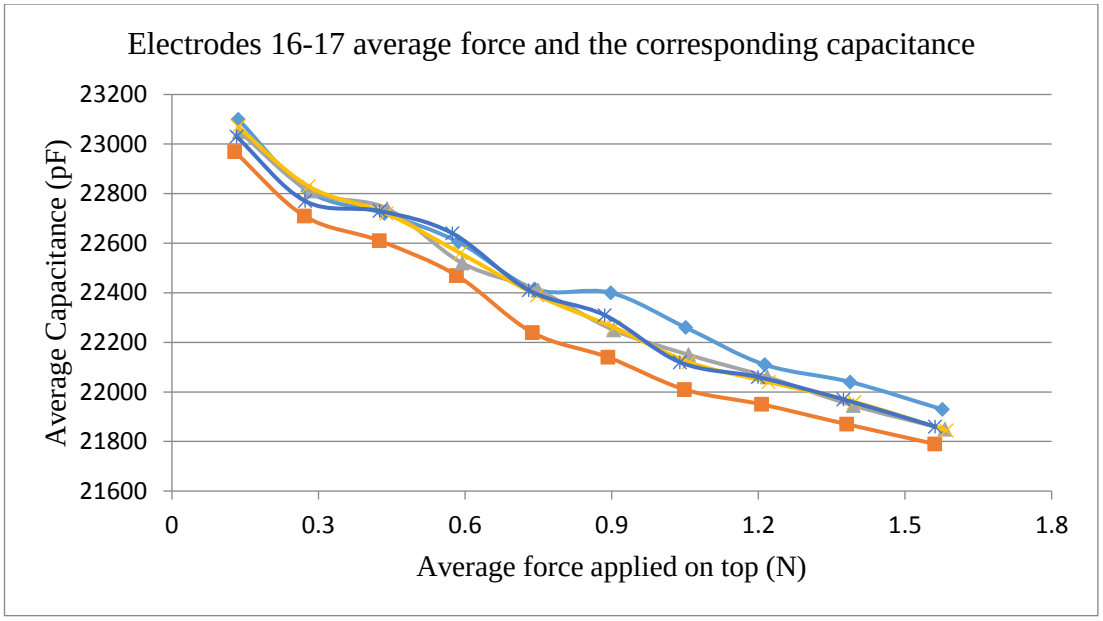

(i)

Figure 5-29 (i): Average force applied on top against to the corresponding capacitance for electrode pair 16-17.

In Figure 5-29 the x-axis in each plot represented the applied force on top in N and the y-axis indicated the reactive capacitance in pF. In each of the experiments, a force increased from 0 to 0.12N with eight increments was applied on top. From the literature review in Chapter 2, an electrode array insertion force as low as 0.1N would result in inner-cochlear tissue damage [62]. Therefore, 0.12 N of applied force would cover the entire electrode array insertion period.

Overall, with the increase of the applied force, the capacitance decreased in a corresponding fashion. However, the relationship between them was not consistent. For electrode pairs 1-2, 3-4, 15-16 and 15-17, the capacitance decreased linearly with the increase of the force. For electrode pairs 1-4, 2-4 and 16-17, before 0.07 N, the capacitance decreased slowly with force elevation. After 0.07 N, A dramatic drop took place, leading to an inconsistent relationship between them. Lastly, for electrode pairs 1-3 and 2-3, the capacitance decreasing became limited after 0.06 N. This led to an inconsistent relationship between the applied force and capacitance. According to this, the half-cell circuit model in Figure 5-2 could be improved by adding a force/ pressure sensitive component in series with the capacitor. The modified model is shown in Figure 5-30.

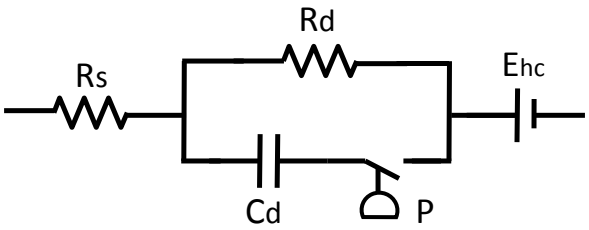

Figure 5-30: Modified half-cell equivalent circuit model of an electrode-electrolyte interface. A force/ pressure sensitive component represented by P was connected in series with the double layer capacitance.

As the force applied to the top of electrodes was one of the dominating causes of capacitance variations. A force sensitive component P was added to the circuit model to demonstrate the inverse relationship between the applied force and measured capacitance. In experiments, the relationship between them was not linear, although in electrode pairs 1-2, 3-4 and 15-16, linear decreases were observed between the applied force and capacitance. That was the reason they were selected to implement the measurements. The linear relationship could not be defined in other electrodes or in other cochlear implant array until experiments proved. However, the inverse relationship occurred and it could be treated as non-linear. Based on the assumption, further improvements could be made to improve the insertion force model and link to the electrical circuit model. As such, a complete insertion model could be generated in sensing of the CI electrode array insertion progress.

In summary, during the electrode array insertion experiments, the capacitance variations were measured and determine to violate the basic capacitance theorem. One of the reasons was because the shape of the electrodes was polygonal, it was difficult to calculate the overlaid electrodes area during the electrode array insertion process. Another reason was the electric charge exchanging phenomenon between electrodes and electrolyte. These causes were complex and impossible to quantify the analysis. However, it was found that the force applied to the top of electrodes was one of the dominating causes of capacitance variations. The reverse relationship of them made the electrode capacitance became a possible approach to measure force on top. Overall, with the increase of the applied force, the capacitance measured decreases correspondingly.

In order to investigate the detailed relationship between them, evolution experiments were implemented with electrode pair: 1-2, 1-3, 1-4, 2-3, 2-4, 3-4, 15-16, 15-17 and 16-17. The results demonstrated that electrode pairs 1-2, 3-4, 15-16 and 15-17 had a linear relationship between the applied force and capacitance. Therefore, the electrode pairs 1-2, 3-4 and 15-16 were selected to conduct the further insertion experiments.

5.3 Electrode Array Insertion Results

5.3.1 Preparations

Setup of the automated electrode array feed system was featured in Section 3.1. The electrode array feed system was composed of two translation stages [110], one rotational device [112], one three-axis force sensor [113] and an electrode array holder. Two translation stages and one rotational device were driven by one servo controller [111] individually. As shown in Section 3.5, three LCR meters [115] contacted the measuring tasks. A translucent cochlear model was firmly glued onto the holder before experiments. The tip of the electrode array was placed at the entry of the cochlear model before experiments. The preparation and alignment depicted in Figure 3.14. The electrode array insertion speed was 0.1mm/s and insertion length was 29 mm. The temperature of the liquid was room temperature, 24.5^{o}C, and its conductance was 14.3 S/m.

5.3.2 Smooth and Buckling Insertion Results

During the electrode array insertion, the array should fellow the outside cochlear wall to 270^{o}. However, owing to obstacles or jamming of the inner path, the electrode array tip would stop insertion with the bottom still inserting. The incident would result in a buckling pattern inside of the model path, leading to structural damage to the cochlear inner tissues. The electrode array's smooth insertion and buckling-inside pattern are demonstrated in Figure 5-31.

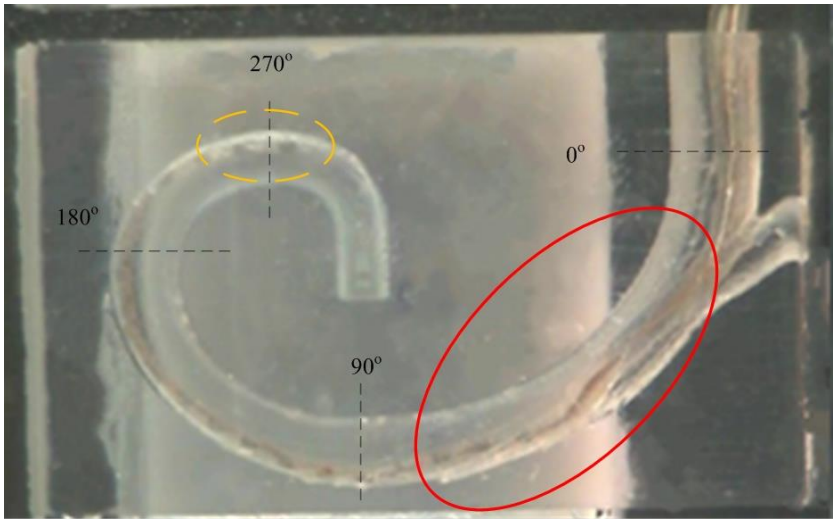

(a)

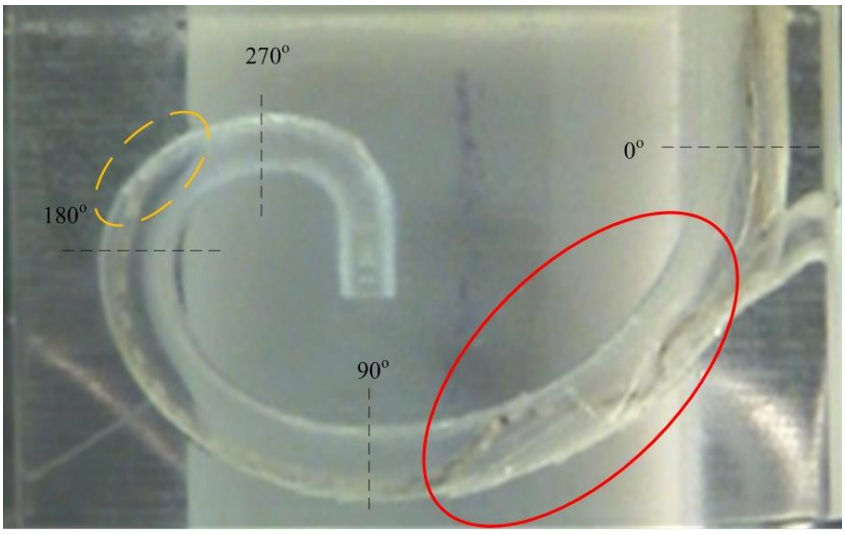

(b)

Figure 5-31: The electrode array smooth insertion and buckling inside pattern. The dash yellow circuit showed the finish position of electrodes 1 and 2. The solid red circuits represented the buckling pattern and non-buckling pattern. (a) The finish position of the electrode array was around 270 degree, (b) The tip stopped at 220 degree which caused the electrode array buckling pattern in red circuit.

Bipolar electrode capacitance measurement was applied to discriminate between the two types of behaviour. The measurements were conducted between electrodes 1 and 2, and electrodes 15 and 16. Electrodes 1, and 2 were located at the electrode array tip and electrodes 15, and 16 were located at the buckling position.

In our experiments, 38 smooth insertions and 26 buckling-inside insertions were recorded. Among the smooth insertions, 20 measurements of electrodes 1, and 2 and

18 measurements of electrodes 15 and 16 were recorded. Among buckling-inside insertions, 12 measurements of electrodes 1, and 2 and 14 measurements of electrodes 15 and 16 were recorded. All of the smooth and buckling insertion measurement results are shown in Figure 5-32.

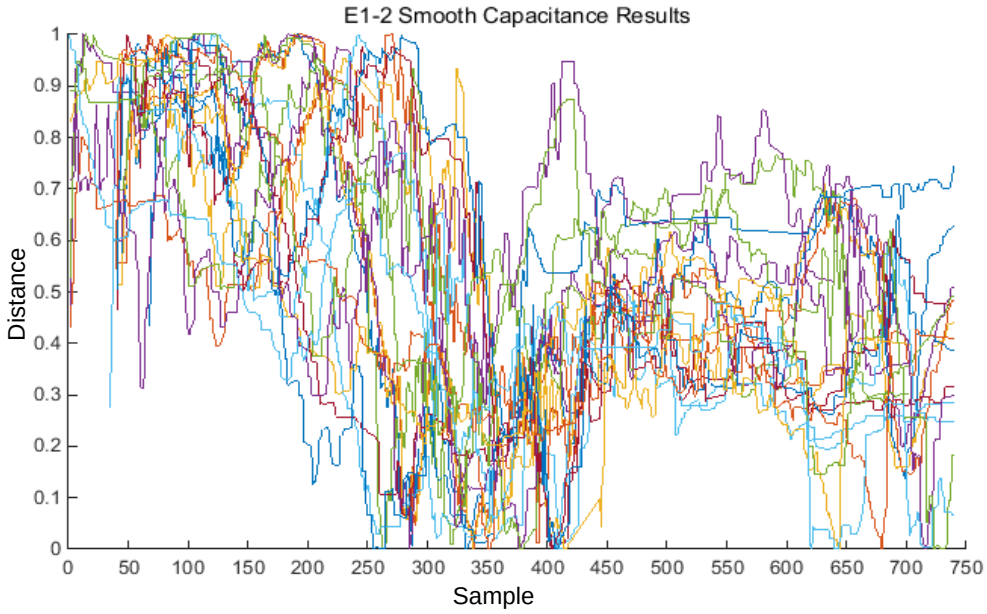

(a)

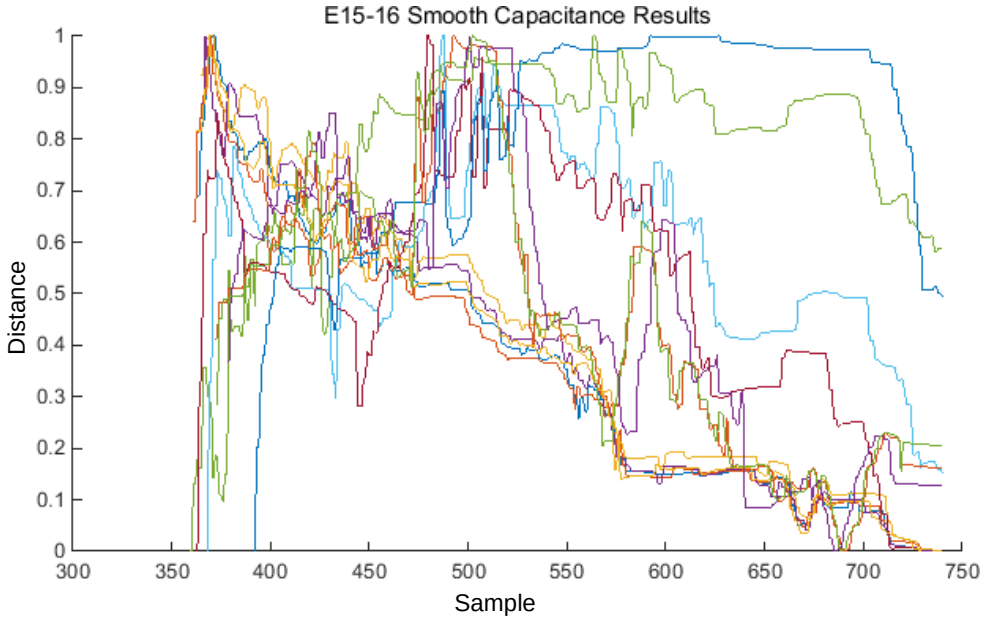

(b)

Figure 5-32 (a) and (b): Capacitance measurements results of the electrodes 1-2 and 15-16 of smooth electrode array insertions. The x-axis represented the original sample length recorded and the y-axis represented the normalised capacitance measurements to a range between 0 and 1.

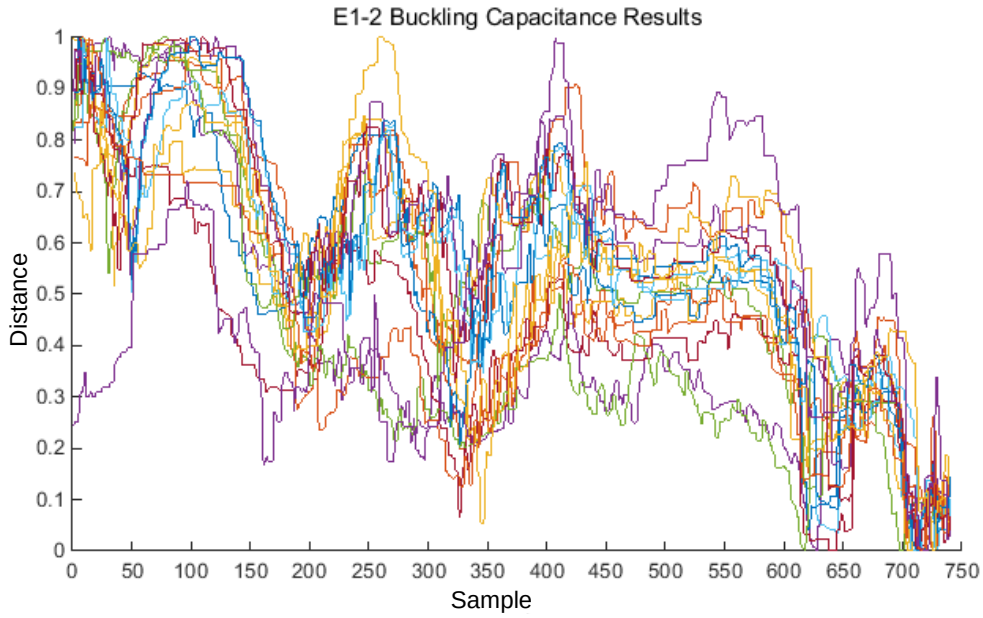

(c)

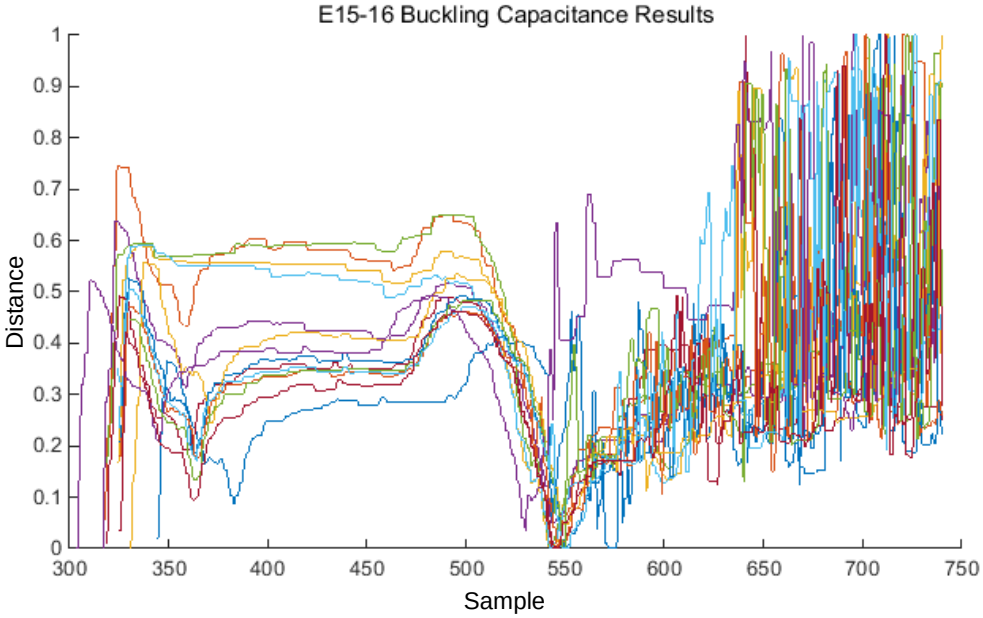

(d)

Figure 5-33 (c) and (d): Capacitance measurements results of the electrodes 15-16 of electrode array insertions with buckling patterns. The x-axis represented the original sample length recorded and the y-axis represented the normalised capacitance measurements to a range between 0 and 1.

In Figure 5-33, the x-axis represented the original sample length recorded. The sample length presented had the benefits of easy-conversion and generality. As the LCR meter

recording frequency was 2 Hz and the electrode array insertion speed was 1mm/s, the sample length could be easily converted to the insertion length or insertion angle. Besides, intervals of sample length were identical to all insertions and measurements, which were of universal application. The y-axis represented the normalised capacitance measurements to a range between 0 and 1. This was applied to minimise the environmental noises and normalised all capacitive measurements.

In Figure 5-33, each line represented an individual electrode array insertion. In Figure 5-32 (a) and (c), the x-axis started from 0 and finished at 750, but in Figure 5-33 (c) and (d), the x-axis started from 300. This was because electrodes 15 and 16 had not been filled into solutions before a sample length of 300. The capacitances measured between them were approximately 30 pF. These values should be omitted to enlarge utilitarian measures between a sample length of 300 and 750.

With respect to Figure 5-32 (a) and (c), overall measurements were the same apart from signals between a length of 600 and 700. The differences were considered to be caused by electrodes 1 and 2 buckling feature. The signal 'bridge' between 600 and 700 in (c) represented the relationship between the electrode array tip and the cochlear inner wall such that they were from in contact to separate and then back to contacting condition. The simultaneous video recording system also proved the changes, which were shown in Figure 5-32 (b). Differences between Figure 5-33 (d) and Figure 5-32 (b) were obvious. Capacitance values fluctuated heavily after sample 650. Owing to electrodes 15 and 16 buckling feature, the electrodes were squeezed and randomly making contacted with the wall. The lag effect of electrodes 15 and 16 delayed the buckling pattern location from sample 600 to 650. This was because a result of the electrode array not being able to transmit the resisting force from the tip to middle immediately because of its low stiffness. By comparing the results and videos, the variations of capacitive signals followed the array movements simultaneously. Electrode array behaviours such as intermitting insertion, buckling bridge, steady insertion were all reflected in the capacitive measurement results.

In order to discriminate the buckling pattern during the electrode array insertion, Principal Component Analysis (PCA) of the capacitance measurements was applied to electrodes 1-2 and 15-16 measurements. Details of the discrimination process would be shown in Section 6.1.

5.3.3 Fold-over Insertion Results

Similar to the causes of the buckling feature, obstructed, abnormal cochlea, array stiffness, and faulty insertion would result in electrode array tip fold-over. As introduced in the Literature Review section, the tip fold-over feature would lead to severe inner structural damage [51]. Therefore, it was necessary to discriminate and prevent the pattern.

In the experiments, the electrode array was inserted into a special cochlear model. The cochlear model was formed by the first 90-degree track, which was the most common place for the tip fold-back feature. By adjusting the entry angle, the tip of the array would make contact with the inner cochlear wall and fold back. The experiments' process is shown in Figure 5-34.

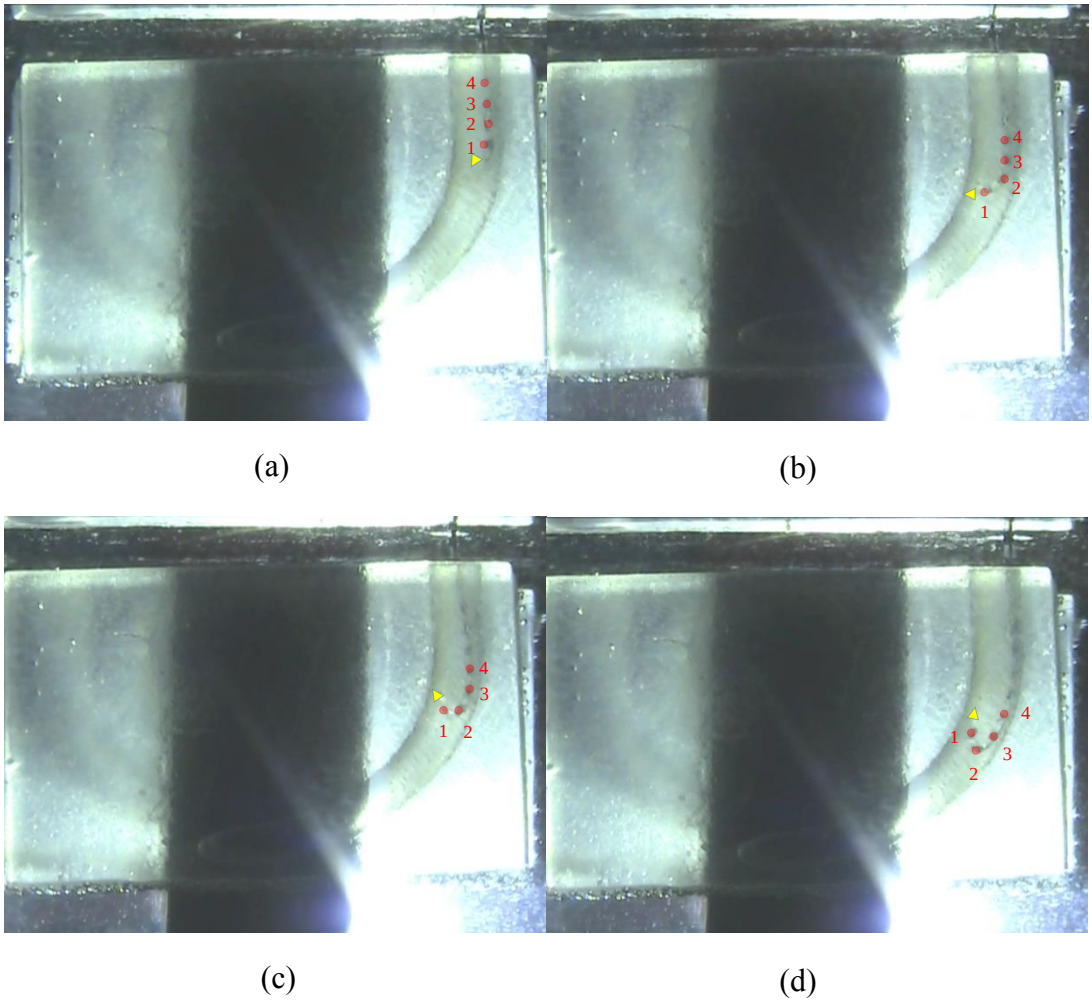

(a) (b)

(c) (d)

Figure 5-34: The electrode array tip fold back experiments. Each red dot highlighted an electrode. For example, dot 1 represented the first electrode and dot 2 represented the second.

In all of the experiments, the model was filled with the conducting solution at a concentration of 0.8% prior to the experiment. The inner path was washed by a needle to avoid any air bubbles attaching to the inner track. The temperature of the liquid was measured at room temperature (25±0.5^{o}C). The bottom of the electrode array was held by the automated insertion arm. The electrode array insertion speed was 0.1mm/s.

As shown in Figure 5-34, the four red dots represented the position of the front four electrodes and the yellow triangle represented the array tip. In Figure 5-34 (a), depicted was that how electrode array was inserted into the model at an angle of 45^{o}. Based on the low stiffness of the array, the tip of the array bent towards the inner wall, as seen in Figure 5-34 (b). Afterwards, the tip of the electrode array was obstructed by the wall, while the body of the array was still moving forward (Figure 5-34 (c)). Electrodes 1-4 were squeezed together by the compressing force. In Figure 5-34 (d), the fold-over pattern arose if the obstruction was not removed. The electrode array tip stopped advancing and kept making contact with the inner wall. At this stage, the electrode array would not be able to be recovered by itself. The insertion should be stopped immediately and the array would have to be pulled out. During the insertion, the circumstances of electrodes 1 and 2 changed frequently. They were utilised to conduct the sensing measurements. The capacitance sensing results are shown in Figure 5-35.

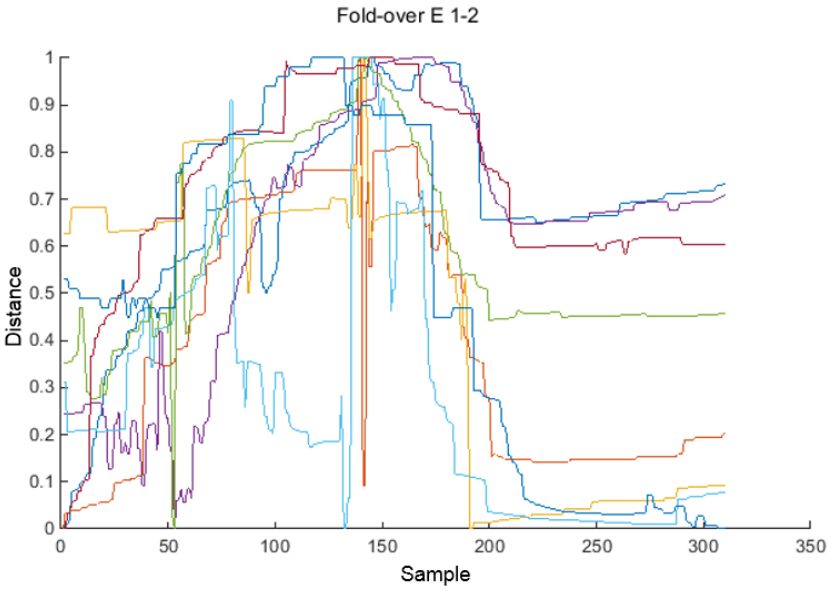

Figure 5-35: The electrode array insertions with the tip fold-over pattern.

Figure 5-35 depicted the capacitance measurements of electrodes 1-2 during the electrode array insertion with the fold-over pattern presented. The x-axis represented the original sample length with a recording frequency of 2 Hz. The y-axis represented the normalised capacitance measurements within a range between 0 and 1. Each curve indicated an individual insertion. Eight fold-over insertions were conducted in the experiments.

Before the sample length of 150, the overall trend of the capacitance measurement rose, this was supposed to be caused by the initial advancing activity. Before the sample length of 150, electrodes 1 and 2 filled with the saline solution and did not make contact with the wall. By comparing the distance inserted, the behaviour matched the video screenshot in Figure 5-34 (a) and (b). Between sample length of 150 and 200, the first electrode began to make contact with the wall, and the distance between electrode 1 and 2 was squeezed. The complex operation resulted in capacitance measurement fluctuations. The behaviour matched Figure 5-34 (c). Between the sample length of 200 and 230, the first electrode in the array was firmly pressed onto the inner wall. This led to dramatic capacitance decreases, which matched Figure 5-34 (d). After that, the status of the electrode distances and their on-top pressures remained steady. As a result, the value of the capacitance fluctuated within a restricted range. In our analysis, the fold-over pattern occurred around the sample length of 180. In order to discriminate the fold-over pattern, it was essential to extract the falling capacitance and steady states afterwards. The discrimination process would be detailed in Section 6.2.

5.4 Conclusion

The reasons for the bipolar electrode capacitance variation when filling with solutions had been investigated in this chapter. The reasons demonstrated that, the capacitance value measured was produced not only by the electrode capacitance, but also by the capacitance owing to liquid conductivity. Solution conductivity was one of the dominating factors that affect measurements. When electrodes were filled with conductivity solutions exclusively, the value of capacitance rose along with increasing solution conductivity. When the array slid along the insulation materials, the capacitance was examined to be 80% higher than filling with just the solution. The vertical tensile force at the tip of the electrode array resulted in restricted changes to the capacitance measured.

The distance between two electrodes affected the capacitance measured. Shortening the distance resulted in the increment of the capacitance. However, on account of the varied permittivity and incalculable overlaid electrodes area, it was impossible to quantify the relationship between the capacitance measured and the distance between them.

During the electrode array insertion experiments, the capacitance variations were recorded and interpreted to violate the basic capacitance theorem. It was found that the force applied to the top of the electrodes was another domineering factor that causes capacitance variations. With the increase of the applied force, the capacitance measured decreased correspondingly. The results demonstrated that the electrode pairs 1-2, 3-4, and 15-16 had a relative linear relationship between force and capacitance. Thus, they were chosen to conduct the further insertion experiments.

The insertion measurements also demonstrated that the electrode capacitance provided a sensitive method for investigating electrode array behaviour, instead of the cochlear model. The highly sensitive and reliable capacitive sensing system could be employed to discriminate certain electrode array insertion patterns. The discrimination process would be detailed in Chapter 6.

Chapter 6

Single Pair of Electrodes Capacitance Measurement Discrimination Process

According to the last chapter, the measurements had confirmed that the capacitive signals values were systematically influenced by intracochlear insertion forces between the scala tympani wall and the contact electrodes. The findings revealed that the capacitance-sensing method was capable of recognising electrode array patterns when fed into the cochlear model. In this chapter, discrimination algorithms would be applied to separate three electrode array insertion patterns.

This chapter was organised as follows[3]. Section 6.1 introduced the discrimination algorithm: the k-nearest neighbour (k-NN) and pre-processing algorithms: the Principal Component Analysis (PCA) and The Pearson Correlation Coefficient (PCC). Section 6.2 covered the separation process between the buckling pattern and smooth insertion pattern with the algorithm PCA. Section 6.3 presented the discrimination process of the fold-over insertion pattern. The pattern could be separated from the other two insertion patterns with the Pearson Correlation Coefficient (PCC). Lastly, Section 6.4 concluded the chapter.

[3] The contents of this chapter have partly appeared in "A Novel Cochlear Implant Electrode Array Sensing System to Discriminate Failure Patterns" by Hou et. al. in Journal of *Hearing Research.* (Submitted)

6.1 Introduction

6.1.1 The k-Nearest Neighbour Analysis (k-NN)

In order to recognize the occurrence of buckling pattern and fold-over pattern from smooth insertions during electrode array insertions, the k-nearest neighbour analysis (k-NN) was applied. Two pre-processing algorithms were used to discriminate buckling insertions and fold-over insertions.

The k-NN was a non-parametric algorithms that was widely used for classification and regression [137]. As k-NN was based on feature similarity, classification could be done by using k-NN classifier. k-NN stored all available cases in training set and classified new cases in test set based on a similarity measure [138]. k in k-NN was a parameter that referred to the number of nearest neighbours to participate in the majority voting process.

Capacitive resulted from electrode pair (1, 2) and electrode pair (15, 16) had been collected and analysed. A pre-processing algorithm: the Principal Component Analysis (PCA) on the acquired sequence of capacitance measurements was applied to discriminate certain buckling features. Experimental results with regards to the Buckling and Smooth feature pattern were shown in Chapter 5 (Figure 5-32)

Another pre-processing algorithm the Pearson Correlation Coefficient (PCC) was applied to discriminate the fold-over pattern from the other two insertion patterns: smooth insertions and buckling insertions. It was due to the fact that electrode array folding over during the CI insertion was a crucial faulty pattern that must be detected and avoided. Experimental results with regards to the fold-over pattern were shown in Chapter 5 (34).

6.1.2 The Principal Component Analysis (PCA)

The PCA method was a statistical approach to reduce the variables in the buckling feature [127]. It was applied in the method due to the fact that it was eligible to recognise the buckling and folding-over pattern in experiments. The method was applied by comparing weight factors of two group of data and the similarity between them was recognised. Therefore, a threshold could be determined to separate these two groups. A block diagram shown in

Figure 6-1 detailed the PCA discrimination process.

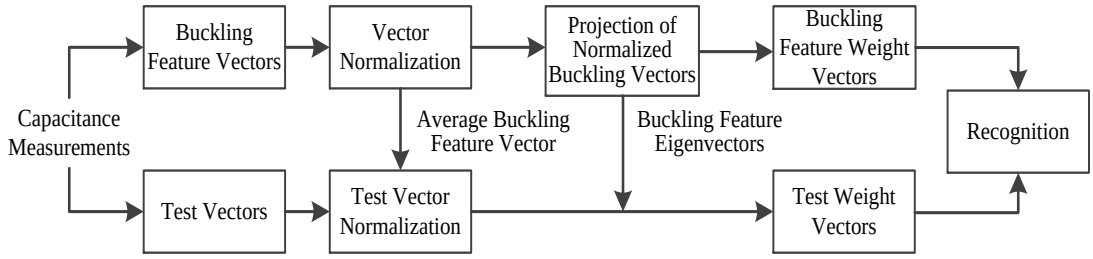

Figure 6-1: Block diagram of discriminating the electrode array insertion patterns.

All the capacitive measurements were divided into two sets- the buckling feature set (training set) and the testing set. All the vectors from the two sets were converted within a range of 0 and 1. This was to normalise all the capacitive measurements and minimise environmental noise. Vectors in the buckling set were averaged to achieve the average buckling feature. After processing of the normalised feature vectors, the buckling feature Eigenvector was obtained. The buckling feature Eigenvector was projected onto the normalised buckling and test group to receive the weight factors for the groups. Finally, low dimensional vectors (weight factors) in each group were compared to discriminate the buckling feature and its location during electrode array insertion.

6.1.3 The Pearson Correlation Coefficient (PCC) analysis

The Pearson Correlation Coefficient (PCC) analysis was a measure of the linear correlation between two samples [133]. The coefficient was represented by r with a range between -1 to 1 [134].

The PCC formula [133] between one dataset $\{x_1, ..., x_n\}$ and another dataset $\{y_1, ..., y_n\}$ was expressed as.

$$r = \frac{\sum_{i=1}^{n}(x_i - \overline{x})(y_i - \overline{y})}{\sqrt{\sum_{i=1}^{n}(x_i - \overline{x})^2}\sqrt{\sum_{i=1}^{n}(y_i - \overline{y})^2}} \tag{6.15}$$

where both of the two datasets contain *n* values and *n* was the dataset size; x_i and y_i indicated the single data indexed with *i*; $\overline{x}$ and $\overline{y}$ represented the mean value of the datasets.

When $r > 0$, the measured two samples were positively correlated. When $r < 0$, the measured two samples were negatively correlated. When $r = 0$, there were no linear correlations between the samples. A value of $r = 1$ indicated there was a prefect linear correlation between the samples [133].

6.1.4 Conclusion

To this end, we used two sets of measurements; the training set and the testing set. We acquired measurements from 68 independent insertions and we used 12 of them for training purposes i.e. 6 for electrode pair (1, 2), and 6 for electrode pair (15, 16), while the remaining 56 formed the test set. The output three electrodes insertion patterns (Smooth, Buckling and Fold-over) were classified by the method. As the training vectors dimensional was high, a pre-processing of featured vectors was necessary before applying the k-NN algorithm. The Principal Component Analysis (PCA) was employed to extract features and reduce dimensions. The method was used to discriminate buckling insertions and smooth insertions. The Pearson Correlation Coefficient (PCC) analysis was applied in discriminating fold-over insertions from the other two insertion patterns.

6.2 Application of Principal Component Analysis (PCA)

6.2.1 Recognise the Buckling Feature from an Unknown Insertion

To this end, we used two sets of measurements; the training set and the testing set. We acquired measurements from 68 independent insertions and we used 12 of them for training purposes i.e. 6 for electrode pair (1, 2), and 6 for electrode pair (15, 16), while the remaining 56 formed the test set. Before the application of PCA, all capacitance values were normalized in the range 0 to 1. It was a process of the PCA algorithm and it could be achieved by that each capacitance value divided by the capacitance range measured. In order to make the process clear, a flowchart of the PCA discrimination is generated and summarized in Figure 6-2.

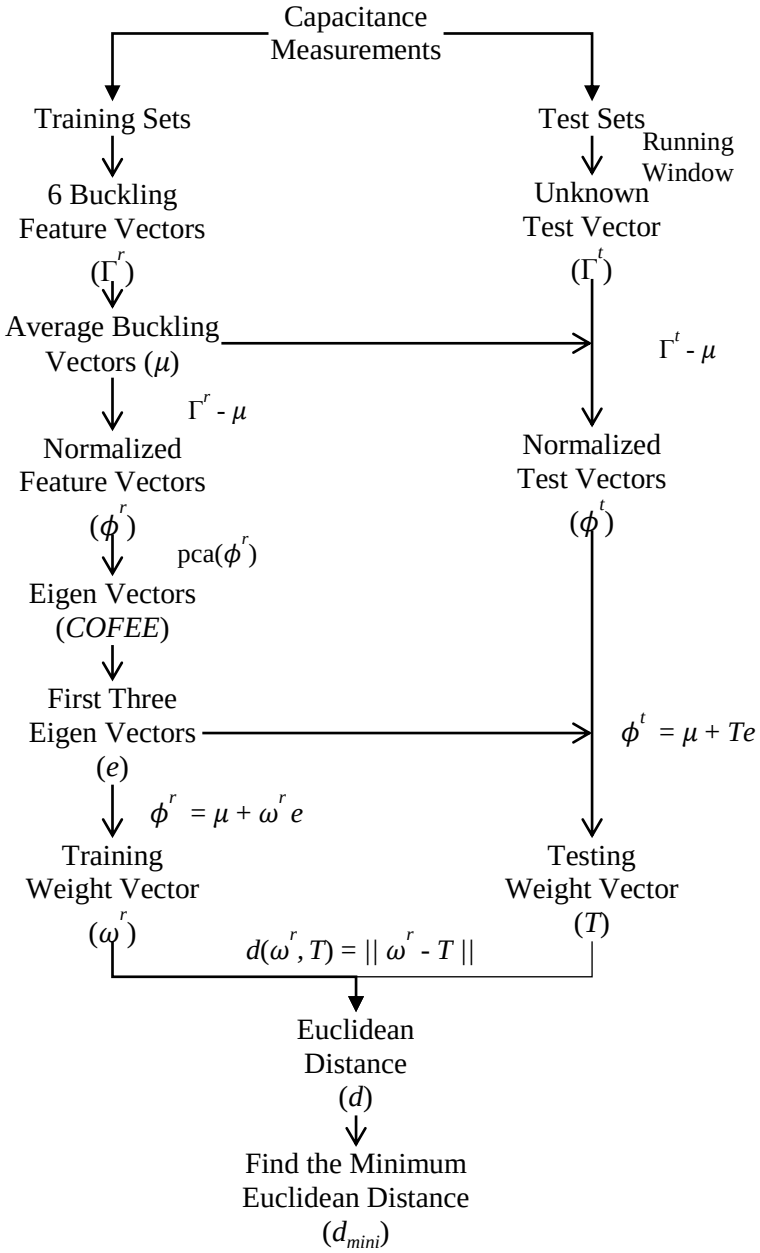

Figure 6-2: Flowchart of the PCA discrimination process.

The training set was formed by M = 6 feature vectors: $\Gamma_i^r, i = 1, \dots, M$, representing measurements where buckling had occurred, where r indicated the training set. Each of the vectors had length N. Thus, the training set was arranged in an M by N matrix, where M was 6 and N was determined by the length of the buckling features. The number was chosen according to the length of a complete buckling feature.

$$\Gamma^r = [\Gamma_1^r, \Gamma_2^r, \Gamma_3^r, \Gamma_4^r, \Gamma_5^r, \Gamma_6^r]^T \tag{6.1}$$

These buckling features needed to be normalized to train the recognizer. Normalizing the training vector indicated that the common feature from the training set would be

removed, so that the unique buckling pattern would be left [128]. The average feature vector (μ) of the training set was calculated as:

$$\mu = \frac{1}{M}\sum_{i=1}^{M}\Gamma_i^r \tag{6.2}$$

The lengths of the average buckling feature vectors were identical to the original buckling feature vectors, which were $N_{1,2}$ and $N_{15,16}$.

Subsequently, the average vectors μ was subtracted from each feature vector Γ_i^r in order to calculate the normalized training feature vectors, ϕ_i^r.

$$\phi_i^r = \Gamma_i^r - \mu \tag{6.3}$$

Where ϕ_i^r represented the normalized feature vector for training set, Γ_i was the original feature vector and μ was the average feature vector and r represented of the training set.

$$\phi^r = [\phi_1^r, \phi_2^r, \phi_3^r, \phi_4^r, \phi_5^r, \phi_6^r]^T \tag{6.4}$$

In order to calculate the eigenvectors, we then calculated the covariance matrix *C* of the combination of the normalized feature vectors $\phi_i^r, i = 1, \dots, M$ [129]. For the calculation of *C*

$$C = \frac{1}{M}\sum_{i=1}^{M}\phi_i^{rT}\phi_i^r \tag{6.5}$$

We could calculate its eigenvector matrix *e* of the covariance matrix *C*. Each of the normalized buckling features could be represented as a linear combination of the *K* eigenvectors, $e_k, k = 1, \dots, K$. In our analysis, $K = M - 1 = 5$.

$$e = [e_1, e_2, e_3, e_4, e_5] \tag{6.6}$$

Size of $e = 84 \times 5$. Each normalized buckling feature ϕ_i^r in the training set could be represented as a linear combination of the *K* eigenvectors e_k plus the mean buckling feature [126].

$$\phi_i^{r^T} = \mu^T + \sum_{k=1}^{K} \omega_i^k \, e_k, i = 1, \dots, M \tag{6.7}$$

ω_i^k was the weights of the associated *k* eigenvectors for the training set. This could be calculated

$$\omega_i = \phi_i^r e \tag{6.8}$$

The weights vector ω_i for each feature vector in the training set was

$$\omega_i = \left[\omega_i^1, \omega_i^2, \omega_i^3, \omega_i^4, \omega_i^5\right], i = 1, \dots, M \tag{6.9}$$

The process could be achieved by the MATLAB function: *pca* [130]. The function returned three coefficients *C*, *SCO* and *LAT*.

$$[COEFF, SCO, LAT] = pca\ (\mathrm{X}) \tag{6.10}$$

Where *COEFF* represented the principal component coefficients, *SCO* was the principal component scores; *LAT* represented latent that was a vector containing the eigenvalues of the covariance matrix of normalized buckling features [131]. These transformations had the advantage of reducing the effect of noise [132].

In testing, the sequence of capacitance measurements was long and, in each time, instant, a running window of length *N* was applied in order to keep only *N* samples and facilitate comparison with the available training vectors. After applied the running window, each testing sequence of capacitance measurements would create up to 711 testing vectors.

Then, the average vector μ of the training set was subtracted from each test vector in order to obtain normalized test vectors.

$$\phi_i^t = \Gamma_i^t - \mu \tag{6.11}$$

Where ϕ_i^t represented the normalized test vectors, Γ_t represented the unknown testing vector.

Each of the normalized test vectors was formed as a combination of *k* eigenvectors by projecting onto the buckling feature eigenvectors.

It was applied to represent the unknown testing vector as a combination of *k* eigenvectors. Therefore, a test weight vector *T* of the unknown testing vector could be expressed as:

$$\phi_i^{t^T} = \mu^T + \sum_{k=1}^{K} t_i^k \, e_k, i = 1, \dots, L \tag{6.12}$$

$$T_i = \left[t_i^1, t_i^2, t_i^3, t_i^4, t_i^5\right], i = 1, \dots, L \tag{6.13}$$

t_i^k was the weights of the associated *k* eigenvectors for an unknown testing vector.

Finally, the Euclidean distance between each test weight vector T_i and all the training weight vectors ω_i from the training set was calculated. Again, the running window method was applied to calculate the Euclidean distance between each of the weight vectors in the test set and all the training weight vectors, following the Equation 6.14.

$$d(\omega_i, \mathrm{T}_i) = ||\omega_i - \mathrm{T}_i|| \tag{6.14}$$

Where *d* represented the Euclidean distance, ω_i represented the weights vector for each buckling feature vector in the training set, and T_i showed the weights vector for an unknown test vector.

6.2.2 PCA Recognition Results

In our analysis, vector length for electrode pair (1, 2) was $N_{1,2} = 84$, whereas vector length for electrode pair (15, 16) was $N_{15,16} = 30$. The feature vector when electrode pair (15, 16) was examined was shorter because the effect of buckling made a shorter but stronger appearance in the measurements acquired through that pair. Size of the training set was $\Gamma_{1,2}^{r} = 6 \times 84$ and $\Gamma_{15,16}^{r} = 6 \times 30$. Four of the buckling features in the training set for electrode pair (1, 2) and (15, 16) respectively were shown in

.

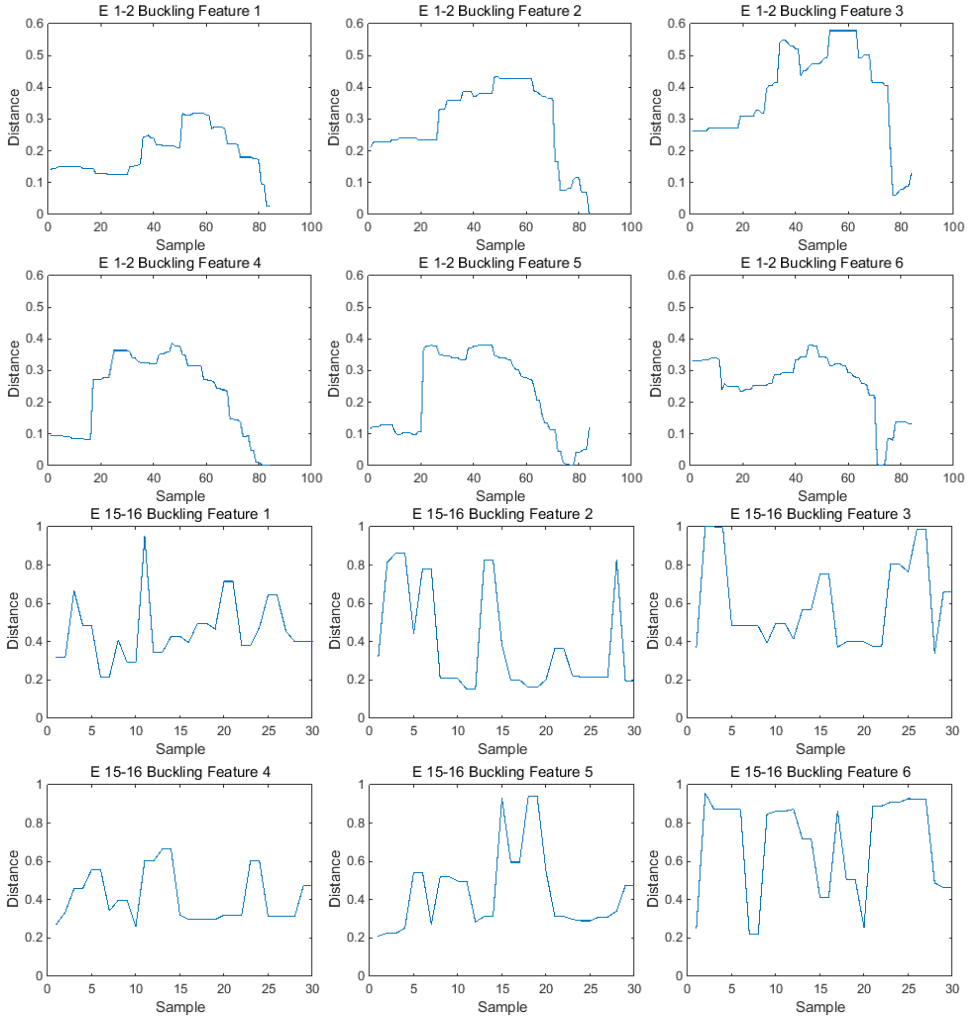

Figure 6-3: (top row) Normalised capacitance signal measurement for electrode pair (1, 2) under buckling pattern condition, (bottom row) normalized capacitance signal measurement for electrode pair (15, 16) under buckling pattern condition.

These buckling features shown in Figure 6.3 needed to be normalized to train the recognizer. It meant the average feature was removed to identify the unique buckling

pattern. According to the equation 6.2, the average buckling feature vectors of electrode pair (1, 2) (μ_{12}) and electrode pair (15, 16) (μ_{1516}) are calculated and shown in Figure 6-4.

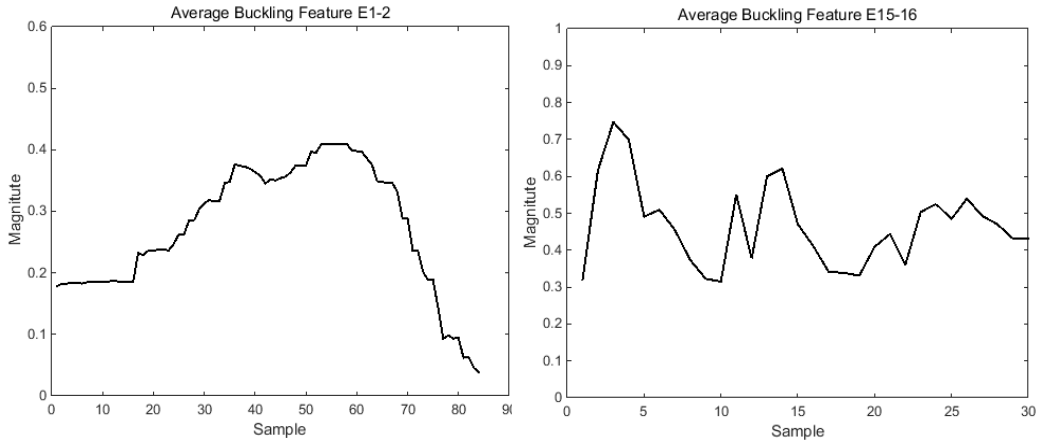

Figure 6-4: (Left) The average buckling feature vectors of electrode pair (1, 2) (μ_{12}) and (Right) electrode pair (15, 16) (μ_{1516}).

In total, there were 56 measurements in the test set. As shown in Table 6.1, these measurements were divided into 4 groups.

Table 6.1: The test measurements set were formed by 4 groups. It showed the buckling/smooth set, and the rows indicated the measurement of the electrode pair. For the buckling feature insertions, there were 12 measurements of electrode pair (1, 2) (group 1) and 12 measurements of electrode pair (15, 16) (group 2). For the smooth insertions, there were 20 measurements of electrode pair (1, 2) (group 3) and 12 measurements of electrode pair (15, 16) (group 4).

	Buckling Set	Smooth Set
E 1 - 2	Group 1: 12	Group 3: 20
E 15 - 16	Group 2: 12	Group 4: 12

The Euclidean distance between each test weight vector and all six training weight vectors were calculated. Among each comparison results, the minimum, average and maximum distances were gathered and recorded.

The three distance types of electrode pair (1, 2) and electrode pair (15, 16) in the buckling insertion set (groups 1 and 2) are shown in Figure 6-5. The three distance types of electrode pair (1, 2) and electrode pair (15, 16) in the smooth insertion set (groups 3 and 4) are shown in Figure 6-6.

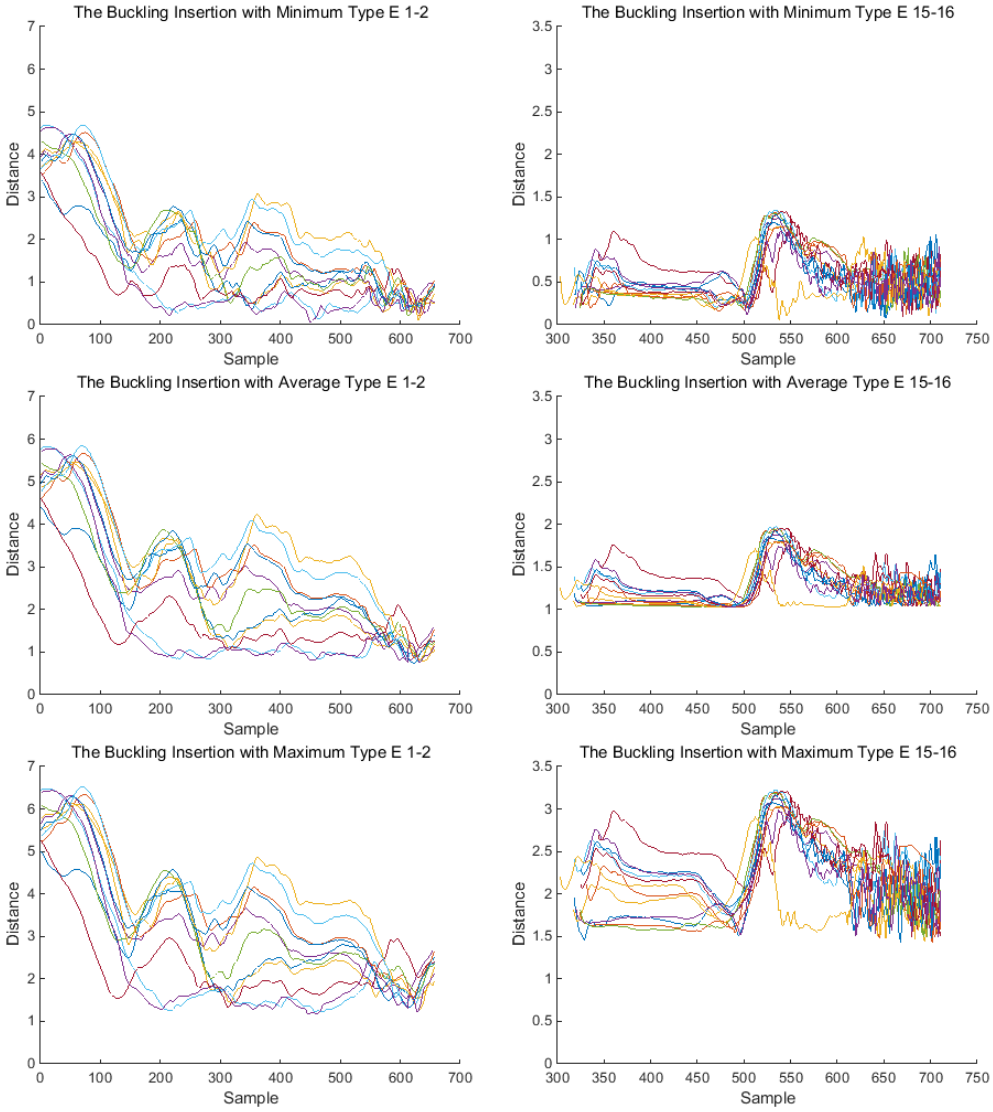

Figure 6-5: The minimum, average, and maximum distance types in the buckling insertion set (groups 1 and 2).

Figure 6-5 presented the three Euclidean distance types of the electrode array buckling insertions between test weight factors and the training weight factors of electrode pair (1, 2) and electrode pair (15, 16). The x-axis indicated the sample length with respect insertion time, and the y-axis indicated the Euclidean distance.

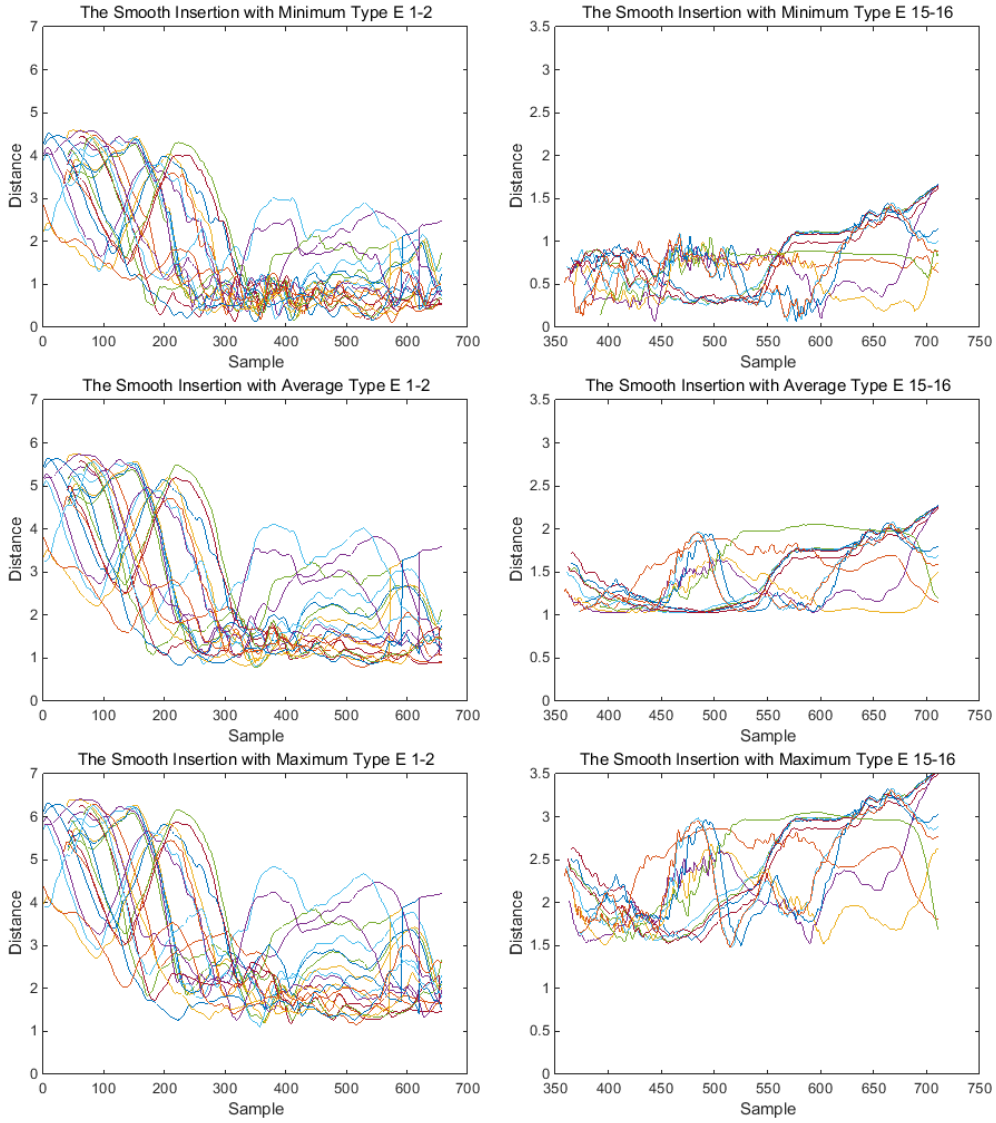

Figure 6-6: The minimum, average, and maximum distance types in the smooth insertion set (groups 1 and 2).

Figure 6-6 presented the three Euclidean distance types of the electrode array smooth insertions between the test weight factors and the training weight factors of electrode pair (1, 2) and electrode pair (15, 16). The x-axis indicated the sample length with respect to time, and the y-axis indicated the Euclidean distance. The smaller the distance was, the more similar the test vector was to the training vector. Each curve indicated an independent full insertion. The minimum distance for each insertion would be gathered and analysed in order to separate the two insertion patterns.

6.2.3 Discrimination for Each Group

After calculating every vector in the test set, minimum Euclidean distances of the three types were obtained. The minimum distances of the comparison results for the electrode pair (1, 2) (group 1 and 3) are depicted in Figure 6-7.

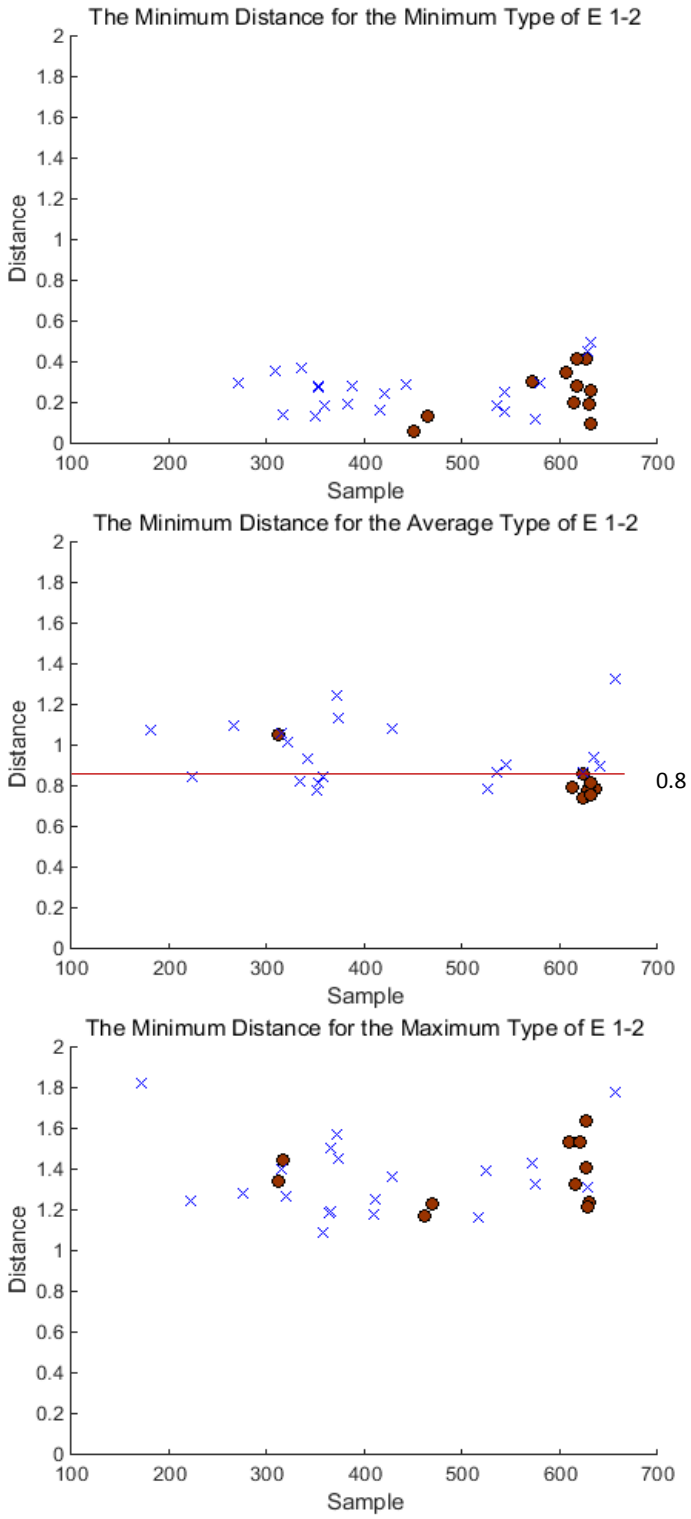

Figure 6-7: Minimum Euclidean distances between electrode pair (1, 2) for the buckling and smooth insertions.

Figure 6-7, the x-axis indicated the sample length with respect to time, and the y-axis indicated the minimum Euclidean distance. Red dots demonstrated the minimum Euclidean distance of all the buckling insertions, and the blue crosses represented the minimum Euclidean distance of all the smooth insertions.

For the buckling insertions, most of the minimum distance positions were larger than 600 sample length. However, the minimum distance positions for the smooth insertions varied from 200 to 650. Apart from the average type of electrode pair (1, 2), it was unlikely to appoint a threshold to separate the two insertion types. The Euclidean distance values for the rest types were similar. In regarding of the average type of electrode pair (1, 2), distance value ranged from 0.82 to 0.84 and could be appointed as a threshold to separate them. It was due to that only 2 smooth insertions out of 20 minimum distances of electrode pair (1, 2) were lower than the thresholds, and 2 buckling insertions out of 12 minimum distances were larger than the thresholds. Thus, an average value of 0.83 could be used as the threshold to separate the two insertion patterns by the average case of electrode pair (1, 2). The success rate was 75% for the buckling insertions (group 1), 90% for the smooth insertions (group 3), and 84.38% in overall.

The discrimination method of electrode pair (1, 2) was also applied to the fold-over group. The fold-over group was formed by eight individual insertions. All of the insertions in the group contained the fold-over pattern. The buckling pattern was examined in the fold-over group by the running window method. The weight factors of the buckling pattern were compared with the weight factors of the fold-over group. The distance profiles of the minimum, average, and maximum types are collected and depicted in Figure 6-8.

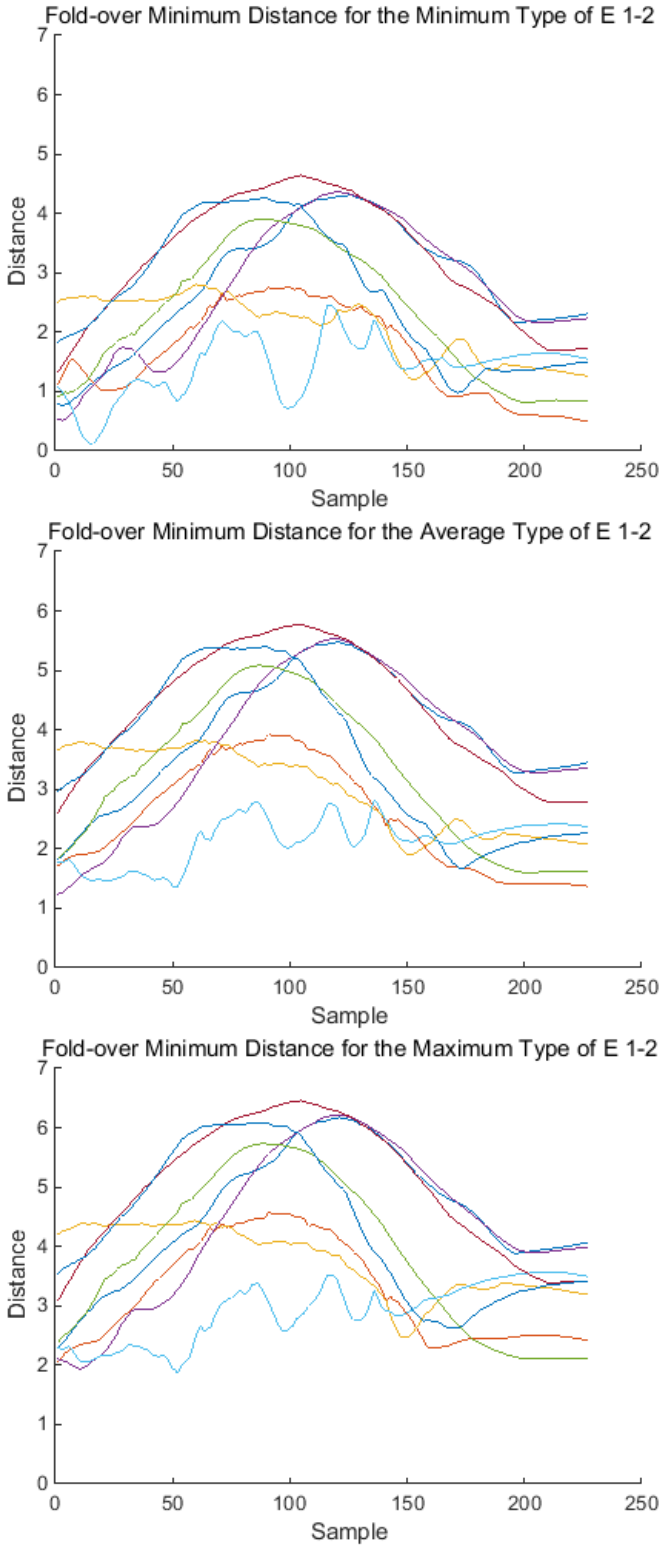

Figure 6-8: the minimum, average, and maximum types of the fold-over insertions.

The x-axis indicated the sample length with respect to time, and the y-axis indicated the compared Euclidean distance. The minimum positions of Euclidean distance profiles are portrayed in Figure 6-9.

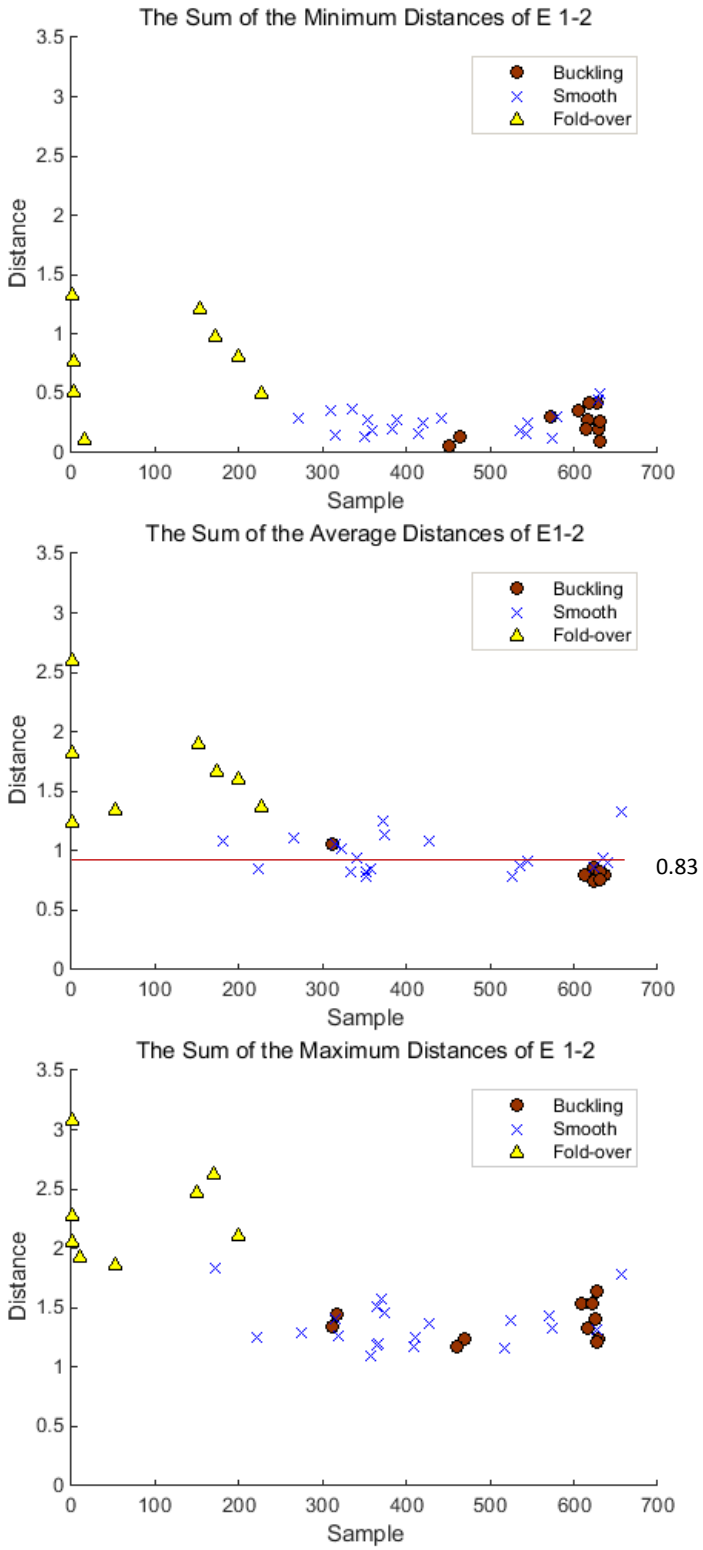

Figure 6-9: Minimum Euclidean distances between electrode pair (1, 2) for the fold-over insertions.

In Figure 6-9, red dots indicated the minimum Euclidean distance of all the buckling insertions, the blue crosses represented the minimum Euclidean distance of all the smooth insertions and the yellow triangles represented the minimum Euclidean

distance of all the fold-over insertions. From Figure 6-9, all the yellow triangles were above the threshold 0.83 for the average type. This suggested that the chosen threshold of 0.83 could be appointed to discriminate the insertions with the fold-over pattern with a success rate of 100%.

Similar to group 1 and group 3, the three types of minimum Euclidean distances between electrode pair (15, 16) for the buckling and smooth insertions (groups 2 and 4) are plotted in Figure 6-10.

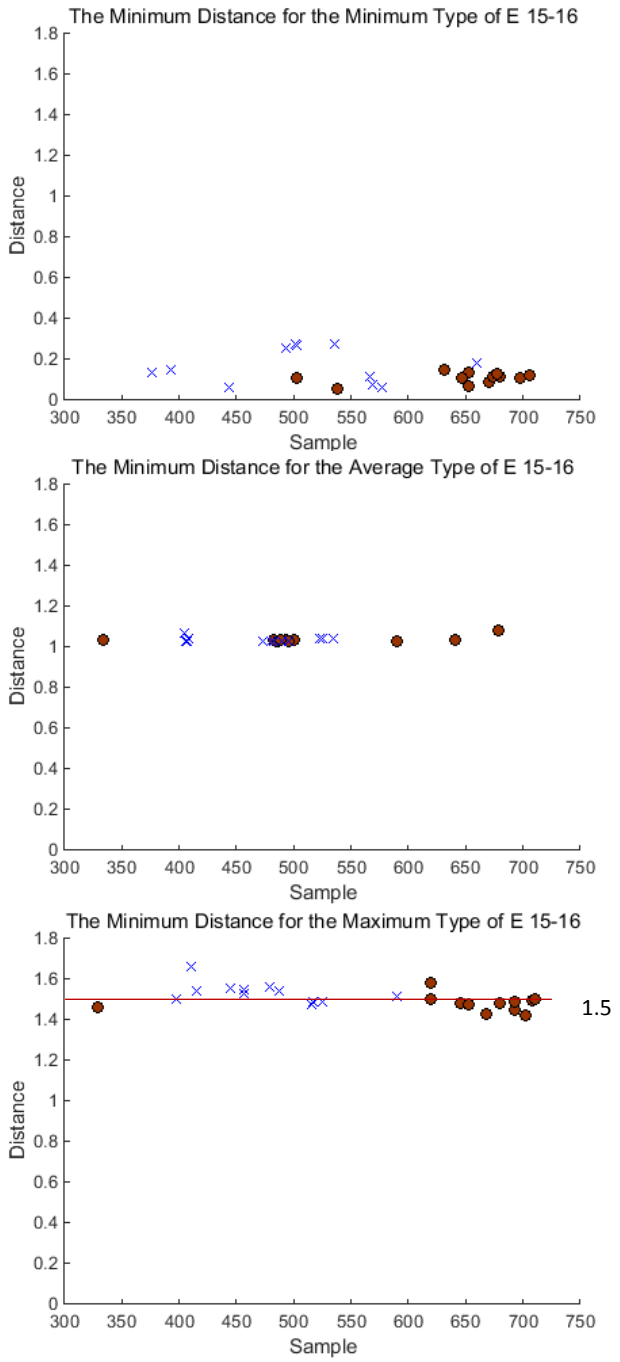

Figure 6-10: The minimum Euclidean distances between electrode pair (15, 16) for the buckling and smooth insertions (group 2 and group 4).

In Figure 6-10, red dots indicated the minimum Euclidean distance of all the buckling insertions (group 2), and the blue crosses represented the minimum Euclidean distance of all the smooth insertions (group 4).

A threshold of 1.50 could be applied to the distance maximum type to separate the buckling pattern. It was due to that 3 smooth insertions out of 12 minimum distances of electrode pair (15, 16) (group 4) were lower than the thresholds, and 2 buckling insertions out of 12 minimum distances (group 2) were larger than the thresholds. Thus, the successful separation rate was 75% for the buckling insertions (group 4), 83.33% for the smooth insertions (group 2), and 79.17% in overall.

A summary of the Euclidean distance between the buckling insertions testing weight vectors and all the training weight vectors are shown in Figure 6.11(a) and a summary of the Euclidean distance between the smooth insertions testing weight vectors and all the training weight vectors are shown in Figure 6.11(b).

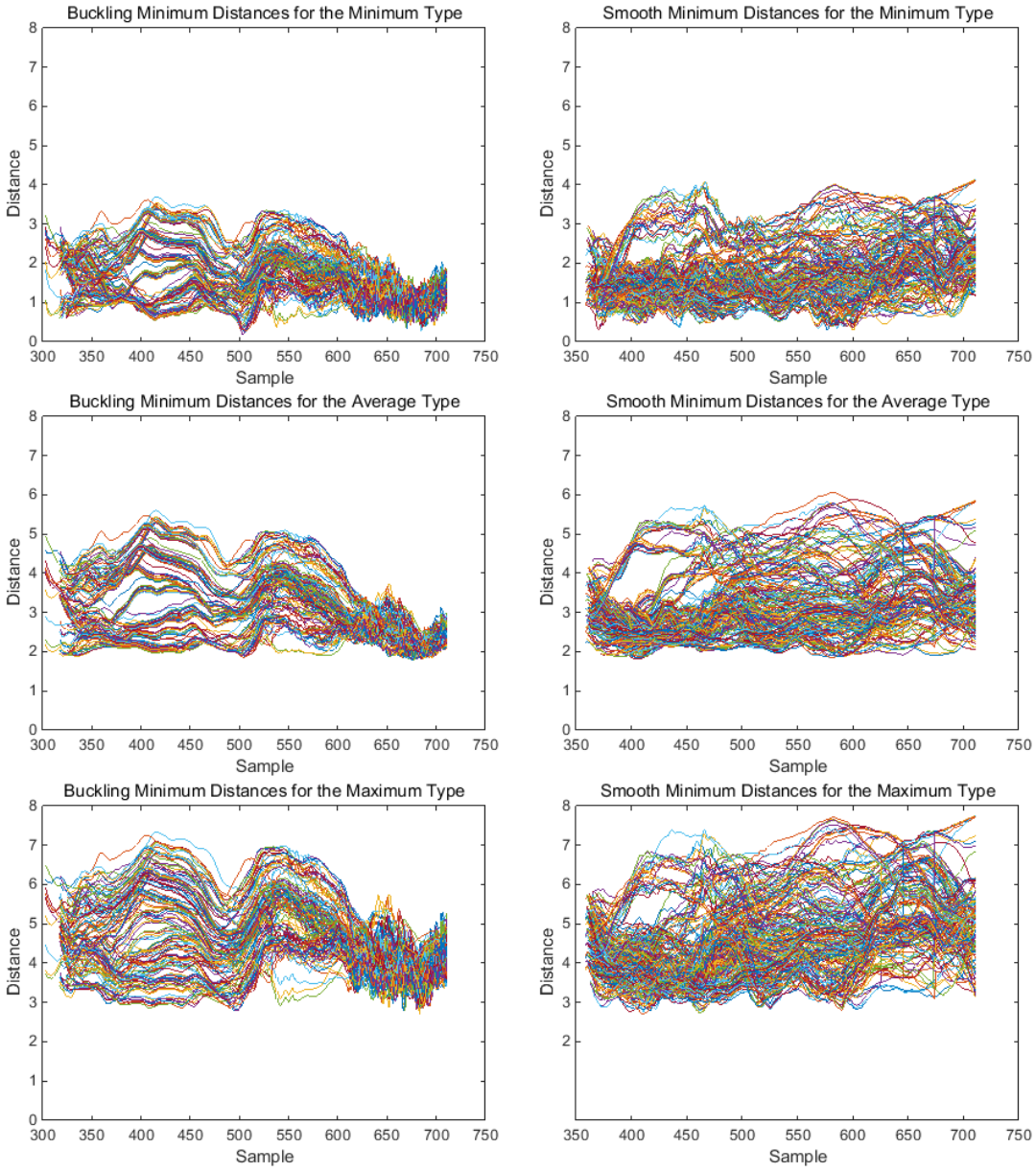

(a) (b)

Figure 6-11: (a) Summary of the Euclidean distance between the buckling insertions testing weight vectors and all the training weight vectors, (b) Summary of the Euclidean distance between the smooth insertions testing weight vectors and all the training weight vectors. The left column indicated the buckling insertions testing weight comparison results and the right column indicated the smooth insertions testing weight comparison results. The first, second and third columns showed the minimum distance for the minimum type, the average type respectively.

In our analysis, each insertion in the test and training set was an independent measurement. Thus, each distance profile of electrode pair (1, 2) in the buckling set

(group 1) was added to every distance profile of electrode pair (15, 16) (group 2). In total, 12*12 = 144 distance profiles of the insertions with buckling pattern were plotted, as shown in Figure 6-11 (a). Similar to the buckling set, 20*12 = 240 smooth distance profiles were generated according to Figure 6-11 (b). The three types of the Euclidean distance: minimum, average and maximum were depicted in Figure 6-11. The minimum Euclidean distance and their associated positions for all the measurements are plotted in Figure 6-12.

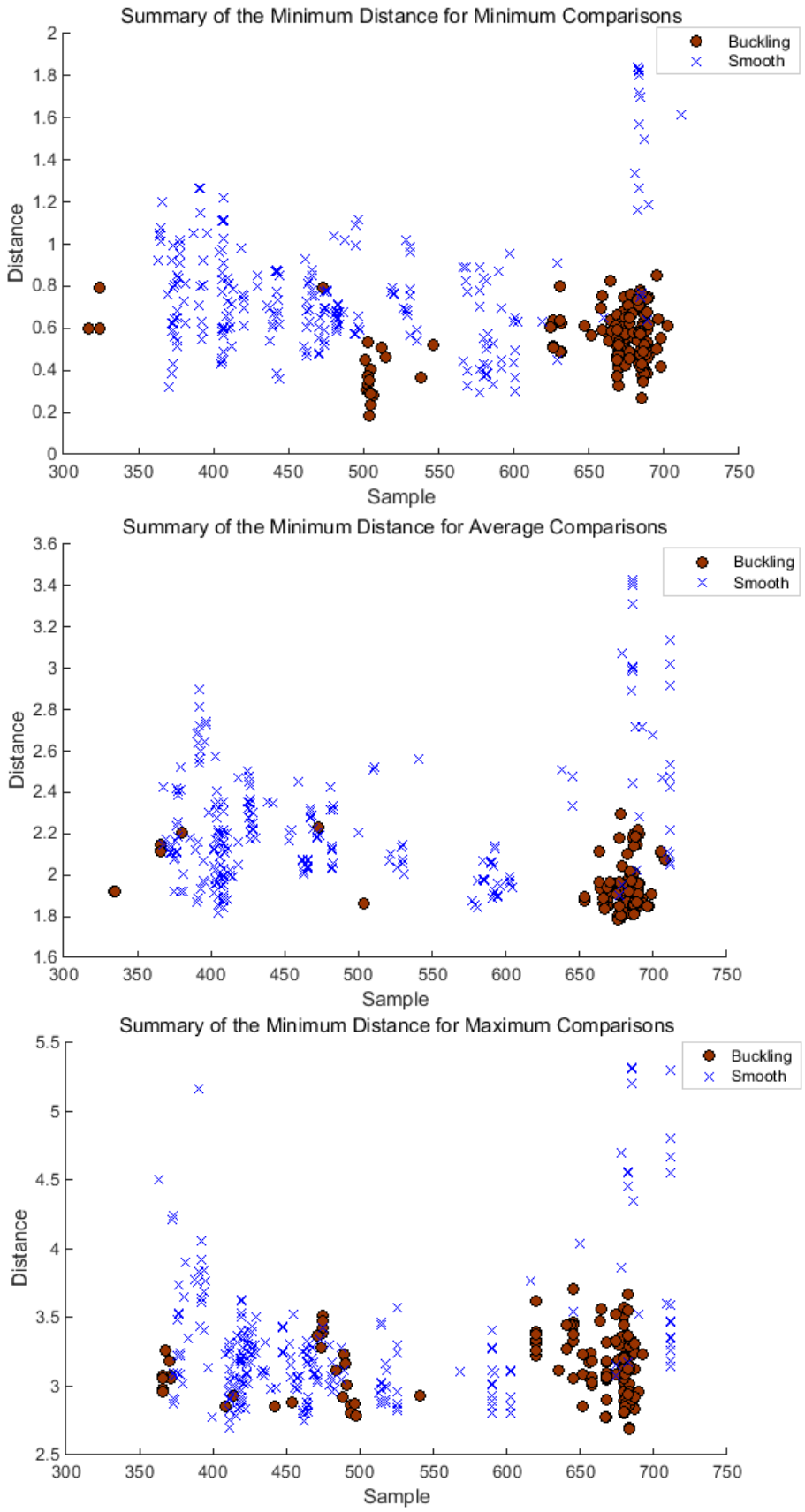

Figure 6-12: Summary of the minimum Euclidean distance of the smooth insertions and buckling feature insertions.

From Figure 6-12, red dots indicated the minimum Euclidean distance of all the buckling insertions, and the blue crosses represented the minimum Euclidean distance of all the smooth insertions. The top plot depicted the minimum Euclidean distance of the minimum comparison type for all measurements. The middle plot showed the minimum Euclidean distance of the average comparison type for all measurements. Lastly, the bottom plot demonstrated the minimum Euclidean distance of the maximum comparison type for all measurements. The x-axis indicated the sample length with respect to time, and the y-axis indicated the minimum Euclidean distance.

In order to discriminate the buckling and smooth insertion pattern, thresholds were appointed to separate the two scenarios: the Euclidean distance was less than the threshold and the distance was larger than or equal to the threshold. If the Euclidean distance was less than the threshold, the testing set would be discriminated as a buckling insertion. If the threshold was larger than or equal to the threshold, the pattern was discriminated as a smooth insertion.

An enumeration method was employed to acquire threshold for minimum, average and maximum comparisons respectively. The threshold value for each type increased from 0 to 5 with an increment 0.01. Accuracies for the buckling and smooth pattern examined by the threshold are portrayed in Figure 6-13.

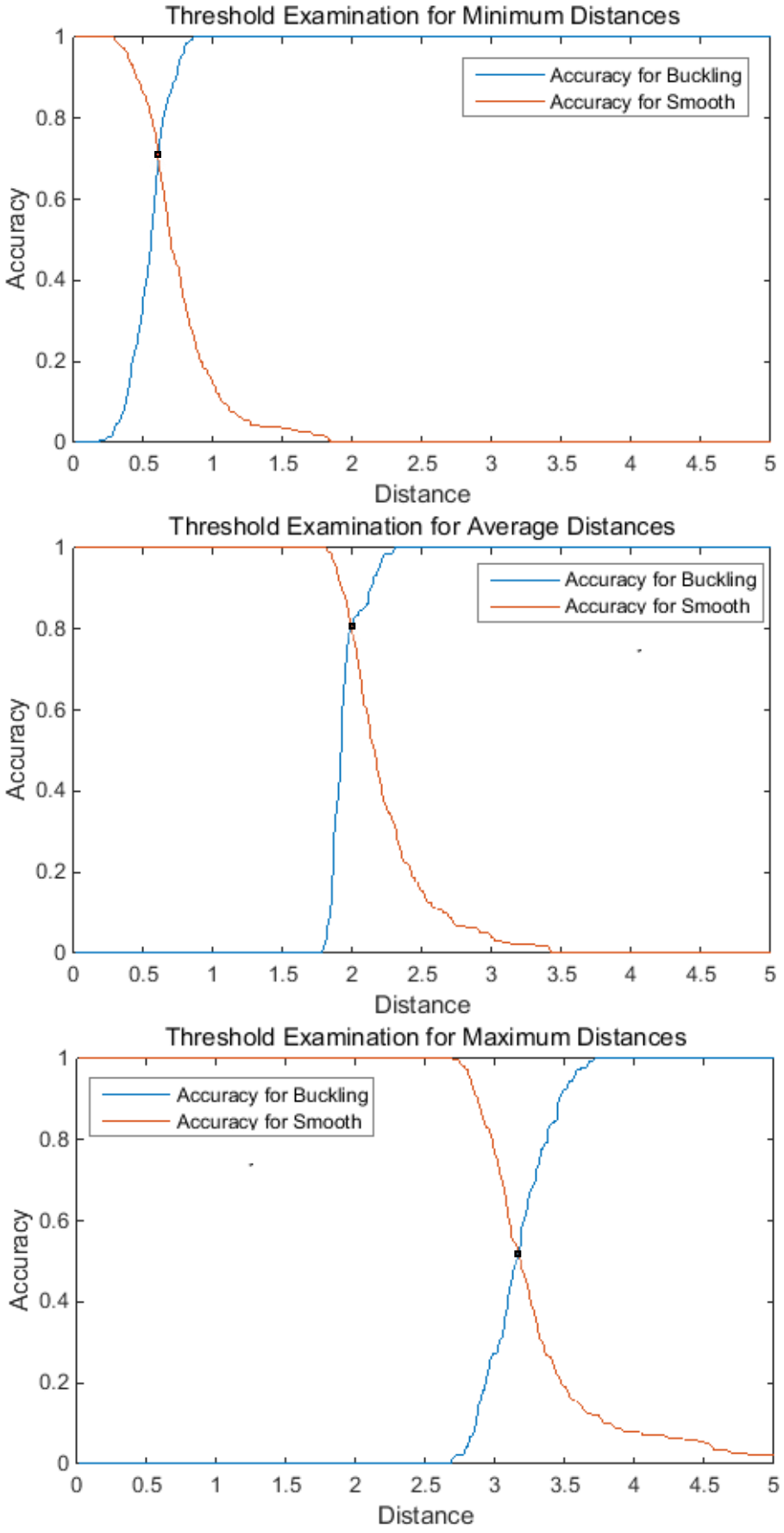

Figure 6-13: Threshold examination for minimum, average and maximum distances.

In Figure 6-13, the threshold for the minimum, average and maximum types were examined. The x-axis indicated the threshold distance and the y-axis indicated the discrimination accuracies. As the threshold distance (*d*) increased, the number of buckling minimum distances below the threshold increased. It resulted in an increase of the buckling pattern discrimination accuracy. Whereas, as the threshold distance increased, the number of smooth minimum distances below the threshold decreased. It led to a decrease of the smooth pattern discrimination accuracy. The point where the two curves meet was appointed as the discrimination threshold distance. Under the examination of the threshold value, the discrimination accuracy for both the buckling pattern and smooth pattern were the highest. The discrimination threshold distance for each comparison types as well as their examination accuracies were detailed in Table 6.2

Table 6.2: Threshold discrimination results for each type.

	Minimum (d =0.61)		Average (d =1.99)		Maximum (d =3.17)	
	Buckling	Smooth	Buckling	Smooth	Buckling	Smooth
Buckling Set	72.92%	27.08%	80.56%	19.44%	52.08%	47.92%
Smooth Set	31.67%	68.33%	19.17%	80.83%	48.33%	51.67%

In Table 6.2, the first section indicated of the three comparison types as well as their threshold distance value. The second section showed the comparison results under the associated distance value.

The first column showed the buckling set and smooth set were under examination. The possibility to discriminate a measurement as buckling or smooth was demonstrated in the results section. For the minimum comparison type, the threshold distance was examined to be d = 0.61. The success rate to discriminate the buckling pattern from the buckling set was 72.92% and the success rate to discriminate the smooth pattern from the smooth set was 68.33%. For the maximum comparison type, the threshold distance was examined to be d = 3.17. The success rate to discriminate the buckling pattern from the buckling set was 52.08% and the success rate to discriminate the

smooth pattern from the smooth set was 51.67%. Lastly, for the average comparison type, the threshold distance was examined to be d = 1.99. The success rate to discriminate the buckling pattern from the buckling set was 80.56% and the success rate to discriminate the smooth pattern from the smooth set was 80.83%.

6.2.4 Conclusion

In conclusion, the discrimination results showed that the average comparison type has the highest discrimination success rate. Therefore, the average type was selected for the buckling pattern during the electrode array insertion process. In this type, the threshold value 1.99 was appointed to examine the buckling pattern with a success rate over 80%.

The Principal Component Analysis (PCA) was employed to discriminate the buckling insertion pattern. 436 capacitance profiles from electrode pair (1, 2), and electrode pair (15, 16) were analysed and compared. Among them, the buckling pattern could be discriminated from the average comparison type. The successful discrimination rate of electrode pair (1, 2) was 84.38%, electrode pair (15, 16) was 79.17%. In account of both the electrode pairs, the threshold distance was examined to be d = 1.99 at the average comparison type. The success rate to discriminate the buckling pattern from the buckling set was 80.56% and the success rate to discriminate the smooth pattern from the smooth set was 80.83%.

6.3 Recognise the Fold-over Feature from an Unknown Insertion

A block diagram shown in Figure 6-14 demonstrated the PCC discrimination process.

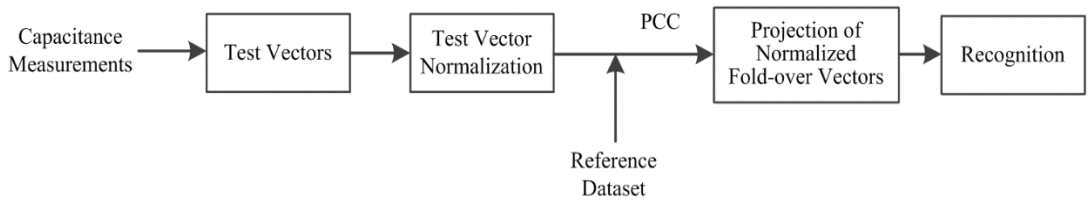

Figure 6-14: Block diagram of discriminating the electrode array fold-over insertion patterns.

The running window method was applied to convert the input experimental measurements to test vectors. Identical to buckling and smooth insertions, before the analysis, all capacitive measurements were converted to the range 0 and 1. This was used to normalise all the capacitive measurements and minimise the environmental noise.

A reference dataset was used to compare with test vectors by the PCC method which was formed by a sharp drop curve and a flat curve. It was applied to compare with the test vectors to identify the similar pattern (drop and flat) in the test vectors. Thus, the size of the reference dataset was same to a test vector, which was 70 x 1. The shape of the reference dataset is located in Figure 6-15.

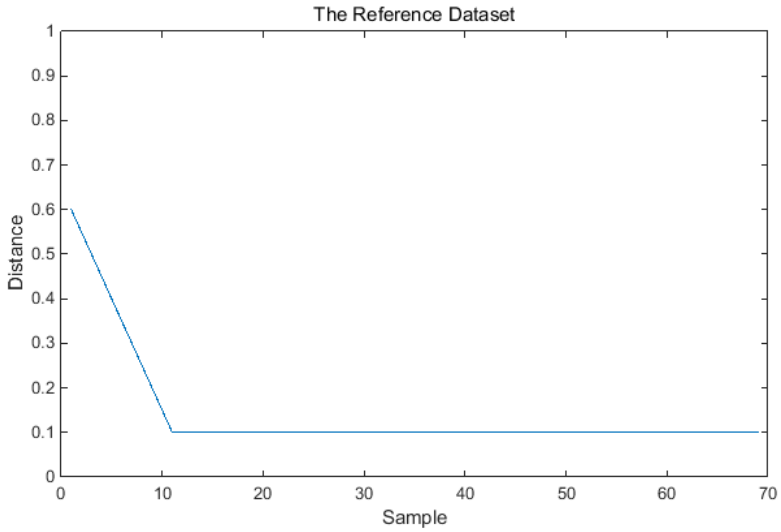

Figure 6-15: A reference dataset, start from distance 0.6 to 0 within 10 sample distance

The x-axis represented the sample length, and the y-axis was the nominalised capacitance measurements. The reference dataset consisted of a dramatical decrease from 0.6 to 0.1 within 10 sample length, and a flat curve 0.1 continues to the end.

After normalising the reference dataset, the PCC method was applied to project the normalised test vectors into the normalised reference dataset. As introduced in Section 5.3, based on the electrode array insertion patterns, test vectors were divided into three subgroups: the fold-over group, the smooth group and the buckling group. The normalised test vectors from each subgroup were compared with the normalised reference dataset by the PCC analysis. The similarity results of the comparisons were presented in Figure 6-16.

The PCC between the Fold-over group and the reference dataset is shown in Figure 6-16(a). The PCC between the Smooth group and the reference dataset is depicted in Figure 6-16(b). The PCC between the Buckling group and the reference dataset is portrayed in Figure 6-16(c). In all of the three figures, the x-axis represented the sample length; the y-axis represented the PCC.

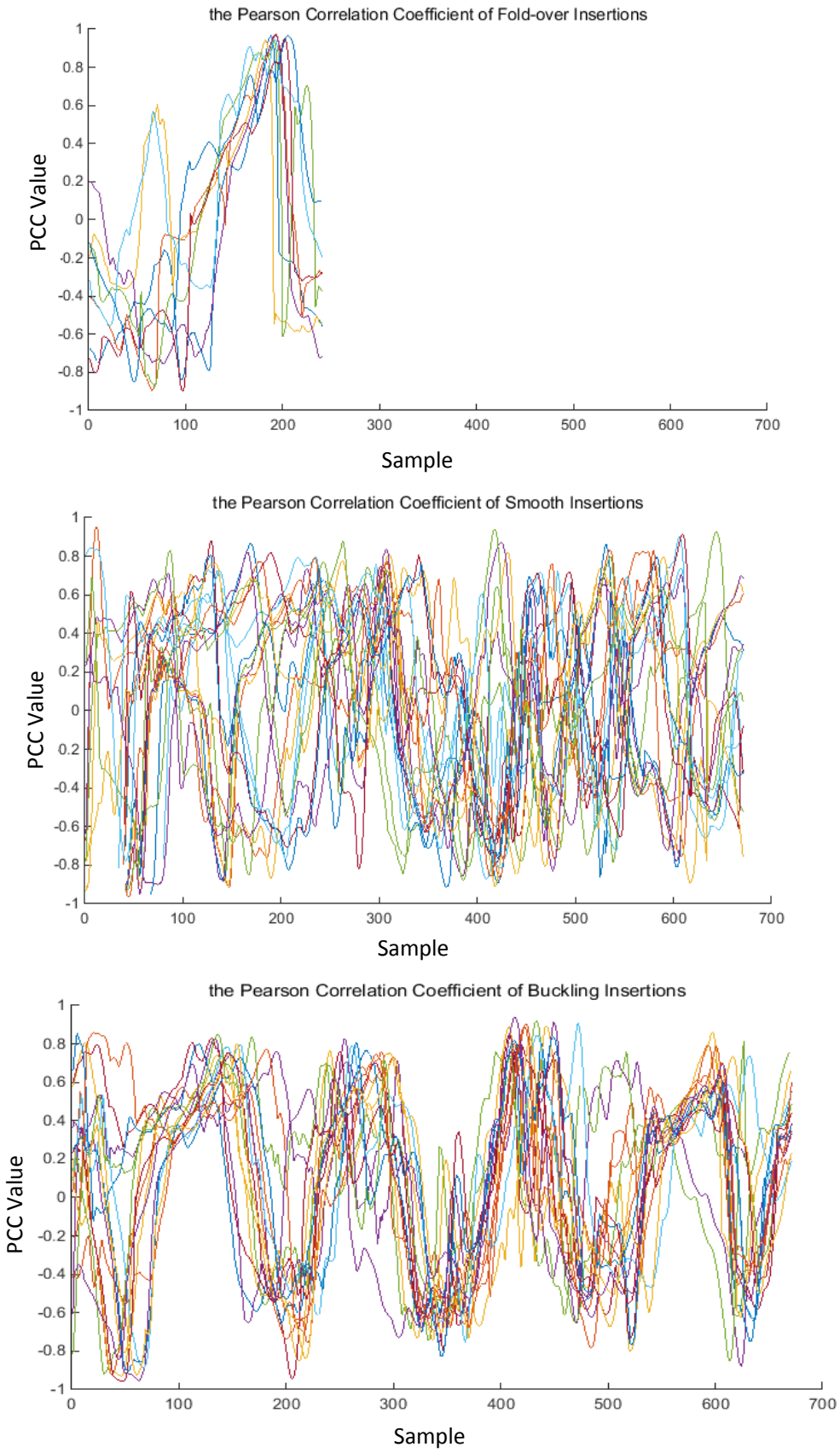

Figure 6-16: The similarity comparison between normalized test vectors and the normalized reference dataset.

Each of folding-over, buckling and smooth insertions was compared with the reference dataset by running window method. The comparison result from each insertion is shown as a single curve in Figure 6.16. The PCC analysis was a measure of the linear correlation between two sets of data [133]. The coefficient was represented by r with a range between -1 to 1 [134]. When $r > 0$, the measured two samples were positively correlated. When $r < 0$, the measured two samples were negatively correlated. When $r = 0$, there were no linear correlations between the samples. A value of $r = 1$ indicated there was a prefect linear correlation between the samples [133]. From the Figure, the PCC coefficient was represented in y axis from -1 to 1.

As each curve indicated an independent single electrode array insertion, the maximum PCC for each insertion and its associated sample position is detailed in Figure 6-17.

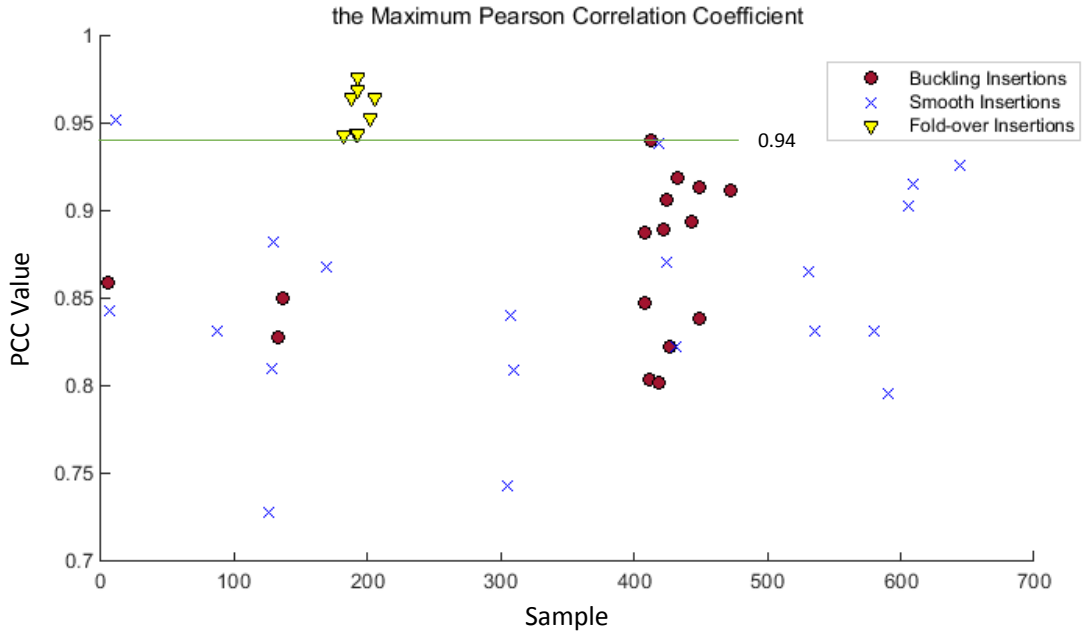

Figure 6-17: The maximum PCC between normalized test vectors and the normalized reference dataset.

In Figure 6-17, the red dots represented the maximum PCC value of the buckling insertion group, the blue crosses represented the maximum PCC value of the smooth insertion group and the yellow triangles represented the maximum PCC value of the fold-over insertion group. All of the maximum PCC values in the fold-over insertion group had an approximate sample length of 200. However, the maximum PCC values in the other two groups were scattered on the x-axis.

Normalised test vectors from the three groups were compared with the reference dataset to find the fold-over pattern. When the maximum PCC value became larger, the test vectors and reference pattern became more similar. When PCC = 1, the test vector matched the reference pattern completely. In our analysis, a threshold could be applied to discriminate the fold-over pattern from the other two patterns.

Similar to the threshold determination method in Section 6.1.5, the number of maximum PCC in the fold-over group above the threshold and number of maximum PCC in buckling and smooth groups below the threshold were summed. The sum results are shown in Figure 6-18.

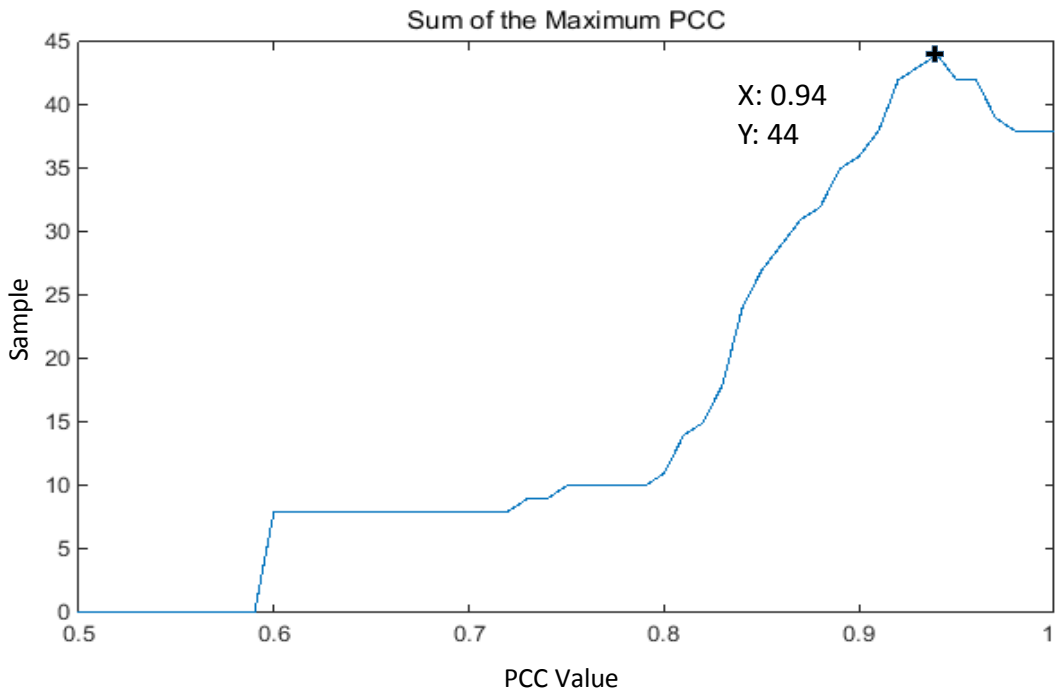

Figure 6-18: Finding the fold-over pattern threshold by summation of the maximum PCC values.

The threshold value to separate the fold-over pattern from the other two patterns was examined from 0.5 to 1, with an increment of 0.01. The number of the maximum PCC in the fold-over group above the threshold and number of the maximum PCC in buckling and smooth groups below the threshold were summed. In Figure 6-18, the x-axis represented the maximum PCC distance value and the y-axis showed the sample length. The peak point indicated the number of maximum PCC summation reached to

the largest. Thus, 0.94 was appointed to be the threshold to separate the fold-over pattern from the buckling and smooth insertion group.

In order to examine the threshold, the value would be applied to the three measurement groups. For the fold-over group, the all 8 fold-over insertions met the examination. For the smooth insertion group, 1 out of 20 failed the examination, with a success rate 95%. For the buckling insertion group, 1 out of 18 failed the examination, with a success rate 94.4%. Overall, the threshold could successfully discriminate 44 out of 46 (8+20+18) insertions, with a success rate of 95.65%.

6.4 Conclusion

In this chapter, the bipolar capacitance experimental results were analysed and three CI electrode array insertion patterns were discriminated. The Principal Component Analysis (PCA) was employed to discriminate the buckling insertion pattern. 436 capacitance profiles from electrode pair (1, 2), and electrode pair (15, 16) were analysed and compared. Among them, the buckling pattern could be discriminated from the average comparison type. The successful discrimination rate of electrode pair (1, 2) was 84.38%, electrode pair (15, 16) was 79.17%. In account of both the electrode pairs, the threshold distance was examined to be d = 1.99 at the average comparison type. The success rate to discriminate the buckling pattern from the buckling set was 80.56% and the success rate to discriminate the smooth pattern from the smooth set was 80.83%.

The Pearson Correlation Coefficient (PCC) was used to discriminate the fold-over insertion pattern. The running window method was utilised to divide all the insertion results to examine datasets. These examined datasets were compared with the reference dataset by the PCC method. The result threshold of 0.94 demonstrated that for the fold-over group, all 8 fold-over insertions met the examination criteria. For the smooth insertion group, 1 out of 20 failed the examination, with a success rate of 95%. For the buckling insertion group, 1 out of 18 failed the examination, with a success rate of 94.4%. Overall, the threshold successfully discriminated 44 out of 46 insertions, with a success rate of 95.65%.

Chapter 7

Multi-Channel Capacitive Sensing Method

The results from the present study indicated that bipolar capacitance measured correlate to the electrode array movements. Three insertion patterns were discriminated based on single pair of electrodes measurements. Utilising multiple pairs of electrodes at the same time to predict the array's motion was impossible. The reason for this was that when measuring multiple pairs of electrodes the voltages applied to them influenced each other. Measurement results by this method were unacceptable. In order to solve the problem, a multi-channel switch board was developed to measure one pair of electrodes at one time. The methodology and results would be detailed in the Section 7.2.

The arrangement of this chapter was organised as follows. Section 7.1 introduced the multiple channel switch board. Section 7.2 presented the intermittent and continuous capacitive measurements using the switch channel board. Lastly, Section 7.3 concluded the chapter.

7.1 The Multiple Channel Switch Board

As introduced in Section 3.5.2, a circuit board was developed to switch between multiple channels. Each channel was connected to two electrodes for measurement. The circuit board and its circuit diagram are shown in Figure 7-1.

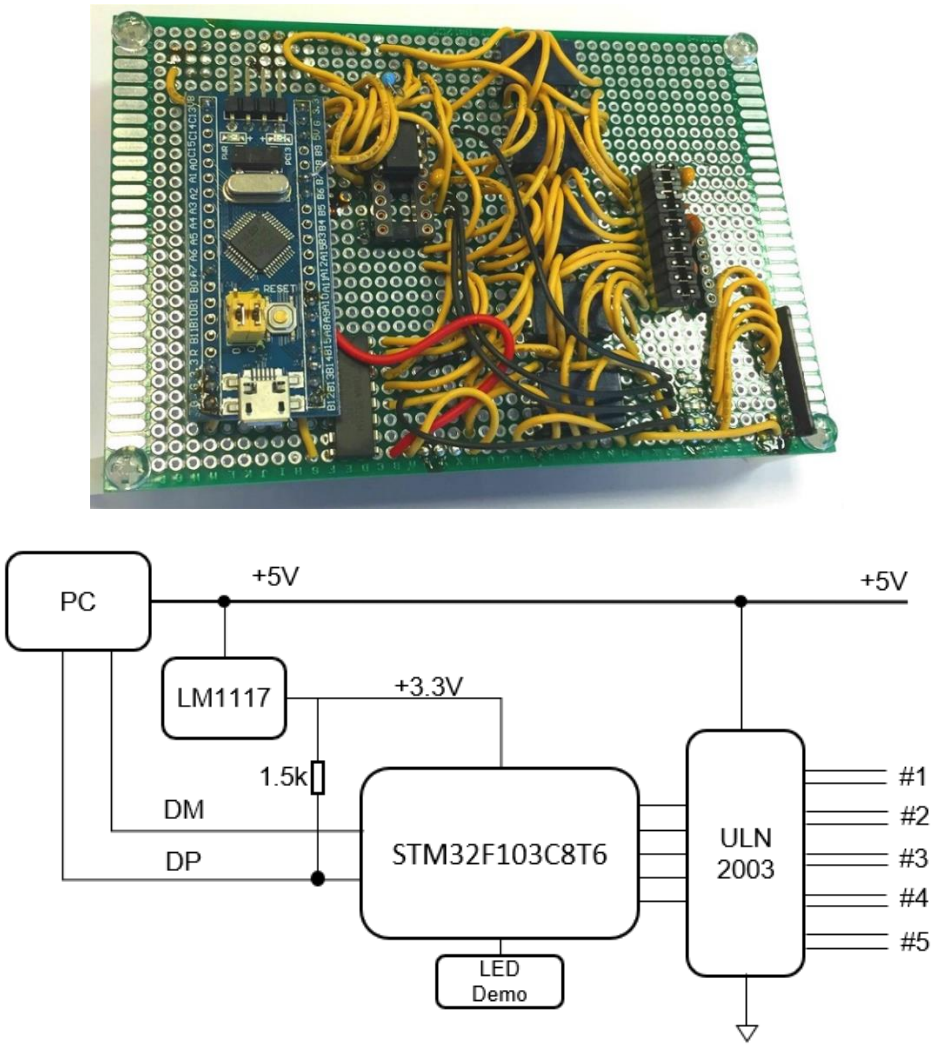

Figure 7-1: The multiple channel switch board and circuit diagram. The channel switchboard was built based on a microcontroller (STM32F103C8T6) and a transistor array (ULN2003). The microcontroller incorporated ARM® Cortex®-M3 32-bit RISC core and it operated at 72 MHz frequency [116].

The microcontroller was powered by the PC and worked from 2.0 V to 3.6 V. The device was recognized as a virtual port after connecting to the PC through a mini type USB. Commands were sent to the microcontroller to select output ports' on and off state by a serial port communication software. Each capacitor meter had two measuring ports and connected to an output port from the microcontroller. By controlling duration of the on and off states of 10 output ports, capacitor meters could

be programmed to measure or standby. The function provided a solution to intermittently measure electrodes capacitance.

The board was used for the preliminary research of the capacitance measurement switching function. I proposed a solution to switch the measurement by controlling output signal to an array. The board was designed and made with the help from Mr Yifan Zhang. He also did tests of the board to realize that the switching function was functioning within requirements.

The microcontroller (STM32F103C8T6) of the switch board incorporated ARM® Cortex®-M3 32-bit RISC core and it operated at 72 MHz frequency [116]. The device worked from 2.0 V to 3.6 V, supplied by the PC connected to it. The microcontroller was programmed to control the on and off states of five transistor arrays. Each transistor array had two output wires. By sending commands to the microcontroller, each channel was switched to be 'ON' and 'OFF'. A mini USB cable was utilised to communicate between the circuit board and the PC. The embedded programming environment was ARMKeil - MDK 5.17 [117] and a serial port debug tool SSCOM was used to send commands to the microcontroller. After establishing communications between them, commands 's30500005099d' was sent to the microcontroller, where s3 indicated the programming state was 3, 0500 represented the channel 'ON' time was 5000ms, 0050 represented the switching time was 500 ms, and 99d showed the programme would be executed 99 times. With this method, each channel was switched 'ON' 500ms, for measuring and then switched 'OFF'. There was a gap delay of 50ms between switching channels. The execution of the programme 99 times allowed sufficient time to conduct all measurements.

7.2 Capacitive Measurements Using the Switch Channel Board

From the investigations in Section 5.2.5, electrodes 1-2, 3-4, and 15-16 were selected to implement the measurements. Electrodes 1 and 2 were connected to channel 1, electrodes 3 and 4 were connected to channel 2, and electrodes 15 and 16 were connected to channel 3. Setup of the capacitive measurements using the switch channel board is shown in Figure 3-17.

The goal of the first experiment was to examine the capacitive measurements of the electrode array intermittent insertions by the switching board. In the experiments, the electrode array inserted into the cochlear model intermittently from 0 mm with step increments of 1mm. At each increment, the array stopped for 5 seconds and the capacitance between electrodes 1-2, electrodes 3-4 and electrodes 15-16 were measured through the switching board. The insertion length was 36mm and the average capacitance resulted at each increment are plotted with the continuous insertion results in Figure 7-2.

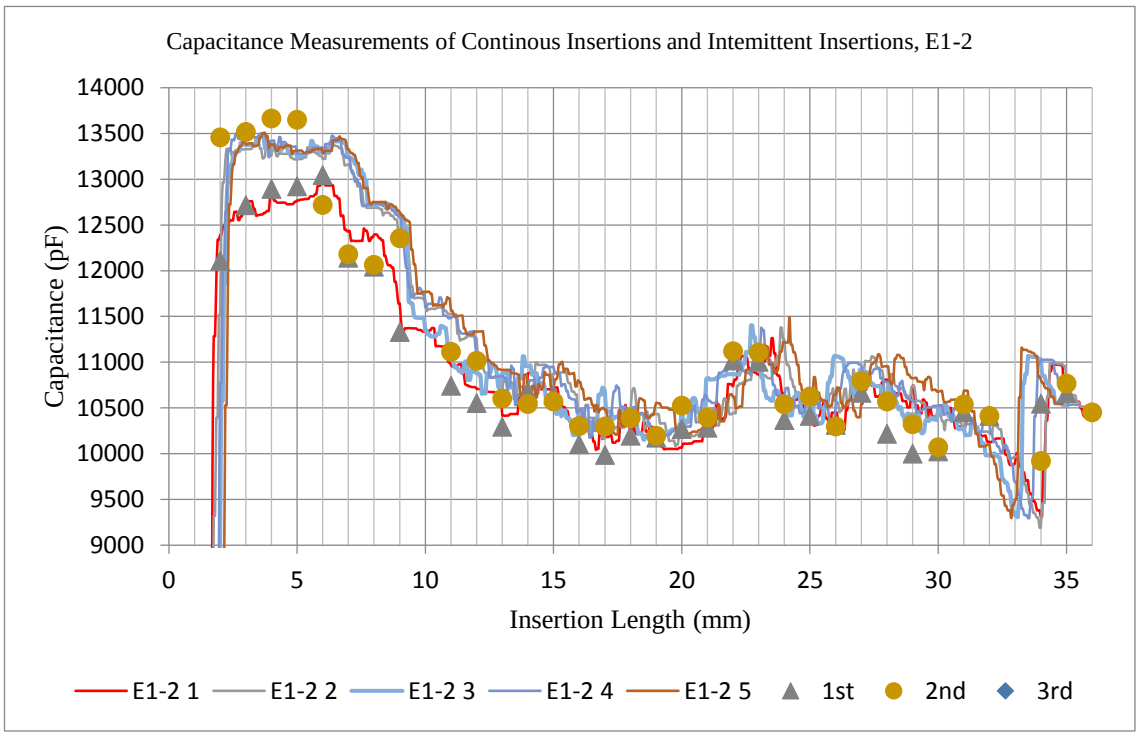

(a)

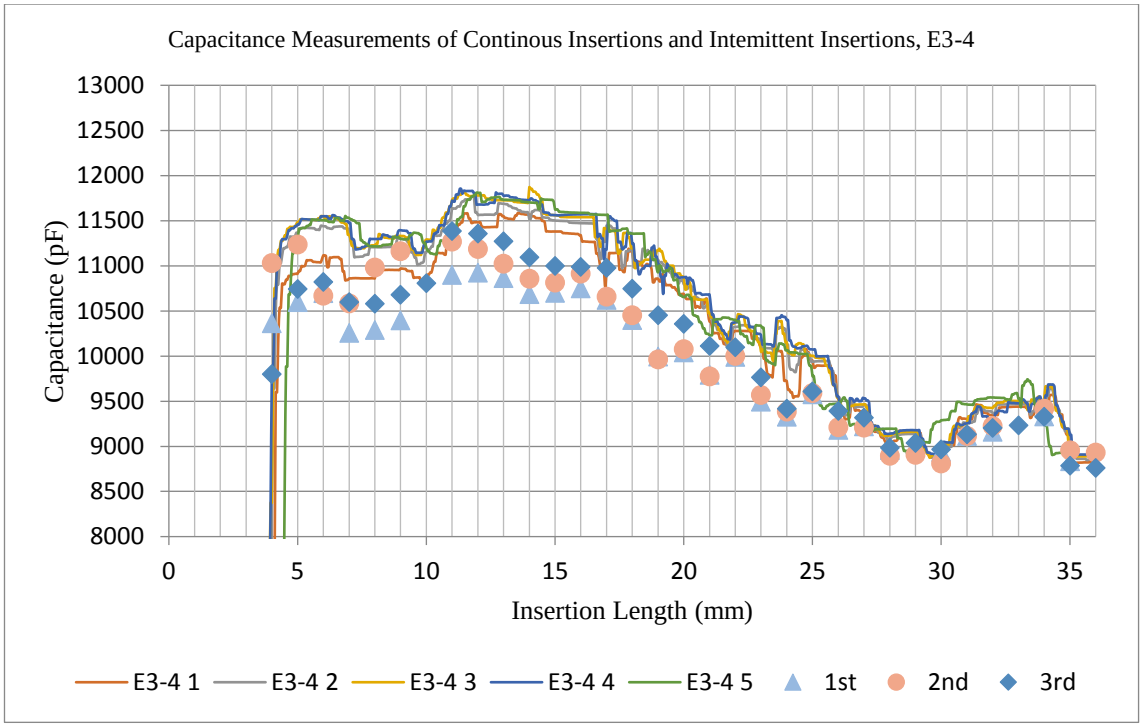

(b)

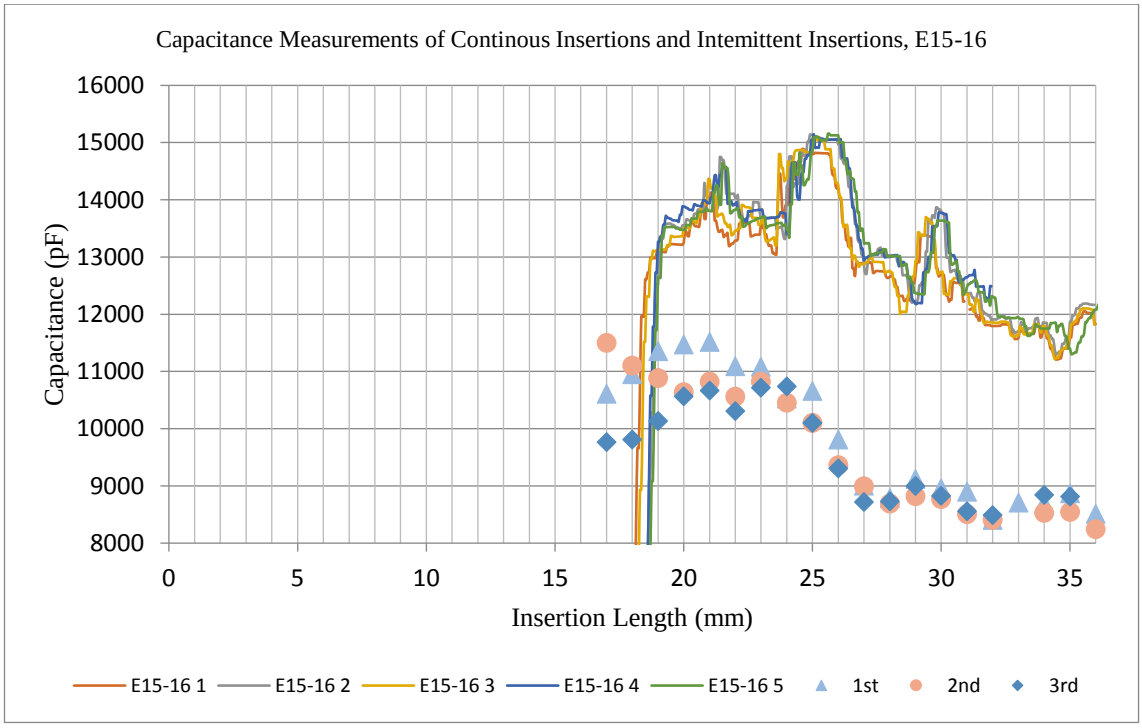

(c)

Figure 7-2: Capacitance measurement results of intermittent insertions and smooth insertions of the (a) electrodes 1-2, (b) electrodes 3-4 and (c) electrodes 15-16. The x-axis showed the insertion length up to 36mm; and the y-axis demonstrated the capacitance measured in picofarads (pF). In each figure, five independent continuous insertions were implemented for comparisons. The smooth insertions were shown as continuous curves. The three intermittent insertions at each increment were shown as triangular (first), dot (second) and diamond (third).

Within Figure 7-2, the capacitive measurement results of intermittent insertions and continuous insertions were plotted. The record frequency of the capacitor meter was 2 Hz. The array stopped at each position for 5 seconds. Therefore, 10 data were recorded at each increment position. However, the first two data were neglected due to inconsistency of the meter. The remaining 8 data were averaged and plotted.

In Figure 7-2 (a), the overall trend of the measurement results of the intermittent insertions matched that of the smooth insertions. Before 20mm, the capacitance gradually fell from the peak, which could also be identified by intermittent insertion results. From 20mm to the end, the capacitance measurements fluctuated largely. The peaks of the fluctuations were recognised while the values between each peak were not detected. Similar to Figure 7-2 (a), the measurements trend in Figure 7-2 (b) were able to be detected. The capacitance fell and rose from 10mm to 34mm were identified by the intermittent insertion measurement results. However, in Figure 7-2 (c), the measurements between electrodes 15 and 16, the capacitance measured by intermittent insertion was much less than the continuous insertions. The outcome could be explained by the higher force applied between the electrodes and the cochlear inner wall during the intermittent insertions. The overall trend of the measurement results of the intermittent insertions was detected. But the capacitance peaks and fluctuations of the smooth insertion measurements could not be identified by the intermittent insertion measurements.

Based on the intermittent insertions results, the trend of the capacitance measured matched that of the continuous insertions. Other experiments were conducted to evaluate the performance of the switching board when applied to the array continuous insertions. For the switching board, three channels were utilised and the measuring time for each channel was 5s, with the switching time being 500ms. Results of the capacitance measured with and without the switching board are depicted in Figure 7-3.

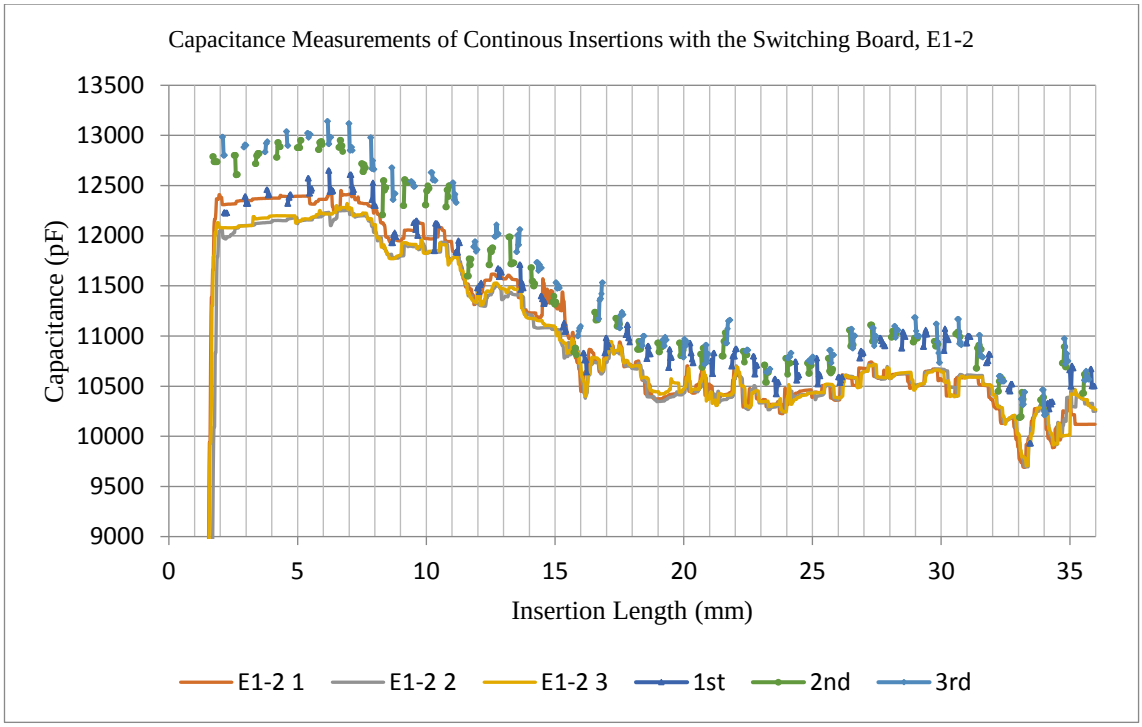
Capacitance Measurements of Continous Insertions with the Switching Board, E1-2
Capacitance (pF)
13500
13000
12500
12000
11500
11000
10500
10000
9500
9000
0
5
10
15
20
25
30
35
Insertion Length (mm)
E1-2 1
E1-2 2
E1-2 3
1st
2nd
3rd

(a)

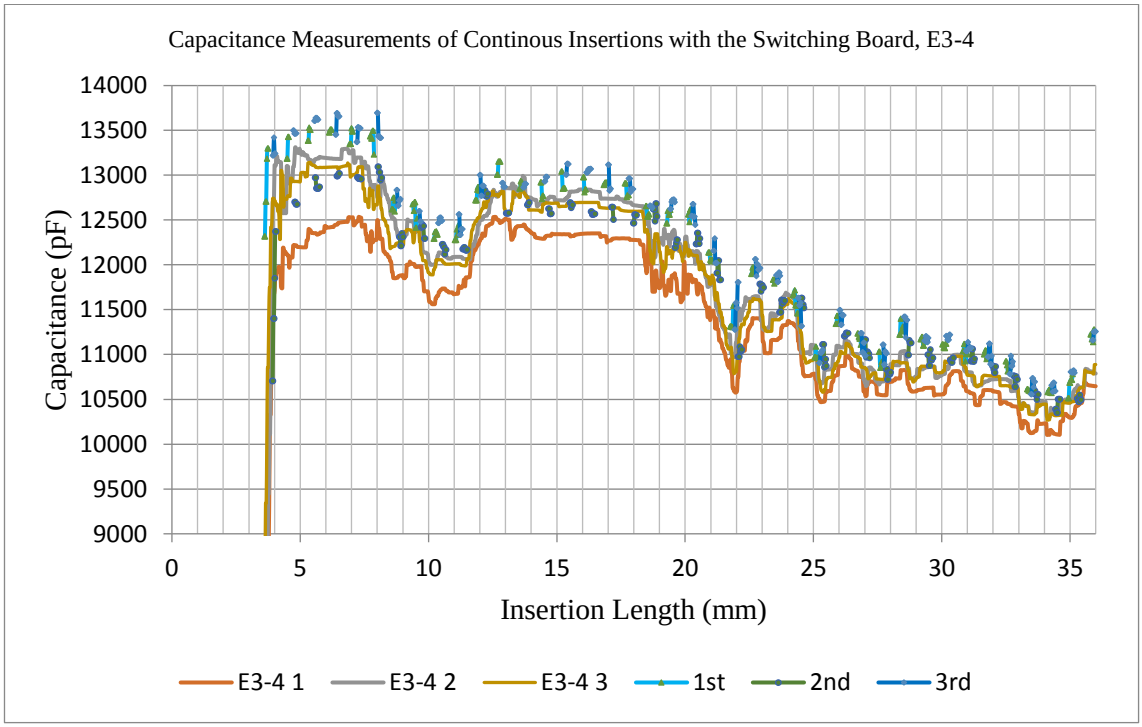
Capacitance Measurements of Continous Insertions with the Switching Board, E3-4
Capacitance (pF)
14000
13500
13000
12500
12000
11500
11000
10500
10000
9500
9000
0
5
10
15
20
25
30
35
Insertion Length (mm)
E3-4 1
E3-4 2
E3-4 3
1st
2nd
3rd

(b)

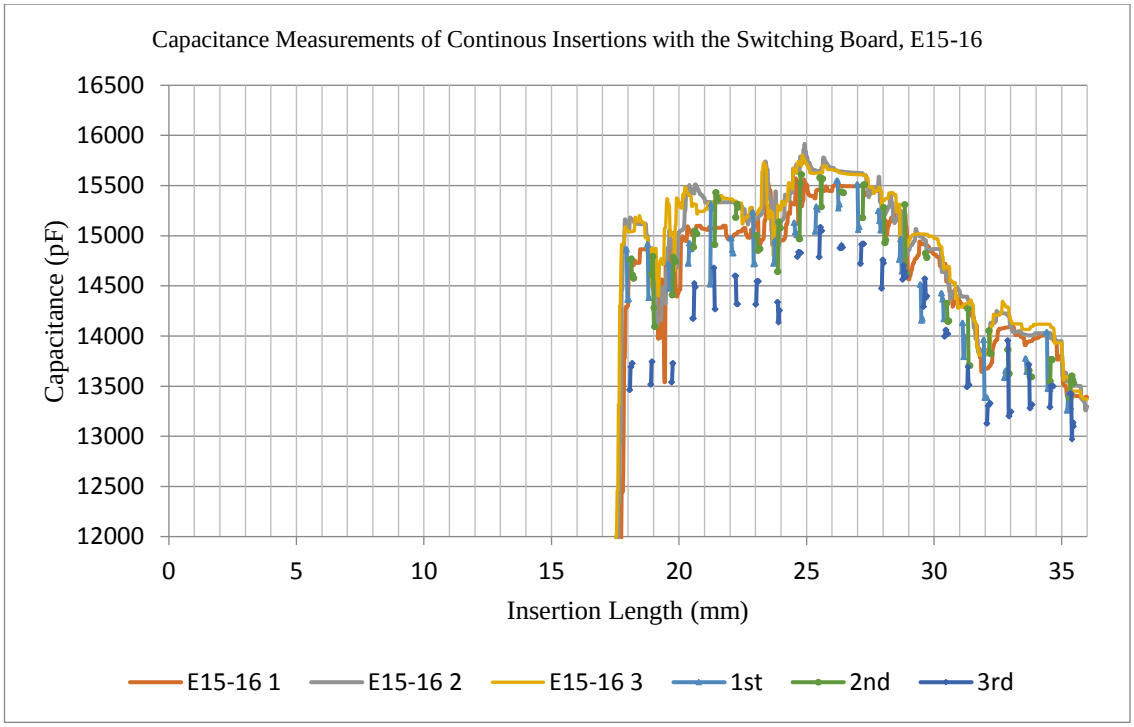

(c)

Figure 7-3: Capacitance measurement results of continuous insertions with and without the switching board of the (a) electrodes 1-2, (b) electrodes 3-4 and (c) electrodes 15-16. The x-axis showed the insertion length in mm, and the y-axis showed the capacitance measured in pF. In each figure, three independent smooth continuous insertions and three continuous insertions using the switching board were compared.

In Figure 7-3, as with the intermittent insertion experiments, the insertion length was up to 36 mm with a constant insertion speed of 0.1mm/s. The record frequency of the capacitor meter was 2 Hz. Continuous insertions without the switching board were shown as continuous curves, while insertions with the switching board were marked as the first, second, and third intermittent curves.

In Figure 7-3 (a), the overall trend of the measurement results of insertions with the switching board matched that of the insertions without the board. The capacitance gradual reduction event was detected by using the switching board. Between the insertion length of 32 mm and 35 mm, the capacitance falling behaviour was also identified by applying the switching board.

In Figure 7-3 (b), capacitance between electrodes 3 and 4 was measured. The capacitance falls and rose from 7 mm and 12 mm were identified by using the

switching board. After 20 mm, the peaks of the capacitance fluctuations were recognised while values between each peak were not detected.

However, in Figure 7-3 (c), the measurements between electrodes 15 and 16, capacitance measured by applying the switching boards were inconsistent. Values of the capacitance measured using the switching board varied greatly and were unstable throughout the insertions. Even the rise of the capacitance from position 18mm to 26mm could not be identified by the switching board due to the variations. Although the capacitance falling event from 26 mm to 36 mm was detected by applying the board, details of the fluctuations were completely lost. Thus, measurements between electrodes 15 and 16 with the switching board were not adequate in discriminating the three insertion patterns.

7.3 Conclusion

In order to detect more signals during the electrode array insertion operation, a channel switching board was developed. The board was able to help record the capacitance between electrodes 1 and 2; 3 and 4; and 15 and 16 by switching the measuring channels. Functionalities of the switching board had been evaluated in this chapter.

Two sets of experiments were conducted using the board. The first set of experiments compared the capacitance measured of the intermittent and smooth insertions. For intermittent insertions, the array was inserted into the model in increments of 1mm. The capacitive measurement results of intermittent insertions were plotted on the same graph with the smooth insertions for comparisons. The results demonstrated that the overall capacitance trend of the intermittent insertions of electrodes 1-2 and 3-4 matched that of the smooth insertions. The capacitance measurement results of electrodes 15-16 were much less than the continuous insertions.

The other set of experiments investigated the capacitance measurements of continuous insertions with and without the switching board. Capacitance results from the two types of recording method were plotted in the same graph for comparison. The results showed that the overall capacitance trend of electrodes 1-2 and 3-4 continuous insertions with and without the switching board were similar. However, the capacitive

measurements using the switching boards between electrodes 15 and 16 were inconsistent. Thus, electrodes 15 and 16 with the switching board were not adequate in sensing the electrode array behaviours.

In both of the experiment sets, the overall trend of the capacitance results using the switching aboard was detected. The continuous capacitive measurement system using the switching aboard was feasible to record the capacitance as expected. But the capacitance peaks and fluctuations of the continuous insertions could not be identified by the method. The disadvantage was that the recording frequency was 2Hz due to the restrictions of the meter. Only 2 data samples could be recorded when the array was inserted at 0.1mm, which was insufficient. It could be improved by developing a quick, precise, and manageable LCR meter. A meter with a higher recording frequency would detect more data during the electrode array insertion. Furthermore, development could be applied in establishing an optimal insertion model, classifying particular failure patterns and characterizing the array position.

Chapter 8

Conclusion

8.1 Summary of Findings

The aim of this thesis was to investigate an electrode capacitive sensing system for an electrode array feed into the cochlea. Electrode capacitive information from the array during the insertion was gathered and analysed to discriminate the three insertion patterns (smooth, buckling, and fold-over). For this purpose, a mathematical model for the cochlear electrode array first contact to the cochlear wall was created. It helped analyse the mechanical behaviour of an inserting electrode array. Based on the insertion force, the efforts of speed, position and trajectory angle of the electrode array insertion into a plastic cochlear model had been investigated. The results demonstrated that the array had to be inserted closely to the inner track of the model with a low insertion speed 0.1mm/s to avoid the buckling and damage. Force profiles for the three insertion patterns had been evaluated. The results revealed that the insertion force was useful in designing CI arrays and insertion strategies. It was able to record the contact force between the array and cochlear inner wall at first around. The average force profile was similar to the results in some literature review.

Based on analysing the insertion force profile, the best insertion tragedy was proposed. The results demonstrated that the array had to be inserted close to the inner track with a low insertion speed of 0.1 mm/s selected to avoid buckling and damage.

The insertion force could not identify the position where the buckling or fold-over pattern occurred. The force measured was the overall insertion force applied at the entry point of the cochlear model. Even whether the insertion was smooth or which faulty pattern occurred could be recognized, it was impossible to identify where the error took place. The process was like inserting an array into a black box that surgeons would know when errors happened, but could not identify the exact location of the errors. During the electrode array insertion process, behaviours of the array inside of the cochlea remained unknown for surgeons. Besides, in all of the force profiles, the force deviation was much larger than a standard value. The deviation value changed from a range between 20% and 30%. This suggested that there were significant differences between each individual insertion. The differences and deviations made CI array insertion pattern discrimination lack of accuracy from the insertion force. In account for the unknown location information, small force variations and large deviations, the force sensing method was not sufficient in discrimination of the faulty patterns.

An electrodes bipolar capacitive sensing system was proposed to fulfil the research gap. The method was found highly sensitive at conducting solutions. Thus, it was a useful method to detect the CI electrode array behaviour inside of the cochlear model. However, the sensing method was easily affected by environments parameters, array materials and sensing methods. Reasons and modelling for the bipolar electrodes' capacitance variation when filling with conducting solutions were investigated. The results demonstrated that, the capacitance value measured was formed not only by the electrodes' capacitance, but also by the capacitance due to the liquid conductivity. Other parameters such as material permittivity, electrodes distance, and the vertical tensile force at the tip of the electrode array were examined to have restricted changes to the capacitance measured. During the electrode array insertions, the capacitance measured was found violating the basic capacitance theorem. This was due to the force applied to the top of electrodes was also a domination cause to capacitance variations. With the increasing of the applied force, the capacitance measured decreases correspondingly. The results demonstrated that the electrode pair (1, 2), (3, 4), and (15,

16) had a relative linear relationship between the force and capacitance. Thus, they were selected to conduct the further insertion experiments.

By analysing the bipolar capacitance experimental results, three CI electrode array insertion patterns were discriminated. The Principal Component Analysis (PCA) was employed to discriminate the buckling insertion pattern. 436 capacitance profiles from electrode pair (1, 2), and electrode pair (15, 16) were analysed and compared. Among them, the buckling pattern could be discriminated from the average comparison type. The successful discrimination rate of electrode pair (1, 2) was 84.38%, electrode pair (15, 16) was 79.17%. In account of both the electrode pairs, the threshold distance was examined to be d = 1.99 at the average comparison type. The success rate to discriminate the buckling pattern from the buckling set was 80.56% and the success rate to discriminate the smooth pattern from the smooth set was 80.83%.

In order to detect more signals during the electrode array insertion operation, a channel switching board was developed. The board was able to help record the capacitance between electrode pair (1, 2), (3, 4), and (15, 16) during a single insertion. Two sets of experiments were conducted using the board. The results demonstrated that the overall trend of the capacitance results using the switching aboard was detected. The continuous capacitive measurement system using the switching aboard was feasible to record the capacitance as expected. But the capacitance peaks and fluctuations of the continuous insertions could not be identified.

8.2 Limitations of the Research

In the thesis, a cochlear implant electrode array was robotically inserted into an artificial model. The model was 3D printed with a 2D inner path and was twice the average size of a real cochlea. The enlarged model helped observe and investigate the electrode array behaviours inside of the model. However, the longer and 2D insertion path might significantly affect signals measured. The methodology was based on an assumption that capacitive signals trending was similar between an actual cochlear size and the enlarged model.

The CI array insertion force measured in the model proved the assumption was reasonable by comparing to others' results in literature review. The average force measured was similar both in the trending shape and magnitude. But the force measured varied significantly from individual insertions and could not detect the CI array behaviours inside the cochlea. As the problem was also mentioned by others in literature review, further investigations could be addressed on the electrode array starting position and its stiffness. Model inner path friction force was another factor that should be investigated in further as the friction factor was different between 3D printed models and a real cochlea. The factor was often neglected by scientists, as lubricating oil was added to the cavity to help the array insertion in past experiments.

In order to investigate the CI electrode array behaviour inside of a cochlea, a force model was developed. However, the model could only simulate the array deflection less than 90 degree in two dimensional. Large array deflection would involve highly non-linear analysis and could not use the model. In a real CI electrode array surgery, the insertion depth could up to 290 degree in three dimensional. Hence, the model was useful in simulating the first contact between the array tip and cochlear inner wall. In addition, the stiffness of the electrode array was soft. The force conduction mechanism might be different and the force model should be improved based on the array with low stiffness and large deflection.

To minimize the trauma induced by electrode array insertions, an electrode capacitive sensing method was proposed to discriminate among certain insertion failure patterns. Theoretical model and experimental results revealed that the capacitance value was produced not only by the electrodes capacitance, but also by the capacitance owing to

liquid conductivity. The LCR meter reading was greatly affected by solution conductivity variations.

Although in experiments, the environmental parameters were controlled and investigated, other parameters such as solution temperature, solution oxygen content, air bubbles, solution pressure and array gravity, volume and buoyancy were assumed to be constant. Among them, solution temperature had the biggest influence to the results. As in human inner ear, the temperature of perilymph was higher than room temperature, capacitive measurements based on room temperature would be different. Limitations of the research were that all measuring and threshold results were mainly based on analysing of experimental results.

Lastly, all of the insertions were conducted by one electrode array. The limitation was due to the cochlear implant company only supplied two electrode arrays and I broke one in experiment. All measurement results were recorded and analysed based on electrodes on this array. Although the electrode array was standard and for clinical use, materials and size of electrodes manufactured from different types of arrays would affect the capacitance readings.

8.3 Further Improvements

A force model of the electrode array deflections was developed. The model could be extended to simulate the whole insertion process to a three dimensional cochlea. The contact force between the electrode array and the cochlear wall would be modelled to explain the capacitance variations in detail.

For the LCR meter, the recording frequency was only 2 Hz due to the limitations. Only 2 data samples could be recorded when the array was inserted at 0.1 mm, which was insufficient. It could be improved by developing a quick, precise, and manageable LCR meter. A meter with a higher recording frequency would detect more data during the electrode array insertion. Furthermore, a real-time communication between the meter and the PC could be established. It enabled the signal discrimination process in real-time and demonstrated on screen whether the array had been placed correctly during the insertion process. This would help to maximize the performance of cochlear implant and reduce trauma of the insertion.

The switching board could be integrated with the meter to have more precise measurements. Based on the results, further development could be applied in establishing an optimal insertion model, classifying particular failure patterns and characterizing the array position.

Appendix 1: Published Papers

Capacitance Measures during Cochlear Implants Electrode Array Positioning

Lei Hou
Brunel Institute for Bioengineering
Brunel University
London, UB8 3PH. The UK
lei.hou@brunel.ac.uk

Xinli Du
Brunel Institute for Bioengineering
Brunel University
London, UB8 3PH. The UK
xinli.du@brunel.ac.uk

Nikolaos V. Boulgouris
Howell Building 208
Brunel University
London, UB8 3PH. The UK
nikolaos.boulgouris@brunel.ac.uk

ABSTRACT

During cochlear implant surgery, atraumatic electrode array insertion was considered to be a crucial step. However, during cochlear implantation, the mechanical behavior of an electrode array inside the cochlea was not known. The behavior of an electrode array inside of the cochlea was hardly diagnosed by normal methods. In this study, the mechanical behavior of the cochlear implant (CI) electrode array was studied. A CI electrode array capacitance sensor system was proposed. It was able to automatically determine the array position as a result of the capacitance variations. Instead of applying sensors to the electrode array, capacitance information from the electrodes would be gathered and analyzed. Results reveal that this sensing method was capable of recognizing electrodes' positions when fed into a pre-shaped model.

CCS Concepts

• Applied computing → Life and medical sciences → Health care information systems.

INTRODUCTION

Currently, over 80,000 cochlear implants were applied in patients. Cochlear implant devices were approved for adults in 1985 and for children in 1990 by the Food and Drug administration [1]. Minimally invasive techniques were applied in the cochlear implant surgery that includes the entrance to the inner ear via cochleostomy to maximize the hearing preservation. There were several reasons for minimally invasive to become a trend for cochlear implant technology. Firstly, cochlear implantation surgery had been proved to have benefits in a growing number of patients. Also, the size of the cochlear implant device had been reduced significantly and it would be further reduced in the future. Lastly, hearing preservation becomes possible because of the insertion of short and standard electrode length to the cochlea [1].

Although the process of cochlear insertion has many procedures and variations, the insertion process was still the crucial step. Many reasons may result in poor cochlear implant function and poor outcomes such as the suboptimal or even improperly insertion of electrode or damaged electrode.

The cochlear array insertion requires the facial recess approach, the first step was to visualize and perform the facial recess by thinning the posterior external auditory canal [2]. During the cochleostomy, the computerized tomography method can be applied to warn the surgeons to the facial nerve. This cochleostomy was created by using a 1.0 – 1.5mm diamond burr around the round window membrane and the size depends on the electrode choice and insertion tool used [3]. In general, the receiver should be fixed before the insertion of the cochlear implant electrode that would avoid the extrusion or movement of a perfectly placed electrode array. The insertion of electrode should be attempted to insert the entire array to the inside of cochleostomy or until feeling significant resistance. However it was essential to avoid the excessive force to kink and damage both to the cochlea and the electrode tool.

There were various electrode insertion tools available from the manufacture such as straight electrode array, Perimodiolar electrode array, advanced bionics helix electrode array, cochlear corporation contour and contour advance electrode array. Among the straight electrode arrays, there were three different types: cochlear corporation K electrode array, MED-EL 40+ electrode array and advanced bionics J electrode array.

The K electrode array can be used in the Nucleus receiver stimulators, which have 21 active banded contacts and 10 stiffness rings. MED-EL 40+ electrode was a 31mm straight electrode by using with a claw or alligator forceps. Advanced bionics J electrode array was the most commonly used provided by advanced bionic corporation. The electrode array can be inserted manually and should be exerted from the plastic tube package prior to reattachment [4].

The Perimodiolar electrode array was brought to the market within this 5 years and it was manufactured to coil during the insertion to lay closer to the modiolar wall of the cochlea [5]. It requires different insertion techniques than straight electrode array. The contour advance electrode array was inserted along the cochlear outer wall approximately 11mm. The electrode array would coil during the insertion to reduce the force to the outer wall; hence it can obtain a more consistent perimodiolar position [5]. Advanced bionics helix electrode array was loaded with an array and tool tip [6]. The electrode was an advanced off-stylet insertion technique by pushing gently toward the cochleostomy.

Conference:10th International Conference on Bioinformatics and Biomedical Technology, May 16–18, 2018, Amsterdam, The Netherlands.

THEORETICAL ANALYSIS

Purpose of the theoretical analysis was to analyze the mechanical behavior of an inserting electrode array. When inserting a cochlear implant electrode array straight, the array would bend during the insertion along the cochlear outer wall of scala tympani (ST). Exerted force between the array tip and the ST wall during the first turn was the primary cause of trauma in cochlea [7].

Therefore, the extorted force which was the resultant force felt by surgeon should be minimized during the electrode array insertion. The model created was able to interpret the deformation when the electrode tip sliding along the ST wall. In order to analyze the behavior of electrode array, a numerical analysis method: A finite difference method (FDM) was applied to divide the electrode into finite segments. Each of the segments was treated as a small deflection cantilever beam with the linearly elastic material [8].

For this study, a long, slender cantilever beam made of the linear elastic material was modelled. It was assumed that the beam was inextensible because any change in length was assumed negligible compared with the original beam length. The cross section of the beam was assumed to be constant which indicates the effect of Poisson's ratio was neglected [9]. It was also assumed that the Bernoulli-Euler bending theory was valid. Lastly, the deflection due to the weight of the beam was assumed negligible.

Although the contact between the electrode array and the ST wall was three dimensional, the following analysis and model developed can be extended to electrode behavior and tip contact. At any of the contact point, the directional insertion force would be represented by F. It was composed of the advancing force F_1 and the force exerted on the ST wall F_s in basal turn. The insertion force breakdown diagram was shown in Figure 1.

From Figure 1, insertion force *F* determines an advancing force F_1 and a force perpendicular to ST wall. The angle of the electrode impact onto the ST was represented by α. The relationship between them was shown in the equation (1) and (2).

$$F_s = Fsin\alpha \tag{1}$$

$$F_1 = Fcos\alpha \tag{2}$$

It was assumed the insertion speed was slow and constant, thus the electrode insertion can be treated as quasi-steady. Hence, the advancing force F_1 was equal to the resisting friction force *f*. In regarding of the electrode array, the only support force F_s acts at the tip. Orthogonal components of F_s was composed of vertical axis force F_y and horizontal axis force F_x. The breakdown of support force F_s in the x and y directions were redrawn in Figure 2.

A cantilever beam of length L with a concentrated force F_s was shown in the Figure 2. The concentrated force was applied at the free end. θ_0 represents the maximum slope of the beam. δx and δy were the x and y axis displacements at the free end. Point A represents any point along the beam with coordinates (x,y). s was the arc length between point A and the fixed end of the beam.

Fig.1 Insertion force diagram when electrode array first contacts the ST outer wall in the plane of the basal turn.

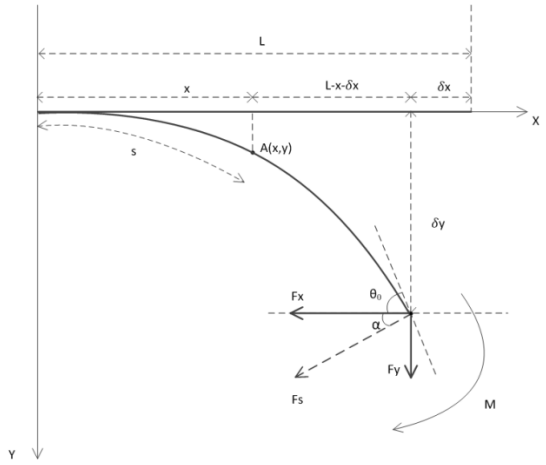

Fig.2 Breakdown of support force in the x and y axis

In Figure 2 M was the bending moment. *Fx* and *Fy* were the reaction forces in the x and y directions. α was the constant angle where force F was applied, yields

$$EI\frac{d^2\theta}{ds^2} = -(Fsin\alpha)\frac{dx}{ds} - (Fcos\alpha)\frac{dy}{ds} \tag{3}$$

In order to solve the equation, the relationship between

x, y and θ have to be found. An arc length of the cantilever beam can be approximately treated as a straight line, under the conditions of an infinitesimally small section. Substituting *ds* with trigonometry relationship for solving *dx* and *dy*, yields

$$dx = \sqrt{\frac{EI}{2F}}\frac{(cos\theta)d\theta}{\sqrt{(sin\alpha)(sin\theta_0 - sin\theta) - (cos\alpha)(cos\theta_0 - cos\theta)}} \tag{4}$$

$$dy = \sqrt{\frac{EI}{2F}}\frac{(sin\theta)d\theta}{\sqrt{(sin\alpha)(sin\theta_0 - sin\theta) - (cos\alpha)(cos\theta_0 - cos\theta)}} \tag{5}$$

Equations (4) and (5) should be integrated to describe the vertical and horizontal deflections at any points along the electrode array. However, there was no exact analytical solution to these equations. In order to find the deflected shape of the beam, MATLAB algorithm and commercial software ANSYS were applied to approximate the solutions.

To solve the equations (4) and (5), the value of the maximum angle θ_0 under constant force *F* has to be calculated. An integrating function *quadl* in MATLAB was employed to integrate θ from 0 to θ_0. The function separates the beam into 100 sections. Each section was assumed to be small enough that its arc length was approximated as a straight line. Thus, the maximum angle θ_0 in each section was calculated by the equation (3). The bisection method was applied to calculate the maximum angle θ_0 in each section. The

bisection method was a root finding algorithm, which repeatedly bisects an interval and locates the root [10]. The error between the exact maximum angle and the approached root was controlled within $1x10^{-4}$, which was 0.1‰ larger than the exact maximum angle. Next, the maximum angle θ_0 in each section was substituted into the equations (4) and (5) to calculate the *x* and *y* coordinates. After storing the first section coordinates in MATLAB, the process repeats itself to find *x* and *y* coordinates in the next section. Lastly, coordinates in every section were gathered and plotted as the deflected beam curvature.

There were a few limitations of the MATLAB solution. Firstly, the maximum angle at the free end was limited between zero and ninety degrees. Also, the program can only compute deflections of beams with a constant force applied at the free end. Lastly, during the electrode insertion, electrode length (L) inside of the cochlea would continually increase. The program could be extended to incorporate a beam with increasing length. This could be achieved by adding a variable *L(s)* to the deflection curve equation in place of the *L*. Moreover, the program could be adjusted to handle the maximum angle greater than ninety degrees.

MATERIALS AND METHODS

The electrode array used in the experiment was supplied by OTICON. The electrode array has the average diameter 0.8mm, 20 contact poles and length 26mm. To manipulate the precise impedance measurement, each wire connected from the contact poles was soldered to a circuit board and they were numbered to avoid environment disturbance. The electrode array and the circuit board were shown in Figure 3.

Each wire from the contact poles was soldered to the circuit board to force the distance fixation between them. For the reason that the capacitance of each wire changes according to the distance between them, distance fixation would minimize the capacitance disturbance and be convenient for implementing of the measurement. Measurement of electrodes impedance value would be applied both in air and conductive liquid respectively which was capable to simulate the environment of round window that was filled with perilymph. The electrodes impedance was measured by an ISO-TECH LCR1703 Meter. A software application Windmm 700 was utilized to synchronize with the meter and a PC. Readings from the meter were recorded and stored as a txt file in the PC every 0.5 seconds for further analysis.

The electrode array was inserted into a model by hand. The model was printed by a 3D printer to provide insertion track with different radius. The model and electrode array insertions were shown in Figure 4.

In Figure 4, each track was formed of a straight path 20mm following by a quarter-circle path. The radius of quarter circle paths various from 5mm to 70mm, to investigate the relationship between electrode capacitance and track radius. The diameter of each track entrance window was 2mm but the path width appeared on the surface of the model was 1mm. The arrangement not only allows an experimenter to observe electrode position but also prevents electrode protruding from the track during the insertion. The model was immersed in salt water to simulate the environment of intra-cochlear that was filled with perilymph.

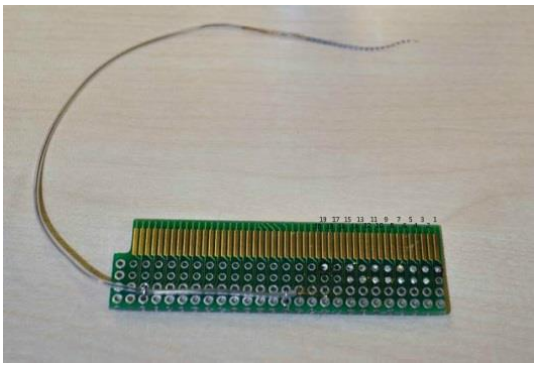

Fig.3 each wire from the contact poles of the electrode was soldered to the circuit board and numbered

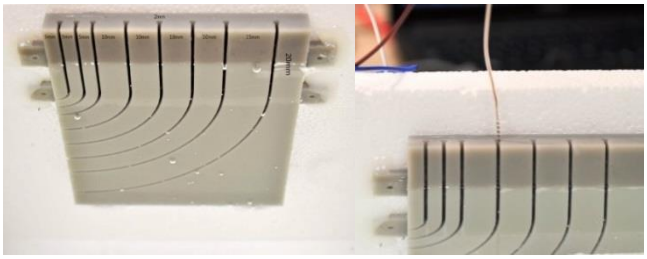

(a) **(b)**

Fig.4 A model with different radius tracks and electrode array insertion, (a) the model has eight tracks with radius from 5mm to 70mm, (b) An electrode was inserted into the fourth track

The model was fixed to the wall to allow consistent and repeatable measurements.

RESULTS AND DISCUSSION

Among the eight tracks shown in Figure 4, three tracks were selected to perform the measurement: the 1st track, the 4th track and the 8th track. Before insertions, the electrode array was filled with the liquid for 3 minutes statically to identify the capacitance noise under steady state. The maximum error was 0.75pF that was 1.9% of the original value. The error was considered as the random error and can be neglected. The 1st track in the model has the smallest radius and results of the capacitance measurement were shown in Figure 5.

In Figure 5, the y-axis represents capacitance measured in unit pF and x-axis was the insertion time in second. As can be seen from the figure, the capacitance was slowly increasing until the 10th second that represents the electrode was inserted into a straight path. It was because the distance between the two poles was slightly squeezed by hand. After that, capacitance revealed a trend of rapid increase before reaching to the steady state from 10s to 17s. It shows the electrode was passing through a quarter-circle path and distance between the two poles move rapidly closer. After 17s, the steady state indicates the electrode was fully inserted, and the inserting action was stopped for 5 seconds. Capacitance continues to decline significantly from the 26s to 30s due to the electrode was pulled out from the model, and it was passing through the quarter-circle path. From the 30s to 36s, capacitance revealed a trend of gradual decrease that shows the electrode was pulling through the straight path.

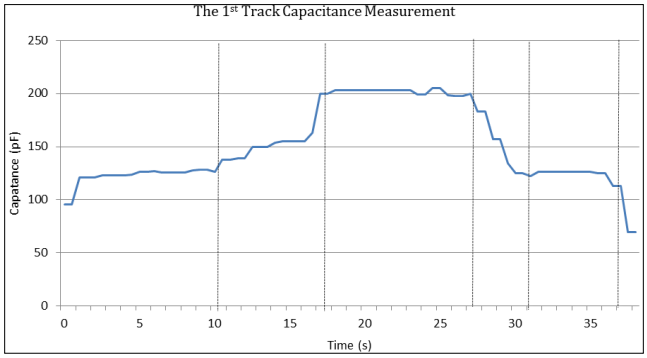

Fig.5 the 1st track capacitance measurement with capacitance measured against the insertion time

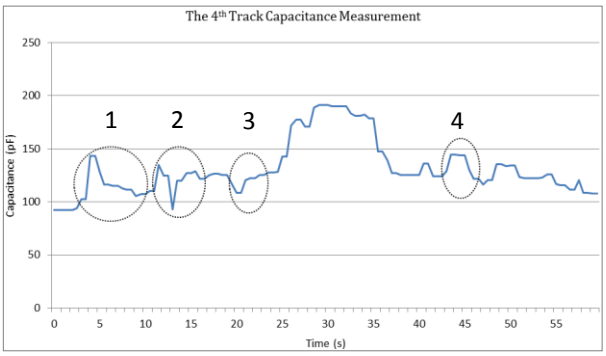

Fig. 6 the 4th track capacitance measurement with capacitance measured against the insertion time

Finally, capacitance drops dramatically to the lowest value that indicates the electrode was pulled out from the liquid. It was because the capacitance of the electrode in the air was much lower than filled with liquid.

Figure 6 shows the process of the electrode array was inserted and pulled out from the track four. During the insertion, the electrode array was inserted with extra effort intentionally to examine the relationship between the capacitance value and insertion force. The waveform fluctuations circled as 1, 2 and 3 reflect that additional force was applied to the electrode. It was because the electrode between the two measured poles was shortened and extended by extra force. That leads to the capacitance waveform fluctuations.

The capacitance was gradually increasing until the 25th second that represents the electrode was passing through the model. The slope of rising was 2.02pF/s that was 59% lower than passing through the first track. It was because the quarter-circle path radius of the fourth track was 400% longer than the first track. In order to examine the outcome, an extreme condition was applied. The electrode was inserted into the 8th track whose radius was 1300% longer than the first track. The result was shown in Figure 6. The capacitance was at a steady state from 26s to 35s that indicate the electrode was fully inserted and the inserting movement was stopped for 9 seconds. After that, capacitance continues to decline accompanied with four waveform fluctuations, for example, circled 4. They were due to the pulling pauses in the process of dragging out.

Track eight has the largest radius, and the result of the capacitance changing was shown in Figure 7. In Figure 7, the capacitance stays in the same range, between 99pF and 130pF, during all the inserting and pulling out period. There were three fluctuations of the waveform.

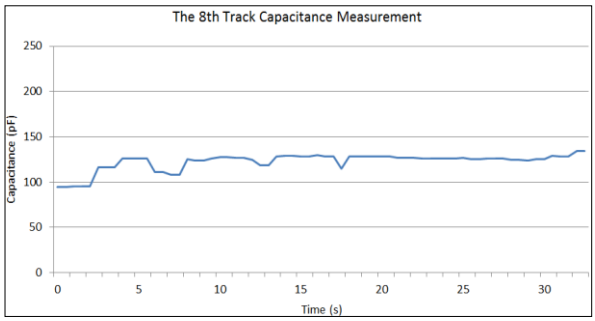

Fig.7 the 8th track capacitance measurement with capacitance measured against the insertion time

However, it was challenging to associate waveform variations with inserting actions, straight path and the quarter-circle path. It was due to the distance between the two measured poles was not changing significantly throughout the experiment.

The results of these feasibility experiments prove that capacitance measurement can contribute significantly in detecting the curvature of an electrode. Capacitance changes were noticeable when electrode position changes as demonstrated by fluctuation. In order to further investigate the changing of capacitance, MATLAB was used to drive the first derivation on the capacitance waveform. The result of the first track was shown in Figure 8. The y-axis represents capacitance difference, and the x-axis was the insertion time in second. As can be seen from the Figure 8, the capacitance largest changes occurred when the electrode was fully inserted at 17s. There were also capacitance variations at the beginning of insertion and extraction. These variations were not significant compared to the largest changes. In general, the electrode in this experiment was inserted and extracted smoothly.

The result of the first derivation on the capacitance waveform in the fourth track was shown in Figure 9. The electrode was inserted with extra effort intentionally, and the waveform fluctuates significantly. The changing of capacitance was indeed sensitive to the relative force and movement of the electrode to the model. During the insertion and extraction process, the electrode was surmised not to be manipulated continually, due to the fluctuations from the waveform. The largest change occurred when the electrode was fully inserted, disregarding of the first fluctuation which was caused by jamming. The capacitance change at full insertion was 21.6% lower comparing to the Figure 8. It proves that the capacitance variation was lower at a larger radius.

The conclusion can also be proved from the first derivations on the eighth track capacitance change waveform, which was shown in Figure 10. The maximum capacitance change appears at the beginning of insertion. However the value of the changing was 54% lower than the largest capacitance change in previous two experiments. It was due to the distance between the two measured poles was not changing significantly. The result demonstrates the capacitance measured was sensitive to the distance between the two poles. The capacitance changes would not be static due to the electrode movement. However, through the investigation on the capacitance changes in optimal insertion, operational failures such as tip rollovers and penetrations can be discriminated and avoided.

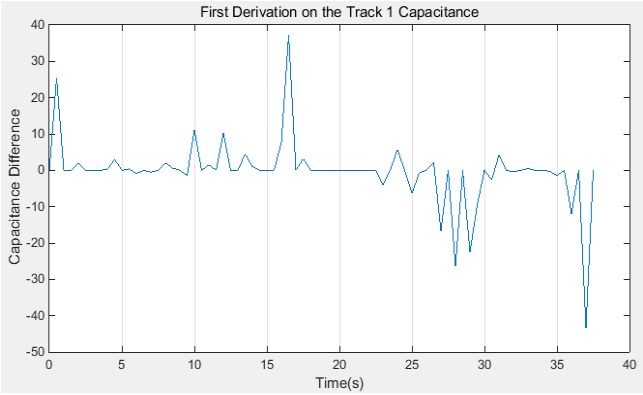

Fig. 8 First derivation on the first track capacitance waveform with capacitance changes against the insertion time

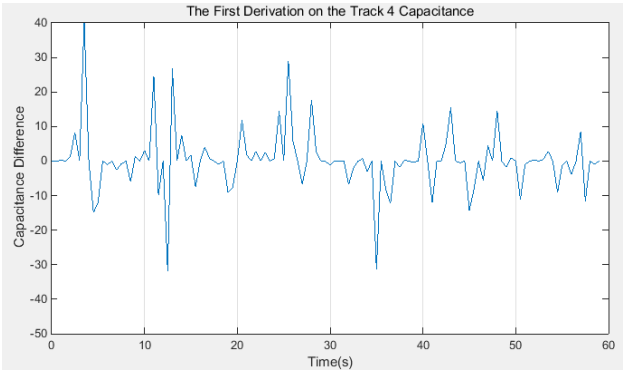

Fig. 9 First derivations on the fourth track capacitance change waveform with intended extra force

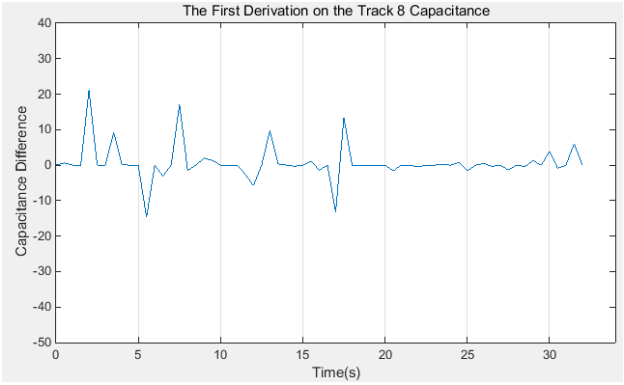

Fig.10 First derivations on the eighth track capacitance change waveform

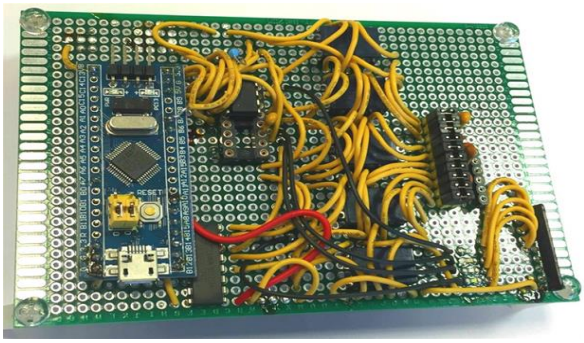

Fig. 11 a circuit board was developed to switch the measuring channel and measure only one couple of poles at a time.

CONCLUSION

A mathematical model for a large beam deflection had been created to simulate the contact between CI electrode and scala tympani wall. Based on the model, an aluminum beam was simulated by MATLAB. The result compares with ANSYS simulation result with only 2% differences. Feasibility of measurement of electrode capacitance and impedance during electrode insertion had been implemented. The analysis demonstrated that capacitance could reflect the electrode shape was changing as expected. However, the measurement can only measure one pair of metal poles at a time, which was not enough to thoroughly investigate the changing of the electrode shape. Therefore, a circuit board had been programmed to implement a multi-channel capacitance measurement.

The continuous capacitance measurement system was feasible for implementation with cochlear implant electrode insertion. It was able to record the capacitance as expected. The capacitance measurements change with electrode array shape and force as identified on capacitance change waveform.

Results from the present study indicate that continues capacitance respond appropriately to an electrode inserting movement. At the moment, only one coupled poles were measured. It was due to the voltage across the poles would influence each other when measuring two or more couples of poles. In order to solve the problem, a circuit board was developed to measure a pair at a time. The circuit board had been designed and displaced in Figure 11. The circuit board was based on an oscillation circuit to measure the capacitance. It had been programmed to switch the channels automatically. In this method, five couples of poles can be measured within 500ms, and the results were available to be transmitted to a PC for further analysis.

REFERENCES

[1] Joseph B. Roberson, Jr, MD (2005) 'Cochlear implant surgery: Minimally invasive technique', Operative Techniques in Otolaryngology, 16(2), pp. 74-77.

[2] Wilson, B.S., 2004. Engineering design of cochlear implants. In Cochlear implants: auditory prostheses and electric hearing (pp. 14-52). Springer New York.

[3] Niparko, J. K. (Ed.). 2009. Cochlear implants: Principles & practices. Lippincott Williams & Wilkins.pp.103-108

[4] Susan B. Waltzman, J. Thomas Roland Jr (2006) Cochlear Implants, 2nd edn., New York: Thieme Medical Publishers. pp. 120-122.

[5] Roland, P. S., & Wright, C. G., 2006. Surgical aspects of cochlear implantation: mechanisms of insertional trauma. In Cochlear and Brainstem Implants (Vol. 64, pp. 11-30). Karger Publishers.

[6] Kratchman, L.B., Schurzig, D., McRackan, T.R., Balachandran, R., Noble, J.H., Webster III, R.J. and Labadie, R.F., 2012. A manually operated, advance off-stylet insertion tool for minimally invasive cochlear implantation surgery. IEEE Transactions on Biomedical Engineering, 59(10), pp.2792-2800.

[7] Lee, J., Nadol Jr, J. B., & Eddington, D. K. (2010). Factors associated with incomplete insertion of electrodes in cochlear implant surgery: a histopathologic study. Audiology and Neurotology, 16(2), 69-81.

[8] Wang, T. M., Lee, S. L., & Zienkiewicz, O. C. (1961). A numerical analysis of large deflections of beams. International Journal of Mechanical Sciences,3(3), 219-228.

[9] Feynman, R. P., Leighton, R. B., & Sands, M. (1963). The Feynman: Lectures on Physics, Mainly Electromagnetism and Matter. Vol. 2. 1963.

[10] Burden, R. L., & Faires, J. D. (1985). 2.1 The bisection algorithm. Numerical Analysis. Prindle, Weber & Schmidt, Boston, MA., pp. 31

A Novel Sensing System for Robotic Cochlear Implants Electrode Array Placement

Lei Hou, Xinli Du, and Nikolaos V. Boulgouris

***Abstract*— Intracochlear electrode array insertion was a crucial process for cochlear implant surgery. However, the behavior of the intracochlear electrode array during the insertion remains unclear to surgeons. In order to minimize or eliminate the trauma induced by electrode array insertion, we propose an electrode capacitive sensing method to sense the behaviors of the electrode array during the robotic insertion process. To this end, we take a single capacitance measurement between electrode pair 1 and 2 during the robotic insertion and show experimentally that capacitance signal curves were systematically affected by intracochlear forces between the scala tympani wall and the contact electrode. Therefore, electrode capacitance measurements help track the motion between the electrode array and the cochlear lateral wall during surgeries.**

INTRODUCTION

A Cochlear electrode implant (CI), was a small electronic device that can directly stimulate the auditory nerve, which was located in the inner ear. Unlike a hearing aid, a cochlear implant converts sounds into electrical pulses [1]. Adults and children with severe or profound hearing loss can be helped with a cochlear implant [2]. The cochlear implant consists of two parts: the external (outside) part and the internal part, which combine to assist patients to perceive sound.

The internal part of the cochlear implant consists of a radio receiver and a cochlear implant electrode array [3]. They were surgically placed under the skin. The receiver can detect the coded electric impulses and outputs to the electrode array that had been surgically implanted into the cochlea. The electric impulses stimulate the auditory nerve, and they were interpreted by the brain as sound.

Electrode arrays have the capacity of electrical stimulation of the auditory nerve in the cochlea that was differentially sensitive to sound frequencies to initiate sound sensations. Picture of an electrode array was shown in Figure 1.

An electrode array was formed by conductive, corrosion-resistant, noble metal platinum-iridium alloy that was separated by insulating material, e.g., poly dimethyl siloxane (PDMS) [4]. Ideally, each electrode should be placed directly to contact with a single nerve ending that allows receiving sound waves of appropriate frequencies. The number of electrodes in the array depends on the manufacturer, but typically was between 4 to 22, which was less than 1% of the number of hair cells present in the cochlea [4].

L. Hou was with Brunel University, London, UB8 3PH. the UK (corresponding author, e-mail: lei.hou@brunel.ac.uk).

X. Du was with Brunel University, London, UB8 3PH. the UK. (E-mail: xinli.du@brunel.ac.uk).

N.V. Boulgouris was with Brunel University, London, UB8 3PH. the UK. (E-mail: nikolaos.boulgouris@brunel.ac.uk).

Fig. 1 Example of an electrode array.

Insertion of the cochlear implant electrode array was the most crucial step in the cochlear implant surgery. The insertion progress was a pierce event: the round window (RT) membrane was incised. The electrode array should be optimally inserted into the scala tympani. Round window insertion causes greatest initial intra-cochlear damage. It was due to the inserting electrode being bent significantly to follow the cochlear canal [5].

The insertion also results in more abnormal tissue formation in the basal cochlea. To date, the insertion of electrode array had been done by hand, and the tools implemented by surgeons do not provide any feedback or other means of sensing. The method reflected as electrode feed and placement was a particularly skilled surgical task. It would be expected that a more experienced surgeon would enhance the ideal result. The electrode was small, flexible and has a particular orientation to align with the tissue structure [6].

The electrode array insertion often damages the cochlear structures, such as the basilar membrane and cochlear lateral wall. In order to preserve the cochlea and minimize the intracochlear trauma, means of robotic-assisted insertion system, the evaluation of insertion force, insertion friction force and electrode impedance would be applied.

In 2005, Roland first evaluated the manual insertion characteristics of Contour electrode arrays with the Advance Off-Stylet (AOS) versus the Standard Insertion Technique (SIT) [8]. Five Contour electrode arrays with the Standard Insertion Technique (SIT) were evaluated in the same cochlear models and temporal bones. The applied forces during electrode arrays insertion in the cochlear model and in whole human temporal bones were measured by a load cell. According to the experimental force results, the average insertion forces in human temporal bones could be twice as high as those recorded in a plastic cochlear model.

A preliminary study of robotic assistance by a steerable electrode array for cochlear implant surgery was proposed in [8]. The work in [8] developed the mathematic model, path planning and calibration for the cochlear steerable electrode array in an effort to minimize the contact forces between the electrode array tip and the cochlear outer wall. A robotic assistance system had been designed to compare the insertion

forces of steerable electrode arrays with those non-steerable electrode arrays.

In 2008, Zhang et al. improved the steerable electrode array to adjust its angle of approach according to the opening of scala tympani [9]. It demonstrated that changing the angle of approach by a four DoF robot can further reduce the electrode array insertion forces [9]. In the same period, Schurzig et al. improved the automated insertion tool which could not only sense insertion forces but also setup the insertion velocity profiles and settings repeatable [10].

Hussong et al. developed a prototype automated insertion system for the cochlear implant surgery in 2008 [11]. The mechatronic device was capable of achieving the Advance Off-Stylet (AOS) technique and proofed the tool's ability in cochlear implant surgery. The first experimental result demonstrated that the device has the capability to perform general automatically cochlear implant electrodes insertions. After that, they improved the automated insertion tool and developed a mathematical model to stimulate the entry angel and path-planning [11]. 30 insertions were performed by the device to insert into an artificial model. Under the condition of lubrication, the electrode array was inserted into the model in 29 out of 30 insertions, with one electrode tip fold-over. It was claimed that the automated insertion tool was the only possibility for cochlear implant electrodes insertion at that time.

Force application of the automated insertion tool was evaluated in 2010 [12]. A transparent artificial scala tympani model was utilized to achieve standard experimental conditions. However, the major drawback of the system was the lacked of an integrated haptic feedback. Haptic feedback was necessary for minimally invasive surgery as it was the only information about possible damage to tissue structures. The force measurement and feedback have to be integrated into the automated insertion tool. Secondly, the measurement system only applied in a plane but not in 3D of the cochlea. Lastly, the recorded force data by the automated insertion system has to be compared and evaluated with the manual insertion under the same conditions in three dimensions. This research gap was fulfilled by Majdani et al. in 2010.

The force data of the Advance Off-Stylet (AOS) technique during the cochlear implant electrodes insertion operated by human and by an automated insertion tool was collected by Majdani et al. [13]. The force data was recorded and compared by three experienced surgeons who inserted the CI electrode array 26 times and by the robotic insertion tool 8 times. Experimental results demonstrated that although the average insertion force of the insertion tool was larger than that of the surgeons, the automated device was more reliable during the insertions [13].

In the same period, Schurzig et al. improved the automated insertion tool which could not only sense insertion forces but also setup the insertion velocity profiles and settings repeatable [14]. These insertion profiles help to quantify the insertion characteristics such as electrode forces, velocities and displacements.

However, among the mentioned robotic tools above, electrode insertion paths had to be planned prior to experiments. It indicates that a high-resolution CT scanner has to be applied to obtain a high-resolution image of the cochlea before operations. The process would increase the cost to a great extent and extend the operation time significantly [15]. Also, additional actuators and sensors had to be integrated into the electrode to control the shape of the electrode. The study provided a significant indication to the potential improvement of robotic-assisted cochlear implant surgery.

In 2012, Clark et al. proposed a new prototype device to reduce electrode insertion forces [16]. The authors utilized a manipulator magnet to guide a magnetically tipped cochlear implant electrode during the insertion. In 2014, the first reported master-slave–assisted cochlear implant cochleostomy using the da Vinci Si system was performed [17]. Among them, insertion force directly applied to the intracochlear structures was a key element of intracochlear trauma and residual hearing loss [7]. Electrode array insertion force as low as 26mN to 35mN may result in a rupture of the basilar membrane [19]. Consequently, the assessment of array insertion force was necessary to evaluate the electrode array's design and its mechanical behavior.

MATERIALS AND METHODS

Electrode Array

The electrode array utilized in this project was a standard electrode array designed by OTICON with the basal diameter of 1.07mm and 0.5mm at apex [19]. The electrode array holds 20 active platinum contact electrodes and has deep insertion length of 26mm. These contact electrodes have the capacity to simulate the complete sound spectrum of the human cochlea.

In order to implement a precise capacitance measurement, each wire connected from the contact electrodes was soldered to a 20-pin male dual row header connector. The connector, as well as the electrode, was mounted onto a circuit board to avoid damaging the wires. The electrode and the mounted circuit board were shown in Figure 2.

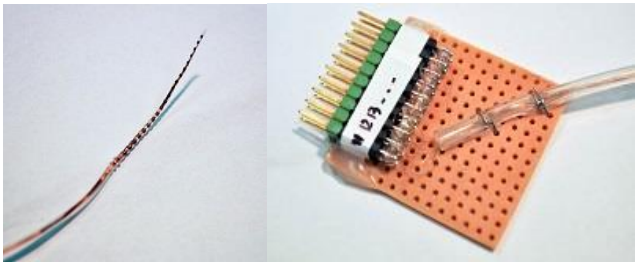

(a) (b)

Fig. 2 Electrode array and mounted circuit board. (a) The electrode array utilized in the experiment that holds 20 active platinum contact electrodes, (b) The electrode was fixed onto a circuit board with wires connected to a 20-pin male dual row header connector.

This mounted circuit board forces the distance fixation between each wire. It would minimize the capacitance disturbance and be reliable for implementing the measurement. The board would be glued onto the insertion arm.

Automated Electrode Array Feed System

The electrode array feed system was composed of two translation stages (M-404, Physik Instrumente, Germany), one

rotational device (M-061, Physik Instrumente, Germany), one three-axis force sensor (Nano17 Titanium Transducer, ATI Industrial Automation, USA) and an electrode array holder. Two translation stages and one rotational device were driven by one servo controller individually (C-863, Physik Instrumente, Germany). The automated electrode array feed system was set up as shown in Figure 3.

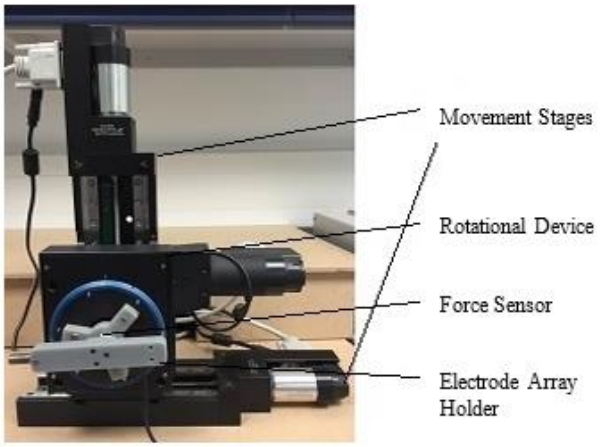

Fig. 3 The electrode feed system was composed of two axis movement stages, one rotational device, one three-axis force sensor and an electrode array holder.

They were controlled by software MATLAB (2012b, MathWorks Inc., USA) to generate precise horizontal, vertical and rotational movement with high resolution up to 0.012 μm. The three-axis force sensor was integrated between the electrode array holder and the rotational device to collect force data from all three Cartesian Coordinates (ATI). Force data was collected by a data acquisition card (DAQ) device (USB-6211, National Instruments Corporation Ltd, U.K.). Before each experiment, the system was calibrated by a supplied load file to convert the input voltage signal to a force reading.

A translucent cochlear model was firmly glued onto a supporter before experiments. The cochlear model and the supporter were printed by 3D printers with the materials Veroclear and Accura 60 respectively. Both were non-conductive materials. The supporter was glued onto the bottom of a glass. The glass was filled with conducting liquid that has the same conductance as the biologic liquid inside of the cochlea. The inner path was carefully washed by a needle to avoid any bubbles attaching to the inner track.

The electrode array holder was screwed onto the force sensor and the rotational device. It has a central lumen to clip the electrode array straight before insertion. The tip of the clinically used electrode array was placed at the entry of the cochlear model. The progress was shown in Figure 4.

Due to the electrode array's own stiffness, the tip of the array was placed in close proximity to the inner side wall. After alignment, the electrode array was inserted into the cochlear model at a constant speed 0.1mm/s to a depth of 37mm. Twelve insertions were performed by the automated feed system. The insertion force and capacitive information

Fig. 4 Before the insertion, the electrode array was clipped straight at t entry of the translucent cochlear model. It was placed in close proximity to the inner side wall.

from electrode pair 1 and 2 were collected and evaluated. The average force and capacitive results of them were shown in Figure 6.

Electrodes Capacitance Sensing

As there were 20 contact electrodes in the electrode array and each of the electrodes has a wire connect to a pin header, the capacitance between any two electrodes can be measured by a capacitance meter (LCR-1703, ISOTECH, U.K.). The measured data can be recorded and stored in software WINDMM700 at 2 Hz.

The whole insertion progress was recorded by a HD video camera (FS200, Canon, Japan) to analyze the behavior of the electrode array inside of the model. The start position of the first spiral was defined as 0° following the horizontal axis, as shown in Figure 5.

The path above the start position of spiral was straight, which simulates the round window insertion. The finish position of the first spiral was defined to be 90° which follows the vertical axis. The finish position of the second spiral was defined to be 180° and the finish of the third spiral was defined to be 270°. This logarithmic spiral shape follows the biological structure of the cochlea. However, during the insertion, the electrode array would only follow the spiral curve until full contact occurs between the first two electrodes with the outer side wall.

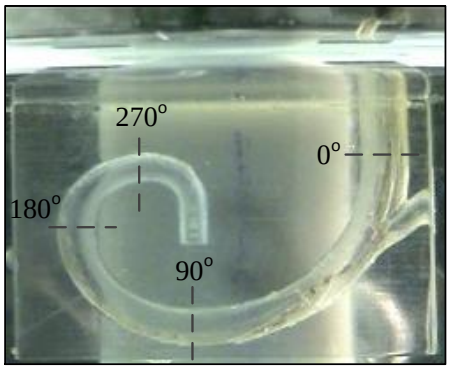

Fig 5. Definition of the angle of insertion. The start position of the first spiral was defined to be 0°.

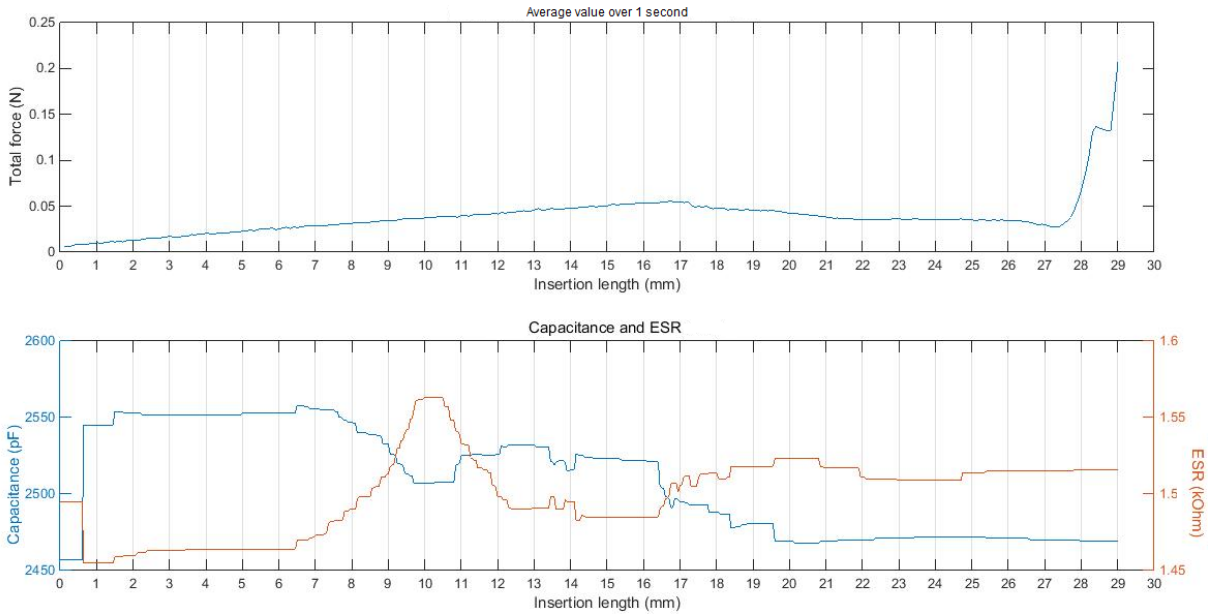

Fig. 6 Comparison between the force and impedance results. Top: average force profile against the insertion length, Bottom: Capacitance and Equivalent Series Resistance signals against insertion length.

RESULTS AND DISCUSSION

In our experiments, the insertion position was close to the inner wall of the cochlear model. The insertion speed was 0.1mm/s and insertion length was 29 mm. After the insertion, the tip of the electrode array stayed at 180º of the cochlear model. The temperature was at room temperature, 25ºC. The fluid conductance was 14.3 S/m.

The insertion progress was repeated twelve times, and all of the insertions were smoothly inserted, i.e., to 180 degree of the artificial model. A representation of the average force and impedance measurements during one of the experiments was shown in Figure 6.

In the beginning, before the angle was 0 degree, the electrode array was inserting along a straight, inner wall, where there was limited force applied to the electrodes. Thus, the capacitance increases slowly. During the second stage, there were many activities. First, both of the electrodes made contact with the inner wall, leading to the capacitance to drop dramatically from 2550 to 2500 (2%). After 11mm, the tip of the electrode started to move away from the inner wall, leading to an increase of the capacitance due to the conductivity effect. At 13mm, the first electrode starts to make contact with the bottom wall. The buckling and releasing event caused buckling of the electrode array. In the capacitance panel, there were fluctuations after 16.5mm. From the insertion length, both of the electrodes contacted the bottom wall, thus, leading the capacitance to decrease slowly. After 20mm, the electrode array had been inserted smoothly and the capacitance was shown as stable. The results demonstrated that the array has to be inserted close to the inner track with a low insertion speed of 0.1 mm/s selected to avoid buckling and damage. The insertion force profiles for the twelve insertions were evaluated. From Figure 6, the insertion force was demonstrated as not an efficient method in detecting the array behaviors inside of the cochlear model. Thus, another sensing method should be developed in order to sense the detailed behaviors during the electrode array insertions.

By comparing the recorded video with the capacitance fluctuation, the movement of the electrode array was shown in the screen cut. There were four sections of the electrode array insertion up until 180º: before 7mm, between 7mm and the first contact at the bottom of the outer wall, between when the tip first makes contact and the slide along the wall, and, lastly, the continually sliding section following along the cochlear wall. From the signal fluctuations, the corresponding four insertion lengths of changing were: 9mm, 13mm 16mm, and 19mm. The video screen shot of these insertion lengths were shown in Figure 7.

The major factor affecting the capacitance reading was the conductance of the liquid. Thus, at the beginning, the electrode array started to slide along the inner cochlear wall. The capacitance was slowly increasing until it reached 8.5mm.

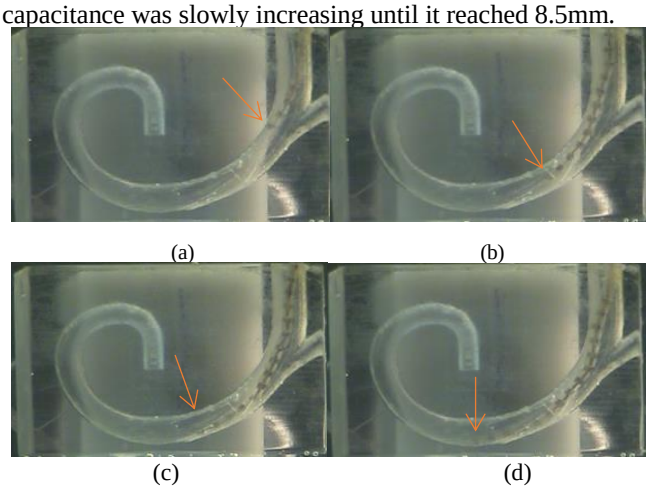

Fig. 7 Different insertion progress states. (a) 9mm insertions, the tip of the electrode starts to touch the inner wall. (b) The electrode array has already separated from the inner cochlear wall. (c) The electrode array touches the outer cochlear wall. (d) 19mm; the electrode array lies down at the bottom of the model.

After that, the electrodes contacted the cochlear inner wall, which decreased the signals to a great extent. After 11mm, the tip of the electrode started to leave the inner wall and no force was applied to the electrodes. The capacitance started to increase and the series resistance was slowly decreasing. At the insertion length of 16.5mm, buckling and rushing happened, which resulted in fluctuations of the capacitance and small changes in the ESR series. After 19mm, the tip of the electrode array was laying completely at the bottom of the cochlear model. The electrode array began to insert, following the shape of the cochlear model until 29 mm, where it was 180 degrees in regards to the entry point. From 19mm, the capacitance between the tips of the two electrodes was slowly increasing and became steady after 22mm. It demonstrated a uniform insertion progress of the electrode array.

Further improvement can be applied in establishing a force model of the electrode array deflections. The model could simulate the contact force between the electrode array and the cochlear wall during the whole insertion process. As the capacitive sensing method would provide more insertion details, it can be improved to discriminate certain failure patterns inside the cochlea.

CONCLUSION

The impact force of the electrode array on the cochlear lateral wall had been assessed as a key element of intra-cochlear trauma and residual hearing loss. The electrode array design and mechanical behaviour were on the basis of the force profiles. However, insertion force profiles could not reflect the electrode array motions during the insertion in detail. Failure inserting features such as tip fold-over and buckling may occur without changing of the insertion forces. Continuous impedance measurement (CIM) had been recognized to fulfil the research gap. Among the measured impedance signals, for the first time, the capacitive signal from the electrodes was gathered and evaluated. Comparing to resistance and inductance signals, capacitance signal was more sensitive, consistent and reliable. The measurements have confirmed that the capacitive signals values were systematically affected by intracochlear forces between the scala tympani wall and the contact electrode. Results reveal that the capacitance sensing method was capable of recognizing electrode array positions when fed into the cochlear model.

Further work would be on the direction of improving the insertion model, classifying particular failure behaviours, and characterizing electrode array position.

References

[1] J. P. Rauschecker and R. V. Shannon, “Sending sound to the brain,” Science, vol. 295, no. 5557. 2002.

[2] A. A. Eshraghi, N. W. Yang, and T. J. Balkany, “Comparative study of cochlear damage with three perimodiolar electrode designs,” Laryngoscope, vol. 113, no. 3, pp. 415–419, 2003.

[3] A. R. Møller, “Physiological basis for cochlear and auditory brainstem implants,” Advances in Oto-Rhino-Laryngology, vol. 64. pp. 206–223, 2006.

[4] B. S. Wilson, “Engineering Design of Cochlear Implants,” in Cochlear Implants: Auditory Prostheses and Electric Hearing, 2004, pp. 14–52.
G. M. Clark et al., “A Multiple-Electrode Intracochlear,” Arch Otolaryngol Head Neck Surg, vol. 113, pp. 825–828, 1987.

[5] J. K. Niparko, Cochlear Implants: Principles and Practices, 2nd ed. Lippincott Williams and Wilkins, 2008.

[6] P. S. Roland and C. G. Wright, “Surgical aspects of cochlear implantation: Mechanisms of insertional trauma,” Advances in Oto-Rhino-Laryngology, vol. 64. pp. 11–30, 2006.

[7] J. Zhang, K. Xu, N. Simaan, and S. Manolidis, “A Pilot Study of Robot-Assisted Cochlear Implant Surgery Using Steerable Electrode Arrays,” MICCAI Int. Conf. Med. Image Comput. Comput. Interv., vol. 9, no. Pt 1, pp. 33–40, 2006.

[8] J. Zhang, W. Wei, S. Manolidis, J. T. Roland, and N. Simaan, “Path planning and workspace determination for robot-assisted insertion of steerable electrode arrays for cochlear implant surgery,” in Lecture Notes in Computer Science (including subseries Lecture Notes in Artificial Intelligence and Lecture Notes in Bioinformatics), 2008, vol. 5242 LNCS, no. PART 2, pp. 692–700.

[9] D. Schurzig, R. J. Webster, M. S. Dietrich, and R. F. Labadie, “Force of cochlear implant electrode insertion performed by a robotic insertion tool: Comparison of traditional versus advance off-stylet techniques,” *Otol. Neurotol.*, vol. 31, no. 8, pp. 1207–1210, 2010.

[10] Hussong, A., Rau, T., Eilers, H., Baron, S., Heimann, B., Leinung, M., Lenarz, T. and Majdani, O., 2008, August. Conception and design of an automated insertion tool for cochlear implants. In Engineering in Medicine and Biology Society, 2008. EMBS 2008. 30th Annual International Conference of the IEEE (pp. 5593-5596).

[11] T. S. Rau, A. Hussong, M. Leinung, T. Lenarz, and O. Majdani, “Automated insertion of preformed cochlear implant electrodes: Evaluation of curling behaviour and insertion forces on an artificial cochlear model,” *Int. J. Comput. Assist. Radiol. Surg.*, vol. 5, no. 2, pp. 173–181, 2010.

[12] O. Majdani *et al.*, “Force measurement of insertion of cochlear implant electrode arrays in vitro: Comparison of surgeon to automated insertion tool,” *Acta Otolaryngol.*, vol. 130, no. 1, pp. 31–36, 2010.

[13] D. Schurzig, R. J. Webster, M. S. Dietrich, and R. F. Labadie, “Force of cochlear implant electrode insertion performed by a robotic insertion tool: Comparison of traditional versus advance off-stylet techniques,” Otol. Neurotol., vol. 31, no. 8, pp. 1207–1210, 2010.

[14] T. Stöver et al., “Evaluation of the Advance Off-Stylet insertion technique and the cochlear insertion tool in temporal bones,” Otol. Neurotol., vol. 26, no. 6, pp. 1161–1170, 2005.

[15] J. R. Clark, L. Leon, F. M. Warren, and J. J. Abbott, “Investigation of magnetic guidance of cochlear implants,” IEEE Int. Conf. Intell. Robot. Syst., pp. 1321–1326, 2011.

[16] T. Ishii, M. Takayama, and Y. Takahashi, “Mechanical properties of human round window, basilar and reissner’s membranes,” Acta Otolaryngol., vol. 115, no. S519, pp. 78–82, 1995.

[17] M. L. Carlson et al., “Prevalence and timing of individual cochlear implant electrode failures,” Otol. Neurotol., vol. 31, no. 6, pp. 893–898, 2010.

[18] oticonmedical, “Digisonic® SP cochlear implant.,” 2017. [Online]. Available: https://www.oticonmedical.com/cochlear-implants/solutions/systems/digisonic-sp-cochlear-implant. [Accessed: 22-May-2018].

Appendix 2 Electrode array insertion force profiles

In this section, 14 force profiles during CI array insertions were randomly selected and displayed. The insertion conditions for them were identical. Plots of insertion force varied significantly from individual insertions, although the average force profile followed expectation. The results high deviations demonstrated that the insertion force was not an efficient method in detecting the array behaviours inside of the cochlear model.

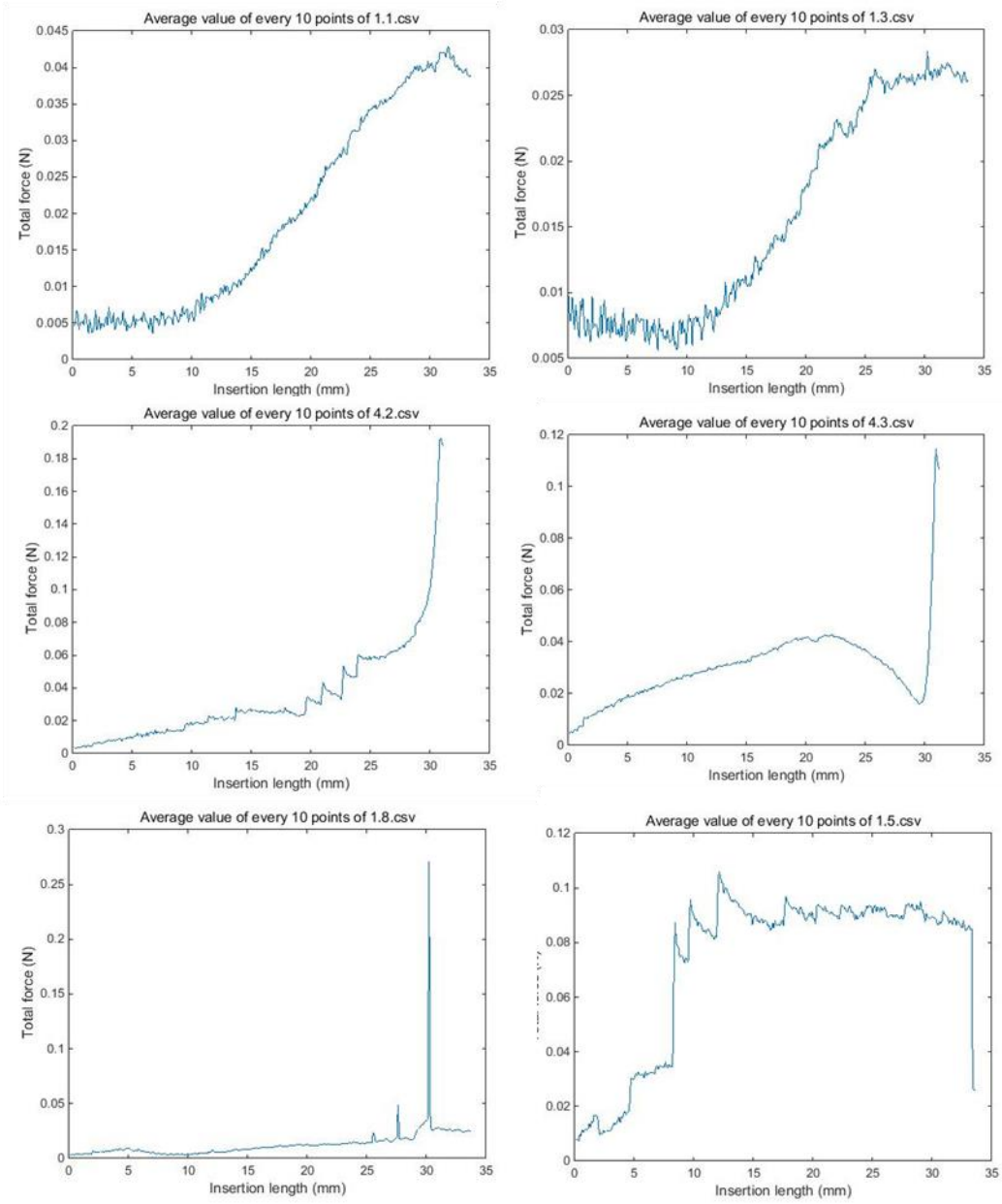

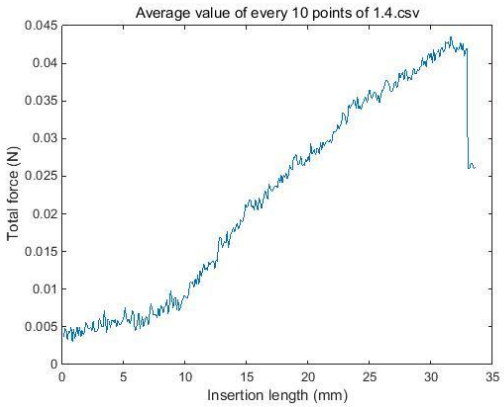
Average value of every 10 points of 1.4.csv
Total force (N)
Insertion length (mm)

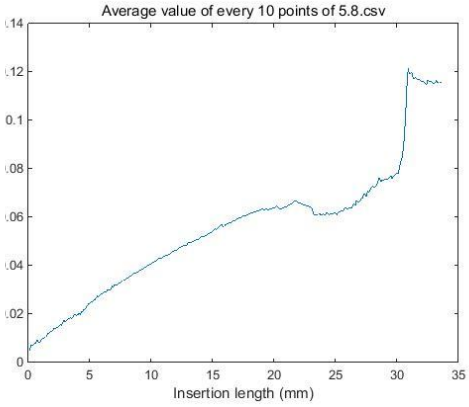
Average value of every 10 points of 5.8.csv
Insertion length (mm)

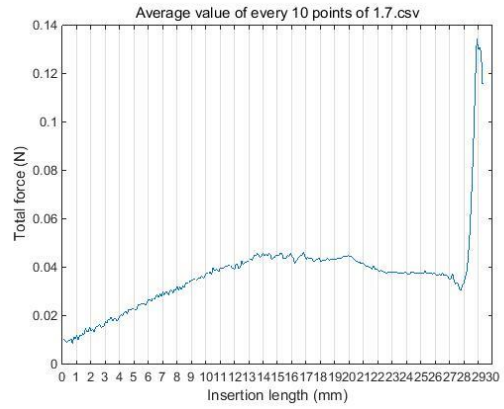
Average value of every 10 points of 1.7.csv
Total force (N)
Insertion length (mm)

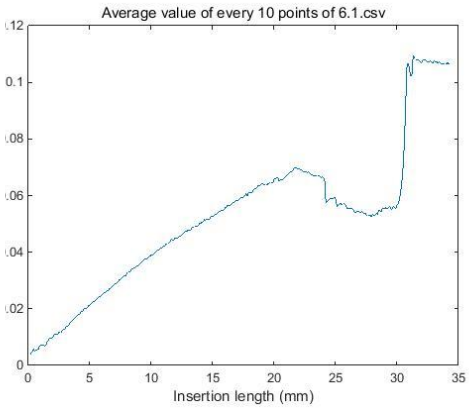
Average value of every 10 points of 6.1.csv
Insertion length (mm)

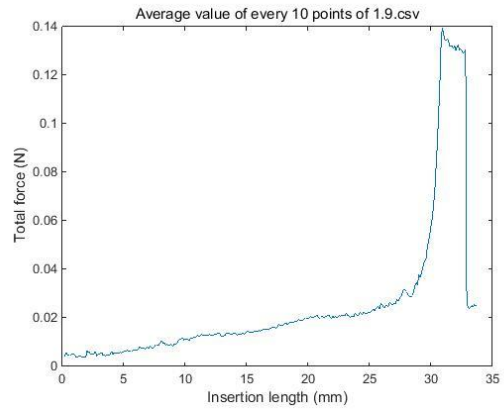
Average value of every 10 points of 1.9.csv
Total force (N)
Insertion length (mm)

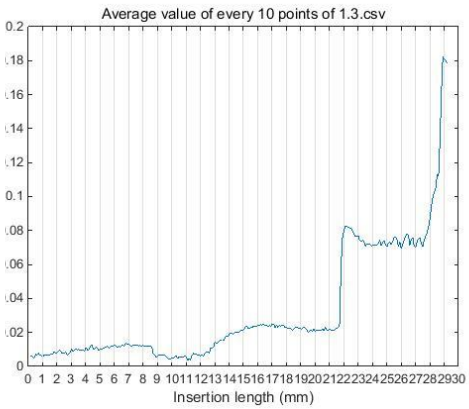
Average value of every 10 points of 1.3.csv
Insertion length (mm)

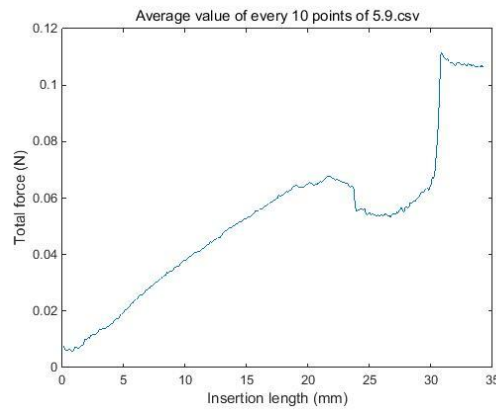
Average value of every 10 points of 5.9.csv
Total force (N)
Insertion length (mm)

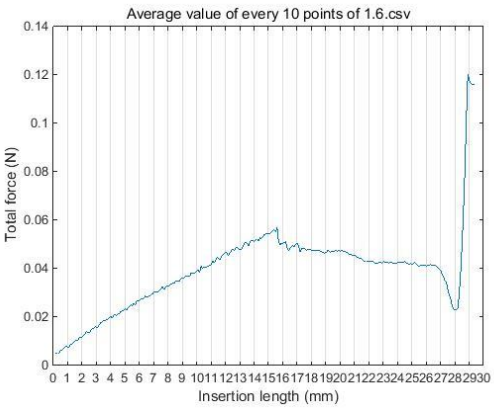
Average value of every 10 points of 1.6.csv
Total force (N)
Insertion length (mm)

Appendix 3: Continuous Capacitance and Switching Channel Capacitance

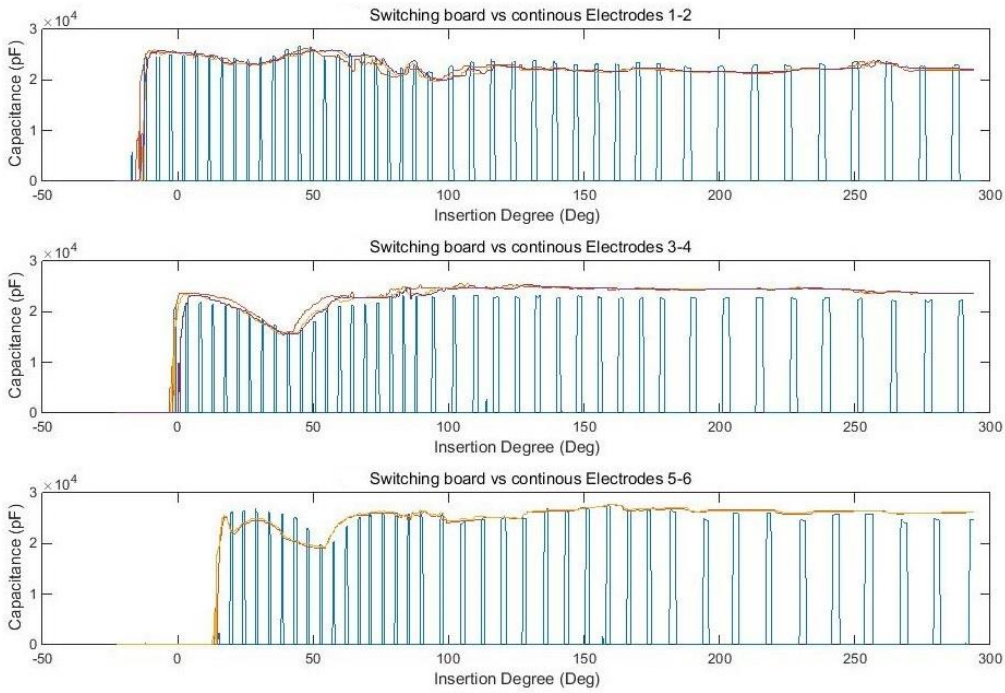

Continuous capacitance measurement and switching channel board measurement of three coupled electrodes, with electrode pair (1, 2) (top panel), electrode pair (3, 4) (middle panel) and electrode pair (5, 6) (bottom panel). The abscissa axis was insertion angle in regard of the first two electrodes and the ordinate unit was capacitance in pF. Each trace from the panel represents one individual robotic insertion.

The top panel represents the continuous capacitance measurement of electrode 1-2 as well as the first channel of the switching channel board measurement. Electrodes 1 and 2 were also the tip two electrodes of the electrode array. Electrode 3-4 and the second channel in the switching board measurements were shown in the middle panel. Electrode 5-6 and the third channel were represented in the bottom panel. All the insertions were made to at the same speed 0.05mm/s and with the same depth. Each trace in every panel represents 1 individual insertion, with 3 insertions for the top panel, 3 insertions for middle panel and 2 insertions for the bottom panel. The switching board capacitance measurement was represented by the square wave. In the beginning of each trace, capacitance increases significantly, which indicates the two measured electrodes were filled with liquid. As could be seen from this figure, the fluctuations of switching board measurement match all continuous measurements well, especially in the rapid descent and ascent area.

Appendix 4: Curvature of the Deflected Cantilever Beam solved by MATLAB program and software ANSYS.

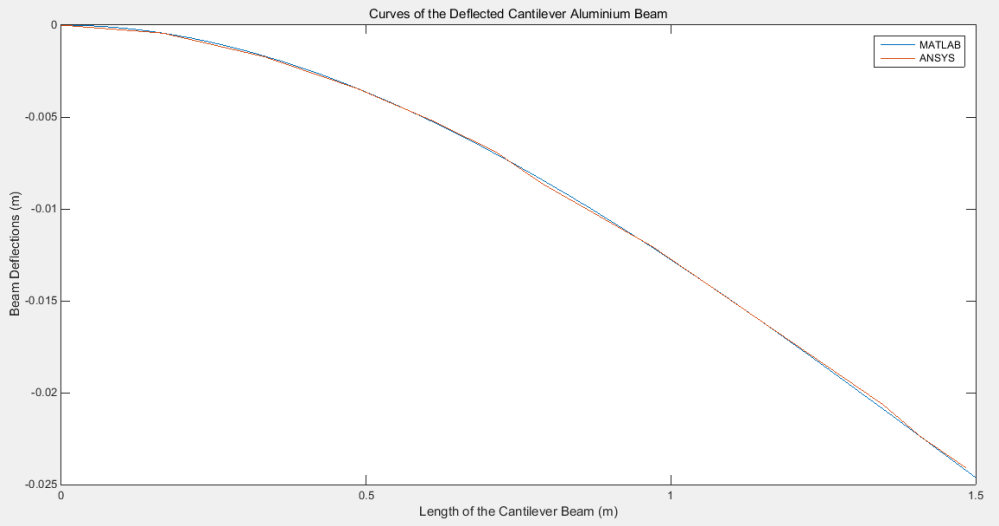

REFERENCES

[1] O.-H. and N. Hopkins, Johns Medicine; Surgery, "Cochlear Implant Information," *CI Information*, 2014. .

[2] Action on Hearing Loss, "Facts and figures on hearing loss and tinnitus," *Action Hear. Loss Factsheet*, pp. 1–11, 2015.

[3] G. Pouryaghoub, R. Mehrdad, and S. Mohammadi, "Interaction of smoking and occupational noise exposure on hearing loss: A cross-sectional study," *BMC Public Health*, vol. 7, 2007.

[4] G. Clark, *Cochlear Implants: fundimentals and applications*, 1st ed. New York: Springer-Verlag , 2003.

[5] P. W. Alberti, "The Anatomy and Physiology of the Ear and Hearing," in *Occupational Exposure to Noise: Evaluation, Prevention and Control*, 1995, pp. 53–62.

[6] M. Teimouri *et al.*, *Detecting diseases in medical prescriptions using data mining tools and combining techniques*, 2nd ed., vol. 15, no. September. London: Academic Press, 2016.

[7] P. Simmons and D. Young, *Nerve Cells and Animal Behaviour*, 3rd ed., no. April. Cambridge University Press, 1989.

[8] H. Davis, "XXXVIII The excitation of nerve impulses in the cochlea," *Ann. Otol. Rhinol. ... Laryngol.*, vol. 63, no. 2, pp. 469–480, 1954.

[9] R. Smith, Hildebrand, and G. Van Camp, "Deafness and Hereditary Hearing Loss Overview," *GeneReviews*, vol. 6, pp. 1–13, 2010.

[10] Y. Raz and L. Lustig, "Surgical management of conductive hearing loss in children," *Otolaryngologic Clinics of North America*, vol. 35, no. 4. pp. 853–875, 2002.

[11] S. Epstein and J. S. Reilly, "Sensorineural hearing loss.," *Pediatr. Clin. North Am.*, vol. 36, no. 6, pp. 1501–1520, 1989.

[12] L. Poissant, *Interfaces et sensorialité*. 2003.

[13] A. A. Eshraghi, R. Nazarian, F. F. Telischi, S. M. Rajguru, E. Truy, and C. Gupta, "The Cochlear Implant: Historical Aspects and Future Prospects," *Anat. Rec.*, vol. 295, no. 11, pp. 1967–1980, 2012.

[14] G. M. Clark, Y. C. Tong, R. Black, I. C. Forster, J. F. Patrick, and D. J. Dewhurst, "A multiple electrode cochlear implant," *J. Laryngol. Otol.*, vol. 91, no. 11, pp. 935–945, 1977.

[15] G. M. Clark, "The multiple-channel cochlear implant: the interface between sound and the central nervous system for hearing, speech, and language in deaf people--a personal perspective," *Philos. Trans. R. Soc. B Biol. Sci.*, vol. 361, no. 1469, pp. 791–810, 2006.

[16] A. Djourno and C. Eyries, "Auditory prosthesis by means of a distant electrical stimulation of the sensory nerve with the use of an indwelt coiling," *Press. médicale*, vol. 65, p. 1417, 1957.

[17] J. Zhang, K. Xu, N. Simaan, and S. Manolidis, "A Pilot Study of Robot-Assisted Cochlear Implant Surgery Using Steerable Electrode Arrays," *MICCAI Int. Conf. Med. Image Comput. Comput. Interv.*, vol. 9, no. Pt 1, pp. 33–40, 2006.

[18] C. J. Brown, P. J. Abbas, H. Fryauf-Bertschy, D. Kelsay, and B. J. Gantz, "Intraoperative and postoperative electrically evoked auditory brain stem responses in nucleus cochlear implant users: Implications for the fitting process," *Ear Hear.*, vol. 15, no. 2, pp. 168–176, 1994.

[19] J. P. Rauschecker and R. V. Shannon, "Sending sound to the brain," *Science*, vol. 295, no. 5557. 2002.

[20] A. A. Eshraghi, N. W. Yang, and T. J. Balkany, "Comparative study of cochlear damage with three perimodiolar electrode designs," *Laryngoscope*, vol. 113, no. 3, pp. 415–419, 2003.

[21] Health Direct, "Cochlear Implant" 2012. [Online]. Available: https://www.healthdirect.gov.au/cochlear-implant. [Accessed: 23-May-2018].

[22] A. R. Møller, "Physiological basis for cochlear and auditory brainstem implants," *Advances in Oto-Rhino-Laryngology*, vol. 64. pp. 206–223, 2006.

[23] A. J. Parkinson, J. Arcaroli, S. J. Staller, P. L. Arndt, A. Cosgriff, and K. Ebinger, "The nucleus 24 contour cochlear implant system: adult clinical trial results.," *Ear Hear.*, vol. 23, no. 1 Suppl, p. 41S–48S, 2002.

[24] B. S. Wilson, "Engineering Design of Cochlear Implants," in *Cochlear Implants: Auditory Prostheses and Electric Hearing*, 2004, pp. 14–52.

[25] J. K. Niparko, *Cochlear Implants: Principles and Practices*, 2nd ed. Lippincott Williams and Wilkins, 2008.

[26] S. J. Rebscher, "Considerations for design of future cochlear implant electrode arrays: Electrode array stiffness, size," *J. Rehabil. Res. Dev.*, vol. 45, no. 5, pp. 731–748, 2008.

[27] J. R. Clark, L. Leon, F. M. Warren, and J. J. Abbott, "Magnetic Guidance of Cochlear Implants: Proof-of-Concept and Initial Feasibility Study," *J. Med. Device.*, 2012.

[28] W. Gstoettner, P. Franz, J. Hamzavi, H. Plenk, W. Baumgartner, and C. Czerny, "Intracochlear position of cochlear implant electrodes," *Acta Otolaryngol.*, 1999.

[29] J. T. Roland, "A model for cochlear implant electrode insertion and force evaluation: Results with a new electrode design and insertion technique," *Laryngoscope*, vol. 115, no. 8, pp. 1325–1339, 2005.

[30] C. T. Tan *et al.*, "Real-time measurement of electrode impedance during intracochlear electrode insertion," *Laryngoscope*, vol. 123, no. 4, pp. 1028–1032, 2013.

[31] P. S. Roland and C. G. Wright, "Surgical aspects of cochlear implantation: Mechanisms of insertional trauma," *Advances in Oto-Rhino-Laryngology*, vol. 64. pp. 11–30, 2006.

[32] J. Zhang, W. Wei, S. Manolidis, J. T. Roland, and N. Simaan, "Path planning and workspace determination for robot-assisted insertion of steerable electrode arrays for cochlear implant surgery," in *Lecture Notes in Computer Science (including subseries Lecture Notes in Artificial Intelligence and Lecture Notes in Bioinformatics)*, 2008, vol. 5242 LNCS, no. PART 2, pp. 692–700.

[33] A. Hussong, T. S. Rau, T. Ortmaier, B. Heimann, T. Lenarz, and O. Majdani, "An automated insertion tool for cochlear implants: Another step towards atraumatic cochlear implant surgery," *Int. J. Comput. Assist. Radiol. Surg.*, vol. 5, no. 2, pp. 163–171, 2010.

[34] T. S. Rau, A. Hussong, M. Leinung, T. Lenarz, and O. Majdani, "Automated insertion of preformed cochlear implant electrodes: Evaluation of curling behaviour and insertion forces on an artificial cochlear model," *Int. J. Comput. Assist. Radiol. Surg.*, vol. 5, no. 2, pp. 173–181, 2010.

[35] O. Majdani *et al.*, "Force measurement of insertion of cochlear implant electrode arrays in vitro: Comparison of surgeon to automated insertion tool," *Acta Otolaryngol.*, vol. 130, no. 1, pp. 31–36, 2010.

[36] D. Schurzig, R. J. Webster, M. S. Dietrich, and R. F. Labadie, "Force of cochlear implant electrode insertion performed by a robotic insertion tool: Comparison of traditional versus advance off-stylet techniques," *Otol. Neurotol.*, vol. 31, no. 8, pp. 1207–1210, 2010.

[37] T. Stöver *et al.*, "Evaluation of the Advance Off-Stylet insertion technique and the cochlear insertion tool in temporal bones," *Otol. Neurotol.*, vol. 26, no. 6, pp. 1161–1170, 2005.

[38] J. R. Clark, L. Leon, F. M. Warren, and J. J. Abbott, "Investigation of magnetic guidance of cochlear implants," *IEEE Int. Conf. Intell. Robot. Syst.*, pp. 1321–1326, 2011.

[39] W. P. Liu *et al.*, "Cadaveric feasibility study of da Vinci Si-assisted cochlear implant with augmented visual navigation for otologic surgery," *JAMA Otolaryngol. - Head Neck Surg.*, vol. 140, no. 3, pp. 208–214, 2014.

[40] E. Lehnhardt, "[Intracochlear placement of cochlear implant electrodes in soft surgery technique].," *HNO*, vol. 41, no. 7, pp. 356–9, 1993.

[41] A. V Hodges, J. Schloffman, and T. Balkany, "Conservation of residual hearing with cochlear implantation," *Am. J. Otol.*, vol. 18, no. 2, pp. 179–183, 1997.

[42] O. Adunka and J. Kiefer, "Impact of electrode insertion depth on intracochlear trauma," *Otolaryngol. - Head Neck Surg.*, vol. 135, no. 3, pp. 374–382, 2006.

[43] C. Von Ilberg *et al.*, "Electric-acoustic stimulation of the auditory system. New technology for severe hearing loss," *Orl*, vol. 61, no. 6, pp. 334–340, 1999.

[44] B. J. Gantz and C. W. Turner, "Combining acoustic and electrical hearing," *Laryngoscope*, vol. 113, no. 10, pp. 1726–1730, 2003.

[45] J. Kiefer *et al.*, "Conservation of low-frequency hearing in cochlear implantation," *Acta Otolaryngol.*, vol. 124, no. 3, pp. 272–280, 2004.

[46] D. De Seta *et al.*, "Damage to inner ear structure during cochlear implantation: Correlation between insertion force and radio-histological findings in temporal

bone specimens," *Hear. Res.*, vol. 344, pp. 90–97, 2017.

[47] T. Ishii, M. Takayama, and Y. Takahashi, "Mechanical properties of human round window, basilar and reissner's membranes," *Acta Otolaryngol.*, vol. 115, no. S519, pp. 78–82, 1995.

[48] O. F. Adunka, H. C. Pillsbury, and J. Kiefer, "Combining perimodiolar electrode placement and atraumatic insertion properties in cochlear implantation - Fact or fantasy?," *Acta Otolaryngol.*, vol. 126, no. 5, pp. 475–482, 2006.

[49] C. A. Todd, F. Naghdy, and M. J. Svehla, "Force application during cochlear implant insertion: An analysis for improvement of surgeon technique," *IEEE Trans. Biomed. Eng.*, vol. 54, no. 7, pp. 1247–1255, 2007.

[50] A. Radeloff *et al.*, "A coated electrode carrier for cochlear implantation reduces insertion forces," *Laryngoscope*, vol. 119, no. 5, pp. 959–963, 2009.

[51] R. J. S. Briggs *et al.*, "Development and evaluation of the modiolar research array--multi-centre collaborative study in human temporal bones.," *Cochlear Implants Int.*, vol. 12, no. 3, pp. 129–39, 2011.

[52] G. Kontorinis, T. Lenarz, T. Stöver, and G. Paasche, "Impact of the insertion speed of cochlear implant electrodes on the insertion forces," *Otol. Neurotol.*, vol. 32, no. 4, pp. 565–570, 2011.

[53] S. Helbig, C. Settevendemie, M. MacK, U. Baumann, M. Helbig, and T. Stöver, "Evaluation of an electrode prototype for atraumatic cochlear implantation in hearing preservation candidates: Preliminary results from a temporal bone study," *Otol. Neurotol.*, vol. 32, no. 3, pp. 419–423, 2011.

[54] M. Miroir, Y. Nguyen, G. Kazmitcheff, E. Ferrary, O. Sterkers, and A. B. Grayeli, "Friction force measurement during cochlear implant insertion: Application to a force-controlled insertion tool design," *Otol. Neurotol.*, vol. 33, no. 6, pp. 1092–1100, 2012.

[55] oticonmedical, "Digisonic® SP cochlear implant.," 2017. [Online]. Available: https://www.oticonmedical.com/cochlear-implants/solutions/systems/digisonic-sp-cochlear-implant. [Accessed: 22-May-2018].

[56] L. Rădulescu *et al.*, "Multicenter evaluation of Neurelec Digisonic® SP cochlear implant reliability.," *Eur. Arch. Otorhinolaryngol.*, vol. 270, no. 4, pp. 1507–1512, 2013.

[57] Y. Nguyen *et al.*, "Cochlear implant insertion forces in microdissected human cochlea to evaluate a prototype array," *Audiol. Neurotol.*, vol. 17, no. 5, pp.

290–298, 2012.

[58] Y. Nguyen, G. Kazmitcheff, D. De Seta, M. Miroir, E. Ferrary, and O. Sterkers, "Definition of metrics to evaluate cochlear array insertion forces performed with forceps, insertion tool, or motorized tool in temporal bone specimens," *Biomed Res. Int.*, vol. 2014, 2014.

[59] J. P. Kobler, D. Beckmann, T. S. Rau, O. Majdani, and T. Ortmaier, "An automated insertion tool for cochlear implants with integrated force sensing capability," *Int. J. Comput. Assist. Radiol. Surg.*, vol. 9, no. 3, pp. 481–494, 2014.

[60] J. Pile, G. B. Wanna, and N. Simaan, "Force-based flexible path plans for robotic electrode insertion," in *Proceedings - IEEE International Conference on Robotics and Automation*, 2014, pp. 297–303.

[61] P. Rohani *et al.*, "Forces and trauma associated with minimally invasive image-guided cochlear implantation," in *Otolaryngology - Head and Neck Surgery (United States)*, 2014, vol. 150, no. 4, pp. 638–645.

[62] S. A. Wade, J. B. Fallon, A. K. Wise, R. K. Shepherd, N. L. James, and P. R. Stoddart, "Measurement of forces at the tip of a cochlear implant during insertion," *IEEE Trans. Biomed. Eng.*, 2014.

[63] E. Avci, T. Nauwelaers, V. Hamacher, and A. Kral, "Three-dimensional force profile during cochlear implantation depends on individual geometry and insertion trauma," *Ear Hear.*, vol. 38, no. 3, pp. e168–e179, 2017.

[64] M. Mirsalehi *et al.*, "Insertion forces and intracochlear trauma in temporal bone specimens implanted with a straight atraumatic electrode array," *Eur. Arch. Oto-Rhino-Laryngology*, vol. 274, no. 5, pp. 2131–2140, 2017.

[65] C. C. Finley *et al.*, "Role of electrode placement as a contributor to variability in cochlear implant outcomes," *Otol. Neurotol.*, vol. 29, no. 7, pp. 920–928, 2008.

[66] C. Varley, "Polarization of Metallic Surfaces in Aqueous Solutions, a New Method of Obtaining Electricity from Mechanical Force, and Certain Relations between Electrostatic Induction and the Decomposition of Water. ," *Proc. R. Soc. London*, vol. 19, pp. 243–246, 1870.

[67] C. Pollak, "Improvements in or connected with electrical condensers," 1069, 1896.

[68] H. Helmholtz, "Studien über electrische Grenzschichten," *Ann. Phys.*, vol. 243, no. 7, pp. 337–382, 1879.

[69] E. Warburg, "Ueber das Verhalten sogenannter unpolarisirbarer Elektroden gegen Wechselstrom," *Ann. Phys.*, vol. 303, no. 3, pp. 493–499, 1899.

[70] L. A. Geddes, "Historical evolution of circuit models for the electrode-electrolyte interface," *Ann. Biomed. Eng.*, vol. 25, no. 1, pp. 1–14, 1997.

[71] H. Fricke, "XXXIII. *The theory of electrolytic polarization*," *London, Edinburgh, Dublin Philos. Mag. J. Sci.*, vol. 14, no. 90, pp. 310–318, 1932.

[72] E. E. Zimmerman, "The influence of temperature of polarization capacity and resistance," *Phys. Rev.*, vol. 35, no. 5, pp. 543–553, 1930.

[73] C. C. Murdock and E. E. Zimmerman, "Polarization impedance at low frequencies," *J. Appl. Phys.*, vol. 7, no. 6, pp. 211–219, 1936.

[74] J. E. B. Randles, "Kinetics of rapid electrode reactions," *Discuss. Faraday Soc.*, vol. 1, p. 11, 1947.

[75] M. Sluyters-Rehbach and J. H. Sluyters, "Sine wave methods in the study of electrode processes," *Electroanalytical Chemistry*, vol. 4, no. 1. pp. 1–128, 1970.

[76] I. Epelboin, M. Keddam, and J. C. Lestrade, "Faradaic impedances and intermediates in electrochemical reactions," *Faraday Discuss. Chem. Soc.*, vol. 56, p. 264, 1973.

[77] L. A. Geddes and L. E. Baker, "Principles of Applied Biomedical Instrumentation," *Yale J. Biol. Med.*, vol. 41, pp. 357–358, 1969.

[78] S. B. Brummer and M. J. Turner, "Electrochemical Considerations for Safe Electrical Stimulation of the Nervous System with Platinum Electrodes," *IEEE Trans. Biomed. Eng.*, vol. BME-24, no. 1, pp. 59–63, 1977.

[79] B. Onaral and H. P. Schwan, "Linear and nonlinear properties of platinum electrode polarisation. Part 1: frequency dependence at very low frequencies," *Med. Biol. Eng. Comput.*, vol. 20, no. 3, pp. 299–306, 1982.

[80] T. Ragheb and L. A. Geddes, "The polarization impedance of common electrode metals operated at low current density," *Ann. Biomed. Eng.*, vol. 19, no. 2, pp. 151–163, 1991.

[81] S. Mayer, L. A. Geddes, J. D. Bourland, and L. Ogborn, "Faradic resistance of the electrode/electrolyte interface," *Med. Biol. Eng. Comput.*, vol. 30, no. 5, pp. 538–542, 1992.

[82] L. A. Geddes and R. Roeder, "Measurement of the direct-current (Faradic)

resistance of the electrode-electrolyte interface for commonly used electrode materials," *Ann. Biomed. Eng.*, vol. 29, no. 2, pp. 181–186, 2001.

[83] M. F. Suesserman and F. A. Spelman, "System for making quantitative, in vivo measurements of inner ear tissue impedances," *Images Twenty-First Century. Proc. Annu. Int. Eng. Med. Biol. Soc.*, no. Proceedings of the Annual International Conference of the IEEE Engineering, pp. 1057–1058, 1989.

[84] M. F. Suesserman and F. A. Spelman, "Quantitative In Vivo Measurements of Inner Ear Tissue Resistivities: I. In Vitro Characterization," *IEEE Trans. Biomed. Eng.*, vol. 40, no. 10, pp. 1032–1047, 1993.

[85] M. F. Suesserman and F. A. Spelman, "Lumped-Parameter Model for In Vivo Cochlear Stimulation," *IEEE Trans. Biomed. Eng.*, vol. 40, no. 3, pp. 237–245, 1993.

[86] P. A. Busby, L. A. Whitford, P. J. Blamey, L. M. Richardson, and G. M. Clark, "Pitch perception for different modes of stimulation using the Cochlear multiple-electrode prosthesis," *J. Acoust. Soc. Am.*, vol. 95, no. 5, pp. 2658–2669, 1994.

[87] G. M. Clark, B. C. Pyman, Q. E. Bailey, R. L. Webb, and R. K. Shepherd, "Surgery for an improved multiple-channel cochlear implant," *Ann. Otol. Rhinol. Laryngol.*, vol. 93, no. 3, pp. 204–207, 1984.

[88] G. M. Clark *et al.*, "A Multiple-Electrode Intracochlear," *Arch Otolaryngol Head Neck Surg*, vol. 113, pp. 825–828, 1987.

[89] M. Merzenich and M. White, "Cochlear implant: the interface problem," *Functional electrical stimulation: ...*, vol. 3. pp. 321–340, 1977.

[90] R. C. Black and G. M. Clark, "Differential electrical excitation of the auditory nerve," *J. Acoust. Soc. Am.*, vol. 67, no. 3, pp. 868–874, 1980.

[91] R. C. Black, G. M. Clark, Y. C. Tong, and J. F. Patrick, "Current Distributions in Cochlear Stimulation," *Ann. N. Y. Acad. Sci.*, vol. 405, no. 1, pp. 137–145, 1983.

[92] Y. C. Tong and G. M. Clark, "Loudness summation, masking, and temporal interaction for sensations produced by electric stimulation of two sites in the human cochlea.," *J. Acoust. Soc. Am.*, vol. 79, no. 6, pp. 1958–66, 1986.

[93] C. van den Honert and P. H. Stypulkowski, "Single fiber mapping of spatial excitation patterns in the electrically stimulated auditory nerve," *Hear. Res.*, vol. 29, no. 2–3, pp. 195–206, 1987.

[94] H. H. Lim, Y. C. Tong, and G. M. Clark, "Forward masking patterns produced by intracochlear electrical stimulation of one and two electrode pairs in the human cochlea.," *J. Acoust. Soc. Am.*, vol. 86, no. 3, pp. 971–980, 1989.

[95] C. N. Jolly, F. A. Spelman, and B. M. Clopton, "Quadrupolar stimulation for cochlear prostheses: Modeling and experimental data," *IEEE Trans. Biomed. Eng.*, vol. 43, no. 8, pp. 857–865, 1996.

[96] M. L. French, "Electrical impedance measurements with the CI24M cochlear implant for a child with Mondini dysplasia," *Br. J. Audiol.*, vol. 33, no. 1, pp. 61–66, 1999.

[97] F. J. Vanpoucke, A. J. Zarowski, and S. A. Peeters, "Identification of the impedance model of an implanted cochlear prosthesis from intracochlear potential measurements," *IEEE Trans. Biomed. Eng.*, vol. 51, no. 12, pp. 2174–2183, 2004.

[98] C. T. M. Choi, W. D. Lai, and S. S. Lee, "A novel approach to compute the impedance matrix of a cochlear implant system incorporating an electrode-tissue interface based on finite element method," in *IEEE Transactions on Magnetics*, 2006, vol. 42, no. 4, pp. 1375–1378.

[99] M. L. Carlson *et al.*, "Prevalence and timing of individual cochlear implant electrode failures," *Otol. Neurotol.*, vol. 31, no. 6, pp. 893–898, 2010.

[100] P. Busby, K. Plant, and L. Whitford, "Electrode impedance in adults and children using the Nucleus 24 cochlear implant system," *Cochlear Implants Int.*, vol. 3, no. 2, pp. 87–103, 2002.

[101] E. Saunders *et al.*, "Threshold, comfortable level and impedance changes as a function of electrode-modiolar distance.," *Ear Hear.*, vol. 23, no. 1 Suppl, p. 28S–40S, 2002.

[102] M. Tykocinski, L. T. Cohen, and R. S. Cowan, "Measurement and analysis of access resistance and polarization impedance in cochlear implant recipients," *Otol. Neurotol.*, vol. 26, no. 5, pp. 948–956, 2005.

[103] M. L. Hughes, C. J. Brown, and P. J. Abbas, "Sensitivity and specificity of averaged electrode voltage measures in cochlear implant recipients," *Ear Hear.*, vol. 25, no. 5, pp. 431–446, 2004.

[104] J. L. Goehring, M. L. Hughes, J. L. Baudhuin, and R. P. Lusk, "How well do cochlear implant intraoperative impedance measures predict postoperative electrode function?," *Otol. Neurotol.*, vol. 34, no. 2, pp. 239–244, 2013.

[105] M. Hey *et al.*, "The Intra-Cochlear Impedance-Matrix (IIM) test for the Nucleus®cochlear implant," *Biomed. Tech.*, vol. 60, no. 2, pp. 123–133, 2015.

[106] P. Bhatti *et al.*, "Highly Flexible Silicone Coated Neural Array for Intracochlear Electrical Stimulation," *Biomed Res. Int.*, vol. 2015, 2015.

[107] G. K. A. Van Wermeskerken, A. F. Van Olphen, and G. F. Smoorenburg, "Intra- and postoperative electrode impedance of the straight and Contour arrays of the Nucleus 24 cochlear implant: Relation to T and C levels," *Int. J. Audiol.*, vol. 45, no. 9, pp. 537–544, 2006.

[108] D. M. Zeitler, A. K. Lalwani, J. T. Roland, M. G. Habib, D. Gudis, and S. B. Waltzman, "The effects of cochlear implant electrode deactivation on speech perception and in predicting device failure," *Otol. Neurotol.*, vol. 30, no. 1, pp. 7–13, 2009.

[109] J. Pile, A. D. Sweeney, S. Kumar, N. Simaan, and G. B. Wanna, "Detection of modiolar proximity through bipolar impedance measurements," *Laryngoscope*, vol. 127, no. 6, pp. 1413–1419, 2017.

[110] PI, "M-403 · M-404 Precision Translation Stage," Bedford, the UK, 2017.

[111] Physik Instrumente (PI), "User Manual C-863 Mercury^{TM} DC Motor Controller," Bedford, the UK., 2009.

[112] PI, "M-060, M-061, M-062 Precision Rotation Stages," Bedford, the UK, 2015.

[113] ATI Industrial, "Six-Axis Force/Torque Sensor System. Installation and Operation Manual.," no. March, pp. 40–48, 2016.

[114] N. Instruments, *DAQ M Series M Series User Manual NI 622x, NI 625x, and NI 628x Devices*. Austin, Texas, the U.S., 2007.

[115] ISO-TECH, "LCR1701/LCR1703 Digital Multi-meter Instruction Manual," Merseyside, the UK, 2014.

[116] STMicroelectronics, "Medium-density performance line ARM®-based 32-bit MCU with 64 or 128 KB Flash, USB, CAN, 7 timers, 2 ADCs, 9 com. Interfaces," Marlow, the UK, 2015.

[117] Keil, "ARMKeil - MDK 5.17," Texas, United States, 2016.

[118] M. Heidari and P. Azimi, "Conductivity effect on the capacitance measurement of a parallel-plate capacitive sensor system," *Res. J. Appl. Sci. Eng. Technol.*, vol. 3, no. 1, pp. 53–60, 2011.

[119] J. C. Farmer, D. V. Fix, G. V. Mack, R. W. Pekala, and J. F. Poco, "Capacitive deionization of NH4ClO4 solutions with carbon aerogel electrodes," *J. Appl. Electrochem.*, vol. 26, no. 10, 1996.

[120] E. R. Van Artsdalen and I. S. Yaffe, "Electrical conductance and density of molten salt systems: KCl-LiCl, KCl-NaCl and KCl-KI," *J. Phys. Chem.*, vol. 59, no. 2, pp. 118–127, 1955.

[121] E. L. Lewis, "The Practical Salinity Scale 1978 and Its Antecedents," *IEEE J. Ocean. Eng.*, vol. 5, no. 1, pp. 3–8, 1980.

[122] J. Gray R., "Conductivity Analyzers and Their Application," in *Environmental Instrumentation and Analysis Handbook*, 2004, pp. 491–510.

[123] C. C. Finley, B. S. Wilson, and M. W. White, "Models of Neural Responsiveness to Electrical Stimulation," in *Cochlear Implants*, 1990, pp. 55–96.

[124] W. Duff, *A Text-Book of Physics*, 4th ed. Philadelphia: P. Blakiston's Son & Co, 1908.

[125] G.- Siedel, "Finite Difference Method for Ordinary Differential Equations," *Differ. Equations*, no. 4, pp. 0–7.

[126] Davis, J.L. & Annan, Peter. Annan, A.: Ground penetrating radar for high-resolution mapping of soil and rock stratigraphy. 1989, Geophysical Prospecting 37, 531-551. Geophysical Prospecting. 37. 531 - 551. 10.1111/j.1365-2478.1989.tb02221.x.

[127] L. C. Paul and A. Sumam, "Face Recognition Using Principal Component Analysis Method," *Int. J. Adv. Res. Comput. Eng. Technol.*, vol. 1, no. 9, pp. 135–139, 2012.

[128] M. A. Turk and A. P. Pentland, "Face recognition using eigenfaces," *Proceedings. 1991 IEEE Comput. Soc. Conf. Comput. Vis. Pattern Recognit.*, pp. 586–591, 1991.

[129] A. Dhanasingh and C. Jolly, "An overview of cochlear implant electrode array designs," *Hearing Research*, vol. 356. pp. 93–103, 2017.

[130] S. K. Sen and G. A. Shaykhian, "MatLab tutorial for scientific and engineering computations. International Federation of Nonlinear Analysts (IFNA); 2008 World Congress of Nonlinear Analysts (WCNA)," *Nonlinear Anal. Theory, Methods Appl.*, vol. 71, no. 12, 2009.

[131] H. Cevikalp, M. Neamtu, M. Wilkes, and A. Barkana, "Discriminative common vectors for face recognition," *IEEE Trans. Pattern Anal. Mach. Intell.*, vol. 27, no. 1, pp. 4–13, 2005.

[132] V. Kwatra and M. Han, "Fast covariance computation and dimensionality

reduction for sub-window features in images," in *Lecture Notes in Computer Science (including subseries Lecture Notes in Artificial Intelligence and Lecture Notes in Bioinformatics)*, 2010, vol. 6312 LNCS, no. PART 2, pp. 156–169.

[133] K. Pearson, "Note on Regression and Inheritance in the Case of Two Parents," *Proc. R. Soc. London*, vol. 58, no. 1, pp. 240–242, 1895.

[134] F. Galton, "Regression Towards Mediocrity in Hereditary Stature.," *J. Anthropol. Inst. Gt. Britain Irel.*, vol. 15, p. 246, 1886.

[135] Bohinc, Klemen & kralj-iglic, Veronika & Iglic, Ales. Thickness of electrical double layer. Effect of ion size. 2001. Electrochimica Acta. 46. 3033-3040.

[136] Cyrustek Corporation. ES51919/ES51920 LCR meter chipset (2nd), 2014. [Online]. Avaliable: http://www.cyrustek.com.tw/spec/ES51920.pdf. [Accessed: 02-Apr-2019] 10.1016/S0013-4686(01)00525-4.

[137]Altman, N. S. "An introduction to kernel and nearest-neighbor nonparametric regression". (1992) The American Statistician. 46(3): 175–185. doi:10.1080/00031305.1992.10475879. hdl:1813/31637.

[138] Beyer, Kevin, et al.. 'When was "nearest neighbor" meaningful?. Database Theory—ICDT'99, 217-235. 1999

[139]Mcadams, E.T.; Henry, P.; Anderson, J.M.; Jossinet, J. Optimal electrolytic chording of silver ink electrodes for use in electrical impedance tomography. Clin. Phys. Physiol. Meas. 1992, 13, 19–23

[140] LTspice Genealogy - The Heritage of Simulation Ubiquity. LTwiki. Archived from the original on December 2, 2018.)

[141] Dickinson, E. (2017). Electrochemical Impedance Spectroscopy: Experiment, Model, and App. [online] COMSOL Multiphysics. Available at: https://uk.comsol.com/blogs/electrochemical-impedance-spectroscopy-experiment-model-and-app/ [Accessed 6 May 2019].

[142] Ohno, R., Ohnuki, H., Wang, H., Yokoyama, T., Endo, H., Tsuya, D. and Izumi, M., 2013. Electrochemical impedance spectroscopy biosensor with interdigitated electrode for detection of human immunoglobulin A. Biosensors and Bioelectronics, 40(1), pp.422-426

[143] P. Drude, Zur elektronentheorie der metalle, Annalen der Physik, 1, 566–613, 1900; 3, 369–402, 1900